The Neoarchean and Palaeoproterozoic metamorphic evolution of the Limpopo Belt's Central Zone in southern Africa

New insights from petrological investigations on amphibolite to granulite facies rocks

Dissertation zur Erlangung
des naturwissenschaftlichen Doktorgrades
der Bayerischen Julius-Maximilians-Universität Würzburg

vorgelegt von

Leo Jakob Millonig
aus
Würzburg

Würzburg 2009

Eingereicht am:

1. Gutachter:
2. Gutachter:

der Dissertation

1. Prüfer:
2. Prüfer:

der mündlichen Prüfung

Tag der mündlichen Prüfung:

Doktorurkunde ausgehändigt am:

In memory of

Prof. Dr. Harald Millonig

Contents

The Neoarchean and Palaeoproterozoic metamorphic evolution of the Limpopo Belt's Central Zone in southern Africa

New insights from petrological investigations on amphibolite to granulite facies rocks

1 Abstract

This study presents new petrological results obtained from high-grade metamorphic rocks of the Beit Bridge, Mahalapye and Phikwe Complexes, which constitute the Central Zone of the Limpopo Belt in southern Africa. These results provide detailed information about the prograde and retrograde pressure-temperature (*P-T)* evolution of the three investigated complexes and, in concert with geochronological data, form the basis for the development of a coherent geodynamic model for the evolution of the Limpopo's Central Zone. The *P-T* paths were inferred by the thorough investigation of silica-saturated and silica-undersaturated metapelitic and metabasic rocks, comprising six sillimanite-garnet-cordierite gneisses, four (garnet)-biotite-plagioclase gneisses, two garnet-orthopyroxene-biotite-K-feldspar-plagioclase gneisses, one garnet-cordierite-orthoamphibole fels, one garnet-biotite amphibolite, and one garnet-clinopyroxene amphibolite. *P-T* points and *P-T* evolutions were derived by the application of conventional geothermobarometers, and quantitative phase diagrams in the systems Na_2O - CaO - K_2O - FeO - MgO - Al_2O_3 - SiO_2 - H_2O - TiO_2 - O (NCKFMASHTiO), and MnO - TiO_2 - Na_2O - CaO - K_2O - FeO - MgO - Al_2O_3 - SiO_2 - H_2O (MnTiNCKFMASH) - using the computer software THERMOCALC and THERIAK-DOMINO.

The petrological information, in particular those obtained by comparison between observed and thermodynamically calculated mineral assemblages, zonations and modes, in combination with new and existing geochronological data provide evidence that rocks from the three investigated complexes underwent slightly different *P-T* evolutions at different times. The samples from the Bulai Pluton area (Beit Bridge Complex) provide evidence for a Neoarchean high-grade metamorphic event at ~2.64 Ga (M2), with peak *P-T* conditions of ~850°C at 8-9 kbar, and a decompression-cooling path to ~750°C at 5-6 kbar. This metamorphic evolution perhaps took place in a magmatic arc setting. In contrast, samples from the Mahalapye and Phikwe Complex document a Palaeoproterozoic event at ~2.03-2.05 Ga (M3), and were subject to different styles of prograde metamorphism. Metamorphic rocks from the Mahalapye Complex experienced a high-temperature low-pressure (*HT-LP*) metamorphic overprint, accompanied by the emplacement of voluminous granite bodies between 2.06 and 2.02 Ga, and provide evidence for a slightly prograde decompression from ~650°C/7 kbar to ~800°C/5.5 kbar. In contrast, the metamorphic rocks

from the Phikwe Complex provide evidence for a simultaneous pressure and temperature increase from ~600°C/6 kbar to ~750°C/8 kbar, in the absence of significant Palaeoproterozoic magmatism. The *HT-LP* metamorphic evolution of the Mahalapye Complex is interpreted to be initiated by the underplating of hot mafic melts, either formed in response to SE-subduction during the Kheis-Magondi orogeny, and/or by contemporaneous mantle plume activities related to the formation of the Bushveld Complex. In contrast, the prograde pressure and temperature increase reflected by the rocks from the Phikwe Complex rather reflects successive crustal stacking at ~2.03 Ga. This stacking, which is also reported from many other units throughout the Limpopo Belt, is interpreted to result from the final convergence between the Kaapvaal and Zimbabwe Cratons, perhaps caused by SE-directed compression in response to the Kheis-Magondi orogeny between ~2.06 and 1.90 Ga.

2 Zusammenfassung

Die vorliegende Doktorarbeit präsentiert neue petrologische Untersuchungen an hochgradig metamorphen Gesteinen des Beit Bridge, Mahalapye und Phikwe Komplexes, welche gemeinsam die Central Zone des Limpopo Belt im südlichen Afrika bilden. Die Ergebnisse liefern detaillierte Informationen über die pro- und retrograde Druck-Temperatur-(*P-T*)-Entwicklung der drei Komplexe und bilden, in Einklang mit geochronologischen Daten, die Grundlage für die Erstellung eines einheitlichen geodynamischen Modells der Bildung der Central Zone des Limpopo Belt. Die abgeleiteten *P-T* Pfade wurden anhand detaillierter Untersuchungen an quartzgesättigten und -untersättigten Metapeliten bis Metabasiten erstellt, wobei sechs Sillimanit-Granat-Cordierit Gneisse, vier (Granat)-Biotit-Plagioklas Gneisse, zwei Granat-Orthopyroxen-Biotit-Kalifeldspat-Plagioklas Gneisse, ein Granat-Cordierit-Orthoamphibol Fels, ein Granat-Biotit Amphibolit und ein Granat-Klinopyroxen Amphibolit untersucht wurden. *P-T* Punkte und *P-T* Entwicklungen wurden mit Hilfe von konventionellen Geothermobarometern und quantitativen Phasendiagrammen in den Systemen Na_2O - CaO - K_2O - FeO - MgO - Al_2O_3 - SiO_2 - H_2O - TiO_2 - O (NCKFMASHTiO) und MnO - TiO_2 - Na_2O - CaO - K_2O - FeO - MgO - Al_2O_3 - SiO_2 - H_2O (MnTiNCKFMASH) berechnet und abgeleitet. Die Phasendiagramme wurden mit den Programmen THERMOCALC und THERIAK-DOMINO berechnet.

Petrologische Informationen, speziell solche, die durch den Vergleich von beobeachteten/gemessenen mit thermodynamisch berechneten Mineralparagenesen, -zonierungen, -zusammensetzungen und Modalgehalten erhalten wurden zeigen, in Kombination mit neuen und bereits existierenden geochronologischen Daten, dass Gesteine der drei untersuchten Komplexe geringfügig unterschiedliche *P-T* Entwicklungen zu verschiedenen Zeiten durchliefen. Proben aus der Gegend des Bulai Plutons (Beit Bridge Komplex) belegen ein hochgradig metamorphes Ereignis im Neoarchaikum um ~2.64 Ga (M2), mit peak-metamorphen Bedingungen von ~850°C/8-9 kbar und einer retrograden Dekompression mit gleichzeitiger Abkühlung zu ~750°C/5-6 kbar. Diese metamorphe Entwicklung erfolgte vermutlich im geodynamischen Umfeld eines Magmatischen Bogens. Im Gegensatz hierzu dokumentieren Proben des Mahalapye und Phikwe Komplexes metamorphe Entwicklungen im Paläoproterozoikum um ~2.03-2.05 Ga (M3), die sich zudem im prograden Verlauf der Metamorphose voneinander unterscheiden. Metamorphe Gesteine des Mahalapye Komplexes kennzeichnet eine Hochtemperatur-Niedrigdruck-(*HT-LP*)-Metamorphose mit schwacher prograder Dekompression von ~650°C/7 kbar nach ~800°C/5.5 kbar, die mit der

Platznahme von ausgedehnten granitischen Intrusionen um ~2.06-2.02 Ga einherging. Metamorphe Gesteine des Phikwe Komplexes hingegen zeigen eine gleichzeitige Druck- und Temperaturzunahme von ~600°C/6 kbar nach ~750°C/8 kbar, die nicht mit Magmatismus im Paläoproterozoikum assoziiert war. Es wird gefolgert, dass die *HT-LP* metamorphe Entwicklung des Mahalapye Komplexes ihre Ursache in dem magmatischen „Underplating" heisser mafischer Schmelzen, als Ergebnis südost-gerichteter Subduktion während der Kheis-Magondy Orogenese, und/oder der zeitgleichen Aktivität von Mantel Plumes, in Zusammenhang mit der Bildung des Bushveld Komplexes, hat. Im Gegensatz hierzu belegen die Gesteine des Phikwe Komplexes eine prograde Druck- und Temperaturzunahme, hervorgerufen durch eine fortschreitende Krustenstapelung um ~2.03 Ga. Diese Stapelung ist bereits für zahlreiche andere geologischen Einheiten des Limpopo Belt belegt. Sie wird als eine Folge der endenden Annäherung/Kollision zwischen dem Kaapvaal und Zimbabwe Kraton interpretiert, welche durch südost-gerichtete Kompression im Zuge der Kheis-Magondy Orogenese zw. ~2.06 und 1.90 Ga hervorgerufen wurde.

3 Introduction

The Limpopo Belt of southern Africa is a high-grade metamorphic province bounded by the Zimbabwe and Kaapvaal Cratons and comprising Archean and Palaeoproterozoic lithological components (Fig. 1) - (*e.g.* Van Reenen *et al.*, 1987; Roering *et al.*, 1992; Rollinson & Blenkinsop, 1995; Berger *et al.*, 1995; Kamber *et al.*, 1995a, 1995b; Holzer *et al.*, 1998, 1999). Lithologically and structurally, it is subdivided into three distinct domains, which are separated by major shear zones. The Central Zone, which hosts several migmatitic gneisses, is bounded by the Southern and Northern Marginal Zones representing reworked rocks of the respective cratons (Fig. 1). The Limpopo Belt has long been regarded as an orogenic belt resulting from the collision of the Zimbabwe and Kaapvaal Cratons at *ca.* 2.7 Ga, with the Central Zone subsequently shifted to the west by wrench faulting (Van Reenen *et al.*, 1987, 1990; McCourt & Vearncombe, 1987, 1992; Roering *et al.*, 1992). However, recently it has been shown that all three zones experienced different *P-T* paths and different styles of tectonism, related to different orogenic processes (*e.g.* Watkeys, 1984; Rollinson, 1993; Rollinson & Blenkinsop, 1995; Berger *et al.*, 1995; Kamber *et al.*, 1995a, 1995b; Holzer *et al.*, 1998, 1999; Zeh *et al.*, 2004b, 2005a, b; Barton *et al.*, 2006).

Despite the new geochronological and petrological results obtained over the past few years, there are still controversies about the tectono-metamorphic evolution of the Limpopo Belt, in particular of the Central Zone (see *e.g.* Barton *et al.*, 2006, Rigby *et al.*, 2008 and Van Reenen *et al.*, 2008). These controversies partly result from the fact that the *P-T* evolutions, especially the prograde *P-T* paths, of many geological complexes (terranes) are unknown. Thus, to understand the structural-metamorphic-magmatic history of the Limpopo Belt unambiguous field information in combination with detailed petrological and geochronological techniques are required (*e.g.* Zeh *et al.*, 2004a; Kelsey *et al.*, 2003; Halpin *et al.*, 2007; see also Baldwin *et al.*, 2005).

This thesis focuses on the petrological evolution of the Central Zone of the Limpopo Belt, as defined by *e.g.* Aldiss (1991). Aldiss (1991) and Barton *et al.* (2006) subdivide the Central Zone into (1) the Mahalapye Complex, (2) the Phikwe Complex and (3) the Beit Bridge Complex (Fig. 1). The criteria used to distinguish these complexes are lithological and stratigraphic criteria, the tectonic style, fabric orientation and metamorphism (Aldiss, 1991). Furthermore, the different complexes contain different mineral deposits and are separated from each other by several kilometer wide shear zones (Barton *et al.*, 2006). Therefore the term

"terrane" rather than "complex" was suggested by Barton *et al.* (2006). However, in this study the term "complex" is applied following the nomenclature used in most of the (recently) published articles about the Limpopo Belt.

In this context the interested reader may be referred to recent studies of Iole Spalla *et al.* (2005), in which the authors adress the "*tectono-thermal memory of rocks* and *the definition of tectono-metamorphic units*" and to Brown (2007), who reviews "*Metamorphic Conditions in Orogenic Belts*". Brown (2007) also gives a comprehensional review about recent advances in the techniques used to obtain geochronological and petrological data (*e.g. P-T* pseudosection calculations) and interpreting this data in a geotectonic context.

4 Geological setting of the Limpopo Belt

The Limpopo Belt of Southern Africa is a high-grade metamorphic province which comprises Archean and Palaeoproterozoic lithologic components, and is bounded by the Zimbabwe and Kaapvaal Cratons (Fig. 1). Detailed overviews of the geological setting, geochronological data and metamorphic *P-T*-paths of the Limpopo Belt are found in *e.g.* Kröner *et al.* (1999), Zeh *et al.* (2004b, 2005a, b, 2007), Barton *et al.* (2006), Kramers *et al.* (2007), and Rigby *et al.* (2008). Here only key information relevant for the present study is repeated.

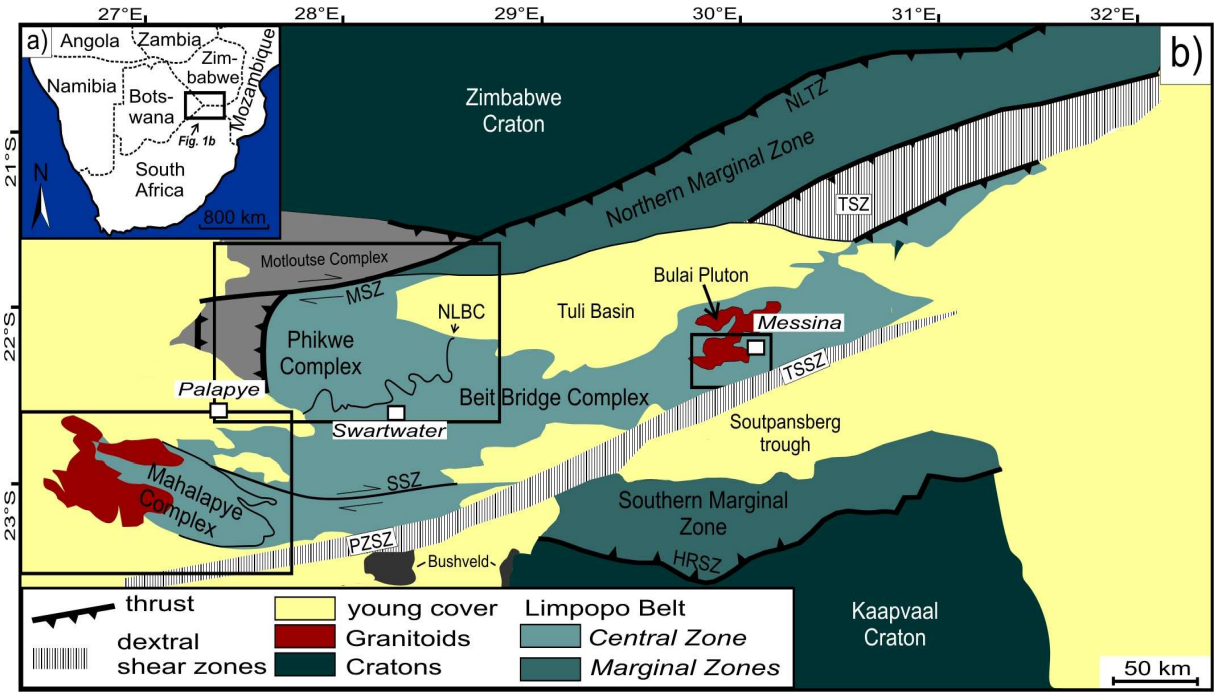

Fig. 1. a) location of the Limpopo Belt in southern Africa (modified after Barton *et al.*, 2006). The box shows the area of b). b) simplified geological map of the studied part of Limpopo Belt showing the complexes comprising it, major magmatic intrusions and faults (modified after Aldiss, 1991; Carney *et al.*, 1994; Holzer *et al.*, 1999 and Barton *et al.*, 2006). NLTZ = Northern Limpopo Thrust Zone, TSZ = Triangle Shear Zone, TSSZ = Tshipise Straigthening Zone, *MSZ* = Magogaphate Shear Zone, SSZ

= Sunnyside Shear Zone, PSZ = Palala-Zoetfontein Shear Zone, HRSZ = Hout River Shear Zone. NLBC = northern limit of Beit Bridge Group (after Aldiss, 1991). Black boxes indicate positions of detailed maps of the respective complexes and study areas as shown in Fig. 2 (Mahalapye Complex), Fig. 20 (Phikwe Complex) and Fig. 44 (Bulai Pluton area (Beit Bridge Complex)).

The Beit Bridge Complex hosts the *ca.* 3.2-3.3 Ga Sand River TTG Suite (TTG = tonalites, trondjemites and granodiorites), the Messina layered intrusion (Barton, 1983; Barton & Sergeev, 1997; Kröner *et al.*, 1999) and numerous Neoarchean granitic to granodioritic orthogneisses with ages between 2.73 and 2.60 Ga, such as the Alldays, Singelele, Bulai, Zanzibar and Zoetfontain gneisses (*e.g.*, Jaeckel *et al.,* 1997; Kröner *et al.*, 1999, Zeh *et al.*, 2007). Based on detrital zircon ages and lithological-structural differences the supracrustal paragneisses of the Beit Bridge Complex may be divided into three, unconformity bounded successions, >3.1 Ga, 3.1-2.6 Ga, and <2.6 Ga (*e.g.*, Brandl, 1992; Kröner *et al.*, 1998, 1999; Barton *et al.*, 2003; Buick *et al.*, 2003). Quartzites and metapelites from within the older unconformity-bounded succession contain zircons with U-Pb ages of 3.2 to 3.8 Ga, suggesting that a yet unrecognized, very old protolith must exist within the Beit Bridge Complex (Armstrong *et al.*, 1988; Barton & Sergeev, 1997; Kröner *et al.*, 1998). Bulk geochemical investigations on quartzites and metapelites from the Messina area indicate a variety of felsic and basic sources, including post- to late-Archean, K-rich granites for the metasediments (Taylor *et al.*, 1986; Boryta & Condie, 1990).

Geochronological, structural and petrological data provide evidence that the Limpopo's Central Zone was affected by at least three structural-magmatic-metamorphic events (see Tab. 1); during the Paleoarchean at 3.0-3.28 Ga (D1, M1), the Neoarchean at 2.52-2.65 Ga (D2, M2) and the Palaeoproterozoic at 2.0-2.03 Ga (D3, M3) - (*e.g.*, Van Reenen *et al.*, 1987; Holzer *et al.*, 1998, 1999; Jaeckel *et al.*, 1997; Kröner *et al.*, 1999; Van Reenen *et al.*, 2004; Barton *et al.*, 2006; Zeh *et al.*, 2007).

Tab. 1. Synopsis of igneous and metamorphic events in the Limpopo Belt

SMZ	Central Zone				NMZ
	Western part		Central part	Eastern part	
	Mahalapye area	W-Alldays area	Venetia area	Messina area BBC SRG 3.28 Ga (I) 3.14 Ga (M1)	
2.66-2.69 Ga (I)		Avoca 2.65 Ga (I) ??? (M2)	Regina 2.65 Ga (I) **Bulai 2.61 Ga (I)**	Singelele 2.65 Ga (I) 2.61 Ga (M2)	2.58-2.71 Ga (I)
	2.02-2.06 Ga (I) 2.00-2.03 Ga (M3) (>750ºC/>6kbar)	2.02 Ga (M3) (>780ºC/>5.7kbar)	2.01 -2.07 Ga (M3) (650-720ºC/6-7kbar)	2.02 - 2.03 Ga (M3) (830ºC/8kbar)	

SMZ - Southern Marginal Zone, NMZ - Northern Marginal Zone, BBC-Beitbridge Complex, SRG-Sand River Gneiss (I) - Intrusion ages, (M1, M2, M3) - metamorphic events , (M1 and M2) - anatexis in the Sand River Gneiss area, (780ºC/5.7kbar) - metamorphic peak conditions (for references see text).

The Paleoarchean event is constrained by geochronological data (Rb-Sr, Pb-Pb and U-Pb) and field relationships, indicating that the TTG's of the Sand River orthogneiss suite (Fig. 44) intruded at 3.2-3.3 Ga and underwent a high-grade structural-metamorphic overprint prior to the intrusion of basalt dykes at 3.0 Ga (Barton *et al.*, 1977, 1990; Kröner *et al.*, 1998; Zeh *et al.*, 2007).The Neoarchean high-grade event (D2/M2) is suggested to be coeval or slightly younger than the voluminous magmatism that affected the Central Zone between 2.61(2.55?) Ga and 2.65 Ga, and is documented by the Bulai, Alldays, Regina, Singelele, Zanzibar and Zoetfontein granite gneisses (Barton *et al.,* 1994; 2006; Kröner *et al.,* 1999; Holzer *et al.*, 1998, 1999; Zeh *et al.*, 2007). This magmatic-metamorphic evolution is coeval with, or younger than those reported from the Northern Marginal Zone (2.58-2.71 Ga: Berger *et al.,* 1995) and the Southern Marginal Zone (2.66-2.69: Kreissig *et al.,* 2001). Based on petrographic and geochronological results from the Bulai Pluton area (Fig. 1 and Fig. 44), Holzer *et al.* (1998) suggested that parts of the Central Zone underwent an anti-clockwise *P-T* evolution during (D2/M2), which started at *c.* 2.60 Ga and prevailed until 2.52 Ga, the so-called "post-Bulai high-grade overprint". This interpretation, however, is refuted by new petrological and geochronological data of Millonig *et al.* (2008). These authors show that metapelitic and charnoenderbitic rocks from the Bulai Pluton area (Fig. 1) underwent a clockwise *P-T* evolution from 830-860°C/8-9 kbar to 750°C/5-6 kbar at 2644±8 Ma prior to the emplacement of the Bulai granite at 2612±7 Ma. Additional evidence for a Neoarchean high-grade event in the Limpopo's Central Zone is provided by an U-Pb age of 2614±11 Ma, obtained from metamorphic zircon overgrowths of the migmatitic Sand River Gneiss (Zeh *et al.*, 2008; Gerdes & Zeh, 2008). Apart from these data, there is no unambiguous evidence for a Neoarchean high-grade metamorphic evolution, even though postulated by several workers (*e.g.*, Van Reenen *et al.*, 2004; Boshoff *et al.,* 2006; Perchuk *et al.,* 2006) - (see discussion in Millonig *et al.,* 2008).

During the Palaeoproterozoic at ~2.03 Ga (D3/M3), rocks from near Musina (Messina) and near Alldays further west were affected by a high-grade metamorphic overprint (Jaeckel *et al.*, 1997; Holzer *et al.*, 1998; Chavagnac *et al.*, 2001; Van Reenen *et al.*, 2004; Zeh *et al.*, 2004b; Buick *et al.*, 2006; Boshoff *et al.*, 2006), whereas rocks from the Venetia area in between suffered amphibolite-facies conditions (Barton *et al.,* 2003; Klemd *et al.*, 2003; Zeh *et al.*, 2005a, b). Based on detailed petrological investigations Zeh *et al.* (2005b) suggested that the Beit Bridge metasediments of the Musina area (Fig. 1 and Fig. 44) underwent a monometamorphic overprint during the Palaeoproterozoic characterized by a prograde *P-T* increase from 600°C/7 kbar to 780°C/9-10 kbar (pressure

peak) to 820°C/8 kbar (temperature peak), followed by a retrograde pressure and temperature decrease to 600°C/4 kbar. The monometamorphic character of this *P-T* path was derived from preserved prograde garnet zoning patterns (Zeh *et al.*, 2004a), and from Pb-Pb and U-Pb zircon ages of about 2.025 Ga obtained by Jaeckel *et al.* (1997) from metapelitic rocks from the adjacent Causeway locality (Fig. 44). Petrological and geochronological data from the area between Alldays and Swartwater also provides evidence for a Palaeoproterozoic high-grade metamorphic evolution. Van Reenen *et al.* (2004) show that rocks from an area west of Alldays (Baklykraal cross fold) underwent a retrograde pressure-temperature decrease from 780°C/5.7 kbar to 600°C/3.3 kbar. The timing of this evolution is constrained by Pb-stepwise leaching ages of 2094±150 Ma and 2023±11 Ma (Boshoff *et al.*, 2006). From the Swartwater area (Fig. 44) Buick *et al.* (2006) presented an upper intercept U-Pb monazite age of 2028±3 Ma, and a concordant U-Pb zircon age of 2022±11 Ma, which was obtained from metamorphic zircon overgrowths from a high-grade sillimanite-garnet-anthophyllite-cordierite gneiss.

The existing data clearly show that metamorphic rocks in the Limpopo's Central Zone were formed during three distinct metamorphic events. Thus, some authors concluded that at least some rocks or rock units must have underwent a polymetamorphic history, with two high-grade metamorphic overprints (Holzer *et al.*, 1998; Van Reenen *et al.*, 2004; Perchuk *et al.*, 2006; Boshoff *et al.*, 2006; Zeh *et al.*, 2007). This point, however, is currently under debate (see the discussion in Millonig *et al.*, 2008; Zeh & Klemd, 2008; Perchuk *et al.*, 2008). So far, unambiguous evidence for a high-grade polymetamorphic overprint in the Central Zone is provided only by U-Pb data from a sample of the migmatitic Sand River orthogneiss, which yielded concordant zircon ages of 3.28, 3.14, 2.61 and 2.03 Ga (Zeh *et al.*, 2008; Gerdes & Zeh, 2008). Furthermore, there is evidence that the 2.61 Ga old Bulai granite, which post-dates the Neoarchean (2.64 Ga) high-grade metamorphic overprint (Millonig *et al.,* 2008), was partially foliated while being juxtaposed with high-grade metasediments of the Beit Bridge Formation at 2.01Ga (Watkeys, 1984; Holzer *et al.*, 1998). Since the degree of Palaeoproterozoic structural-metamorphic overprint of the Bulai granite is much less than that of the surrounding metasediments of the Beit Bridge Formation (Watkeys *et al.*, 1984; Holzer *et al.*, 1998; Fig. 1 and Fig. 44). Millonig *et al.* (2008) concluded that the Bulai Pluton area represents a thrust bounded block, whose structural-metamorphic evolution was originally unrelated to that of the adjacent Beit Bridge metasediments.

5 Analytical techniques

Mineral compositions were obtained using a **CAMECA** SX-50 electron microprobe at the Mineralogical Institute, University of Würzburg, with three independent wavelength-dispersive crystal channels. Instrument conditions were 15 kV acceleration voltage, 15 nA specimen current, and 20 s integration time for all elements except for Fe (30 sec). Natural and synthetic silicates and oxides were used for reference, and matrix corrections were carried out by the **PAP** program, supplied by **CAMECA.** Point analyses were performed with a 30 μm beam diameter for perthitic K-feldspar, and a 1 μm beam diameter for all other minerals. In order to obtain the K-feldspar composition prior to exsolution of the albite-rich lamellae, several analyses obtained from a K-feldspar grain were integrated.

Bulk rock compositions, used for *P-T* pseudosection calculations, were determined on thin section blocks of 3 x 2 x 0.5 cm size. The analyses were carried out by conventional X-ray fluorescence spectrometry using a **Philips PW 1480** spectrometer (Mineralogical Institute, University of Würzburg) and lithium tetraborate fusion disks. The water content, used for the *P-T* pseudosection calculations was estimated by loss on ignition (LOI), assuming neglectable amounts of additional volatiles (*e.g.* Cl and F).

Mineral abbreviations follow the nomenclature of Kretz (1983). Other abbreviations are explained in the text.

Mahalapye Complex

6 Geological overview

The Mahalapye Complex (MC, Fig. 2) is situated in Botswana in the southwestern part of Central Zone of the Limpopo Belt (Fig. 1). It is made up of migmatitic rocks, granites (mainly granodiorite and quartz-monzonite) and so called Central Zone gneisses (Aldiss, 1991; Fig. 2). The Central Zone gneisses, which occur in the eastern part of the MC grade continously into the migmatites of the Mahalapye Complex. This transition is reflected by an overall increase of the melt fraction in the migmatites from east to west (Van Breemen & Dodson, 1972; Chavagnac *et al.*, 2001). The migmatites are intruded and cross-cut by granites: the syn-kinematic Mokgware Granite/Pluton and the post-kinematic Mahalapye Granite (McCourt *et al.*, 2004).

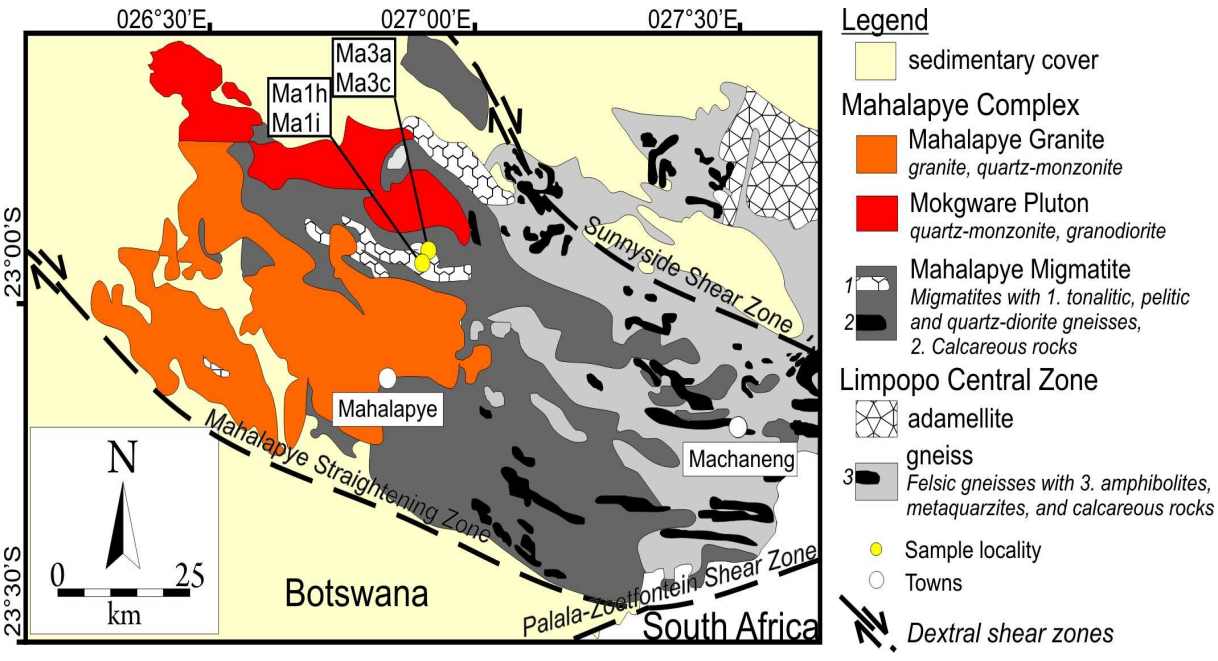

Fig. 2. Geological map of the Mahalapye Complex (modified after Hisada *et al.*, 2005). Shear zones after Schaller *et al.* (1999).

Towards the northeast the Mahalapye Complex is seperated from the Phikwe Complex by the Sunnyside Shear Zone, whereas the southern limit is defined by the several km wide Mahalapye Straightening Zone (*MSZ*), which is a branch of the subvertical dipping, ENE trending Palala-Zoetfontein Shear Zone system (*PZSZ*, *e.g.* McCourt & Vearncombe, 1992; Holzer *et al.*, 1999; Schaller *et al.*, 1999). The afore mentioned shear zone systems are cut off in

their western extent by the Palaeoproterozoic Kheis-Magondi Belt (Majaule *et al.*, 2001; Raganai *et al.*, 2002). Towards the east the Mahalapye Complex is limited by the mapped extent of the migmatite complex, west of the *PZSZ* (McCourt *et al.*, 2004 after Carney, 1994). The north-northwestern contact between the Mahalapye Complex and the Motloutse Complex (see Fig. 1) and the western extent of the Mahalapye Complex are covered by younger stratigraphical sequences of the Transvaal Supergroup (Aldiss, 1991; Key & Ayres, 2000).

Geochronological data, obtained by different techniques and isotope systems, mostly yield ages of ~ 2.0 Ga (Tab. 2) for rocks of the Mahalapye Complex. However, results of zircon dating also yield older ages of ~3.15-2.45 Ga (McCourt & Armstrong, 1998) and ~2.7 Ga (Zeh *et al.*, 2007). The ~3.15-2.45 Ga age were obtained from inherited zircon cores of the Mahalapye Granite and the ~2.7 Ga age from zircon cores of leucosomes from the Lose Quarry. The Palaeo- to Neoarchean ages imply the existence of magmatic protholiths in the region before ~2.45 Ga, while the 2.0 Ga age is interpreted to represent the time of intense migmatization and granite emplacement within the complex. The post-tectonic Mahalapye Granite (2023±7 Ma) provides a minimum age for deformation along the *MSZ* (Chavagnac *et al.*, 2001), and indicates that the migmatisation event occurred prior to 2023±7 Ma (McCourt *et al.*, 2004).

Tab. 2. Compilation of age data from the Mahalapye Complex. * wr = whole rock

Method	age (Ma)	±	Comments	Author
Rb-Sr kfs-pl-ap-wr*	2010	80	migmatite	Van Breemen & Dodson (1972)
Rb-Sr bt	2050	50	migmatite	Van Breemen & Dodson (1972)
Sm-Nd grt-leuc-wr*	2023	7	migmatite, bt breakdown	Chavagnac *et al.* (1997)
U-Pb monazite	2002	10	leucosom	Chavagnac *et al.* (1997)
U-Pb zircons	2023	13	Mahalapye Granite	McCourt & Armstrong (1998)
U-Pb zircons	2053	21	granodiorite dyke cutting the Mahalapye Migmatite	McCourt & Armstrong (1998)
U-Pb zircon	2023	7	Mahalapye Granite	Beukes & Gutzmer (1998) mentioned in McCourt *et al.* (1998)
U-Pb apatite	1998	4	leucosome	Holzer *et al.* (1999)
Pb titanite	2020	8	Koedesrand Window	Schaller *et al.* (1999)
Pb titanite	2017	6	Koedesrand Window	Schaller *et al.* (1999)
Sm-Nd garnet	1982	38	grt-leucosome-palaeosom (Lose Quarry)	Chavagnac *et al.* (2001)
Sm-Nd garnet	2023	7	grt-leucosome-palaeosom (Lose Quarry)	Chavagnac *et al.* (2001)
U-Pb monazite	2004	19	leucosome (Lose Quarry)	Chavagnac *et al.* (2001)
U-Pb monazite	1996	38	leucosome (Lose Quarry)	Chavagnac *et al.* (2001)
U-Pb monazite	2002	15	leucosome (Lose Quarry)	Chavagnac *et al.* (2001)
U-Pb monazite	2002	35	leucosome (Lose Quarry)	Chavagnac *et al.* (2001)
U-Pb zircons	2026	10	Mokgware Granite	Zeh *et al.* (2007)
U-Pb zircons	2061	6	grt-bt gneiss (Lose Quarry)	Zeh *et al.* (2007)
U-Pb zircon cores	2711	11	leucosome (Lose Quarry)	Zeh *et al.* (2007)
U-Pb zircon rims	<2061		leucosome (Lose Quarry)	Zeh *et al.* (2007)

Presently little is known about the *P-T* evolution of the Mahalapye Complex (no prograde *P-T* evolution). Hisada (1997) suggest a retrograde evolution for the Mahalapye Complex starting with near isothermal decompression (ITD) from 1000°C/12 kbar to

900°C/7 kbar followed by near isobaric cooling (IBC) to ~670°C/6 kbar. Chavagnac *et al.* (2001) obtained peak metamorphic temperatures of >750°C by Ti in biotite thermometry for metapelitic samples of the Lose Quarry. A more recent study of Hisada *et al.* (2005) on metapelitic rocks from the Lose Quarry provides evidence for a decompression-cooling path from 770°C/5.5 kbar to 560°C/2 kbar (Fig. 3).

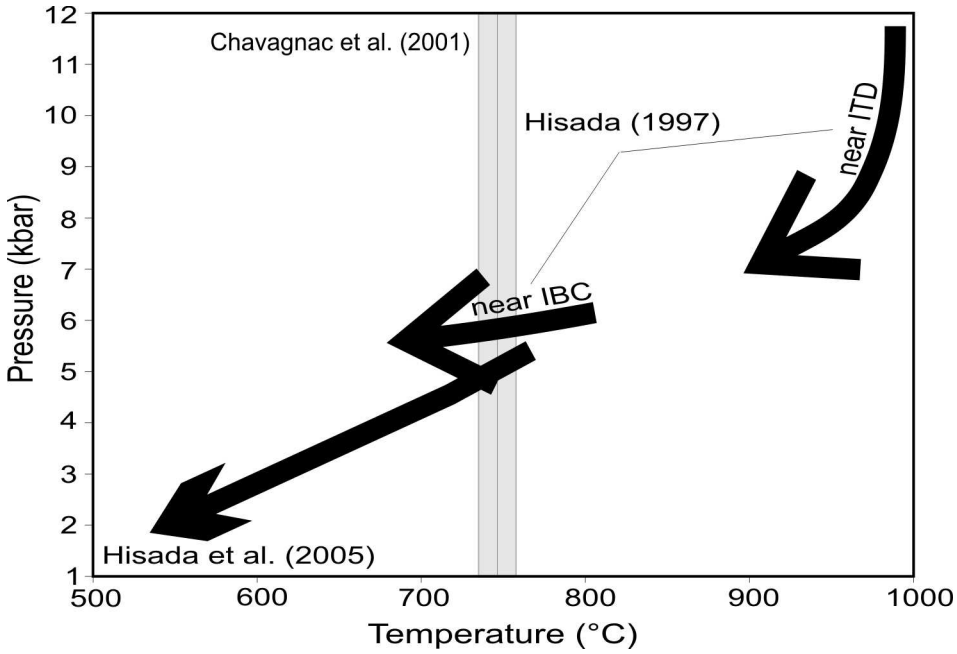

Fig. 3. Inferred metamorphic *P-T* paths for the Mahalapye Complex after Hisada (1997, 2005) and peak temperature conditions after Chavagnac *et al.* (2001; see text for details).

7 Petrography and Mineral Chemistry

Thirteen samples from three sample localities were collected from the Mahalapye Complex. Four of these samples from two localities were selected for detailed petrological investigations (Tab. 3). Samples Ma1h and Ma1i were collected from the Lose Quarry, which is situated *ca.* 20 km north of Mahalapye, and samples Ma3a and Ma3c were taken from a river bed just north of the Lose Quarry (Fig. 2). The sample co-ordinates, mineral assemblages and chemical compositions of the samples are presented in Tab. 3. Representative mineral compositions of the observed minerals are shown in Tab. 4, Tab. 5 and Tab. 7. Additional mineral analyses can be found in the electronical appendix: 24 - Supplementary mineral data.

Tab. 3. Sample co-ordinates, mineral assemblages and *XRF*-analyses of the investigated samples from the Mahalapye Complex

Sample	Ma1h	Ma1i	Ma3a	Ma3c
Rock type	Grt-Bt-Pl-Gneiss	Grt-Bt-Pl-Gneiss	Grt-Sil-Bt-Crd-Gneiss	Grt-Sil-Bt-Crd-Gneiss
Latitude(°S)	22°56'933	22°56'933	22°55'844	22°55'844
Longitude(°E)	26°53'844	26°53'844	26°54'349	26°54'349
Assemblage	Grt-Bt-Pl-Ilm-Qtz	Grt-Bt-Pl-Qtz-Ilm	Grt–Bt–Crd–Spl–Sil–Pl–Kfs–Rt-Ilm	Grt–Bt–Crd–Spl–Sil–Pl-Ilm
XRF-analyses	wt.%	wt.%	wt.%	wt.%
SiO_2	53.20	43.20	42.50	40.50
TiO_2	0.73	1.30	1.70	1.60
Al_2O_3	18.10	20.80	33.20	29.10
$Fe_2O_3^{tot}$	15.30	20.90	15.30	19.70
FeO^{tot}	13.80	18.80	13.80	17.70
MnO	0.40	0.71	0.16	0.22
MgO	3.80	4.60	4.30	5.20
CaO	2.40	2.80	0.27	0.37
Na_2O	2.80	2.20	0.52	0.31
K_2O	3.20	3.80	1.50	2.10
P_2O_5	0.04	0.03	0.03	0.07
LOI	0.24	0.07	1.20	0.82
Total (with FeO^{tot})	98.60	98.20	99.20	98.00
Total (with $Fe_2O_3^{tot}$)	100.10	100.30	100.70	100.00
FeO/(FeO+MgO)	0.78	0.80	0.76	0.77

7.1 Si-undersaturated sillimanite-garnet-cordierite gneiss (sample Ma3a)

Sample Ma3a is a foliated metapelitic gneiss that contains garnet (5-10 vol.%), biotite (~10 vol.%), cordierite (~40 vol.%), sillimanite (~10 vol.%), plagioclase (~10 vol.%), K-feldspar (~10 vol.%), hercynitic spinel (~2-5 vol.%), minor muscovite (<1 vol.%) and relic quartz inclusions in garnet. Macroscopically this sample consists of several cm wide melanocratic and thin, less than 1 cm wide, leucocratic layers. The melanocratic domains are made up of garnet, biotite, cordierite, sillimanite and hercynitic spinel, while the leucocratic domains mainly consist of K-feldspar, plagioclase, garnet and rare biotite. Accessory ilmenite, rutile, zircon and monazite are common phases in both domains (< 5 % total). It should be noted that free matrix quartz does not occur in this sample. Representative mineral compositions of the observed minerals are shown in Tab. 4.

Garnet prophyroblasts are mostly resorbed and max. 1 cm in diameter. They can contain inclusions of sillimanite, biotite, plagioclase, quartz ilmenite and rutile and are commonly surrounded by plagioclase-biotite-cordierite-sillimanite coronas (Fig. 4b). Locally garnet also occurs as isolated grains surrounded by plagioclase/K-feldspar aggregates (Fig. 4a). These garnet porphyroblasts are unzoned (Fig. 8) and have the average composition $Alm_{81}Prp_{13}Grs_{03}Sps_{03}$, whereas resorbed garnet with biotite-cordierite coronas shows a zoning, which is characterized by increasing X_{Fe}

(Fe^{2+}/(Fe^{2+}+Mg)) towards the rim (Tab. 4). These features indicate that the original zoning of the "corona" garnet was modified by diffusive Fe/Mg-exchange with the surrounding Fe/Mg-silicates.

Lepidoblastic matrix biotite is up to 1 mm long and defines the foliation together with sillimanite (Fig. 4d). Furthermore, biotite is a common inclusion in garnet and spinel (Fig. 4b, e). Depending on its textural position biotite shows variation of the X_{Fe} value, and Ti and Al contents (matrix biotite: X_{Fe} = 0.68-0.75, Ti per formula unit (*p.f.u.*) = 0.44-0.64 and Al *p.f.u.* = 3.23-3.49; biotite included in garnet: X_{Fe} = 0.56-0.58, Ti = 0.34-0.42 and Al = 3.42-3.5; Tab. 4).

Plagioclase occurs in three distinct textural positions. Plagioclase I forms rounded inclusions in garnet (Fig. 4b). Plagioclase II occurs in leucrocratic domains, where it forms granoblastic aggregates with diameters of up to 1 mm (Fig. 4f) and can locally contain inclusions of biotite. Plagioclase III forms thin seams (<70 µm wide) between K-feldspar and/or plagioclase II (Fig. 4f). Plagioclase I and II are unzoned and show the chemical composition ~$Ab_{70}An_{30}$, while plagioclase III has the composition $Ab_{80-98}An_{02-20}$ (Fig. 13b; Tab. 4). The plagioclase III seams provide evidence for the former existence of melt (see also Zeh *et al.*, 2004b).

Up to 3.5 mm large granoblastic K-feldspar, which locally contain biotite inclusions, are mostly seperated by thin plagioclase III seams. K-feldspar commonly shows typical microcline cross-hatched patterns (Fig. 4f) and a unzoned composition of ~$Or_{85}Ab_{15}$ (Tab. 4).

Granoblastic cordierite is up to 2 mm long, displays lamellar and cyclic twinning and contains abundant inclusions of sillimanite and minor inclusions of biotite and hercynitic spinel (Fig. 4d, e). The mineral inclusions preferantially occur in the cordierite cores. Cordierite coronas around resorbed garnet and the abundant biotite and sillimanite inclusions in cordierite cores indicate that cordierite was, at least partly, formed during the consumption of these three phases (Fig. 4b, d). Furthermore, pinitization of cordierite is a common feature. Cordierite is chemically unzoned with X_{Fe} ~0.53 (Tab. 4).

Prismatic sillimanite is up to 0.7 mm long and restricted to inclusions in garnet and cordierite (Fig. 4a, d; Tab. 4).

Hercynitic spinel, up to 0.5 mm long, is commonly texturally associated with cordierite, and locally contains inclusions of biotite and sillimanite (Fig. 4d, e). Thus it can be assumed that spinel was formed at the expense of these two phases (see also White *et al.*, 2003). Chemically, spinel is close to the end-member composition of hercynite (Hc), but also contains minor spinel (Spl), gahnite (Ga) and chromite (Cr) components ($Hc_{87-90}Spl_{7-10}Ga_{02}Cr_{01}$; Tab. 4).

Minor muscovite, ilmenite, rutile, zircon and monazite occur in this sample. Rare muscovite is exclusively found in symplectitic intergrowth with quartz near garnet, while rutile is commonly rimmed by ilmenite seams and is

solely included in garnet (Fig. 4c). Additionally, zircon and monazite grains are widely dispersed in this sample. Muscovite in this sample is a nearly pure muscovite end-member with Si contents between 5.99 and 6.45 *p.f.u.*, and K/(K+Na+Ca) ratios between 0.94 and 0.97 *p.f.u.* (Tab. 4). Ilmenite ($Ilm_{94}Pyr_{06}$) and rutile ($Rt_{\sim 100}$) have nearly a end-member compositions (Tab. 4).

Tab. 4. Representative mineral analyses of sample Ma3a. D.a.r. = diffusively altered rim. For further information see text

	grt		bt		ms	pl		kfs	crd	sil	spl	ilm	rt
wt.% oxides	core	d.a.r.	in mx	in grt		in mx +grt	seams						
SiO_2	37.13	35.85	33.76	34.90	47.67	59.98	66.90	63.88	47.41	37.12	0.01	0.04	0.08
TiO_2	0.00	0.02	6.33	3.69	0.00				0.00	0.01	0.02	52.44	98.25
Al_2O_3	21.01	20.34	17.81	19.08	36.08	23.88	20.15	18.57	32.63	62.61	55.57	0.04	0.14
Cr_2O_3	0.06	0.01	0.24	0.07	0.01						0.59	0.12	0.26
Fe_2O_3	0.00	0.00	0.00	0.00	0.00	0.08	0.00	0.04	0.00	0.80	0.00	0.00	0.00
FeO	36.66	39.10	22.49	20.21	1.32	0.00	0.00	0.00	12.04	0.72	39.59	44.19	0.31
MnO	1.33	1.19	0.01	0.02	0.06				0.11	0.03	0.09	2.71	0.02
MgO	3.44	1.50	6.02	8.51	1.09	0.11	0.18	0.16	6.05	0.03	1.95	0.00	
BaO			0.05	0.06	1.53	0.00	0.03	0.50					
CaO	0.87	0.86	0.07	0.03	0.00	6.31	0.90	0.06	0.00	0.00	0.00		
Na_2O			0.38	0.28	0.34	7.98	11.13	1.70	0.24		0.30		
K_2O			8.81	9.05	9.91	0.22	0.06	13.96	0.03		0.99		
sum	100.52	98.87	95.94	95.90	98.02	98.56	99.37	98.87	98.50	101.32	99.12	99.55	99.07
oxygens	12	12	22	22	22	8	8	8	18	5	4	3	2
cations													
Si	2.98	2.97	5.21	5.30	6.20	2.71	2.95	2.98	4.96	1.00	0.00	0.00	0.00
Ti	0.00	0.00	0.73	0.42	0.00				0.00	0.00	0.00	1.00	0.99
Al	1.99	1.98	3.24	3.42	5.53	1.27	1.05	1.02	4.02	1.98	1.93	0.00	0.00
Cr	0.00	0.00	0.03	0.01	0.00						0.01	0.00	0.00
Fe^{3+}	0.06	0.08	0.00	0.00	0.00	0.00	0.00	0.00	0.00	0.02	0.00	0.00	0.00
Fe	2.40	2.62	2.90	2.57	0.14	0.00	0.00	0.00	1.05	0.00	0.97	0.94	0.00
Mn	0.09	0.08	0.00	0.00	0.01				0.01	0.00	0.00	0.06	0.00
Mg	0.41	0.19	1.38	1.93	0.21	0.01	0.01	0.01	0.94	0.00	0.09	0.00	
Ba			0.00	0.00	0.08	0.00	0.00	0.01					
Ca	0.07	0.08	0.01	0.00	0.00	0.31	0.04	0.00	0.00	0.00	0.00		
Na			0.11	0.08	0.09	0.70	0.95	0.15	0.05		0.01		
K			1.73	1.75	1.64	0.01	0.00	0.83	0.00		0.02		
sum	8.00	8.00	15.35	15.49	13.90	5.01	5.01	5.00	11.03	3.00	3.03	2.01	1.00
X_{Fe}	0.85	0.93	0.68	0.57	0.40				0.53	0.00	0.92	1.00	
X_{ab}						0.69	0.95	0.16					

The textural relationships as described above and shown in Fig. 4 provide evidence that the following mineral assemblages were successively formed in sample Ma3a.

Quartz, sillimanite, biotite, plagioclase, rutile and ilmenite inclusions in garnet indicate that garnet grew initialy in the assemblage:

(A1): grt-bt-sil-pl I-rt/ilm-qtz (Fig. 4a, b)

The observation that rutile is absent in the matrix and rutile inclusions in garnet are commonly surrounded by ilmenite, indicates that further garnet growth took place in the assemblage:

(A2): grt-bt-sil-pl I-ilm-qtz (Fig. 4c)

Cordierite coronas around resorbed garnet porphyroblasts indicate that garnet was subsequently consumed in the assemblage:

(A3): grt-bt-crd-sil-pl I-ilm-qtz (Fig. 4b)

The absence of quartz in the matrix indicates that it was completely consumed during cordierite formation. Complementary, the absence of hercynitic spinel in garnet, but its occurrence in the matrix, in particular in cordierite, indicates that it was formed during that stage. Thus, it can be concluded that the system became quartz-free but spinel-bearing, during successive garnet consumption and simultaneous cordierite formation. This process was obviously accompanied by the formation of K-feldspar, plagioclase II and a melt phase, as can be concluded by the finding of abundant matrix K-feldspar, plagioclase II and the plagioclase III seams (Fig. 4f). All these observations support an interpretation that garnet consumption/cordierite formation took place successively under silica-undersaturated conditions in the assemblages:

(A4): grt-bt-crd-sil-pl I/II -kfs-ilm-melt (Fig. 4b, c, f)

(A5): grt-bt-spl-crd-sil-pl I/II -kfs-ilm-melt (Fig. 4d, e)

(A6): grt-bt-spl-crd-sil-pl I/II/III -kfs-ilm (Fig. 4d, f)

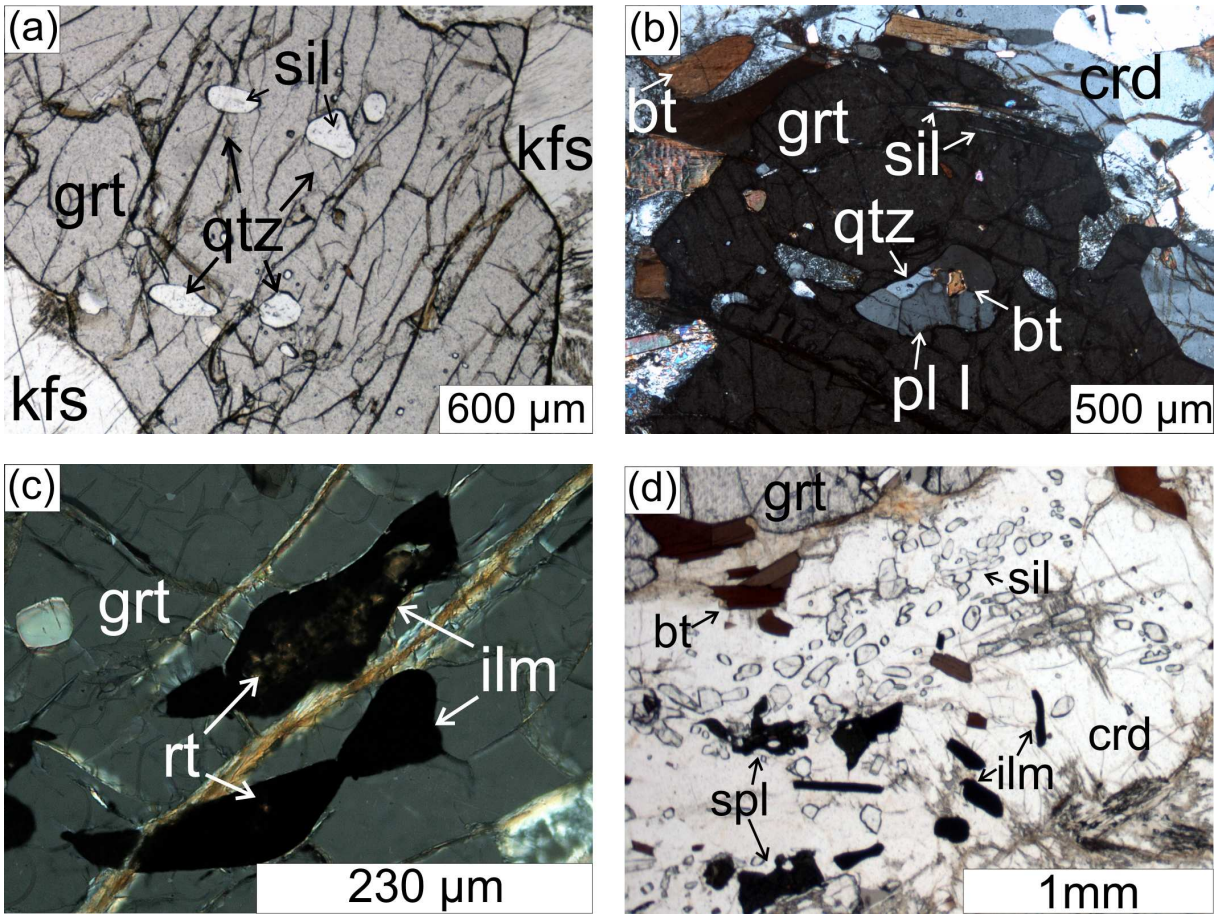

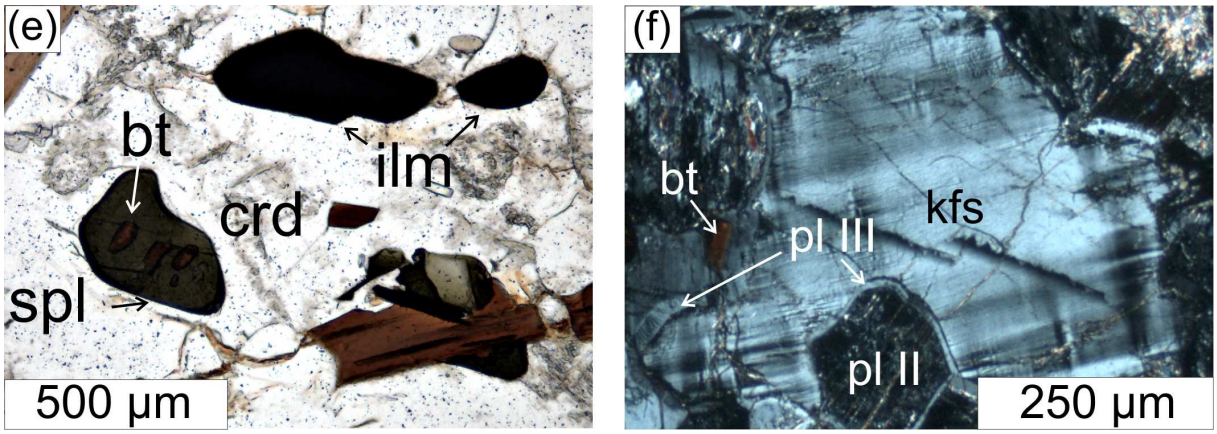

Fig. 4. Photomicrographs of sample Ma3a. Anormal interference colours of in (b) and (c) are caused by nicols not crossed at 90° for illustration purposes. a) quartz with fibrolitic silimanite inclusions is surrounded by garnet, which is rimmed by K-feldspar. Plane polarized light (PPL). b) sillimanite, biotite, plagioclase and quartz enclosed by garnet. Garnet is surrounded by cordierite and biotite. Crossed polarized light (CPL). c) rutile with rims of ilmenite included in garnet. CPL. d) cordierite corona around resorbed garnet with inclusions of hercynitic spinel, sillimanite, biotite and ilmenite. PPL. e) hercynitic spinel with biotite inclusions and ilmenite surrounded by cordierite. PPL. f) K-feldspar with tartan pattern, plagioclase II and thin seams of plagioclase III between K-feldspar and plagioclase II with minor biotite, interpreted to represent crystallized melt. CPL.

7.2 Si-undersaturated sillimanite-garnet-cordierite gneiss (sample Ma3c)

Sample Ma3c is a black foliated metapelitic gneiss consisting of garnet (~10 vol.%), biotite (~10 vol.%), cordierite (50-60 vol.%), sillimanite (5-10 vol.%), plagioclase (<10 vol.%), ilmenite and hercynitic spinel (together ~5 vol.%), minor quartz, K-feldspar and muscovite (< 5 vol.% total) and accessory monazite, zircon and xenotime. Representative mineral compositions of the observed minerals are shown in Tab. 5.

Garnet forms xeno- to hypidiomorph porphyroblasts up to ~12 mm in diameter, but most of these do not exceed 5 mm. Resorbed garnet is commonly surrounded by quartz-free granoblastic cordierite-biotite coronas (Fig. 6a, d) which locally also contain spinel (Fig. 6j). In addition to these coronas there are few garnet grains, which are partly replaced by cordierite-biotite-quartz symplectites (Fig. 6e, f, g, h). This replacement ocurred along previous garnet fractures. The core of one large garnet porphyroblast contains inclusions of biotite, quartz and fine grained ilmenite, whereas the rim is ilmenite-free but additionally contains sillimanite and cordierite (besides biotite and quartz; Fig. 6c). These observations are interpreted to reflect initial garnet growth in a fine-grained matrix with abundant ilmenite and biotite. During progressive garnet growth ilmenite disappeared in the garnet forming domain, causing the formation of the ilmenite-free rims. Garnet shows compositional core plateaus with $Alm_{80}Prp_{15}Grs_3Sps_2$ and a retrograde, diffusion controlled increasing X_{Fe} towards garnet rims and fractures filled with Fe-Mg silicates (Fig. 8; Tab. 5).

Biotite forms rounded inclusions in garnet and spinel and is widespread in the matrix. Matrix biotite commonly forms hypidioblastic laths, which are maximal 1.4 mm long and

define the foliation together with sillimanite (Fig. 6a). In addition there is some biotite, which forms biotite-cordierite-quartz symplectites in resorbed garnet domains (Fig. 6e, f, g, h). Dependent on its textural position, biotite shows different average chemical compositions (matrix biotite: X_{Fe} = 0.7, Ti *p.f.u.* = 0.53 and Al^{tot} *p.f.u.* = 3.33; biotite inclusions in spinel: X_{Fe} = ~0.63, Ti *p.f.u.* = 0.33 and Al^{tot} *p.f.u.* = 3.57; biotite inclusions in garnet: X_{Fe} = 0.58, Ti *p.f.u.* = 0.42 and Al^{tot} *p.f.u.* = 3.3; symplectitic biotite: X_{Fe} = 0.71, Ti *p.f.u.* = 0.48 and Al^{tot} *p.f.u.* = 3.35) – (Tab. 5).

Cordierite occurs in four textural distinct positions. Cordierite I forms inclusions in garnet. These are mostly round or angular, and in some locations form elongated aggregates, which follow the crystallographic garnet planes (Fig. 6c+d). Cordierite II is up to 0.7 mm in diameter, inclusion-free, and forms together with biotite granoblastic coronas with triple-junctions around garnet. Cordierite II is commonly pinitized in direct contact with garnet and/or biotite (Fig. 6a). Cordierite III forms porphyroblasts up to 1.8 mm in diameter,which occur away from garnet and contain abundant inclusions of sillimanite, hercynitic spinel, biotite and minor plagioclase and ilmenite (Fig. 6i, j). Cordierite IV forms symplectites with biotite and quartz (commonly along garnet fractures; Fig. 6e, f, g, h). These four cordierite types show compositional variations in X_{Fe} (crd I: 0.37-0.42; crd II: 0.45-0.48; crd III: ~ 0.49-0.5; crd IV: 0.54-0.57) – (Tab. 5).

Xeno- to hypidioblastic hercynitic spinel is up to 0.9 mm long, locally contains inclusions of biotite, and is a common constituent of sillimanite bands in close contact to cordierite III (Fig. 6j). Spinel is chemically dominated by the hercynite end-member and has the composition $Hc_{88-89}Sp_{07-09}Ga_{01-02}Cr_{02-03}$ (Tab. 5).

Ilmenite occurs in two different textural varieties. Ilmenite I forms small (<0.2 mm) rounded inclusions in garnet cores (Fig. 6c), whereas ilmenite II gets up to 0.8 mm long and is found in the matrix (Fig. 6j). Ilmenite in all domains has nearly a pure end-member composition ($Ilm_{98-100}Pyro_{00-02}$) – (Tab. 5).

Plagioclase is up to 1 mm in diameter, shows albite twinning, and locally contains inclusions of biotite, cordierite and K-feldspar (Fig. 6e). Plagioclase is zoned from core ($Ab_{65}An_{35}$) to rim ($Ab_{72}An_{28}$) - (Tab. 5).

K-feldspar was only found enclosed in plagioclase. Its chemical composition is $Or_{88}Ab_{12}$ (Fig. 5; Tab. 5).

Accessory monazite is preferentially included in matrix cordierite (Fig. 6I, j), while zircon shows no such preference.

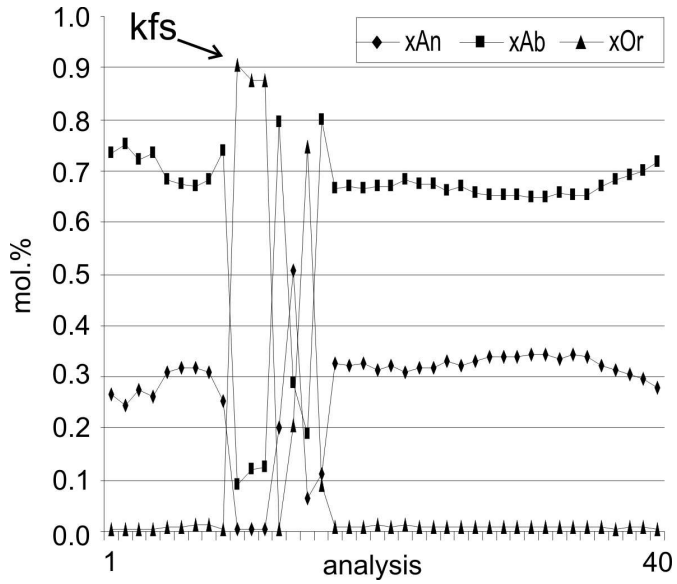

Fig. 5. Microprobe profile across zoned plagioclase with central inclusion of K-feldspar.

Tab. 5. Representative mineral analyses of sample Ma3c. D.a.r. = diffusively altered rim. For further information see text

	grt		pl		kfs	bt				crd				spl	ilm
wt.% oxides	core plateau	d.a.r.	core	rim	in pl	in mx	in spl	in grt	in sympl.	I	II	III	IV		
SiO_2	36.72	36.15	58.26	59.67	62.74	33.32	33.59	35.40	33.72	47.32	46.96	46.21	46.85	0.00	0.02
TiO_2	0.05	0.05				4.47	3.30	2.39	3.59	0.01	0.00	0.00	0.00	0.04	52.25
Al_2O_3	21.18	20.70	24.88	23.69	18.18	18.19	19.41	18.89	18.79	32.20	32.33	31.79	31.47	55.84	0.00
Cr_2O_3	0.00	0.02				0.14	0.04	0.09	0.10					0.81	0.07
Fe_2O_3	0.00	0.00	0.08	0.09	0.06	0.00	0.00	0.00	0.00	0.00	0.00	0.00	0.00	0.00	0.00
FeO	36.91	38.23	0.00	0.00	0.00	24.05	23.22	21.71	27.62	8.60	10.69	11.06	14.35	39.71	46.49
MnO	1.01	1.20				0.06	0.00	0.00	0.06	0.07	0.10	0.11	0.07	0.03	0.51
MgO	3.61	2.47	0.00	0.00	0.00	5.87	7.26	8.65	6.20	8.06	6.96	6.45	6.37	1.92	0.00
BaO			0.00	0.00	1.42	0.11	0.19	0.07	0.66						
CaO	1.00	0.98	7.14	5.96	0.06	0.00	0.01	0.01	0.01	0.06	0.00	0.06	0.54	0.02	
Na_2O			7.46	8.44	1.28	0.31	0.27	0.07	0.19	0.13	0.13	0.20	0.22	0.16	
K_2O			0.18	0.09	13.80	9.15	9.03	8.84	9.07	0.02	0.02	0.01	0.13	0.86	
sum	100.48	99.80	98.00	97.93	97.55	95.66	96.32	96.13	100.00	96.45	97.19	95.89	100.00	99.39	99.34
oxygens	12	12	8	8	8	22	22	22	22	18	18	18	18	4	3
cations															
Si	2.94	2.94	2.65	2.71	2.98	5.21	5.17	5.38	5.12	4.98	4.95	4.95	4.90	0.00	0.00
Ti	0.00	0.00				0.53	0.38	0.27	0.41	0.00	0.00	0.00	0.00	0.00	1.00
Al	2.00	1.99	1.34	1.27	1.02	3.35	3.52	3.39	3.37	3.99	4.02	4.01	3.88	1.93	0.00
Cr	0.00	0.00				0.02	0.00	0.01	0.01					0.02	0.00
Fe^{3+}	0.11	0.12	0.00	0.00	0.00	0.00	0.00	0.00	0.00	0.00	0.00	0.00	0.00	0.00	0.00
Fe	2.36	2.48	0.00	0.00	0.00	3.14	2.99	2.76	3.51	0.76	0.94	0.99	1.26	0.97	0.99
Mn	0.07	0.08				0.01	0.00	0.00	0.01	0.01	0.01	0.01	0.01	0.00	0.01
Mg	0.43	0.30	0.00	0.00	0.00	1.37	1.67	1.96	1.40	1.26	1.09	1.03	0.99	0.08	0.00
Ba			0.00	0.00	0.03	0.01	0.01	0.00	0.04						
Ca	0.09	0.09	0.35	0.29	0.00	0.00	0.00	0.00	0.00	0.01	0.00	0.01	0.06	0.00	
Na			0.66	0.74	0.12	0.09	0.08	0.02	0.06	0.03	0.03	0.04	0.05	0.00	
K			0.01	0.01	0.84	1.82	1.77	1.71	1.76	0.00	0.00	0.00	0.02	0.02	
sum	8.00	8.00	5.01	5.03	4.99	15.54	15.61	15.51	15.68	11.03	11.04	11.04	11.16	3.03	2.00
X_{Fe}	0.85	0.89				0.70	0.64	0.58	0.71	0.37	0.46	0.49	0.56	0.92	1.00
X_{ab}			0.65	0.72	0.12										

Judging from the observed intergrowth relationships it is concluded that the following mineral assemblages were formed successively:

Biotite, plagioclase, sillimanite, ilmenite and quartz inclusions in garnet indicate that initial garnet growth took place in the assemblage:

(A1) grt-bt-sil-pl-ilm-qtz (Fig. 6a, b)

The finding of oriented cordierite I inclusions (together with sil, bt, pl and qtz) near to garnet rims, constraints that further garnet growth ocurred in the assemblage:

(A2) grt-bt-crd I-sil-pl-ilm-qtz (Fig. 6c, d)

Apart from the cordierite IV-biotite-quartz symplectites, quartz is absent in the matrix of sample Ma3c. This indicates that the rock matrix became silica-undersaturated during progressive metamorphism. However, based on the textural observations it cannot be decided whether quartz disappeared during garnet growth together with cordierite I, or during subsequent garnet consumption at the expense of cordierite II and formation of cordierite III. Furthermore, the observation of few K-feldspar inclusions in plagioclase might indicate that it also was stable in the matrix after garnet growth ceased. Taking these information into account it seems most likely that initial garnet resorption occurred in the quartz-free assemblage:

(A3a) grt-bt-crd II+III-sil-pl-ilm (Fig. 6a, i)

In contrast, the observed biotite-cordierite IV-quartz symplectites are assumed to represent a local reaction between melt and garnet. This reaction took place during the retrograde *P-T* evolution, after the formation of cordierite II and III. This is supported by the fact that these symplectites are only observed along resorbed garnet fractures, and cordierite IV has higher X_{Fe} than cordierite I, II and III (indicative for low T). According to Spear *et al.* (1999) and Waters (2001) such garnet-biotite-quartz symplectites are interpreted to result from melt-solid interactions. Thus, this gives a hint that sample Ma3c contained melt at the metamorphic peak, and that this melt reacted with garnet during the retrograde evolution (see also constraints from *P-T* pseudosection calculations in section 8.2). The finding of rare K-feldspar relics in plagioclase indicate that this phase was also present at the metamorphic peak. Thus, it is most likely that the complete peak assemblage was:

(A3b) grt-bt-crd II+III-sil-pl-kfs-ilm-melt (Fig. 6c, d, e, i)

Hercynitic spinel is a common matrix constituent and is commonly associated with cordierite III, but never forms inclusions in garnet, plagioclase or K-feldspar. That hints that spinel grew late during the metamorphic history, perhaps in the assemblage:

(A4) grt-bt-spl-crd II+III(±IV)-sil-pl-kfs-pl-ilm (±melt) (Fig. 6j)

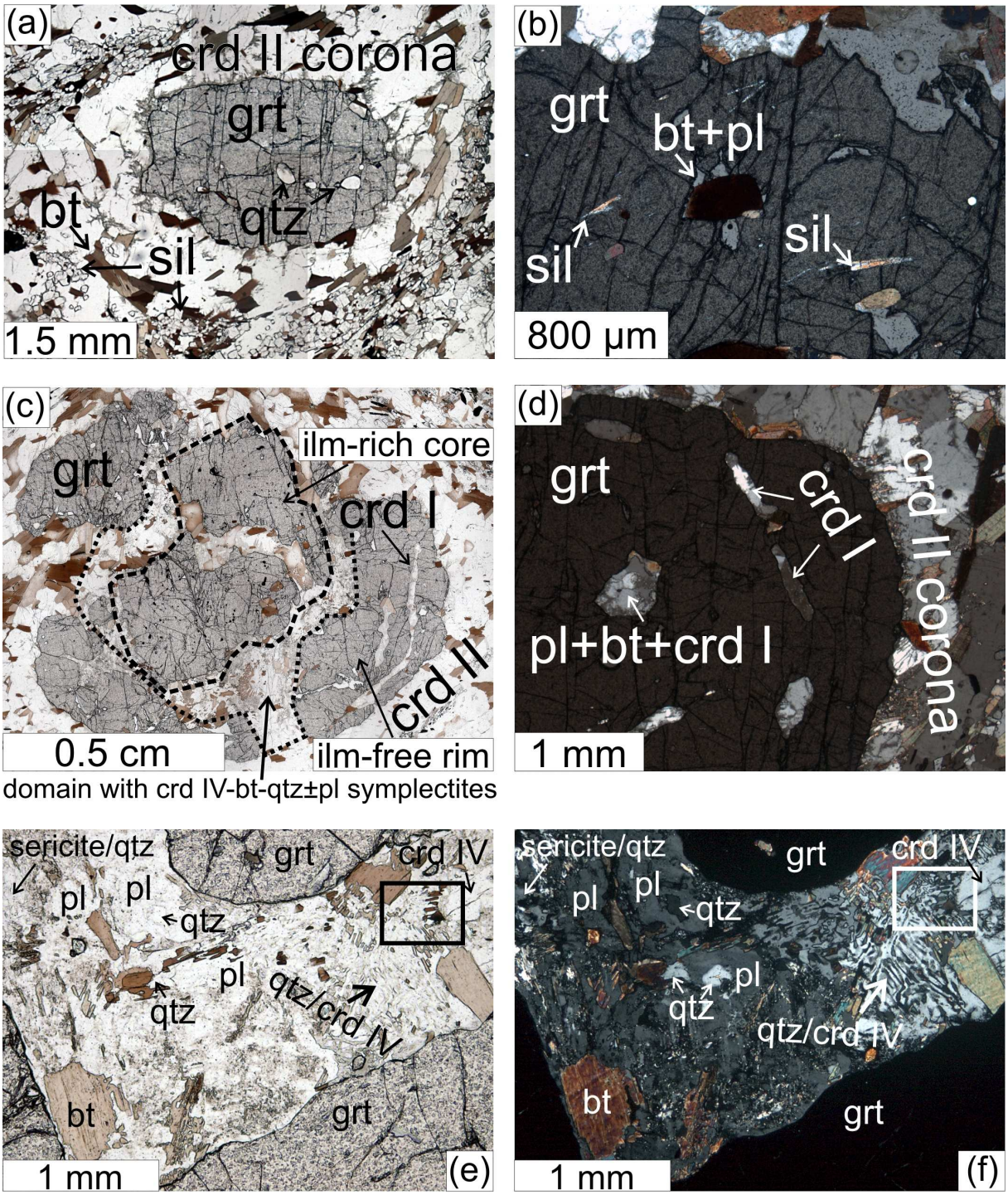
(a)
crd II corona
grt
bt
qtz
sil
1.5 mm
(b)
grt
bt+pl
sil
sil
800 µm
(c)
ilm-rich core
grt
crd I
crd II
0.5 cm
ilm-free rim
domain with crd IV-bt-qtz±pl symplectites
(d)
grt
crd I
crd II corona
pl+bt+crd I
1 mm
sericite/qtz
grt
crd IV
pl
pl
qtz
pl
qtz
qtz/crd IV
bt
grt
1 mm
(e)
sericite/qtz
grt
crd IV
pl
pl
qtz
pl
qtz
qtz/crd IV
bt
grt
1 mm
(f)

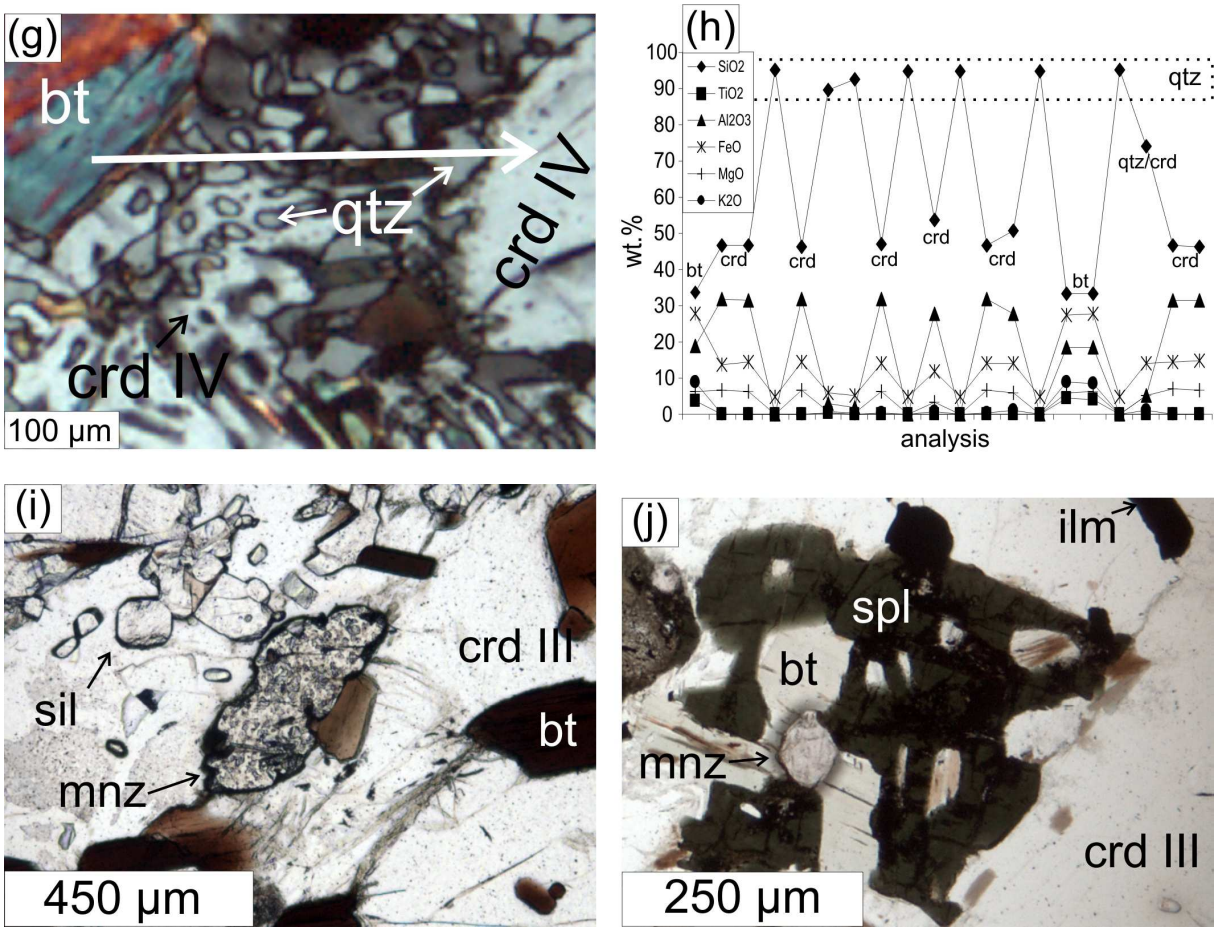

Fig. 6. Photomicrographs of sample Ma3c and microprobe profile across cordierite-biotite-quartz symplectite (h). Anomal interference colours of phases in (b) and (d) are caused by nicols not crossed at 90° for illustration purposes. a) garnet with quartz inclusions surrounded by a corona of cordierite II, brown biotite and sillimanite. PPL. b) inclusions of sillimanite, biotite and plagioclase in garnet. CPL. c) resorbed garnet porphyroblast with an ilm-rich core and an ilm-free rim is surrounded by a corona of cordierite II and biotite. Note cordierite I inclusions in garnet follow the crystallographic planes of the host garnet (lower right corner). PPL. d) cordierite I, plagioclase and biotite inclusions in garnet, which is surrounded by cordierite II. Again, inclusions of cordierite I are aligned parallel to the crystallographic planes of the host garnet. CPL. e) intergrowth between cordierite IV, biotite, quartz and plagioclase in fractured garnet. These textures are interpreted to result from melt-solid phase interaction (see text). Black box marks detail shown in g). CPL. f) same as e) but under CPL. g) crd-bt-qtz symplectite from the detail marked in e) and f). Again, the symplectite is interpreted to represent melt-solid interaction. h) microprobe profile across crd-bt-qtz symplectite shown in g). i) monazite, sillimanite and biotite included in matrix cordierite. PPL. j) hercynitic spinel including chloritized biotite in contact with monazite and cordierite. PPL.

7.3 Garnet-biotite-plagioclase gneiss (samples Ma1h/Ma1i)

According to zircon cathodoluminescence (CL), U-Pb and Lu-Hf investigations of Zeh *et al.* (2007) the garnet-biotite-plagioclase gneisses of the Lose Quarry represent magmatic rocks, which intruded at 2061±6 Ma and were subsequently affected by a high-grade metamorphic overprint. Apart from the geochronological data, this interpretation is supported by the fieldrelationships in the Lose Quarry, indicating that the grt-bt-pl gneisses are transected (cross-cut) by leucocratic dikes and veins. On a microscopic scale, this interpretation is supported by the fact that "magmatic" zircon is overgrown by "metamorphic" garnet (Fig. 7a). Since samples Ma1h and Ma1i display similar mineral assemblages and textures they are discussed together.

Both samples show melanocratic and leucocratic domains on the centimetre scale, both of which contain garnet (15 and 25 vol.%), plagioclase (30 and 35 vol.%), biotite (25 and 40 vol.%) and opaque phases as well as accessory zircon, monazite and epidote (~5 vol.% for both samples). Quartz is a common matrix phase in sample Ma1h (~30 vol.%), but is absent in sample Ma1i. The first value in brackets is the estimated modal amount of the respective phase in sample Ma1h, while the second value is the amount in sample Ma1i. The leucocratic domains possibly represent melt batches, which were formed during the metamorphic overprint of the previously magmatic rocks. Representative mineral compositions of the observed minerals are shown in Tab. 7.

Two textural distinct garnet types can be distinguished. Garnet I is up to 3 mm in diameter, hypidio- to xenoblastic, mostly resorbed and typically surrounded by reaction rims of biotite, plagioclase and ±quartz (Fig. 7a, b). It is inclusion-free, or contains rounded inclusions of biotite, plagioclase, quartz and opaque minerals (Fig. 7b). In contrast, garnet II is up to ~0.3 mm in diameter, idiomorph, inclusion-free, and is restricted to plagioclase dominated domains (Fig. 7c). Both garnet types display diffusion controlled zoning, as reflected by increasing X_{Fe} towards the rim and fractures (Fig. 8; Tab. 7). The chemical composition of garnet cores in sample Ma1h for both garnet types is $Alm_{74}Prp_{18}Grs_{04}Sps_{04}$ (Tab. 7). In sample Ma1i one large garnet shows a relic prograde growth zoning, characterized by a compositional change from core ($Alm_{72-73}Prp_{16}Grs_{07}Sps_{04-05}$) towards the "rim" ($Alm_{74}Prp_{16}Grs_{05}Sps_{05}$; Fig. 8; Tab. 7). The uttermost rims of garnets in both sample have the composition $Alm_{78-83}Prp_{07-14}Grs_{04-05}Sps_{05-08}$ and were affected by retrograde Fe/Mg-exchange with matrix Fe/Mg-silicates (Tab. 7, Fig. 8).

Granoblastic plagioclase has a diameter of up to 4 mm, shows albite twinning and is partly epidotized (Fig. 7c, d). Some plagioclase crystals contain garnet and rounded biotite inclusions (Fig. 7c, d). Furthermore, rare symplectites between plagioclase and quartz are observed. Plagioclase in both samples is unzoned and has the composition $Ab_{69}An_{29}Or_{02}$ (Ma1h) and $Ab_{63}An_{36}Or_{01}$ (Ma1hi) - (Tab. 7).

Greenbrown lepidoplastic biotite is up to ~2.5 mm long and shows dark halos around zircon and monazite grains. Matrix biotite commonly forms unorientated clusters and is locally chloritized. In both samples chemical differences exist between biotite included in garnet cores and matrix biotite (Fig. 7b, d). The differences are shown in Tab. 6 and Tab. 7.

Epidote occurs in plagioclase-rich domains, where it forms up to ~0.25 mm large xenoblastic crystals or fine grained aggregates at the expense of plagioclase (Fig. 7c). The pistacite component (Ps = $Fe^{3+}/(Fe^{3+}+Al)*100$) of epidote ranges between 23 and 29. In most cases, epidote is associated with opaque minerals.

Zircon and monazite form idio- to hypidiomorph grains, up to 0.15 mm large.

These are found throughout the matrix and as inclusions in garnet and biotite (Fig. 7a).

Tab. 6. Average chemical parameters for biotites from different textural domains of samples Ma1h and Ma1i

sample	Ma1h		Ma1i	
	bt in grt	matrix bt	bt in grt	matrix bt
X_{Fe}	0.49	0.59	0.53	0.61
Ti (p.f.u.)	0.24	0.28	0.36	0.41
Al (p.f.u.)	3.17	3.14	3.28	3.21

Tab. 7. Representative mineral analyses of samples Ma1h and Ma1i. D.a.r. = diffusively altered rim. For further information see text

	Ma1h						Ma1i						
	grt		pl	bt		ep	grt			pl	bt		ep
wt.% oxides	core	d.a.r		in grt	in mx		core	rim	d.a.r.		in grt	in mx	
SiO_2	36.78	36.73	59.71	35.20	34.64	37.37	36.66	36.76	36.29	59.05	36.11	33.69	36.81
TiO_2	0.02	0.10		2.01	2.22	0.00	0.03	0.03	0.02		4.12	3.56	0.04
Al_2O_3	20.82	21.07	24.05	17.40	17.56	22.45	21.24	21.15	20.74	25.31	18.69	17.63	23.93
Cr_2O_3	0.03	0.07		0.07	0.07	0.04	0.11	0.07	0.03		0.07	0.10	0.00
Fe_2O_3	0.00	0.00	0.02	0.00	0.00	14.40	0.00	0.00	0.00	0.02	0.00	0.00	11.33
FeO	34.42	36.60	0.00	19.43	22.91	0.00	33.57	34.32	35.76	0.02	19.17	22.90	0.00
MnO	1.61	2.43		0.01	0.05	0.03	1.84	2.24	2.71		0.08	0.08	0.02
MgO	4.36	1.67	0.00	11.31	8.94	0.00	4.27	4.08	2.81	0.06	10.67	8.28	0.00
BaO			0.03	0.05	0.07	0.01				0.00	0.00	0.00	0.00
CaO	1.47	1.48	5.92	0.00	0.01	23.54	2.38	1.66	1.42	7.32	0.02	0.01	23.39
Na_2O			7.72	0.18	0.18	0.00				7.08	0.49	0.15	0.00
K_2O			0.33	9.06	9.25	0.00				0.21	8.78	9.26	0.00
sum	99.51	100.14	97.76	94.70	95.89	97.84	100.09	100.32	99.77	99.06	98.19	95.67	95.50
oxygens	12	12	8	22	22	12.5	12	12	12	8	22	22	12.5
cations													
Si	2.95	2.99	2.71	5.40	5.35	2.99	2.92	2.93	2.94	2.66	5.31	5.23	2.99
Ti	0.00	0.01		0.23	0.26	0.00	0.00	0.00	0.00		0.46	0.42	0.00
Al	1.97	2.02	1.29	3.15	3.20	2.12	2.00	1.99	1.98	1.34	3.24	3.23	2.29
Cr	0.00	0.00		0.01	0.01	0.00	0.01	0.00	0.00		0.01	0.01	0.00
Fe^{3+}	0.11	0.00	0.00	0.00	0.00	0.87	0.15	0.13	0.13	0.00	0.00	0.00	0.69
Fe	2.20	2.49	0.00	2.49	2.96	0.00	2.09	2.16	2.30	0.00	2.36	2.97	
Mn	0.11	0.17		0.00	0.01	0.00	0.12	0.15	0.19		0.01	0.01	0.00
Mg	0.52	0.20	0.00	2.59	2.06	0.00	0.51	0.49	0.34	0.00	2.34	1.92	0.00
Ba			0.00	0.00	0.00	0.00				0.00	0.00	0.00	0.00
Ca	0.13	0.13	0.29	0.00	0.00	2.02	0.20	0.14	0.12	0.35	0.00	0.00	2.04
Na			0.68	0.05	0.05	0.00				0.62	0.14	0.05	0.00
K			0.02	1.77	1.82	0.00				0.01	1.65	1.84	0.00
sum	8.00	8.01	4.99	15.70	15.72	8.01	8.00	8.00	8.00	4.99	15.51	15.67	8.01
X_{Fe}	0.81	0.93		0.49	0.59		0.80	0.82	0.87		0.50	0.61	
X_{ab}			0.69							0.63			

Textural observations indicate that idiomorph garnet was formed in the mineral assemblage:

(1a) grt+bt+pl+qtz±melt (Ma1h) and

(1b) grt+bt+pl±melt (Ma1i).

During the retrograde evolution garnet is locally resorbed and epidote forms at the expense of plagioclase in both samples.

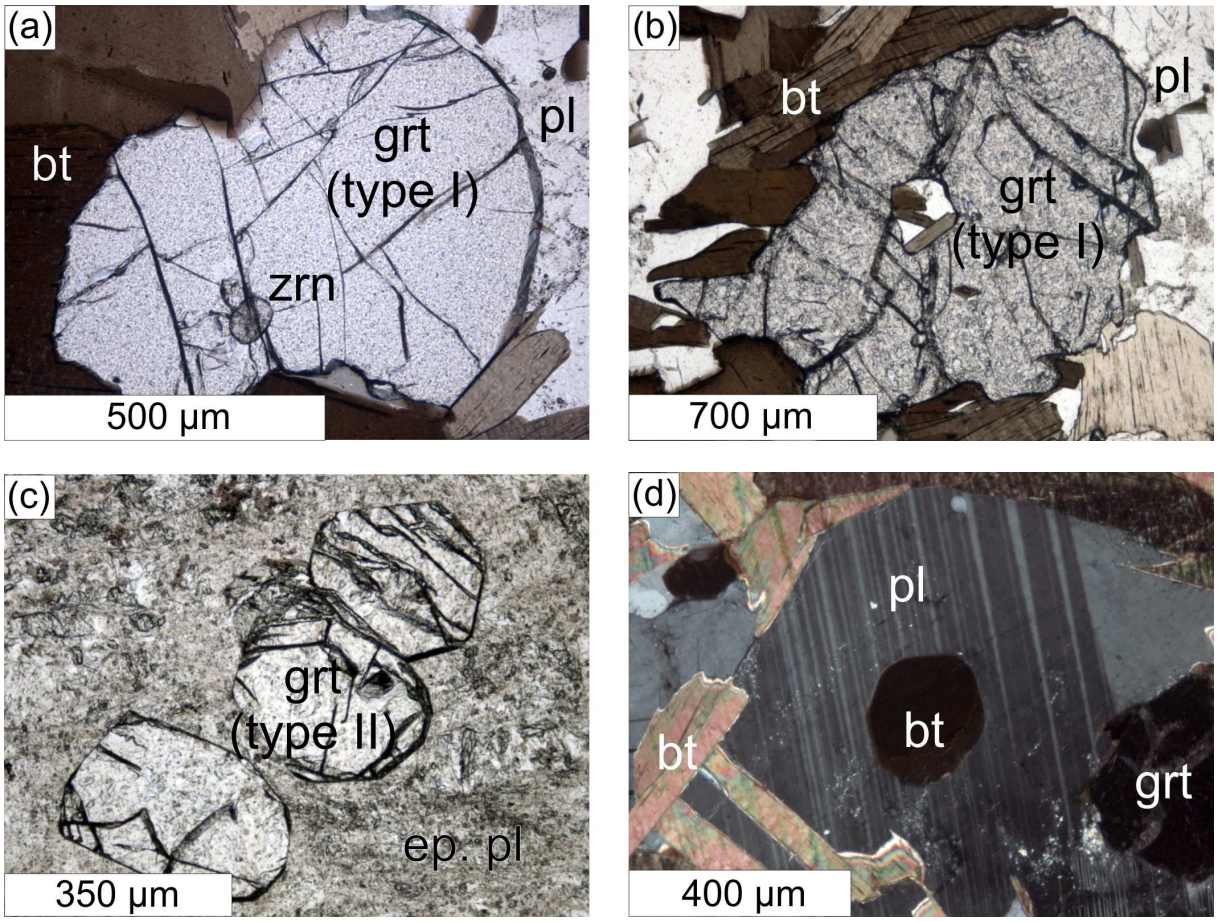

Fig. 7. Photomicrographs of samples Ma1h and Ma1i. a) garnet surrounded by biotite and plagioclase with zircon inclusion. PPL. b) garnet I with inclusions of biotite, plagioclase and quartz. PPL. c) idioblastic garnet II in strongly epidotized plagioclase (ep. pl). PPL. d) rounded biotite inclusion in plagioclase. CPL.

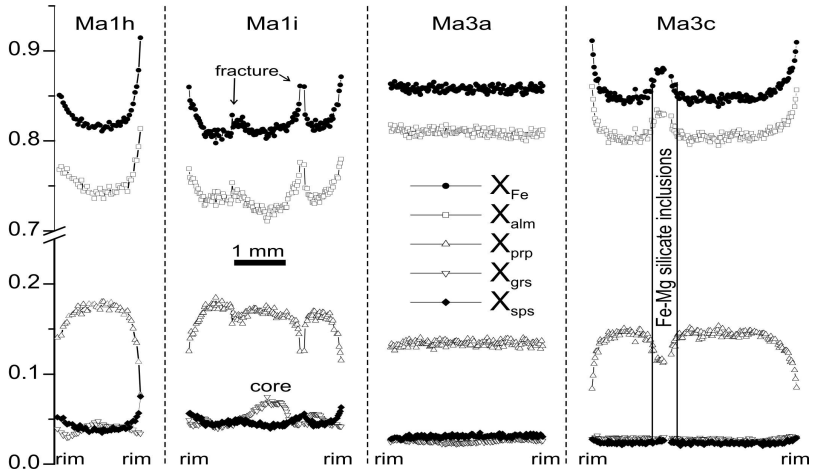

Fig. 8. Rim to rim profiles of garnet from samples Ma1h, Ma1i, Ma3a and Ma3c. Note that only garnet from sample Ma1i preserved a relic prograde growth zoning (see text for details).

8 *P-T* pseudosections

8.1 Sillimanite-garnet-cordierite gneiss (sample Ma3a)

P-T path information for sample Ma3a was obtained by the use of a quantitative phase diagram calculated in the model system MnO - TiO_2 - CaO - Na_2O - K_2O - FeO - MgO - Al_2O_3 - SiO_2 - H_2O (MnTiCNKFMASH) - (Fig. 9). Additionally, contoured pseudosections were constructed in the system MnO - CaO - Na_2O - K_2O - FeO - MgO - Al_2O_3 - SiO_2 - H_2O (MnCNKFMASH) – (Fig. 10). The H_2O content was used from LOI (1.2 wt.%; Tab. 3)

Calculations in the system MnCNKFMASH were carried out using the computer software **THERIAK-DOMINO** v.140205 (de Capitani, 2005) with a modified version of the original "tc321p2.txt" datafile to enable it for the calculation of Mn-bearing phases. Subsequently the phase diagram information obtained with **THERIAK-DOMINO** was extended to the MnTiCNKFMASH system using the computer software **THERMOCALC** v.3.21 with the thermodynamic dataset HP98 (Powell & Holland, 1988; Holland & Powell, 1990; 1998) and employing the procedures and activity-composition (*a-x*) relationships outlined by Mahar *et al.* (1997), White *et al.* (2000, 2001) and Zeh & Holness (2003). Spinel solid-solutions between the end-members hercynite (Hc) and spinel (Spl) were calculated using an ideal mixing model. Consideration of titanium was necessary in order to account for Ti-bearing phases like rutile and ilmenite, and to simulate the stabilyzing effect of Ti on biotite. For a detailed discussion about the effect of Ti on metapelitic assemblages see Stevens *et al.* (1997) and White *et al.* (2000). The absence of magnetite and the nearly pure end-member composition of ilmenite provide evidence that the oxygen fugacity must have been low throughout the *P-T* evolution of the investigated rocks. Therefore, oxygen as an additional component was not considered (see White *et al.*, 2002).

Comparison between the observed mineral assemblages (see p. 15) and those calculated in the model system MnTiCNKFMASH (Fig. 9) provide evidence that sample Ma3a underwent a clockwise *P-T* evolution, with a prograde pressure decrease from about 650°C/7 kbar to 790°C/5 kbar, followed by a retrograde temperature-pressure decrease to 700°C/4 kbar. The prograde *P-T* path conforms to the observations that garnet contains numerous inclusions of quartz, plagioclase, sillimanite, rutile (assemblage A1 in Fig. 9), and that rutile disappears at the expense auf ilmenite at the end of garnet formation (assemblage A2). Furthermore, it agrees with the observation that the rock matrix is quartz-free, consists of abundant cordierite (assemblage A3), and contains leucocratic domains with K-feldspar and plagioclase, seperated by "melt" seams (assemblage A4). The suggested prograde *P-T*

path furthermore agrees with the textural observations that garnet was initially formed in assemblage (A1) and (A2), but became successively resorbed at the expense of cordierite in assemblages (A3) and (A4). This is well supported by the contour diagrams as shown in Fig. 10a and b. The inferred retrograde *P-T* path is constrained by the observation of abundant spinel in the matrix of sample Ma3a (assemblage A5). This spinel obviously was formed at the expense of biotite as supported by round biotite inclusions in spinel (Fig. 4e). The final point of the retrograde *P-T* path is constrained by assemblage (A6), which reflects the situation of melt solidification. The finding of sillimanite and rutile in garnet indicates that pressures at the beginning of the inferred *P-T* history did not exceed ~7 kbar.

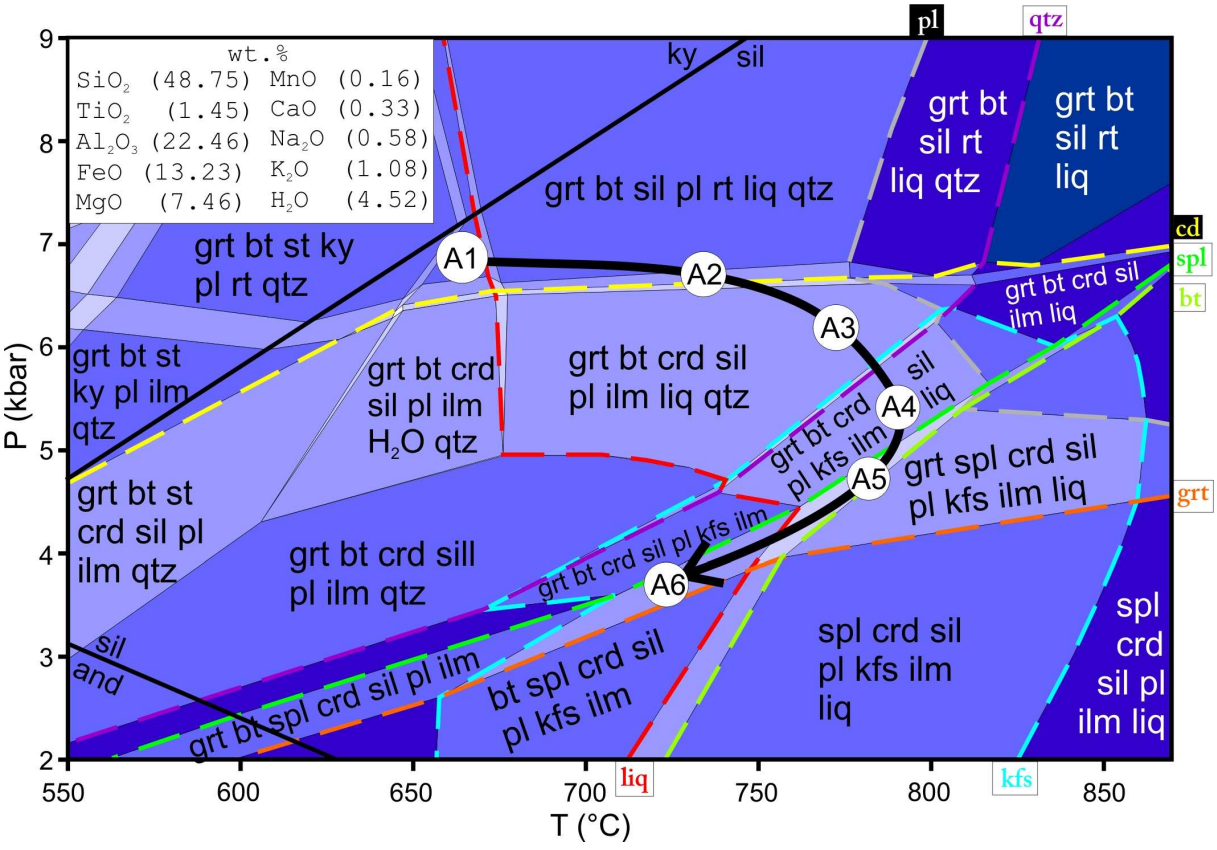

Fig. 9. *P-T* pseudosection for sample Ma3a in the system MnTiCNKFMASH. Thick black arrow indicates the inferred metamorphic *P-T* path. Phase-in/out lines are displayed as coloured dashed lines. Variance increases with darkening colour (brightest fields are divariant). Points A1 to A6 of the metamorphic path correspond to thin section observations (for details see text and petropraphy in section 7.1).

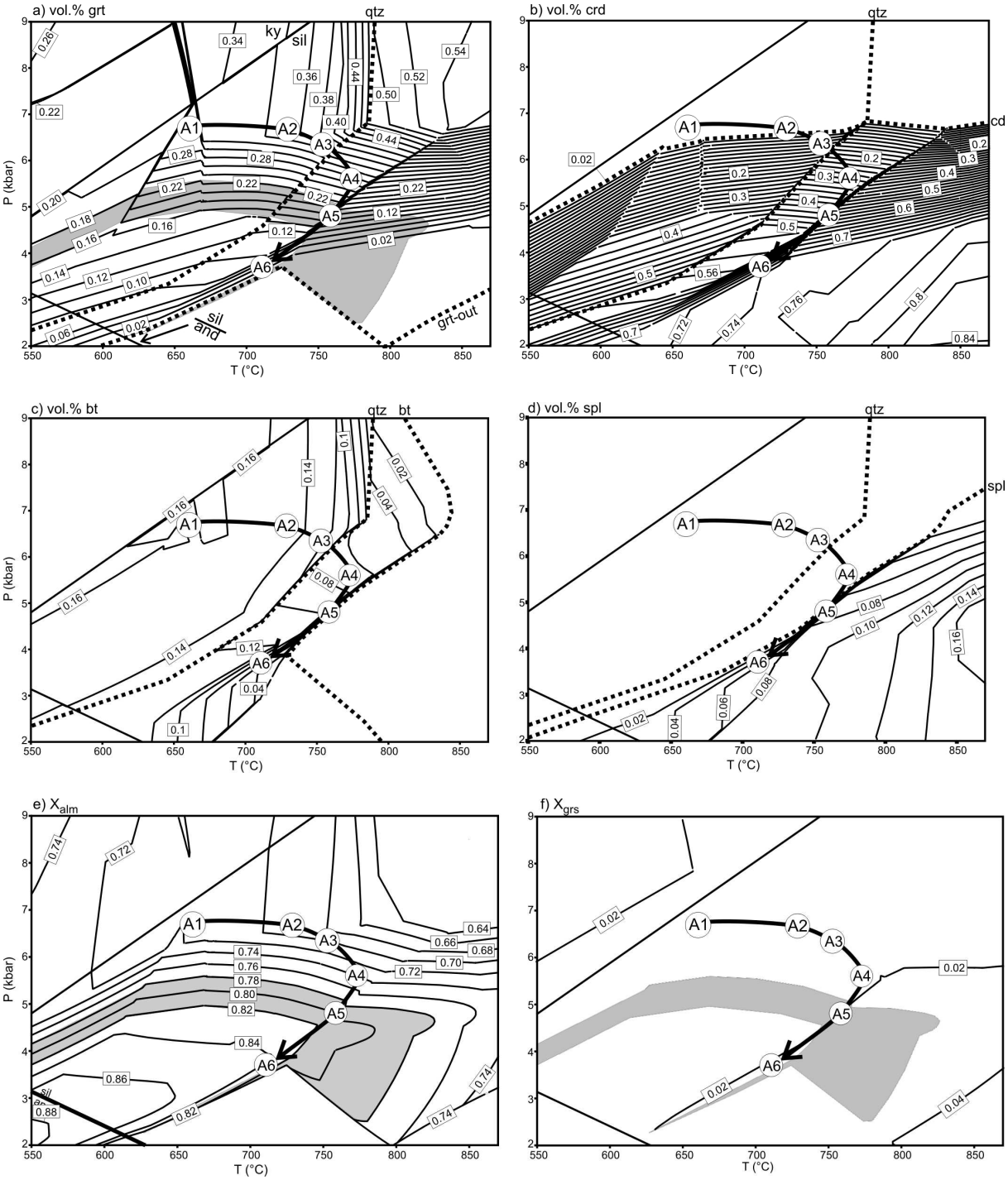
a) vol.% grt
qtz
ky
sil
A1
A2
A3
A4
A5
A6
sil
and
grt-out
P (kbar)
T (°C)
b) vol.% crd
qtz
cd
c) vol.% bt
qtz
bt
d) vol.% spl
qtz
spl
e) X alm
f) X grs

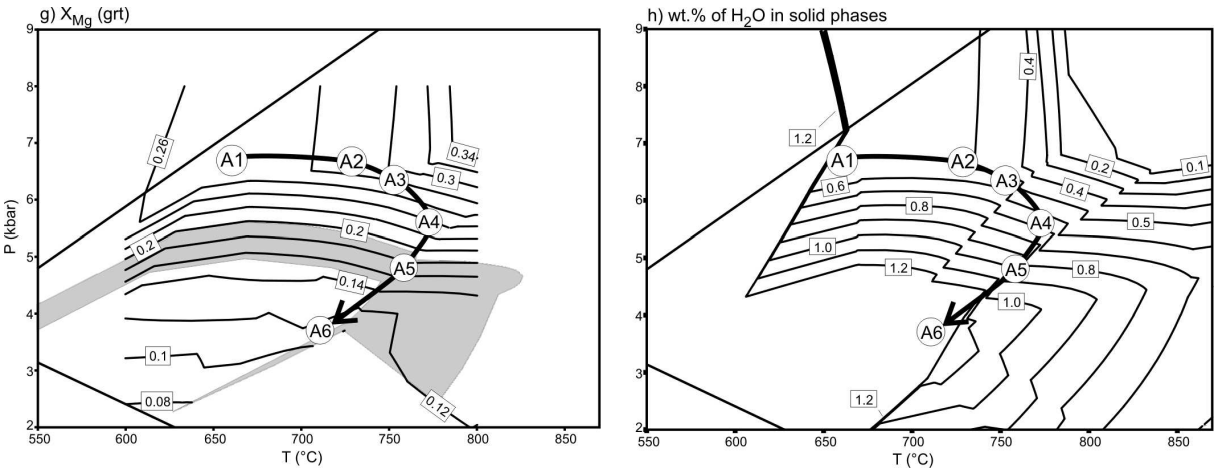

Fig. 10. Contoured *P-T* pseudosections for sample Ma3a constructed with **THERIAK-DOMINO** in the system MnCNKFMASH. The bulk chemistry is Si(38.33)Al(35.32)Fe(10.40)Mg(5.86)Mn(0.12)Ca(0.26)Na(0.91)K(1.69)H(7.10) given as mol.% of cations. Values on isopleths for vol.% of solid phases are given as vol.%/100. The *P-T* path and numbers correspond to Fig. 9. Dotted lines in a) to d) mark the in/out boundaries of the respective phases within their stability fields. Grey shaded field in a), e), f) and g) indicates where measured and calculated compositions of garnet cores coincide. a) vol.% garnet of solid phases. b) vol.% cordierite of solid phases. c) vol.% biotite of solid phases. d) vol.% spinel of solid phases. e) X_{alm} in garnet. f) X_{grs} in garnet. g) X_{Mg} in garnet. h) wt.% of H_2O in solid phases.

The mineral mode evolution in Fig. 11 shows the continous decrease of garnet, sillimanite, biotite and quartz along the inferred metamorphic *P-T* path, while the amount of cordierite, K-feldspar, plagioclase and spinel increases.

Melting in sample Ma3a begins at ~660°C at 6-7 kbar and results in a peraluminous melt with a maximum melt content of ~15 vol.% at point (A3) - (Fig. 11, Fig. 12 , Fig. 13). An interesting feature of sample Ma3a is that melt starts to crystallize during increasing temperature between points (A3) and (A4), immediately after the last free matrix quartz was dissolved in the evolving melt (Fig. 11, Tab. 8). This behaviour is attributed to the change from a qtz-saturated system to a qtz-undersaturated system. As a consequence, no further melting occurs, and existing melt starts to crystallize. Since biotite is consumed at the start of melt crystallization, the released K_2O enhances the formation of K-feldspar, as well supported by the mode evolution as shown in Fig. 11.

Tab. 8. Mineral mode (vol.%) for points (A1) to (A6) as shown in Fig. 9, calculated with **THERIAK-DOMINO** in the system MnCNKFMASH

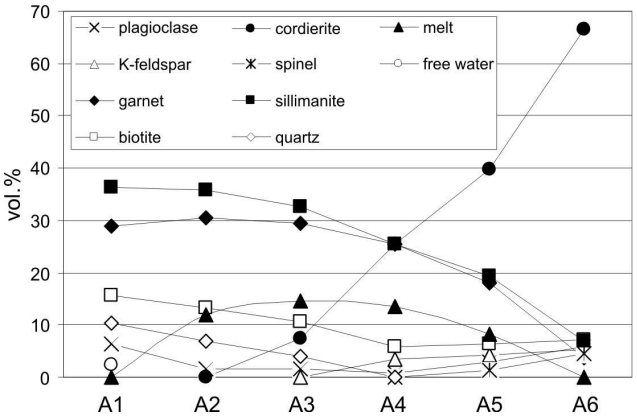

	A1	A2	A3	A4	A5	A6
T (°C)	660	724	752	775	764	710
P (kbar)	6.8	6.7	6.3	5.6	5	3.7
plagioclase	6.4	1.6	1.7	0.9	2.8	5.8
K-feldspar				3.4	4.2	5.3
garnet	28.8	30.6	29.4	25.5	18.1	3.7
biotite	15.6	13.2	10.5	5.9	6.4	7.1
cordierite			7.3	25.4	39.7	66.6
spinel					1.3	4.5
sillimanite	36.5	35.8	32.6	25.4	19.2	7.0
quartz	10.3	6.9	3.9			
melt	0.0	11.9	14.6	13.6	8.1	0.0
free water	2.4					
sum vol%	*100.0*	*100.0*	*100.0*	*100.0*	*100.0*	*100.0*

Fig. 11. Evolution of the mineral mode (in vol.%) from point (A1) to (A6) along the inferred metamorphic *P-T* path as shown in Fig. 9.

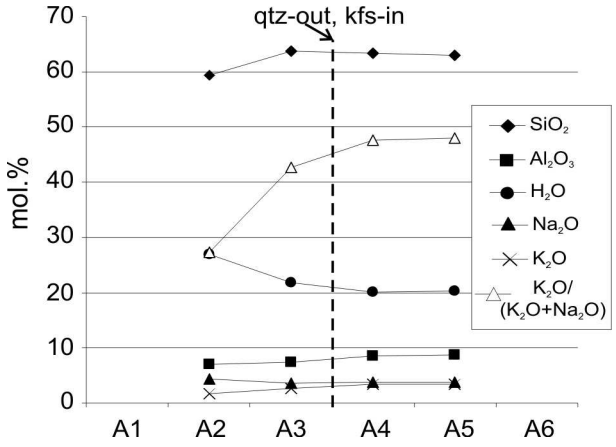

Fig. 12. Melt composition at points (A1) to (A6) along the inferred metamorphic *P-T* path of sample Ma3a (see Fig. 9). Ca, Fe and Mg are neglected since they constitute less than 1 mol.%. Dashed line indicates qtz-out/kfs-in as shown in Fig. 9. Values were calculated with **THERIAK-DOMINO** in the system MnCNKFMASH.

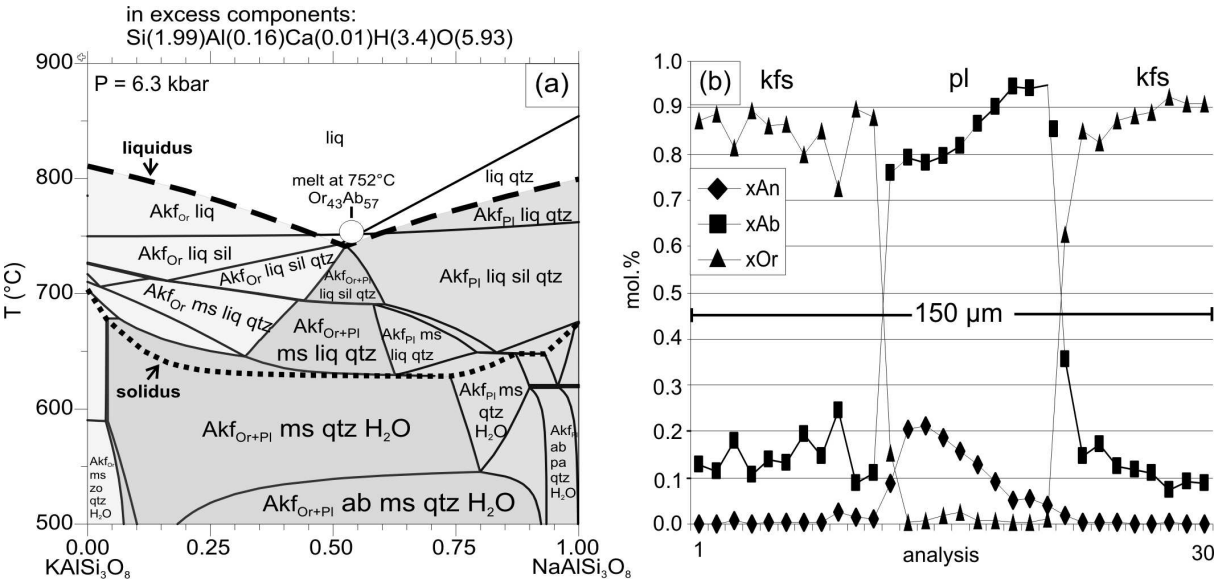

Fig. 13. a) T-X diagram calculated at 6.3 kbar in the system $KAlSi_3O_8$ (Or)-$NaAlSi_3O_8$ (Ab) for the melt composition at point (A3) of the inferred metamorphic *P-T* path of sample Ma3a (see Fig. 9). The excess components were calculated by substracting

the components needed to form binary feldspar from the total amount of the respective components in the melt. Akf_{Or} = Or-dominated (Or >50) Alkalifeldspar. Akf_{Pl} = Pl-dominated (Pl >50) Alkalifeldspar. Note that melt of this composition would almost immediately crystallize two feldspars upon cooling. b) Microprobe profile across plagioclase II seam between two K-feldspars. The seam is assumed to be the result of the final stage of melt crystallization, as it is almost pure albite.

8.2 Sillimanite-garnet-cordierite gneiss (sample Ma3c)

A *P-T* path for sample Ma3c was inferred by the use of a quantitative phase diagram in the system MnO - TiO_2 - CaO - Na_2O - K_2O - FeO - MgO - Al_2O_3 - SiO_2 - H_2O (MnTiCNKFMASH) - (Fig. 14). Additionally, contoured pseudosections were constructed in the system MnO - CaO - Na_2O - K_2O - FeO - MgO - Al_2O_3 - SiO_2 - H_2O (MnCNKFMASH) - (Fig. 16). The H_2O content was used from LOI (0.82 wt.%; Tab. 13). The methods and software programs applied to construct the (contoured) *P-T* pseudosections are the same as explained in section 8.1 for sample Ma3a on p. 28.

The *P-T* pseudosection for sample Ma3c in conjunction with observed mineral assemblages and mineral compositions (see section 7.2, p. 19) allows the interpretation that sample Ma3c underwent the same prograde *P-T* evolution as obtained for sample Ma3a, *i.e.* from ~660°C/6.5-7 kbar to ~750°C/5.5 kbar.

This prograde *P-T* path is well constrained by intergrowth relationships indicating that garnet initially grew in an assemblage with quartz, biotite, plagioclase, sillimanite and ilmenite (assemblage A1). The lower temperature limit of ~650°C for the start of the *P-T* evolution is defined by the absence of staurolite in sample Ma3c and the upper pressure limit of ~7 kbar by the absence of rutile and kyanite and the finding of sillimanite and ilmenite inclusions in garnet. This starting point agrees well to that inferred for sample Ma3a.

The finding of oriented cordierite I inclusions in garnet (= assemblage A2a or A2b) – (Fig. 6e) indicates that late garnet growth took place in assemblage with cordierite. At this point it should be noted that isothermal decompression is inappropriate to explain simultaneous garnet and cordierite growth. This is constrained by the contours for the garnet mode, as shown in Fig. 16a. According to the phase relationships shown in the *P-T* pseudosection (Fig. 14) the prograde formation of cordierite and garnet is always accompanied by the formation of melt, either in the assemblage grt-bt-sil-crd-pl-ilm-qtz-liq (A2a) or grt-bt-sil-crd-pl-kfs-ilm-qtz-liq (A2b). The observed cordierite coronas (crd II) around resorbed garnet, the absence of matrix quartz (except for the biotite-cordierite-quartz symplectites - see below), and the finding of a few plagioclase-K-feldspars intergrowths requires that the *P-T* evolution passed through the quartz-free mineral assemblage: grt-bt-crd-sil-pl(-kfs)-ilm-liq (assemblage A2a and A2b), which requires *P-T* conditions of ~790-810 °C at 5.5.kbar.

The observation of abundant matrix spinel (assemblage A3) and sillimanite provides

evidence for a subsequent pressure decrease at *ca.* 800°C/5 kbar. Furthermore, the widespread occurrence of this mineral assemblage (spinel+sillimanite) constraints that the retrograde *P-T* evolution followed a decompression-cooling path. In fact such a cooling path well conforms to one previously inferred by Hisada *et al.* (2005).

While the *P-T* pseudosection in Fig. 14 well explains most textures and mineral assemblages observed in sample Ma3c, it cannot account for the finding of biotite-cordierite IV-quartz symplectites (Fig. 6g, h), which are observed in some garnet domains, where the garnet is strongly resorbed along previous fractures (Fig. 6c-h). It is most likely that these symplectitic textures are the result of local garnet-melt reactions. This interpretation is well supported by a *P-T* pseudosection (Fig. 15a), which was calculated for the assumption that the melt, formed during the prograde *P-T* evolution of sample Ma3c, mainly reacted with garnet during the retrograde *P-T* evolution. In fact, this assumption conforms to the wide reaction domains with biotite-cordierite IV-quartz symplectites, as shown in Fig. 6c-h. The *P-T* pseudosection was calculated using a bulk composition, which is made up of 50 mol.% melt and 50 mol.% garnet with the compositions of melt and garnet as obtained from the MnCNKFMASH *P-T* pseudosection of the full rock system at 765°C/6.3 kbar. The calculated pseudosection in Fig. 15a supports an interpretation that the formation of the symplectitic assemblage biotite-cordierite IV-quartz±plagioclase at the expense of melt and garnet took place during a retrograde pressure-temperature decrease from ~800°C/6 kbar to ~650°C/4 kbar. This *P-T* path segment is in good agreement with the observation that the symplectitic domains contain neither sillimanite, nor orthopyroxene. Furthermore, it conforms with the retrograde *P-T* evolution constrained by the assemblage spinel+sillimanite in the full bulk rock system of sample Ma3c (Fig. 14), and the retrograde *P-T* evolution inferred for sample Ma3a. Additionally, The *P-T* pseudosection (Fig. 15a) predicts that the melt-out reaction occurs at much lower temperatures in garnet-melt subdomains. This results from the fact, that the melt-bearing subdomain (*i.e.* melt along previous garnet fractures) contains relatively more H_2O than the full rock system and is supported by the T-X diagram in Fig. 15b.

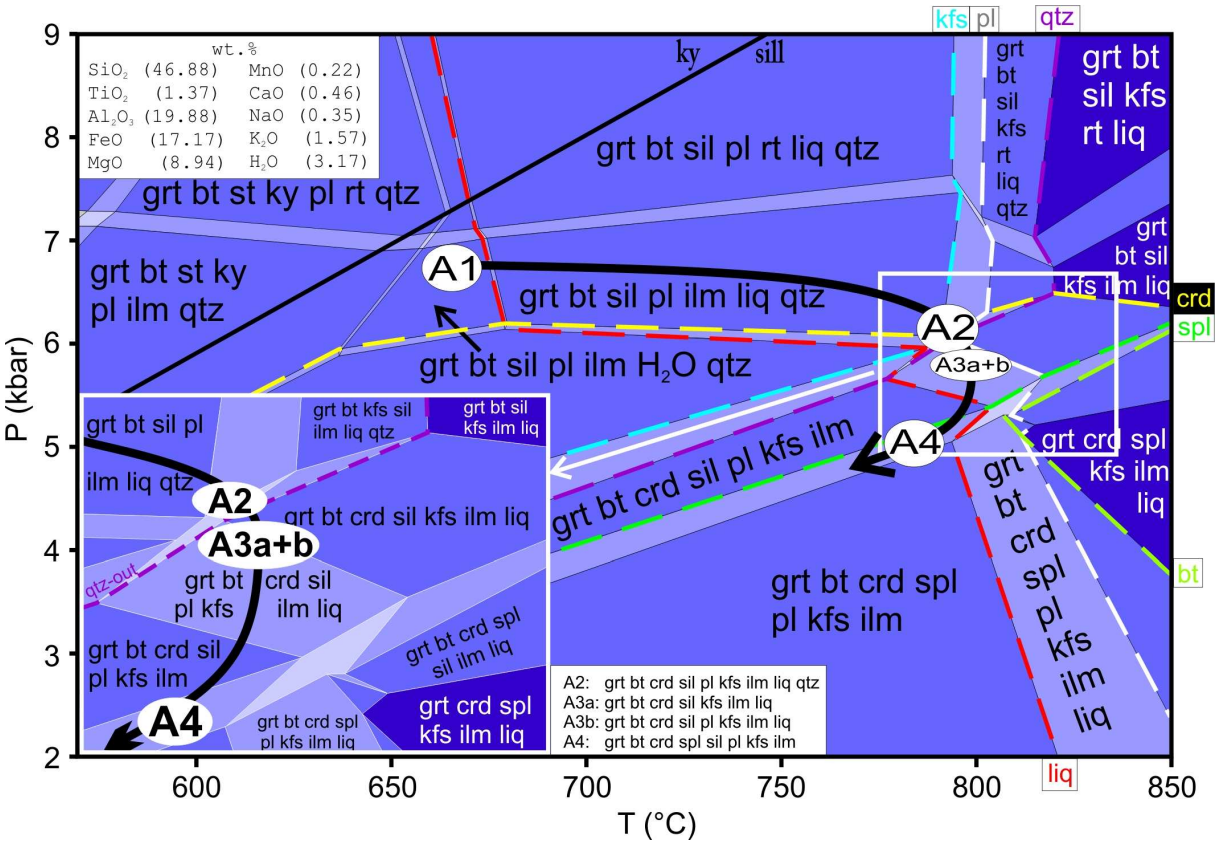

Fig. 14. *P-T* pseudosection for sample Ma3c in the system MnTiCNKFMASH. Thick black arrow indicates the inferred metamorphic *P-T* path. Phase-in/out lines are displayed as coloured dashed lines. Variance increases with darkening colour (brightest fields are divariant). Points (A1) to (A4) of the metamorphic path correspond to thin section observations (for details see text and section 7.2).

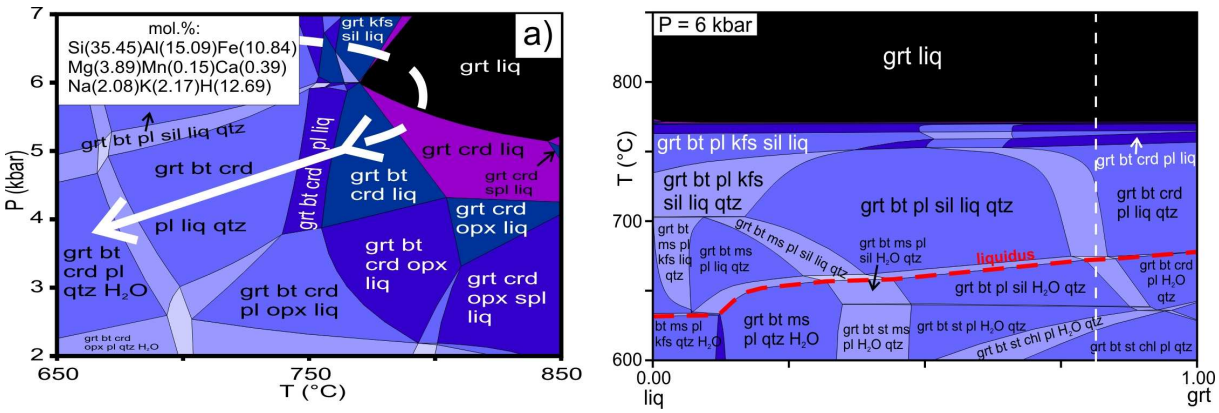

Fig. 15. a) *P-T* pseudosection calculated for melt-garnet interaction as indicated by observed biotite-cordierite-quartz symplectites (±plagioclase; see Fig. 6c-h). Dashed white line represents inferred *P-T* path of Fig. 14 and solid white line indicates retrograde *P-T* path inferred from local symplectititc domains as shown in Fig. 6c-h. b) T-X diagram for melt (=liq; Si(20.4)Al(5.1)Fe(0.1)Mg(0.1)Ca(0.1)Na(2.1)K(2.2)H(12.7) mol.% cations) and garnet compositions (Si(15)Al(10)Fe(10.7)Mg(3.8)Mn(0.2)Ca(0.3)) at point (A2; ~800°C/6 kbar) of Fig. 14. Dashed white line is the compositional ratio of melt:grt (~0.2:0.8) above which the observed biotite-cordierite-quartz±plagioclase symplectites will form by garnet-melt reactions.

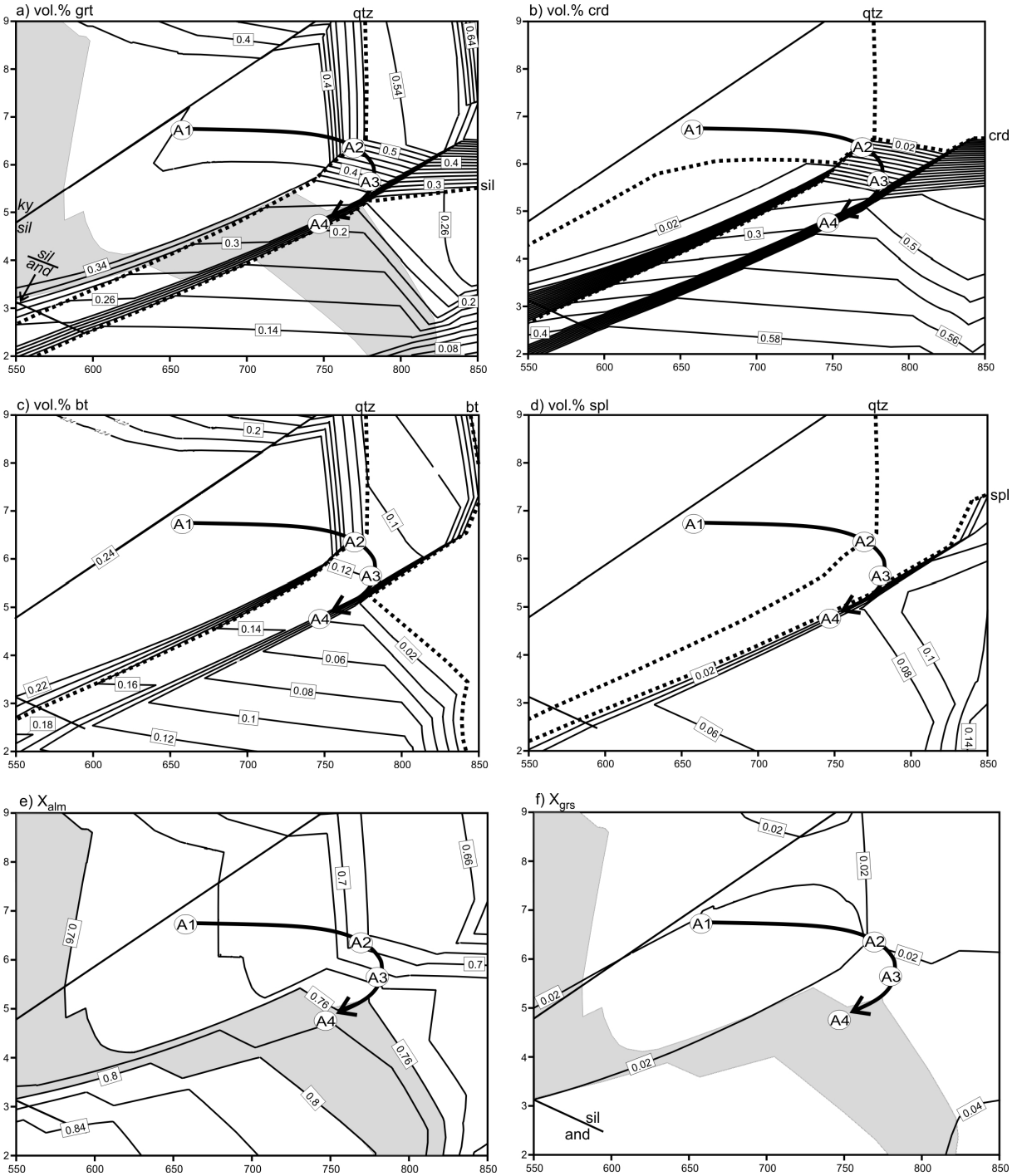

Fig. 16. Contoured *P-T* pseudosections for sample Ma3c constructed with **THERIAK-DOMINO** in the system MnCNKFMASH. The bulk chemistry is Si(37.92)Al(32.17)Fe(13.90)Mg(7.23)Mn(0.17)Ca(0.37)Na(0.56)K(2.53)H(5.13) given as mol.% of cations. Values on isopleths for vol.% of solid phases are vol.%/100. The *P-T* path and numbers (A1) to (A4) correspond to Fig. 14. Dotted lines in a) to d) mark the in/out boundaries of the respective phases within their stability fields. Grey shaded field in (a), (e) and (f) indicates the area where the measured and calculated compositions (X_{alm}) of garnet cores (X_{alm} ~ 0.8, Fig. 8) coincide. a) vol.% garnet of solid phases. b) vol.% cordierite of solid phases. c) vol.% biotite of solid phases. d) vol.% spinel of solid phases. e) X_{alm} in garnet. f) X_{grs} in garnet.

The mineral mode evolution (vol.%) between assemblages A1 to A4 (Fig. 14) is shown in Fig. 17 and Tab. 9. The most obvious feature is the first increase and later decrease of garnet, and the generell decrease of sillimanite and biotite, which react to mainly cordierite, the exhaustion of

quartz, the late formation of spinel and the relatively small pressure and temperature interval, where melt is a noteworthy "phase" in the assemblages (A2) and (A3).

Tab. 9. Mineral mode (vol.%) for points (A1) to (A4) as shown in Fig. 14 and Fig. 17a. Calculated with **THERIAK-DOMINO** in the system MnCNKFMASH.

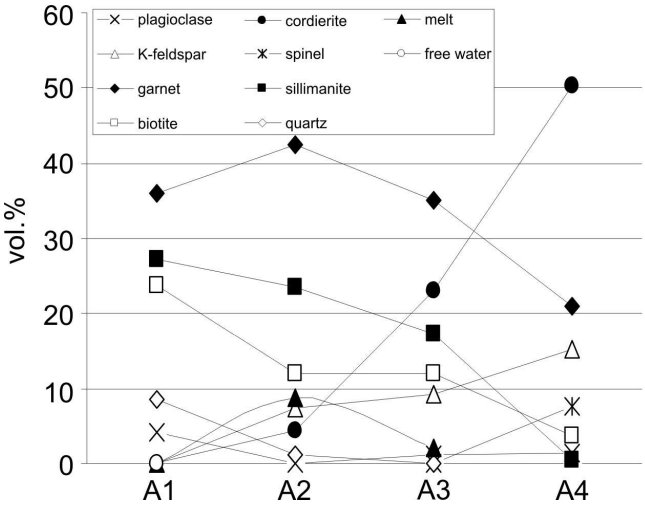

	A1	A2	A3	A4
T (°C)	660	765	770	740
P (kbar)	6.7	6.3	5.6	4.8
plagioclase	4.2	0.0	1.2	1.4
K-feldspar	0.0	7.5	9.3	15.3
garnet	36.1	42.5	35.0	21.1
biotite	23.9	12.0	12.0	3.8
cordierite		4.4	23.0	50.3
spinel			0.0	7.7
sillimanite	27.3	23.6	17.3	0.5
quartz	8.5	1.3	0.0	
melt	0.0	8.8	2.2	
free water	0.1			
sum vol%	*100.0*	*100.0*	*100.0*	*100.0*

Fig. 17. Mineral mode (vol.%) for points (A1) to (A4) as shown in Fig. 14 and Tab. 9. Calculated with **THERIAK-DOMINO** in the system MnCNKFMASH.

The only K-feldspar observed in thin section and analysed with the microprobe was found as central "inclusion/exsolution" in plagioclase (Fig. 5). Although up to ~15 vol.% of K-feldspar are predicted by the calculated *P-T* pseudosection, only little K-feldspar was observed in thin section. This can have different reasons. First, the bulk chemistry used to calculate the *P-T* pseudosection may not be representative for the investigated thin section. Second, the amount of H_2O, used for *P-T* pseudosection calculation was erroneous, due to later hydration of the rock. Less H_2O would shift the fields that involve melt (*i.e.* "liq" in Fig. 14) and K-feldspar to higher temperatures. Third, the formation of K-feldspar is prevented due to the sluggishness of its nucleation. This interpretation is supported by experiments of Naney & Swanson (1980), who investigated "*The effect of Fe and Mg on crystallization in granitic systems*" and found that in the presence of Fe and Mg the nucleation of feldspars and quartz is greatly inhibited, "… *Indeed, plagioclase is the only tectosilicate to nucleate in the granodiorite* (i.e. peraluminous) *composition. Mafic phases nucleate and grow outside their thermal stability fields as defined by the equilibrium phase diagrams*". Furthermore, these authors state that the early nucleation of biotite would inhibit the growth of other K-bearing phases like K-feldspar. This effect is probably caused by the breakdown of the melts Si-O framework due to the presence Fe and Mg, which favors the nucleation of ino-/ phyllosilicates rather than framework silicates (Naney & Swanson, 1980). The point to be made here is that the textural difference between samples Ma3a and Ma3c, *i.e.* abundant K-feldspar and the lack thereof, is probably caused

by, (1) the composition of the melt shortly before crystallization (more K-rich in sample Ma3a) and (2) the amount of melt (~15 vol.% (Ma3a) vs. ~9 vol.% (Ma3c)), which causes the melt in sample Ma3c to be relatively enriched in Fe/Mg compared to sample Ma3a.

8.3 Garnet-biotite-plagioclase gneiss (samples Ma1h/Ma1i)

P-T path information for samples Ma1h and Ma1i were obtained by the use of *P-T* pseudosections calculated in the system MnO - CaO - Na_2O - K_2O - FeO - MgO - Al_2O_3 - SiO_2 - H_2O (MnCNKFMASH) with **THERIAK-DOMINO** v.140205 using a modified version of the original "tc321p2.txt" datafile to enable it for the calculation of Mn-bearing phases (Fig. 18). Calculations performed with the water content estimated from loss on ignition (Tab. 3) are unable to fit the observed assemblages. However, when the water content is adjusted to an amount high enough to disappear during the formation of the first melt (*i.e.* ~1.5 wt.% H_2O), a reasonable explanation is obtained.

The *P-T* pseudosections, as shown in Fig. 18, well explain the observation that sample Ma1h contains quartz, whereas sample Ma1i is quartz-free and that both samples contain garnet, biotite and plagioclase (Fig. 18a, d). Furthermore, the measured composition of the investigated garnets of both samples are in good agreement with the calculations as shown in Fig. 18a and d. In fact, the core compositions of garnet ($Alm_{74}Prp_{17}Grs_{05}Sps_{04}$) in sample Ma1h require *P-T* conditions of ~750°C at ~6 kbar and the rarely observed cores of composition $Alm_{72-73}Prp_{16}Grs_{07}Sps_{04-05}$ in sample Ma1i would require *P-T* conditions of ~800°C at 7 kbar. This *P-T* condition is higher than those obtained from the metapelitic samples Ma3a/Ma3c and may either reflect that this garnet core was formed during magmatic cooling (at 2061±6 Ma, prior to the metamorphic overprint), or it is an artefact of the obtained *P-T* pseudosection calculations, because the size of the mineral stability fields and the position of contours depend on several factors, comprising bulk composition, H_2O content, additional components like Ti, Zn, *etc.* and *a-x* relationships.

A metamorphic origin of the observed garnet assemblages seems to be most likely for several reasons: First, magmatic zircon in the garnet-biotite-plagioclase-gneisses is overgrown by garnet (Fig. 7a), indicating that it was formed later. Second, the field relationships in the Lose Quarry indicate that the garnet-biotite-plagioclase-gneisses are cross-cut by up to several meter-wide granodioritic and leucocratic dikes. This provides evidence that the gneisses were fractured and affected by an additional heat input after the emplacement of the magmatic precursor.

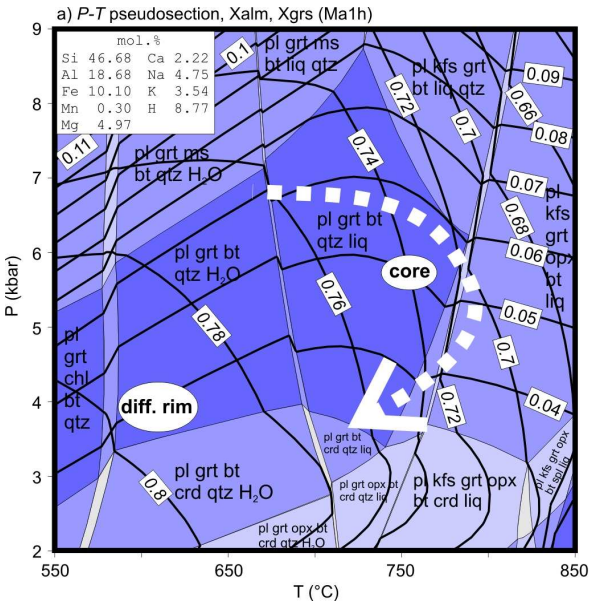
a) P-T pseudosection, Xalm, Xgrs (Ma1h)
mol.%
Si 46.68 Ca 2.22
Al 18.68 Na 4.75
Fe 10.10 K 3.54
Mn 0.30 H 8.77
Mg 4.97
pl grt ms bt liq qtz
pl kfs grt bt liq qtz
pl grt ms bt qtz H2O
pl grt bt qtz liq
pl grt bt qtz H2O
core
pl kfs grt opx bt liq
pl grt chl bt qtz
diff. rim
pl grt bt crd qtz H2O
pl grt bt crd qtz liq
pl grt opx bt crd qtz liq
pl kfs grt opx bt crd liq
pl grt opx bt crd qtz H2O
pl kfs grt opx bt spl liq
P (kbar)
T (°C)

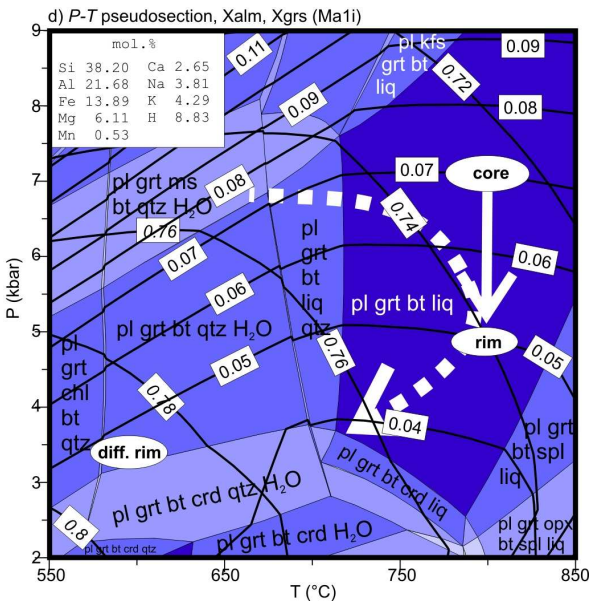
d) P-T pseudosection, Xalm, Xgrs (Ma1i)
mol.%
Si 38.20 Ca 2.65
Al 21.68 Na 3.81
Fe 13.89 K 4.29
Mg 6.11 H 8.83
Mn 0.53
pl kfs grt bt liq
pl grt ms bt qtz H2O
core
pl grt bt liq
rim
pl grt bt qtz H2O
pl grt chl bt qtz
diff. rim
pl grt bt crd qtz H2O
pl grt bt crd liq
pl grt bt spl liq
pl grt bt crd H2O
pl grt opx bt spl liq
P (kbar)
T (°C)

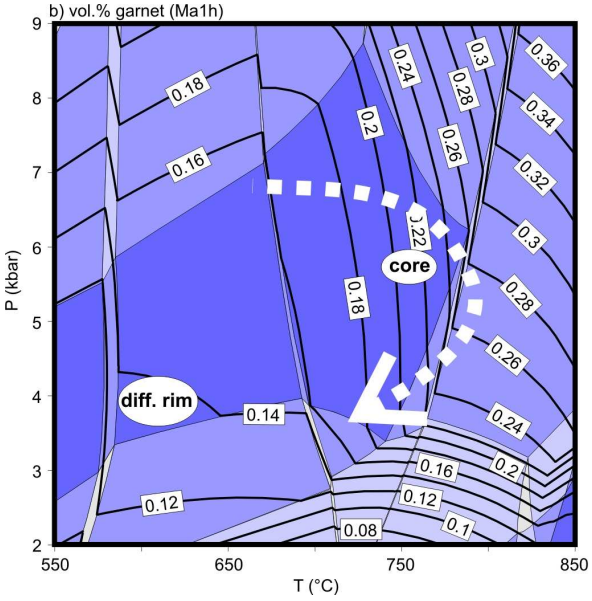
b) vol.% garnet (Ma1h)
core
diff. rim
P (kbar)
T (°C)

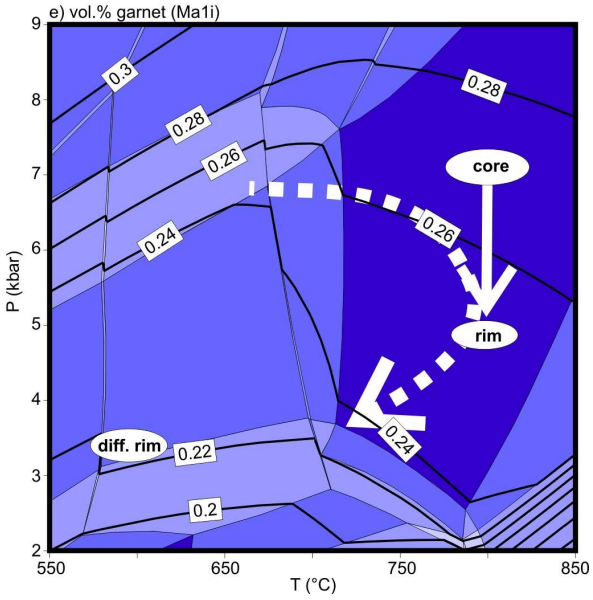
e) vol.% garnet (Ma1i)
core
rim
diff. rim
P (kbar)
T (°C)

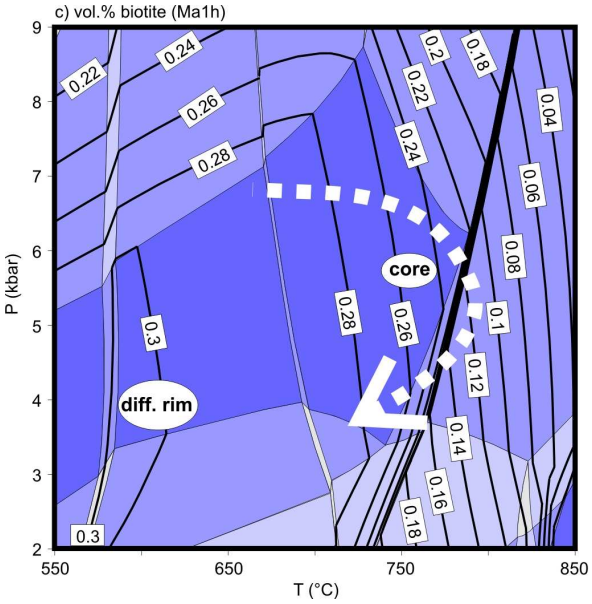
c) vol.% biotite (Ma1h)
core
diff. rim
P (kbar)
T (°C)

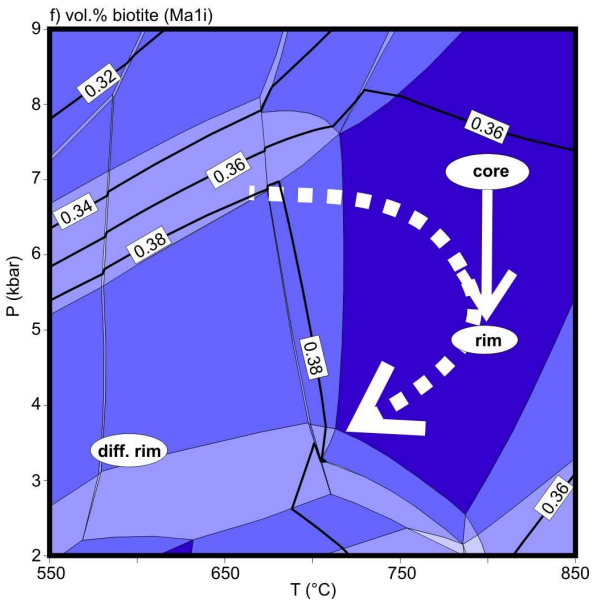
f) vol.% biotite (Ma1i)
core
rim
diff. rim
P (kbar)
T (°C)

Fig. 18. Contoured *P-T* pseudosections for sample Ma1h and Ma1i calculated with **THERIAK-DOMINO** in the system MnCNKFMASH. Variance increases with darkening colour (brightest fields are divariant). Mineral modes are labeled as vol.%/100. Solid white arrow in d), e) and f) indicates the compositional range of relic garnet growth zoning of sample Ma1i. Ellipses indicate where measured and calculated garnet core and rim compositions coincide (see Fig. 8). The inferred metamorphic *P-T* path of sample Ma3a (see Fig. 9) is shown for comparison as the white dashed arrow. Diff. rim = diffusively altered garnet rim. a) + d) *P-T* pseudosection contoured for X_{alm} (steep contours labeled in italics) and X_{grs} ("flat" contours) for sample Ma1h and Ma1i, respectively. b) + e) mode garnet. c) + f) mode biotite.

9 Summary: Metamorphic evolution of the Mahalapye Complex

Petrological investigations on samples with different bulk compositions provide evidence that the Mahalapye Complex underwent a clockwise *P-T* evolution with a prograde pressure decrease/temperature increase from ~650°C/7 kbar to ~800°C/5.5-6 kbar (metamorphic peak), followed by decompression-cooling to ~600°C/3-4 kbar (Fig. 19). This *P-T* evolution is best constraint by mineral assemblages and reaction textures observed in the metapelitic samples Ma3a and Ma3c (see sections 8.1 and 8.2, respectively). The peak metamorphic conditions are additionally constraint by mineral assemblages and compositions (measured and calculated) of samples Ma1h and Ma1i (section 8.3).

The obtained *P-T* path indicates that the rocks of the Mahalapye Complex underwent heating from ~650 to 800°C, while they were exhumed from *ca.* 26 km depth to 20 km depth (7 to 5.5 kbar). Furthermore, it constraints that these rocks underwent uplift from ~20 km depth to ~11 km depth (5.5 to 3 kbar), while they were cooled from ~800°C to 600°C during the retrograde *P-T* evolution.

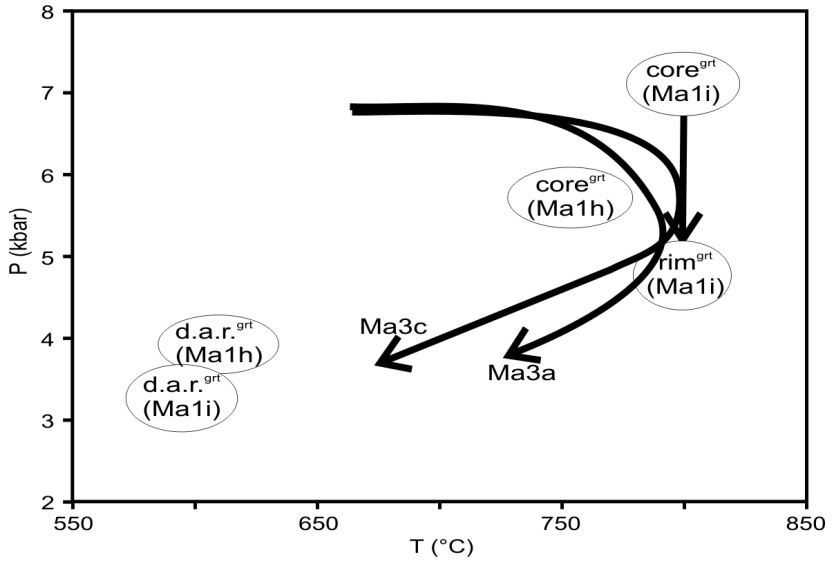

Fig. 19. *P-T* diagram showing the inferred metamorphic evolution for rocks of the Mahalapye Complex. D.a.r. = diffusively altered rim of garnet.

Phikwe Complex

10 Geological overview

The Phikwe Complex, as designated by Aldiss (1991; Fig. 20) forms the northwestern part of Central Zone of the Limpopo Belt and is situated in southeastern Botswana. It is made up of metamorphic and mafic to ultramafic rocks, minor Fe-quartzites and (migmatitic) para-/ orthogneisses, including tonalites, trondhjemites and granodiorites (TTG's) (Aldiss, 1991; Brandl, 1992; Carney *et al.*, 1994; Key & Ayres, 2000; Chavagnac *et al.*, 1999; Barton *et al.*, 2006).

To the north the Phikwe Complex is limited by the Letlhakane Fault, which continues into the Magogapathe Shear Zone (*MSZ*) further to the east. Both structures form part of the moderately south to southeast dipping Triangle-Tuli-Sabi Shear Zone System, which seperates the Northern Marginal Zone of the Limpopo Belt from the Zimbabwe Craton (Fig. 20 and Fig. 1; Aldiss, 1991; McCourt & Vearncombe, 1992; Paya, 1996; Holzer *et al.*, 1999; Chavagnac, 1999; Kramers *et al.*, 2007). Key & Hutton (1976), who follow the argumentation of Coward *et al.* (1972), suggested a dextral offset of about 50 km along the shear zone in the Botswanan sector. So far, the age of shear zone activation is not well constrained. For the Botswanan sector, Hickman & Wakefield (1975) suggested an age of 2.1 Ga on the basis of Rb-Sr isochron data, whereas Robertson & Du Toit (1981) argue that the 2.1 Ga age represents reactivation and suggest that primary faulting occurred at 2.6 Ga. An early Proterozoic activation is also suggested by Van Breemen & Hawkesworth (1980), who obtained Sm-Nd ages of 1974±14 Ma and 1988±14 Ma on garnets from the Triangle Shear Zone (cited in McCourt & Vearncombe, 1992 and Holzer *et al.*, 1999). These ages are interpreted to indicate garnet growth under granulite-facies conditions during deformation. Evidence for an ~2.0 Ga ductile high-grade metamorphic activation of the western part of the shear zone system in Botswana is presented by Holzer *et al.* (1999). These authors obtained ~2.0 Ga U-Pb ages from apatite, and Pb stepwise leaching (PbSL) ages on titanite from the partly deformed Swejane granite near Phikwe. The southeastern boundary between the Phikwe Complex and the Beit Bridge Complex is defined by a gradual (Holzer *et al.*, 1999), lithological and structural change (Barton *et al.*, 2006), but in detail it is ill defined due to poor exposure (Barton *et al.*, 2006). The boundary between the Phikwe and the Motloutse Complex to the west is defined by the Dikalate Shear/Thrust Zone (DSZ; Majaule *et al.*, 2001; see also Aldiss, 1991; Key *et al.*, 1994

and Holzer *et al.*, 1999), whereas the southern contact with the Mahalapye Complex is obscured by post-Archean cover. Aldiss (1991) and Carney *et al.* (1994) postulate that the DSZ forms the southward continuation of the Lethlakane Fault (see above).

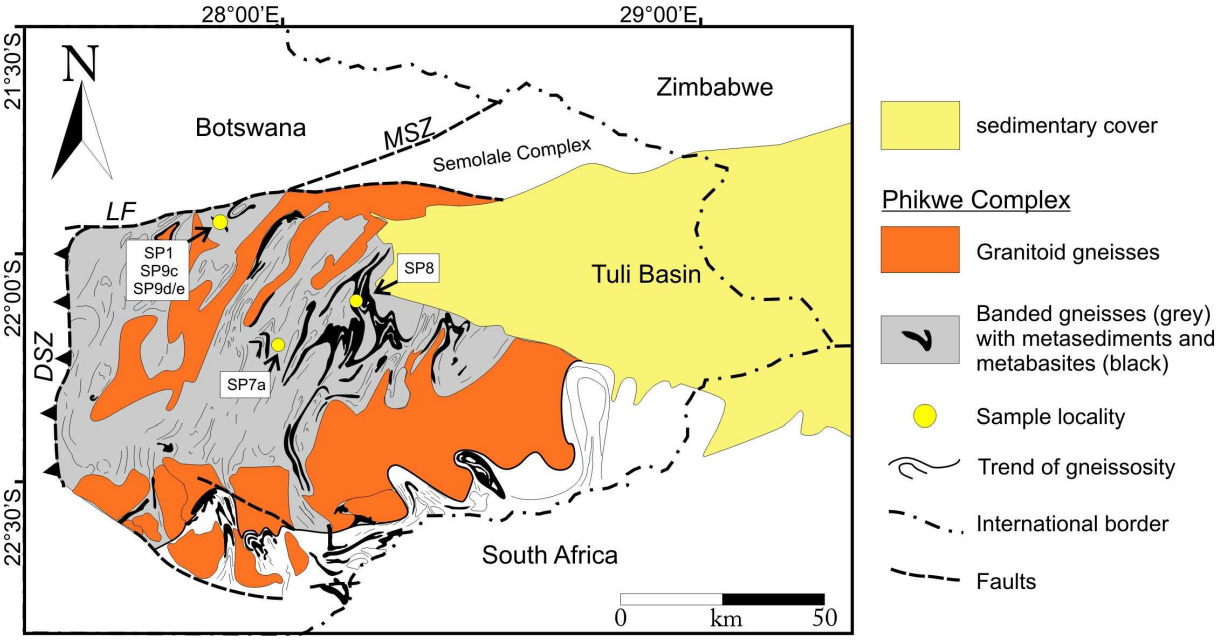

Fig. 20. Simplified geological map of the Phikwe Complex (modified after Carney *et al.*, 1994; Hisada & Miyano, 1996; Holzer *et al.*, 1999 and Majaule *et al.*, 2001). *MSZ* = Magogapathe Shear Zone, LF = Letlhakane Fault, DSZ = Dikalate Shear/Thrust Zone.

Geochronological data obtained by different techniques and isotope systems, mostly yield ages of ~2.0 Ga and ~2.6 Ga for rocks of the Phikwe Complex. Hickman & Wakefield (1975) obtained an Rb-Sr whole rock (gneiss) isochron age of 2660±40 Ma (recalculated by Cahen *et al.*, 1984), which they interpret as the age of metamorphism (M1) accompanied by deformation (D1) in the Phikwe area. Holzer *et al.* (1999) obtained a strongly discordant U-Pb zircon age of 2517±33 Ma from the polyphase deformed Swejane Granite near Selebi-Phikwe, interpreted to reflect the upper limit for the granite emplacement. Furthermore, McCourt & Armstrong (1998) obtained zircon U-Pb (SHRIMP) crystallization ages of 2595±18 Ma and 2652 ±15 Ma from the syntectonic Makowe Granite northwest of Selebi-Phikwe and a syntectonic granite east of Selebi-Phikwe, respectively. These ages are also interpreted to define the upper limits for the granite emplacement (McCourt & Armstrong, 1998).

Rb-Sr and K-Ar ages of ~2.0 Ga (Van Breemen & Dodson, 1972; Wakefield, 1974) were interpreted to date the timing of the final overprint under amphibolite to greenschist-facies conditions (Hickman & Wakefield, 1975). This Palaeoproterozoic event is considered as the final stage of deformation in the Phikwe area, when regional cooling occurred, possibly as the result of uplift and stabilization of that region (Hickman & Wakefield, 1975; Holzer *et al.*, 1999). In contrast to Hickman & Wakefield (1975), Chavagnac *et al.* (1999) interpreted Sm-

Nd mineral-WR and Pb-Pb WR isochron ages of ~2.0 Ga to date the timing of a high-grade metamorphic overprint that caused migmatization of parts of the Phikwe Complex. On the basis of Nd-model ages Chavagnac *et al.* (1999) argue that the protolith of their investigated migmatitic rock formed during the Neoarchean at ~2.7 Ga. This Neoarchean age is considered as the time of an Archean crust formation episode in the Phikwe Complex (Chavagnac *et al.*, 1999) and is therefore contemporaneous with the Archean (D1 and M1) age obtained by Hickman & Wakefield (1975).

Presently little is known about the *P-T* evolution of the Phikwe Complex, especially there are no information about the prograde *P-T* evolution. A summary of *P-T* results obtained by previous petrological studies from the Phikwe Complex is given in Fig. 21.

Most *P-T* data of the previous studies only point to a retrograde *P-T* evolution from upper amphibolite facies to greenschist facies conditions (Tsunogae, 1989; Hisada *et al.* 1994a, 1994b; Hisada & Miyano, 1996), or constrain single *P-T* points (Hickman & Wakefield, 1975; Fig. 21).

P-T estimates carried out during the previous studies mostly yield single points with variable *P-T* conditions ranging ~650-775°C/5-8 kbar to ~400-450°C/3-4 kbar (Hisada *et al.*, 1994a, 1994b; Tsunogae, 1989; Hickman & Wakefield, 1975). These estimates maybe reflect the retrograde *P-T* evolution of the Phikwe Complex. Furthermore, Hisada & Miyano (1996) concluded that rocks of the Phikwe Complex underwent a isothermal decompression from ~800°C/11 kbar to ~800°C/6 kbar, followed by retrograde isobaric cooling, similar to the eastern Central Zone in South Africa and Botswana.

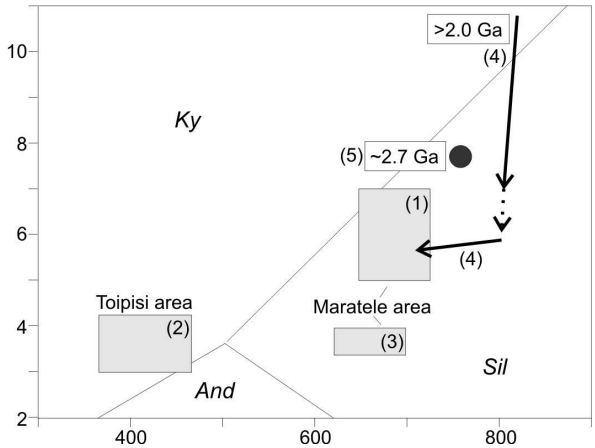

Fig. 21. Compilation of *P-T* results obtained from rocks of the Phikwe Complex (compilation modified after Barton *et al.*, 2006 and Kramers *et al.*, 2007). Data from: (1) Hisada *et al.* (1994a), Maretele, microthermometry, rehydration. (2) Hisada *et al.* (1994b), Topisi, greenschist facies rehydration of granulites. (3) Tsunogae (1989), Maretele, rehydration of granulites (orthoamphibole). (4) suggested *P-T* path of Hisada & Miyano (1996). (5) suggested Archean peak *P-T* conditions of Hickman & Wakefield (1975).

11 Petrography and Mineral Chemistry

From the Selebi-Phikwe complex 19 samples were taken from 11 sample localities. Out of these 19 samples 6 were chosen for detailed petrological investigations (Fig. 20): two amphibolites, one metapelitic gneiss, one orthogneiss and two gedrite-cordierite felses. Bulk rock compositions, co-ordinates of the sample locations and mineral assemblages are shown in Tab. 10. The amphibole compositions were calculated using an updated version of the Excel spreadsheet AMPH-CLASS (Esawi, 2004, 2008 personal communication). Representative mineral compositions and those used for geothermobarometry are shown in Tab. 11 to Tab. 14. Additional mineral analyses can be found in the electronical appendix: 24 - Supplementary mineral data.

Tab. 10. Sample co-ordinates, mineral assemblages and *XRF*-analyses of the investigated samples.

Sample	SP1	SP7a	SP8	SP9c	SP9d	SP9e
Rock type	Grt-Bt Amphibolite	Grt-Px Amphibolite	Grt-Sil-Bt-Crd Gneiss	Grt-Pl-Bt Gneiss	Grt-Oamph-Crd fels	Grt-Oamph-Crd fels
Latitude(°S)	21°56'700	22°12'205	22°06'792	21°56'700	21°56'700	21°56'700
Longitude(°E)	27°51'042	27°58'488	28°10'783	27°51'042	27°51'042	27°51'042
Assemblage	Grt-Bt-Pl-Hbl-Ilm-Qtz	Grt-Bt-Pl-Hbl-Cpx-Ep-Ilm-Qtz	Grt–St-Bt–Crd-Chl-Spl-Sil-Qtz	Grt-Bt-Chl-Ilm-Ap-Pl-Qtz	Grt-Bt-Pl-Anth/Gedr-Chl-Crd-Rt-Ilm-Qtz-(Spl)	Grt-Bt-Pl-Anth/Gedr-Chl-Crd-Rt-Ilm-Qtz
XRF-analyses	wt.%	wt.%	wt.%	wt.%	wt.%	wt.%
SiO_2	60.47	46.58	77.15	38.83	44.96	43.37
TiO_2	1.33	1.88	0.36	0.89	1.06	1.32
Al_2O_3	15.00	13.23	10.66	18.53	17.86	17.45
FeO^{tot}	7.56	16.34	4.62	14.82	18.03	19.74
MnO	0.11	0.61	0.06	0.62	0.53	0.53
MgO	3.33	5.23	4.10	12.07	12.41	12.85
CaO	6.25	12.15	0.12	2.82	1.31	1.48
Na_2O	1.92	1.60	0.12	0.88	0.61	0.65
K_2O	1.75	0.36	0.81	6.08	1.50	1.13
P_2O_5	0.54	0.19	0.02	0.71	0.13	0.13
LOI	0.85	0.89	1.54	3.25	0.83	0.40
Total	*99.11*	*99.06*	*99.56*	*99.50*	*99.23*	*99.05*
FeO/(FeO+MgO)	0.56	0.64	0.39	0.41	0.45	0.46

11.1 Garnet-biotite amphibolite (sample SP1)

Sample SP1 is a massive amphibolite consisting of quartz (42 vol.%), plagioclase (38 vol.%), hornblende (10 vol.%), biotite (8-10 vol.%), garnet (1-2 vol.%), and accessory ilmenite and apatite. Microscopically, the rock shows a layering, defined by bands of mafic minerals, which alternate with leucocratic minerals. Representative mineral compositions used for geothermobarometry are shown in Tab. 11.

Garnet porphyroblasts are poikilitic, up to ~4 mm across, and commonly contain inclusions of biotite, amphibole, quartz and ilmenite (Fig. 22b). Garnet is aligned parallel to the foliation

and is surrounded by a matrix of hornblende, biotite, plagioclase and quartz, whereby the mafic minerals are depleted in the vicinity of the garnet porphyroblast. Garnet only shows a weak compositional zoning ranging from $Alm_{64}Prp_{15}Grs_{15}Sps_{06}$ (core) to $Alm_{68}Prp_{16}Grs_{16}Sps_{08}$ (rim). The slight increase of the X_{Fe} towards garnet rims may be explained by a retrograde diffusive Fe-Mg exchange with matrix Fe-Mg silicates.

The foliation in this sample is traced by hypidioblastic brown biotite and idio- to hypidioblastic green hornblende with max. 0.7 mm elongation. Both minerals are strongly pleochroitic and commonly free of inclusions (rare inclusions of quartz may occur). X_{Fe} in biotite is chemically uniform (~0.53), whereas Ti^{VI} (~0.35-0.45 *p.f.u.*) and Al^{VI} (~0.24-0.44 *p.f.u.*) show considerable scatter (Fig. 22c). The uniformity in X_{Fe} indicates chemical equilibrium of Fe-Mg between individual biotite grains on a thin section scale, whereas the variations in Ti^{VI} and Al^{VI} indicate disequilibrium. Hornblende is classified as ferrotschermakite to tschermakite (Leake *et al.*, 1997; Fig. 22d).

Plagioclase and quartz are equigranular, rounded and have diameters of up to ~0.7 mm. Plagioclase is zoned with X_{ab} decreasing from ~0.53 (core) to ~0.40 (rim) - (Fig. 22a) and is locally epidotized.

Accessory ilmenite reaches ~0.23 mm in diameter, occurs in the matrix and is included in garnet. The average composition of ilmenite is $Ilm_{87}Hem_{08}Pyro_{06}$ (end-members: ilm = ilmenite; hem = hematite; pyro = pyrophanite).

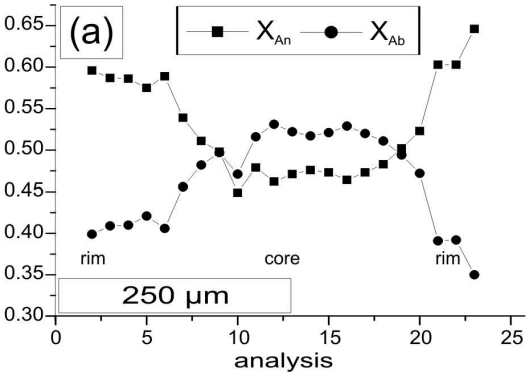

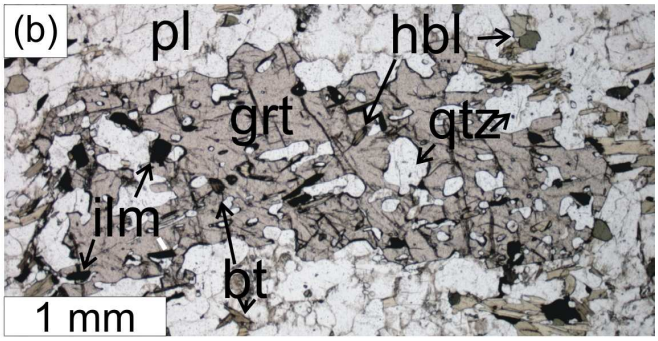

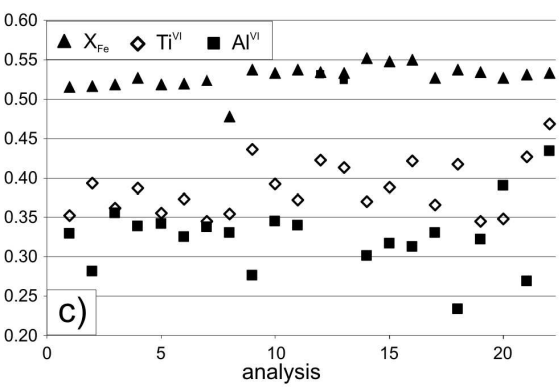

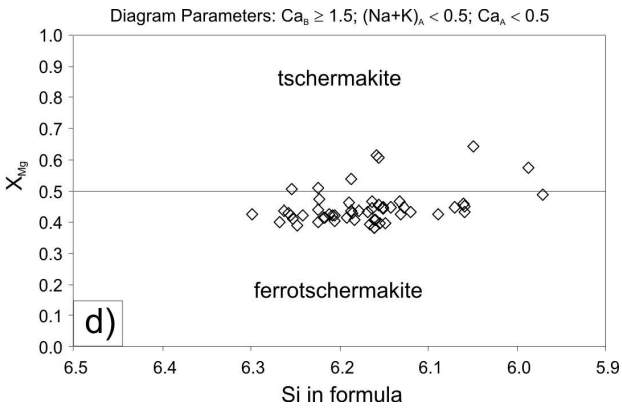

Fig. 22. a) microprobe profile across zoned plagioclase of sample SP1. b) photomicrograph of poikilitic garnet with rounded inclusions of quartz, biotite, hornblende and ilmenite in a matrix of hornblende, biotite, plagioclase and quartz in sample SP1. PPL. c) variable compositions of biotite in sample SP1. X_{Fe} shows a smaller compositional range than Ti^{VI} and Al^{VI}. d) classification diagram for calcic-amphiboles from Leake *et al.* (1997). Most clinoamphiboles of sample SP1 plot in the ferrotschermakite field with few analysis plotting in the tschermakite field.

11.2 Garnet-pyroxene amphibolite (sample SP7a)

Sample SP7a is an unfoliated, massive grey to black rock, which consists of hornblende (~30-35 vol.%), clinopyroxene (~25-30 vol.%), plagioclase (~15 vol.%), garnet (~10 vol.%), epidote (~5 vol.%), quartz (~5 vol.%) and minor biotite, ilmenite and apatite (~5 vol.% total). Representative mineral compositions used for geothermobarometry are shown in Tab. 12.

Two morphological and textural distinct garnet types are observed. Xenoblastic garnet (type I) is up to 1 cm in diametre and commonly contains clinopyroxene, hornblende, plagioclase, biotite, quartz and ilmenite inclusions. Ilmenite inclusions are aligned, indicating a former foliation (Fig. 23a). Inclusion-rich cores are overgrown by inclusion-poor rims (Fig. 23a). Idio- to hypidioblastic garnet (type II) is smaller in size (<0.25 mm), forms single grains or clusters (Fig. 23b), is inclusion-free and preferentially associated with plagioclase (Fig. 23d). These textural features indicate that type II garnet formed together with the rim of type I garnet. Compositionally, the type I garnet porphyroblasts are characterized by decreasing X_{Fe} from ~0.87 (core) to ~0.84 (rim) and increasing X_{Fe} to ~0.90 at the outermost rim, whereas the smaller garnets (type II) show an increase of X_{Fe} from ~0.86 (core) to ~0.90 (rim). These chemical patterns indicate that garnet type I preserve a relic prograde growth zoning (at their cores), whereas garnet type II was completely affected by retrograde diffusive Fe-Mg exchange with matrix Fe-Mg silicates.

Green hornblende is up to ~3 mm long, but mostly less than 1 mm, and commonly contains inclusions of clinopyroxene, plagioclase, ilmenite and biotite (Fig. 23c). Chemically the clinoamphiboles (66 analyses) show variable X_{Fe} and Na/K ratios. Thus, they are classified as ferrotschermakites (n=42) to ferrohornblendes (n=12), or hastingsites (i.e. Na/K-rich ferrotschermakites; n=12; Leake *et al.*, 1997; Fig. 24a, b). All three clinoamphibole types can occur within a single grain.

Clinopyroxene has a diameter of up to ~5 mm, but mostly less than 1 mm. Inclusions of biotite, hornblende and ilmenite are observed (Fig. 23b). Along cracks and on grain boundaries clinopyroxene can partly be altered to Fe-hydroxides. In the wollastonite-enstatite-ferrosilite classification diagram of Morimoto *et al.* (1988) the clinopyroxenes (32 analyses) cluster at the transition between the augit, diopside and hedenbergite fields (Fig. 5c). X_{Fe} in clinopyroxene is between 0.46 and 0.51 and Al ranges from 0.04 to 0.15 (*p.f.u.*). The clinopyroxene cores commonly show lower X_{Fe} and Al values than the rims. The intergrowths

relationships between clinopyroxene and hornblende, as well as their chemical homogenity suggests a textural-chemical equilibrium between both phases.

Plagioclase is xenoblastic, up to ~2.5 mm in diameter, shows a typical albite twinning, and locally contains inclusions of clinopyroxene, hornblende, garnet (type II) and small biotite flakes. Most plagioclase is zoned with X_{ab} decreasing from core (Ab_{45}) to rim (Ab_{35}) - (Fig. 24a). In addition, unzoned plagioclase with a constant composition of Ab_{50} has also been observed.

Epidote is xenoblastic, has a max. diameter of ~0.25 mm and occurs in contact with plagioclase and/or garnet. The composition of epidote is variable, as indicated by the range of the pistacite component (Ps = $Fe^{3+}/(Fe^{3+}+Al)*100$) from ~7 to ~21%. Epidote in local plagioclase-rich domains perhaps formed during the retrograde evolution, or it represents metastable relics of the prograde history.

Ilmenite in the matrix is up to ~3.5 mm across, whereas aligned inclusions in garnet have an average size of max. ~0.25 mm (Fig. 23a). Ilmenite often occurs in contact with amphibole (Fig. 23b). Chemically the investigated ilmenite is homogeneous with the average composition being $Ilm_{94}Pyro_{06}$.

Relic biotite with length of max. ~0.25 mm is found as inclusions in garnet, plagioclase and pyroxene. Characteristic for biotite is the high Ti content (~0.73 *p.f.u.*; Fig. 24d).

The textural relationships (mineral inclusions in garnet and matrix assemblages) and the chemical compositions provide evidence that prograde and peak metamorphic garnet growth (Type I and II) took place in the assemblage: grt-hbl-bt-cpx-pl-qtz-ilm.

The local occurrence of epidote perhaps results from retrograde alteration, which in particular affected plagioclase rich domains. This conclusion is supported by the absense of epidote inclusions in garnet.

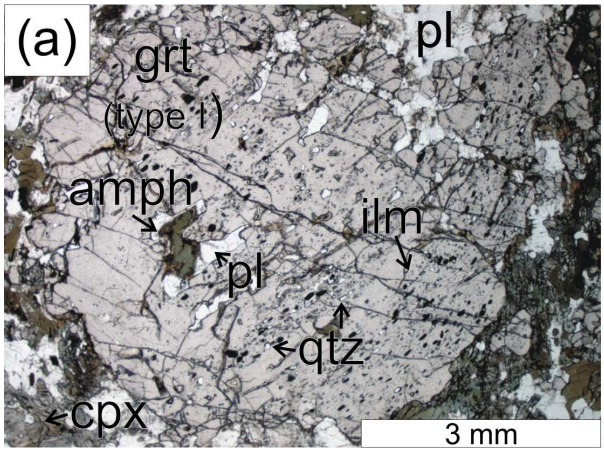

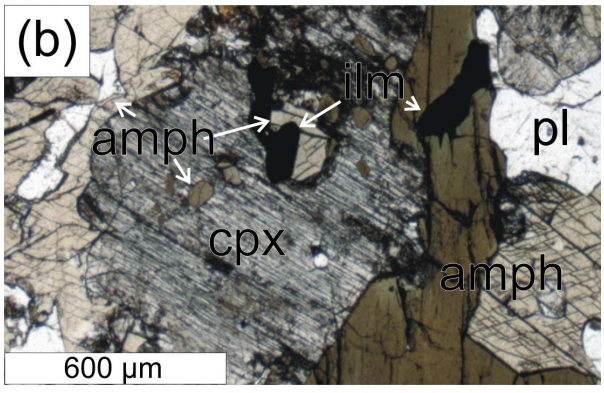

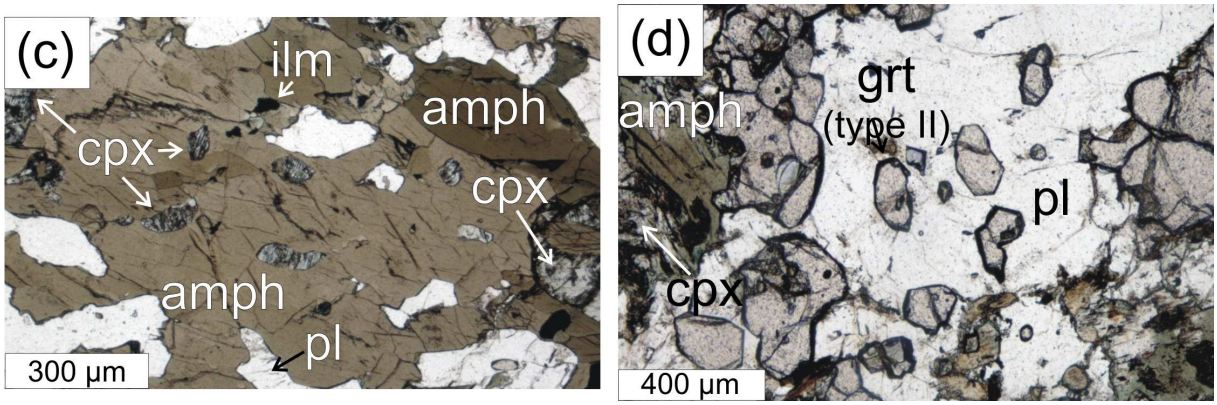

Fig. 23. Photomicrographs of sample SP7a. a) garnet (type I) with inclusions of amphibole (amph), plagioclase (pl), quartz (qtz) and ilmenite (ilm). Note the alignment of ilmenite inclusions (*e.g.* lower right garnet rim) and the inclusion-free rim on the left-hand side of the garnet. PPL. b) amphibole and ilmenite inclusions in clinopyroxene (cpx) next to matrix amphibole (124° cleavage) and plagioclase. PPL. c) clinopyroxene and ilmenite inclusions in amphibole next to matrix clinopyroxene and plagioclase. PPL. d) (hyp-)idioblastic garnet (type II) in plagioclase. PPL.

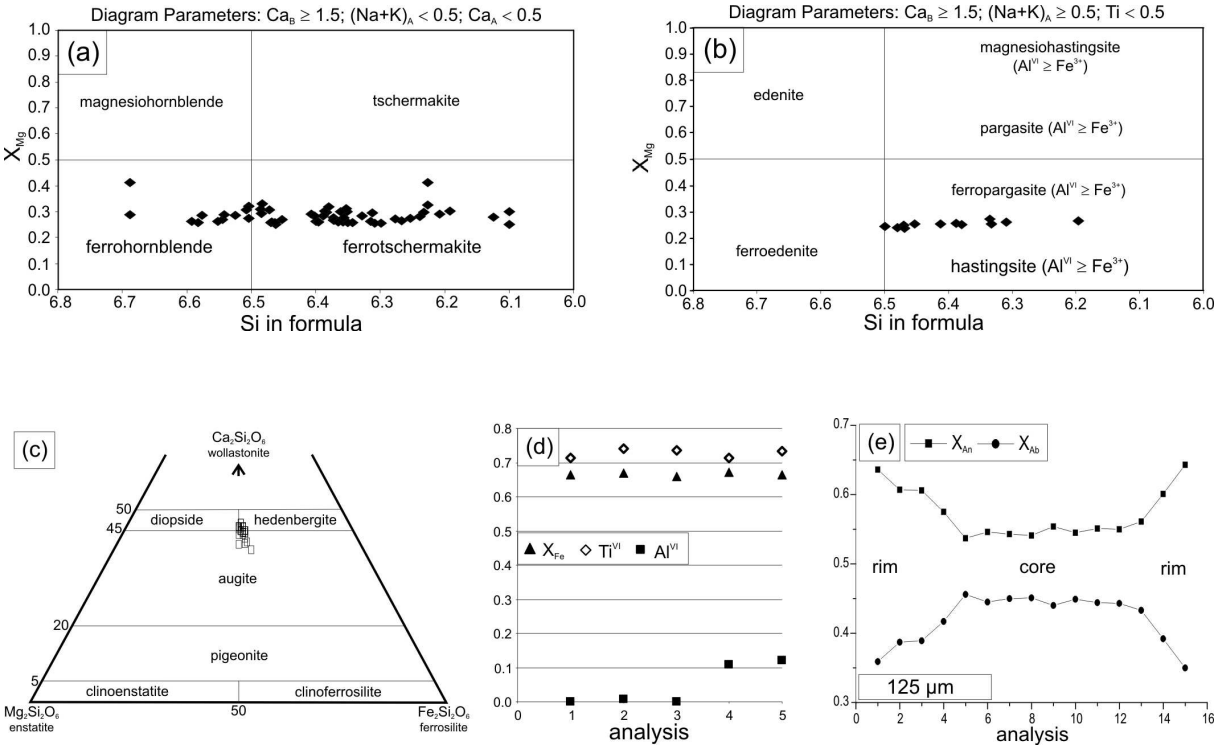

Fig. 24. Mineralchemistry of clinoamphibole, clinopyroxene, biotite and plagioclase of sample SP7a. a+b) clinoamphiboles are classified as ferrotschermakite to ferrohornblende, or hastingsite after Leake *et al.* (1997). c) clinopyroxenes are classified after Morimoto *et al.* (1988) as augite, diopside or hedenbergite, but plot in a small compositional range. d) biotite compositions show constant Ti^{VI} and Al^{VI} contents and small variation in X_{Fe}. e) plagioclase profile showing an marked decrease of X_{ab} from core (0.45) to rim (0.35).

11.3 Garnet-biotite-sillimanite-cordierite gneiss (sample SP8)

Sample SP8 is a foliated metapelitic rock composed of quartz (~50-60 vol.%), cordierite (~20-30 vol.%) and biotite (~5 vol.%) with minor garnet, sillimanite, staurolite, chlorite and spinel (all minor phases ~10-20 vol.%).

Representative mineral compositions used for geothermobarometry are shown in Tab. 13.

Garnet porphyroblasts have a maximum diameter of ~4 mm, are commonly resorbed and contain inclusions of quartz, sillimanite, cordierite, staurolite, biotite and rarely hercynitic spinel (Fig. 25b, c, e). All analyzed garnet porphyroblasts are characterized by increasing X_{Fe} towards their rims (~0.63 to 0.80), indicating that these grains were affected by retrograde Fe/Mg exchange with Fe-Mg matrix silicates. However, large garnet porphyroblasts show plateau cores with compositions of ~$Alm_{63}Prp_{31}Grs_{04}Sps_{02}$ (Fig. 26a, b, c), whereas smaller garnets grains were completely affected by retrograde diffusive Fe/Mg exchange as shown in Fig. 26d. The rim compositions of garnet strongly depend on the adjacent matrix phases, *i.e.* garnet in contact with Fe/Mg-bearing phases has X_{Fe} values of ~0.80, while garnet in contact with Fe/Mg-free phases has X_{Fe} values of ~0.70 (*e.g.* Fig. 26a, b).

Cordierite grains have a maximum diameter of ~2.5 mm and commonly contain sillimanite inclusions (Fig. 25d). In contact with chloritized biotite and/or garnet cordierite is commonly pinitized (Fig. 25e). Cordierite porphyroblasts are chemically homogenous in X_{Mg} (~0.76).

Lepidoblastic brown biotite is up to ~2 mm long, though the bulk has lengths of ~0.25 mm. Dark halos are developed around included zircons and chloritization of biotite is common (Fig. 25a, c, f). Biotite was measured in three textural distinct domains and shows considerable compositional variations with X_{Fe} ranging from 0.28 to 0.42, Ti^{VI} from 0.11 to 0.46 and Al^{VI} from 0.36 to 0.73 (*p.f.u.*). Biotite in contact with garnet has X_{Fe} values of 0.28 to ~0.37 and Ti between 0.11 and 0.40 (*p.f.u.*), whereas biotite in contact with cordierite has higher X_{Fe} and Ti contents of >0.40, respectively. The Al content of both biotite types ranges from 0.4 to 0.64. Biotite enclosed in quartz has an X_{Fe} value of ~0.35, Ti of 0.4 and low Al of 0.36.

Staurolite (X_{Fe} ~0.7; Al ~9.3; Zn ~0.08 (*p.f.u.*)) and hercynitic spinel (X_{Fe} ~0.6; Zn ~0.11 (*p.f.u.*)) relics up to 0.3 mm in diameter, are exclusively found as rounded inclusions in garnet (Fig. 25c), whereas accessory sillimanite needles up to 0.3 mm long are restricted to the cores of large corderite (Fig. 25d). In addition, rare sillimanite needles were found in quartz, which itself was included in big garnet porphyroblasts (Fig. 25b). Monazite and zircon occur as accessory phases (Fig. 25a, d) and were used for geochronological dating (Zeh, 2008, unpub. data).

The textural relationships as described above and shown in Fig. 25 provide evidence that five mineral assemblages were successively formed in sample SP8. Observed quartz, sillimanite, biotite, plagioclase, staurolite and spinel (probably stabilized by Zn = 5.5 wt.% from staurolite breakdown) inclusions in garnet indicate that garnet grew initialy in the assemblage:

(A1): grt-bt-sil-st-qtz (+spl in st-bearing domains)

The absence of staurolite in the matrix indicates that further garnet growth occurred in the assemblage:

(A2): grt-bt-sil-qtz

Corona structures (Fig. 25e) give a hint that garnet and cordierite initially grew together in the assemblage:

(A3): grt-bt-sil-crd-qtz

Subsequently however, garnet was resorbed at the expense of cordierite (Fig. 25c) and sillimanite was consumed. The final feature is concluded from the observation that sillimanite in the matrix is restricted to inclusions in cordierite cores. This indicates that the predominant matrix assemblage was:

(A4): grt-bt-crd-qtz

The late chloritization of biotite and pinitization of cordierite indicates that final retrograde overprint took place in the assemblage:

(A5): grt-bt-crd-qtz-chl

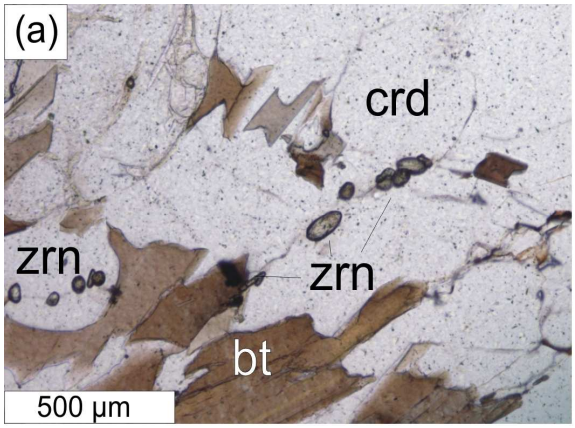

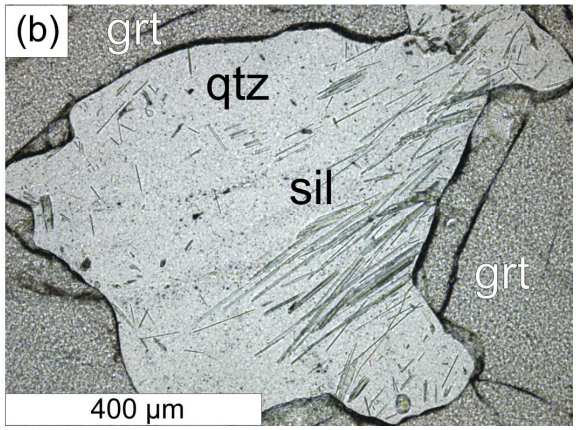

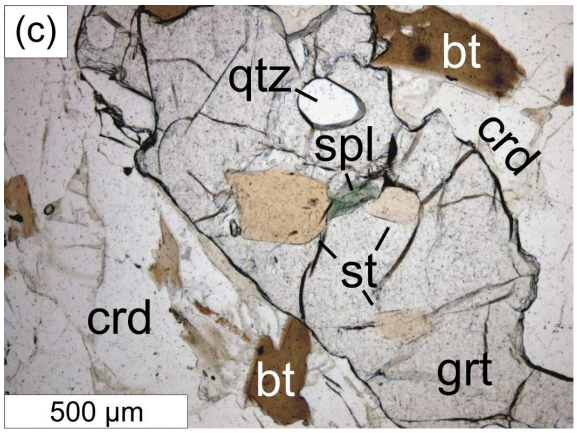

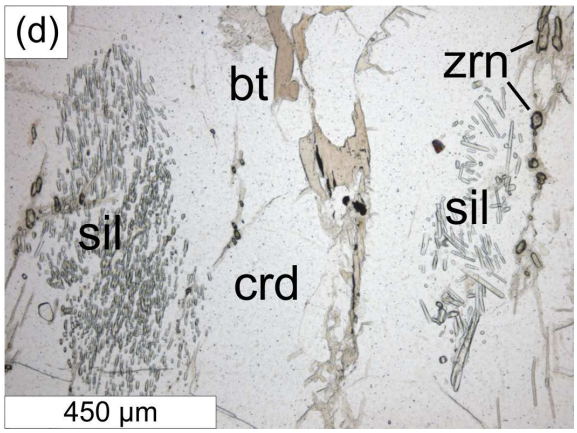

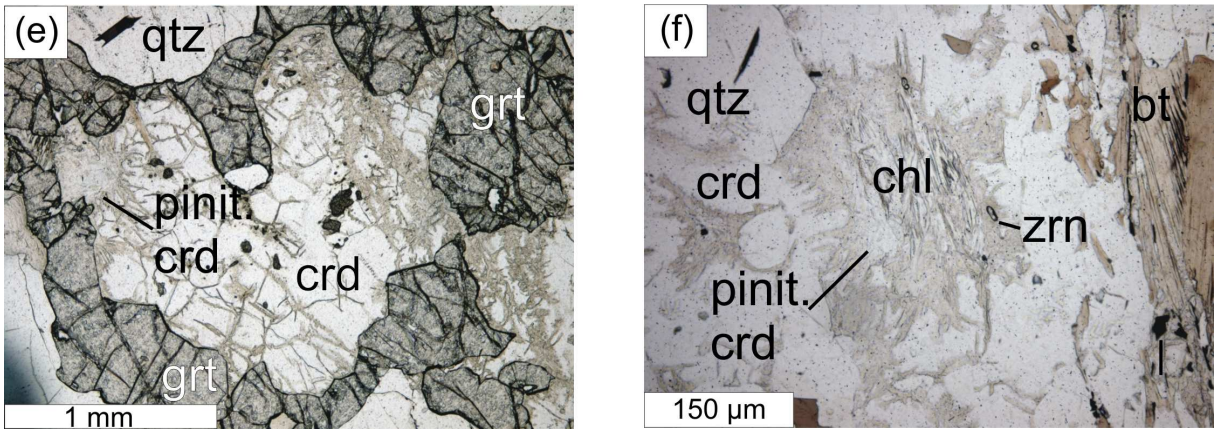

Fig. 25. Photomicrographs of sample SP8. a) zircon grains in a matrix of cordierite and biotite. PPL. b) sillimanite needles included in quartz which is surrounded by garnet. PPL. c) staurolite in contact with hercynitic spinel, and quartz inclusions in a resorbed garnet porphyroblast surrounded by a matrix of cordierite and biotite. PPL. d) cordierite porphyroblasts with sillimanite needles and zircon in their cores and inclusion-poor rims. Cordierite grain-boundaries are traced by biotite. PPL. e) garnet forming a corona around cordierite (partly pinitized) is surrounded by quartz, biotite and cordierite. PPL. f) pinitized cordierite with inclusions of chloritized biotite, zircon and quartz.

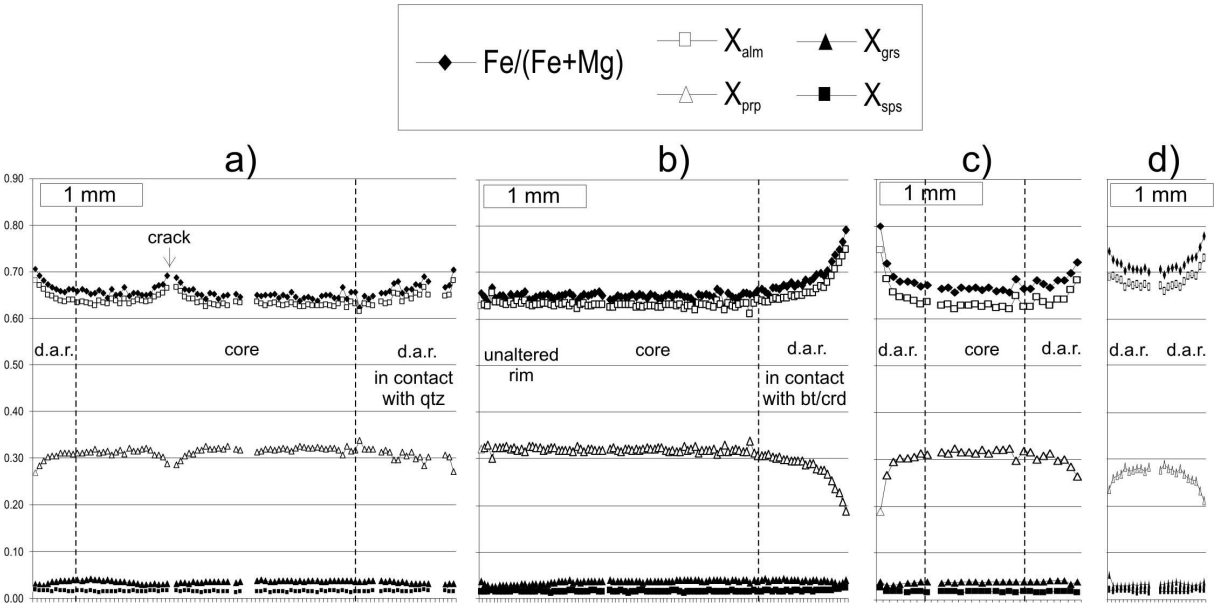

Fig. 26. Microprobe profiles across garnets of different sizes from sample SP8. Large garnets in a, b, and c, show compositional core plateaus and commonly diffusively altered rims (d.a.r.; unaltered rim in b) is in contact with quartz). The smaller garnet in d) shows alteration up to the core, documented by a constant increase in X_{Fe} from core to rim. Note that the intensity of (rim) alteration depends on the neighbouring matrix phases, *i.e.* garnet in contact with *e.g.* biotite or cordierite shows higher rim X_{Fe} values of ~0.80 than garnet in contact with *e.g.* quartz (X_{Fe} mostly ~0.70, or unaltered with X_{Fe} ~0.63).

11.4 Garnet-plagioclase-biotite gneiss (sample SP9c)

Sample SP9c is a dark, well foliated rock that consists of biotite (~55-60 vol.%), garnet (~25 vol.%), plagioclase (~9 vol.%), quartz (~6 vol.%) and accessory apatite, zircon, ilmenite and rutile (all accessory phases <5 vol.%). Representative mineral compositions used for geothermobarometry are shown in Tab. 13.

Garnet porphyroblasts are up to 1 cm in diameter, contain rare inclusions of biotite, plagioclase and apatite, and are typically surrounded by plagioclase rims (Fig. 27a, b, c).

Garnet shows a prograde growth zoning characterized by a significant decrease of X_{Fe} (0.78 to 0.70) and the spessartine component (X_{sps} = 0.13 to 0.07), and an increase in the pyrope component (X_{prp} = 0.16 to 0.23) from core to rim. Garnet rims show a reverse zoning (increase of X_{Fe} and X_{sps}). This feature indicates that prograde growth zoning was subsequently modified by diffusion, *i.e.* the retrograde exchange of Fe, Mg and Mn with surrounding matrix minerals (*e.g.* biotite; Fig. 28a).

Biotite up to 5 mm long is the dominant phase and forms the matrix around plagioclase and garnet. It mostly appears fresh and locally contains apatite (Fig. 27d) and zircon inclusions, but biotite included in plagioclase can locally be chloritized. Biotite has uniform X_{Fe} contents of ~0.36, whereas Ti^{VI} (0.06-0.25) and Al^{VI} (0.27-0.61) - (*p.f.u.*) show considerable scatter. The lowest Ti^{VI} contents are typical for chloritized biotite and the highest contents for biotite inclusions in garnet. Al^{VI} in biotite is also lowest for chloritized biotite, whereas matrix biotite and biotite included in garnet has intermediate to high values.

Plagioclase is up to 2.5 mm in diametre, hypidioblastic and shows albite twinning. Commonly it forms coronas (halos) around garnet porpyhroblasts and envelops biotite inclusions in garnet (Fig. 27c). Matrix plagioclase shows complex zoning patterns with with increasing X_{an} from 0.6 to 0.68 in the cores, followed by a decrease to 0.54 towards the rim (Fig. 28c). Some plagioclase grains only show compositions identical to the rims of the zoned plagioclase (Fig. 28c).

Accessory apatite is up to 1.5 mm long, can be found in the matrix and as inclusions in garnet or biotite (Fig. 27d). Rare ilmenite with a max. extent of 0.25 mm occurs in the matrix and included in garnet (Fig. 27c). Its chemical composition is homogeneous and close to the ilmenite end-member ($Ilm_{92}Hem_{05}Gey_{02}Pyro_{01}$). Furthermore, optical light microscopy indicates rutile needles in garnet, which however could not be analyzed by microprobe due to lacking surface exposure.

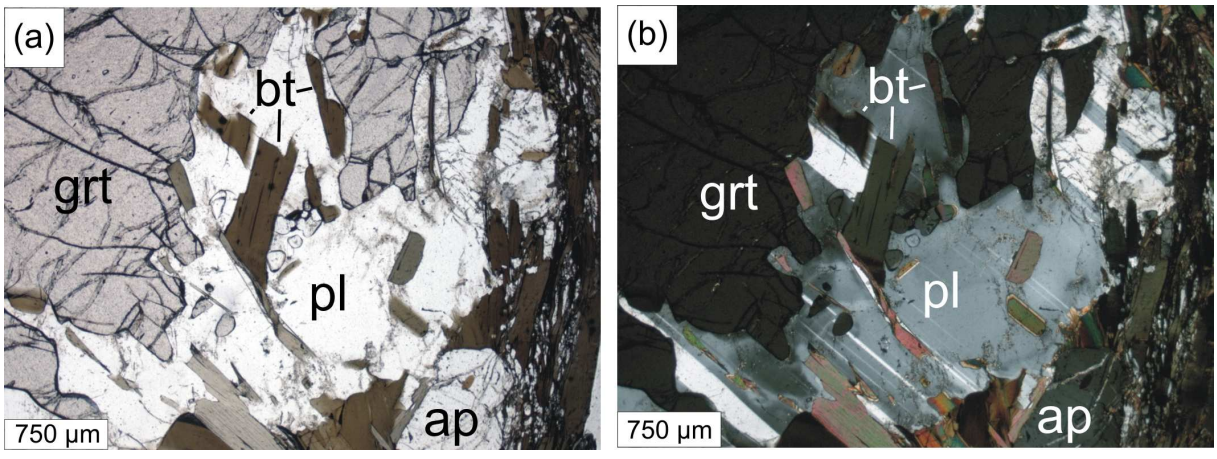

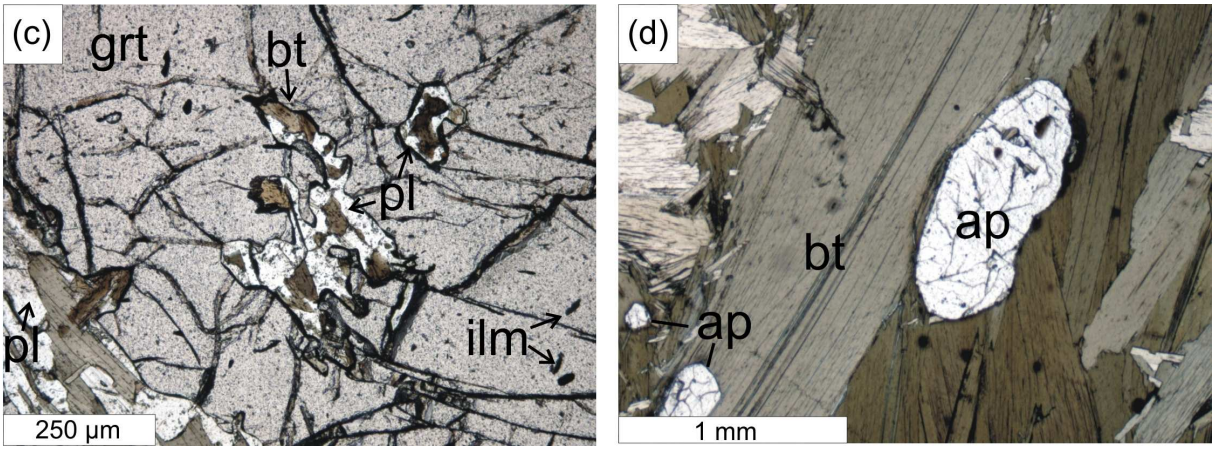

Fig. 27. Photomicrographs of sample SP9c. a) resorbed garnet surrounded by plagioclase, biotite and apatite. PPL. b) the same as a) but under CPL. c) garnet with ilmenite, biotite and plagioclase inclusions is surrounded by plagioclase and biotite. Note that the biotite inclusions are mantled by plagioclase. PPL d) matrix biotite with apatite inclusion and dark halos around zircon inclusions. PPL.

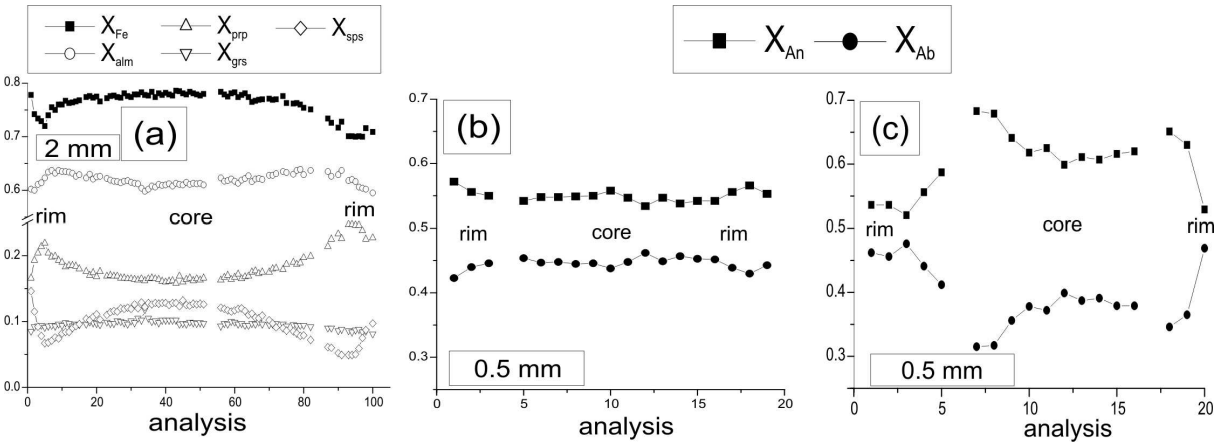

Fig. 28. Microprobe profiles across garnet and plagioclase of sample SP9c. a) garnet with prograde zonation pattern and reverse zoning at its rims. b) matrix plagioclase in contact with apatite. c) matrix plagioclase with pronounced decrease of X_{an} towards the rim.

11.5 Garnet-cordierite-orthoamphibole fels (samples SP9d/SP9e)

Samples SP9d and SP9e show similar textures, mineral assemblages and bulk chemistries (Fig. 29; Tab. 10). Both samples are massive rocks of dark colour composed of orthoamphibole (mostly gedrite, ~25-30 vol.%), garnet (~15-20 vol.%), biotite (~10-15 vol.%), cordierite (~15 vol.%), plagioclase (~10 vol.%), quartz (<5 vol.%) and minor chlorite, rutile and ilmenite (all minor phases ~5 vol.%). Sample SP9e additionally contains minor spinel. Representative mineral compositions used for geothermobarometry are shown in Tab. 14.

Garnet porphyroblasts can reach 1.2 cm in diametre, are poikiloblastic and contain primary inclusions of gedrite, plagioclase, biotite, ilmenite, rutile, quartz (Fig. 29a, c, e, g) and retrograde chlorite. Ilmenite inclusions occur in all garnet domains and are commonly aligned tracing a former foliation (Fig. 29a). Rutile inclusions are only found at garnet rims (Fig. 29e). Resorbed garnet rims are commonly

associated with resorbed orthoamphibole (Fig. 29e). This indicates that garnet resorption took place via the reaction garnet + orthoamphibole + quartz = cordierite. Garnet shows a relic prograde growth zoning with decreasing X_{Fe} from the core (~0.82) towards the rim (~0.64). However, increasing X_{Fe} at the outermost rim (>0.80) - (Fig. 30a) indicates that this growth zoning was modified due to retrograde diffusive Fe/Mg exchange with Fe/Mg-bearing matrix minerals.

Orthoamphibole is up to 3.5 mm long, xeno- to idioblastic and contains biotite, plagioclase, ilmenite and quartz inclusions. The orthoamphiboles around garnet are often resorbed and embedded in cordierite (Fig. 29g). The amphiboles in both samples are commonly zoned. The cores are classified as magnesio-gedrite and the rims as magnesio-anthophyllite according to the nomenclature of Leake *et al.* (2003; Fig. 30c).

Brown biotite has a max. length of 1.25 mm, shows dark halos around zircon inclusions and is commonly closely associated with orthoamphibole (Fig. 29f). Biotite of both samples has X_{Fe} of ~0.3, Ti^{VI} of ~0.23 *p.f.u.* and Al^{VI} between 0.45-0.75 *p.f.u.*. Biotite inclusions in garnet have low Al^{VI} contents (0.45), whereas matrix biotite has higher contents (>0.45; Fig. 30d).

In both samples three cordierite types can be distinguished. Type I cordierite forms small rims between host garnet and biotite (Fig. 29c) and is commonly pinitized. Matrix cordierite type II is up to 2 mm in diametre, commonly shows twinning and appears fresh (Fig. 29f), while cordierite type III forms reaction rims around garnet (Fig. 29a, e, g; see above reaction) and commonly is pinitized. Type II and III cordierite contains inclusions of biotite, orthoamphibole, ilmenite and rutile and pinitization of cordierite commonly starts along fractures (Fig. 29h). Chemically, the three cordierite types can not distinguished with identical X_{Fe} of 0.2.

Plagioclase in both samples is up to 0.25 mm in diameter, is included in garnet (Fig. 29i) and occurs in the matrix (Fig. 29g). Plagioclase commonly appears fresh, but locally shows serizitation. Chemically, most plagioclase has the composition $Ab_{50-65}An_{35-50}$. However, some plagioclase inclusions in garnet have a higher albite component of X_{ab} = 0.73-0.85. Additionally some plagioclase grains enclosed in garnet rims (sample SP9e) show a zonation with X_{ab} decreasing from 0.75 to 0.65 (Fig. 30b). These textural and chemical patterns are interpreted to indicate that X_{ab} in plagioclase increased during prograde and decreased during retrograde metamorphism.

Most chlorite is formed at expense of garnet and orthoamphibole (Fig. 29d) and occurs along garnet fractures. However, there are also a few grains, which are enclosed by garnet that show straight grain boundaries (Fig. 29i). Such flakes may represent primary relics.

Hercynitic spinel is restricted to a single quartz-free domain, where it is completely surrounded by cordierite. Ilmenite and apatite

are common accessory phases. Hercynitic spinel and ilmenite are chemically homogenous, showing compositions of $Sp_{27}Hc_{70}Gah_{03}$ and $Ilm_{95}Hem_{04}Pyro_{01}$, respectively.

The textural relationships as described above and shown in Fig. 29 provide evidence that four mineral assemblages were successively formed in sample SP9d/SP9e. Biotite, gedrite, ilmenite, plagioclase, cordierite I, (±chlorite) and quartz inclusions in garnet indicate that garnet grew initially in the assemblage:

grt-bt-ged-crd I-ilm-pl-qtz (±chl)

Chlorite inclusions in garnet may be a secondary feature, since it seems unlikely that chlorite was preserved metastable ~100°C above its predicted stability (see Fig. 36). However, its primary origin cannot completely be ruled out.

The occurence of rutile inclusions at the garnet rims as well as the occurrence of cordierite (type II porphyroblasts) indicates that final garnet growth took place in the assemblage:

grt-bt-ged-crd II-ilm-rt-pl-qtz

Subsequently garnet and gedrite were resorbed at the expense of cordierite (type III) and ilmenite was formed at the expense of rutile in the assemblage:

grt-bt-ged-crd III-ilm-pl-qtz

The finding of tiny anthophyllite rims around gedrite and the local formation of chlorite in gedrite-anthophyllite-cordierite domains provides evidence, that the final retrograde evolution occurred in the assemblage:

grt-bt-ath-crd III-ilm-pl-qtz-chl

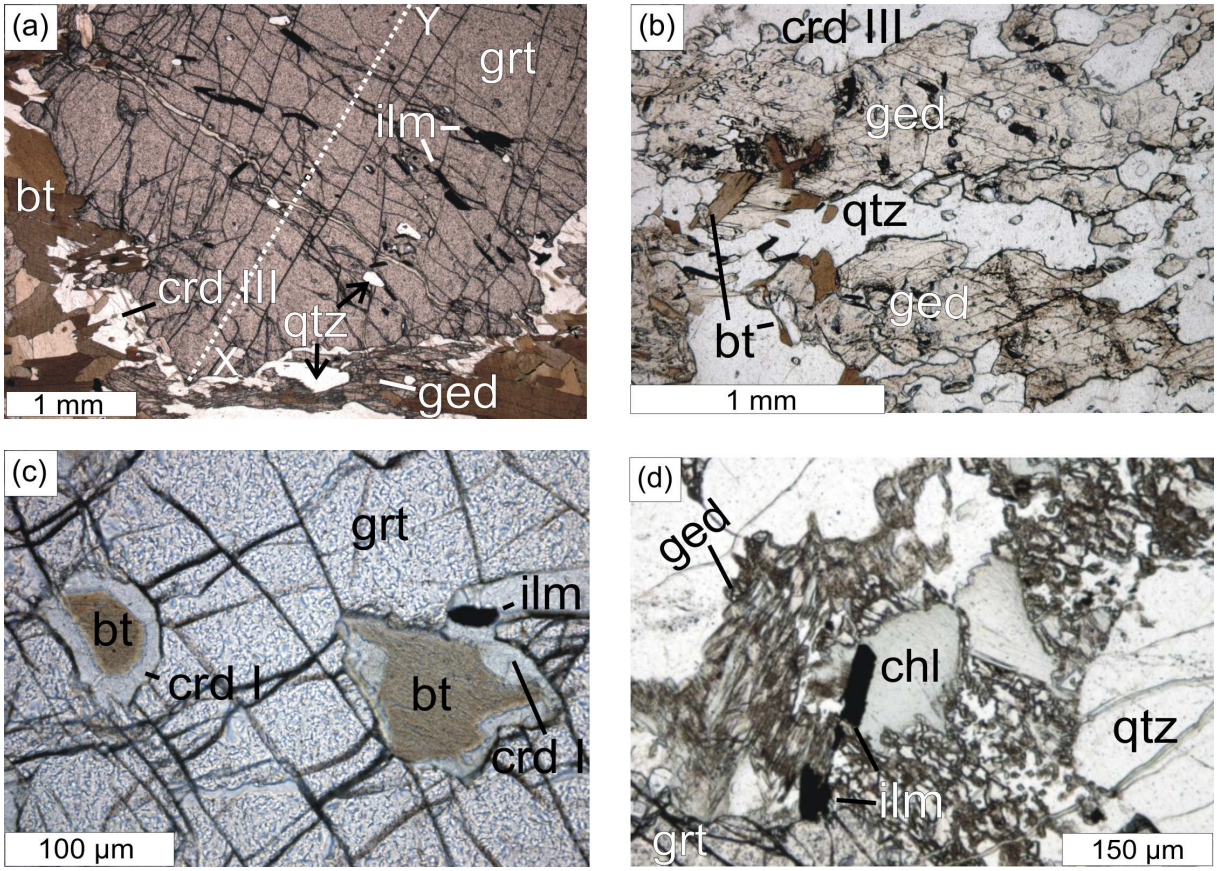

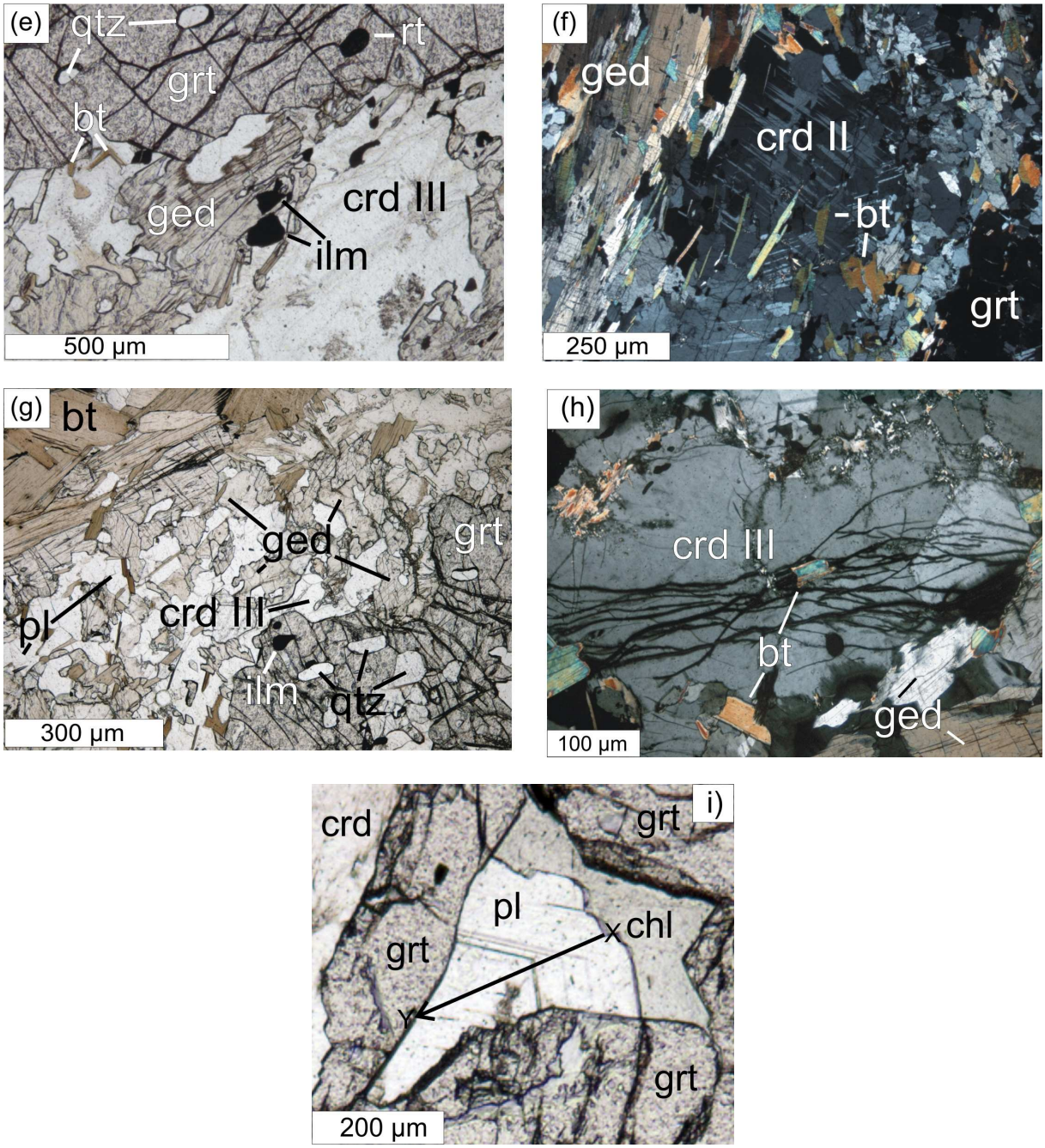

Fig. 29. Photomicrographs of samples SP9d (a-g) and SP9e (h, i). Dotted line in a) and black arrow in i), marked with X-Y, indicates position of microprobe profiles shown in Fig. 30a and b, respectively. Note that in a) not the complete garnet porphyroblast is shown. a) garnet with aligned ilmenite inclusions and little quartz is surrounded by a matrix of cordierite, quartz, biotite and gedrite. b) gedrite with anthophyllite rims (see Fig. 30c) is intergrown with quartz, cordierite and biotite. c) corderite seperates biotite and ilmenite inclusions from host garnet. d) rims of resorbed gedrite intergrown with retrograde chlorite, quartz and ilmenite around garnet. e) garnet rim with quartz and rutile inclusions is surrounded by cordierite, gedrite, biotite and ilmenite. f) matrix cordierite with twinning is intergrown with gedrite, biotite and garnet. g) rim of resorbed garnet with inclusions of quartz and ilmenite is surrounded by cordierite, gedrite, plagioclase and biotite. h) matrix cordierite with biotite inclusions and in contact with gedrite is pinitized along cracks. i) chlorite and zoned plagioclase inclusions in a garnet rim, which is resorbed at the expense of cordierite (see also Fig. 30b).

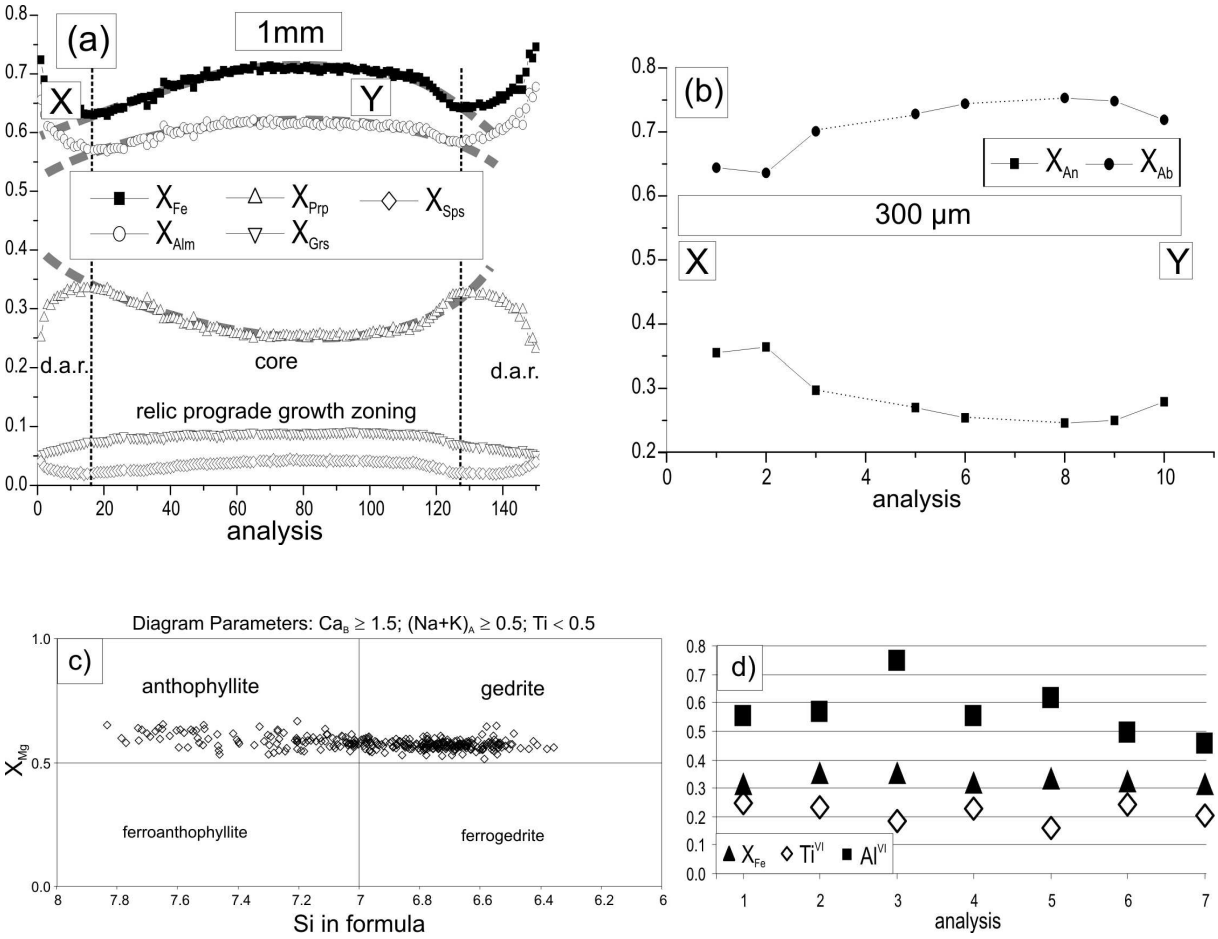

Fig. 30. Microprobe profiles across garnet (a) and plagioclase (b) and mineral chemistry of orthoamphibole (c) and biotite (d) from samples SP9d (a, c, d) and SP9e (b). Note that garnet in a) shows relics of a prograde growth zoning as characterized by decreasing X_{Fe} from core to rim (d.a.r. = diffusively altered rim). The assumed original growth zoning (*i.e.* unaffected by retrograde Fe/Mg diffusion) is shown as grey dashed lines and X-Y indicates the position of the profile in Fig. 29a. Orthoamphiboles in c) are characterized by gedrite cores and anthophyllite overgrowths.

12 *P-T* pseudosections

12.1 Garnet-biotite-sillimanite-cordierite gneiss (sample SP8)

P-T pseudosections were calculated in the system MnO - CaO - Na_2O -K_2O - FeO - MgO - Al_2O_3 - SiO_2 - H_2O (MnCNKFMASH) - (Fig. 32) and MnKFMASH (Fig. 35) using the software **THERIAK-DOMINO** v.140205 (de Capitani, 2005) with an modified version of the "tc321p2.txt"-file with respect to Mn. The *a-x* relationships used by **THERIAK-DOMINO** are identical to those of **THERMOCALC** v3.21 (tc321p2.txt), and described in the "databases.txt"-file of **THERIAK-DOMINO**. Solid-solution phases included in the calculations are: garnet, biotite, cordierite, staurolite, chlorite, muscovite, plagioclase, K-feldspar, orthopyroxene, liquid (i.e. melt) and the end-member phases sillimanite, kyanite, quartz and H_2O.

For the following calculations it is assumed that H_2O was in excess throughout the metamorphic history. To achieve these

conditions, calculations were carried out using a water content of 10 wt.% at temperatures between 450 and 700°C. This step was necessary to calculate the prograde assemblage with chlorite and staurolite. For the calculation of the peak assemblage the water content determined from loss on ignition (LOI = 1.54 wt.%; Tab. 10) was used (temperatures between 700-850°C; see also Guiraud *et al.*, 2001).

Comparison between the observed mineral assemblages (see section 11.3 on p. 48) and those calculated in the model system MnCNKFMASH (Fig. 32) provide evidence that sample SP8 underwent a clockwise *P-T* evolution with a prograde pressure-temperature increase from about 600°C/5-6 kbar to ~750°C/7-7.5 kbar, followed by a retrograde temperature-pressure decrease to <620°C/<5 kbar.

The prograde segment of the *P-T* path conforms to the observation that garnet contains inclusions of staurolite (absent in the matrix) and minor sillimanite (assemblage A1+A2; Fig. 32). Sillimanite needles in the cores of matrix cordierite porphyroblasts additionally indicate that first cordierite growth took place in the assemblage A3 (grt-sill-bt-crd-qtz±liq) and rare garnet corona structures around cordierite provide evidence that garnet was at least temporarily (or locally) formed at the expense of cordierite. The observation that matrix sillimanite is restricted to the cores of cordierite but is absent at their rims (Fig. 25d) indicates that sillimanite reacted out during final cordierite growth. Judging from these observations it seems likely that the peak metamorphic assemblage was A4 (grt-bt-crd-qtz±liq; see Fig. 32). The retrograde segment of the *P-T* path is constrained by the observations that garnet is locally resorbed at the expense of cordierite, that cordierite is occasionally pinitized and that chlorite is formed at the expense of biotite (assemblage A5; Fig. 25e, f). Furthermore, the absence of orthopyroxene and the retrograde diffusive zoning (increasing X_{Fe}) at garnet rims are consistent with the interpretation that sample SP8 underwent a contemporaneous pressure-temperature decrease to about 620°C at 5 kbar.

The inferred *P-T* path is also supported by the contour diagrams for mineral modes and composition as shown in Fig. 33. For the evolution of the minerals also see Fig. 31. Finally it should be noted that the peak assemblage (A4) has a wide stability and thus it is not well suited to determine peak metamorphic conditions. However, comparison of measured and calculated garnet core compositions provide evidence for peak *P-T* conditions of about 750°C at 7 kbar (Fig. 26, Fig. 33c, g). Here it should be noted that the *P-T* pseudosection constructed in the MnCNKFMASH system (with quartz in excess) cannot explain the observed hercynite inclusions in garnet. The inclusions are interpreted to have formed by a local reaction between spinel and staurolite (Zn = 0.05-0.11 *p.f.u.*), perhaps in a former quartz-undersaturated, Zn-enriched domain. A further

problem is that plagioclase, although predicted by the *P-T* pseudosection, has never been observed in sample SP8. This discrepancy may be explained in at least two ways. First, the predicted plagioclase mode is ~1 vol.% (Fig. 31, Fig. 33f). Thus it could easily be overlooked or mistaken for quartz or cordierite (the most abundant matrix phases; Fig. 31), especially if plagioclase is untwinned. Second, the block used to determine the bulk chemistry for *P-T* pseudosection calculations could have had a slightly different composition than the thin section from which the mineral assemblages are observed.

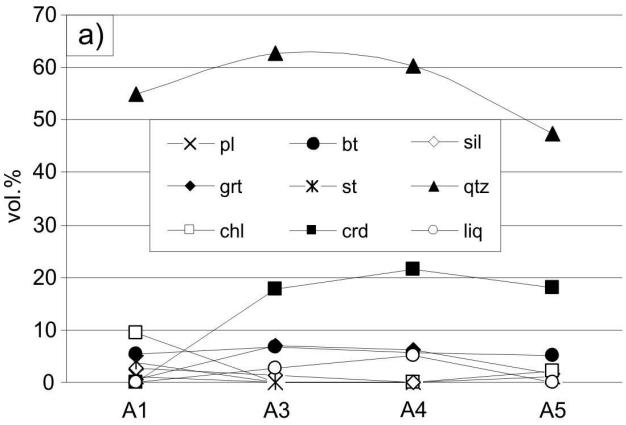

b)

	A1	A3	A4	A5
T (°C)	620	700	750	625
P (kbar)	6	7.5	7	5
pl	1.20	0.00	0.00	1.04
grt	0.42	7.07	6.19	1.75
chl	9.34	0.00	0.00	2.02
bt	5.46	6.66	5.70	5.23
st	3.67	0.00		
crd	0.00	17.69	21.66	17.99
sil	2.78	1.35	0.00	
qtz	54.86	62.70	60.25	47.42
liq	0.00	2.81	5.03	0.00
H_2O	22.27	1.72	1.17	24.55
sum vol%	*100.00*	*100.00*	*100.00*	*100.00*

Fig. 31. Evolution of the mineral mode (in vol.%) for the metamorphic assemblages (A1) to (A5) along the inferred metamorphic *P-T* path of smaple SP8 as shown in Fig. 32 - calculated with **THERIAK-DOMINO** in the system MnCNKFMASH. a) diagram. b) list of normalized compositions.

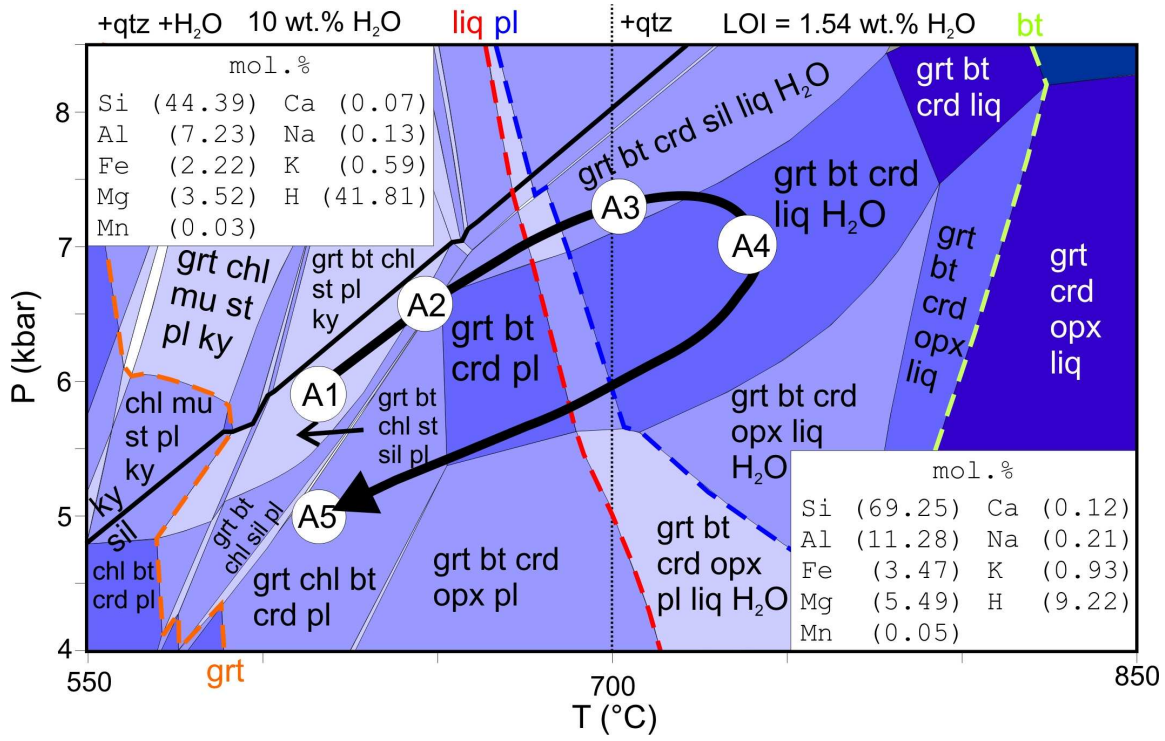

Fig. 32. *P-T* pseudosection for sample SP8 in the system MnCNKFMASH. Coloured dashed lines are the in/out-boundaries of the phases shown at the top and bottom of the diagram. Black arrow indicates inferred metamorphic *P-T* path. Mineral assemblages (A1) to (A5) are inferred from thin section observations (see section 11.3).

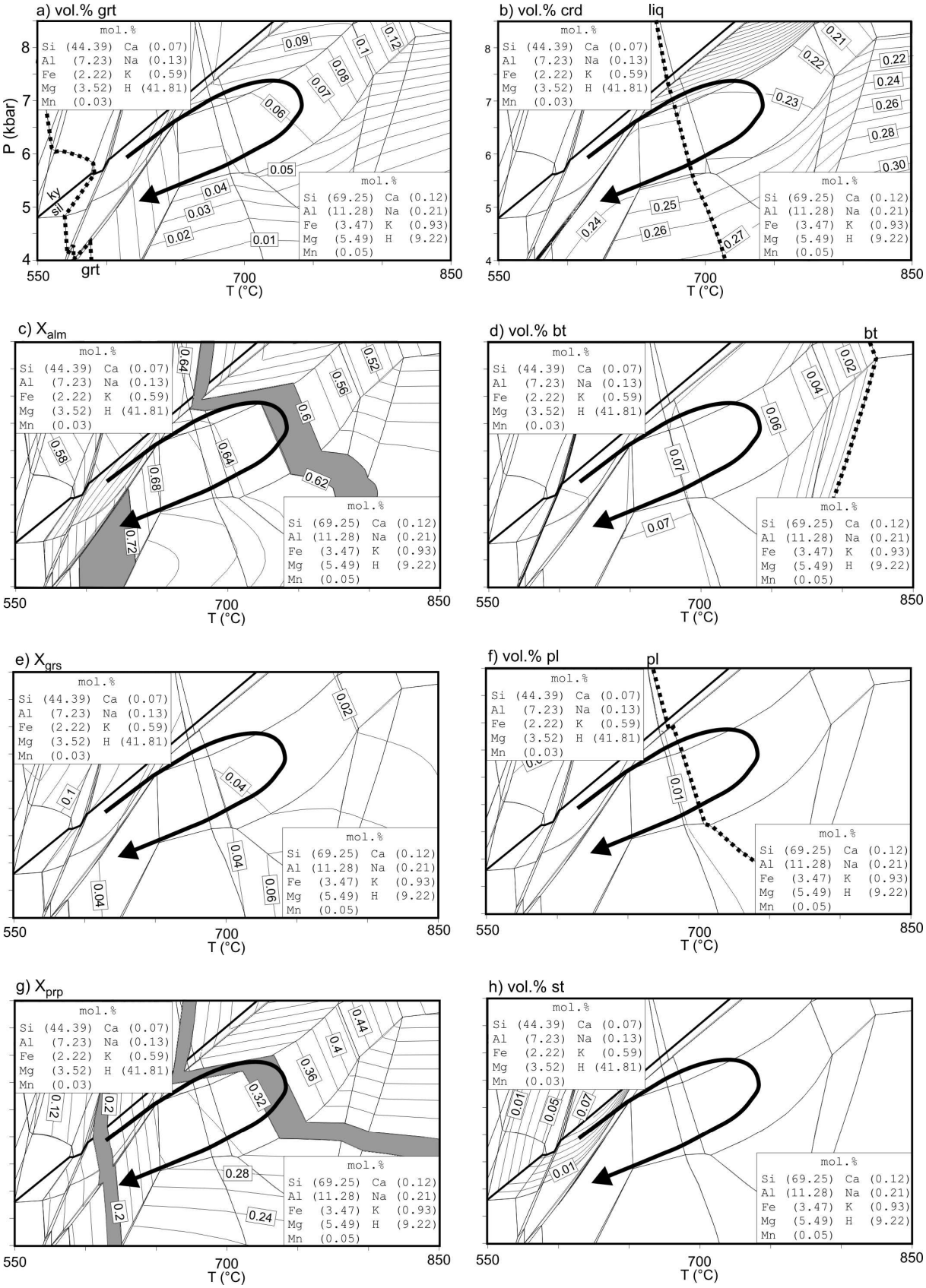

Fig. 33. Contoured *P-T* pseudosections in the system MnCNKFMASH for sample SP8. Mode of the solid phases is given as vol.%/100. Grey shaded fields in c) and g) indicate where measured and calculated garnet core and rim compositions coincide (see section 11.3). Black arrow indicates inferred *P-T* path as shown in Fig. 32. a) garnet mode. b) cordierite mode. c) X_{alm}. d) biotite mode. e) X_{grs}. f) plagioclase mode. g) X_{prp}. h) staurolite mode.

In order to obtain information about the influence of the H_2O activity on the stability of the peak assemblage garnet-biotite-cordierite-quartz-H_2O-liq a T-a(H_2O) diagram was constructed (Fig. 34a). As shown in Fig. 34a at 750°C/7 kbar the water activity has to be >0.8 to stabilize the peak assemblage. A lower a(H_2O) would cause the stabilization of the sillimanite-bearing, melt-free assemblage garnet-biotite-cordierite-plagioclase-sillimanite-quartz-H_2O, which has not been observed in thin section. At higher temperatures between ~750 to 840°C a(H_2O) has to be >0.6 to stabilize the peak metamorphic assemblage. A water activity of <0.6 would result in the formation of K-feldspar, which has also not been observed in thin section. Thus, it is concluded that the water activity during the formation of the peak metamorphic assemblage was between 0.6 and 1.

The *P-T* pseudosection contoured for "wt.% H_2O in solids" (Fig. 34b) indicates that sample SP8 underwent a prograde dehydration, with ~2 wt.% H_2O in the solid phases (*e.g.* chlorite, staurolite, biotite etc.) at the beginning and <0.8 wt.% H_2O at the metamorphic peak (*e.g.* in biotite and cordierite). Furthermore, the diagram predicts that water has to be added to the system (from 0.8 to 1.2 wt.% H_2O) during the retrograde evolution, in order to explain the occurrence of chlorite (Fig. 34b).

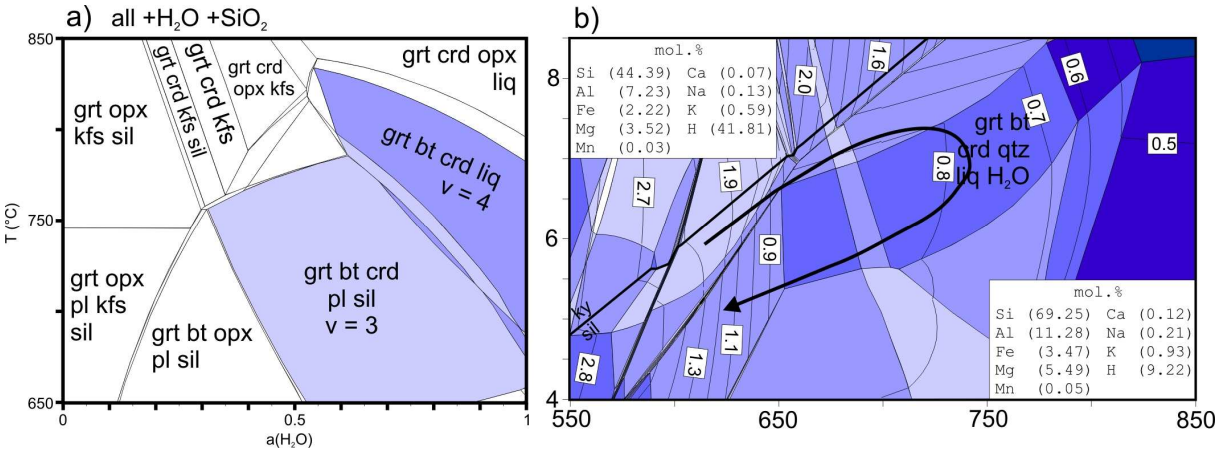

Fig. 34. a) T-a(H_2O) diagram for sample SP8 in the system MnCNKFMASH, calculated for a pressure of 7 kbar. v = variance of the mineral assemblages (coloured). The peak metamorphic assemblage grt-bt-crd-qtz-H_2O-liq is stable at a(H_2O) > 0.8 at 750°C. b) wt.% of H_2O in solid phases. See text for details.

In order to evaluate the influence of minor Ca and Na (~0.25 wt.% total; Tab. 10) on the phase diagram an additional *P-T* pseudosection was constructed in the system MnKFMASH (Fig. 35). A comparison between the diagrams in Fig. 35 (MnKFMASH) and Fig. 32 (MnCNKFMASH) shows that the stability fields of the Fe-Mg silicate assemblages is similar in both diagrams and that the MnKFMASH pseudosection constraints the same *P-T* evolution as the MnCNKFMASH diagram. The main difference between the two *P-T* pseudosections is the shift of the melt-bearing stability fields, caused by the small amount of Na and Ca. In the MnKFMASH system melt formation starts with the breakdown of biotite at

~780°C, whereas in the MnCNKFMASH system melting begins at ~660°C. Furthermore, melt and free H_2O coexist over a relatively broad temperature interval between 660-800°C, even when using the amount of water obtained from LOI. For the MnKFMASH system this interval is much smaller (~10-50°C; see Fig. 32 and Fig. 35).

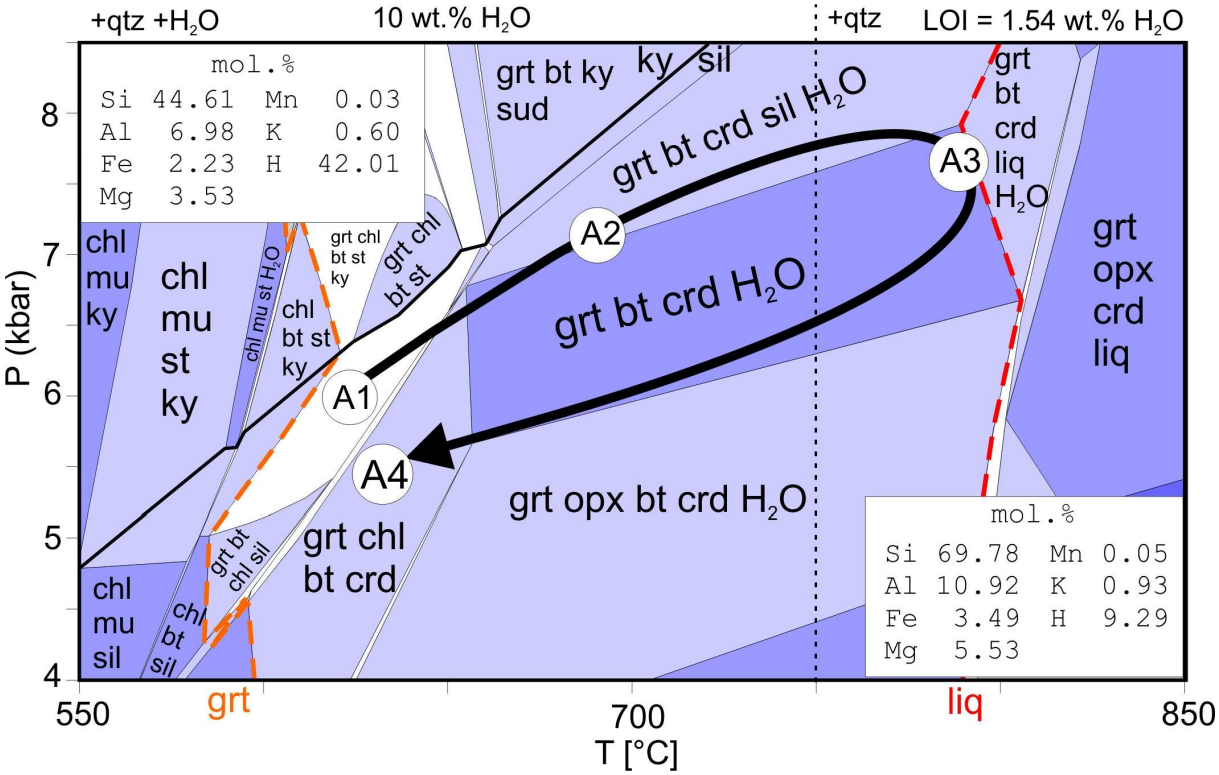

Fig. 35. *P-T* pseudosection for sample SP8 constructed in the system MnKFMASH. For further explanation see caption of Fig. 32.

In summary, the results of detailed petrography and mineral chemistry in combination with the *P-T* pseudosection calculations constraint that sample SP8 underwent a clockwise *P-T* evolution with a prograde pressure-temperature increase from about 600°C/5-6 kbar to ~750°C/7-7.5 kbar, followed by a retrograde temperature-pressure decrease to ~620°C/<5 kbar. These results are consistently obtained by *P-T* pseudosections calculated in the model system MnKFMASH and MnCNKFMASH.

12.2 Garnet-cordierite-orthoamphibole fels (sample SP9d)

P-T pseudosections were calculated in the system Na_2O - CaO - K_2O - FeO - MgO - Al_2O_3 - SiO_2 - H_2O - TiO_2 - O (NCKFMASHTO) using **THERMOCALC** v3.3 (Powell & Holland, 1998; updated 2007; Fig. 36). The applied *a-x* models for garnet, biotite, silicate melt, orthoamphibole (gedrite/anthophyllite), cordierite, orthopyroxene, plagioclase and ilmenite are those described in Diener *et al.* (2008). End-member phases included in the calculations are alumosilicates, rutile and H_2O. For chlorite the *a-x* relationships of Holland &

Powell (1998) were used. In addition, a *P-T* pseudosection was constructed in the system MnNCKFMASHTO (Fig. 38c) in order to investigate the effect of Mn on the phase diagram topology. The *a-x* relationships used for the Mn-bearing phases are those of Mahar *et al.* (1997), White *et al.* (2000, 2001) and Zeh & Holness (2003). The oxygen content used for pseudosection calculations was recalculated from the mineral modes (see petrographic description in section 11.5) and compositions (Tab. 14) of sample SP9d.

Comparison between the observed mineral assemblages (see section 11.5) and those calculated in the model system NCKFMASHTO (Fig. 36) provide evidence that sample SP9d underwent a prograde pressure-temperature increase from ~650°C/6.5-7 kbar to ~750°C/8 kbar, follwed by a retrograde pressure-temperature decrease to <600°C/3.5 kbar.

The prograde segment of the *P-T* path is constrained by the finding of biotite, gedrite, plagioclase and ilmenite inclusions in garnet (assemblage (A1) in Fig. 36). Furthermore, it is in agreement with the relic garnet growth zonation (Fig. 30a), which is charaterized by decreasing X_{grs} and X_{Fe} from core towards the rim (X_{grs}= 0.09-0.05 in Fig. 37c; X_{Fe} = 0.7-0.5 in Fig. 37e), and with rutile inclusions in garnet rims (assemblage A2). The retrograde *P-T* path is constraint by the resorption of gedrite and garnet at the expense of cordierite (via the simplified reaction grt+ged+qtz=crd; see also Fig. 29g), and by the formation of tiny anthophyllite rims around gedrite (Fig. 30c). Furthermore, the presence of retrograde chlorite and the absence of rutile in the matrix (retrograde assemblage A3) also points to a retrograde pressure-temperature decrease. Last but not least, increasing X_{Fe} values of >0.75 toward the outermost garnet rims (Fig. 30a) is also consistent with the proposed retrograde *P-T* path. The final feature results from retrograde diffusive Fe/Mg exchange between garnet and surrounding Fe-Mg silicates, as indicated by microprobe analysis (Fig. 30a).

P-T pseudosections contoured for gedrite mode (Fig. 37g, h), cordierite mode (Fig. 37i) and plagioclase mode (Fig. 37j) "predict" that all three phases were present during the entire *P-T* evolution, but were partly consumed along the prograde *P-T* path.

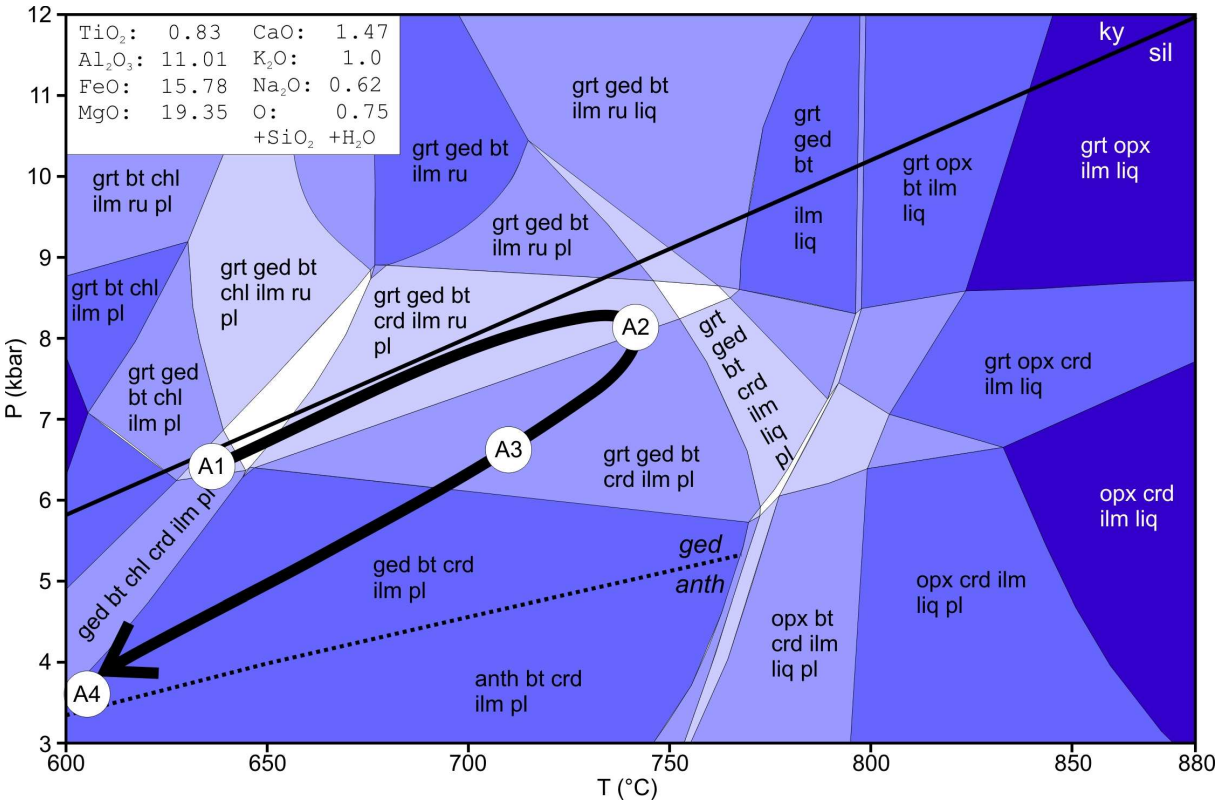

Fig. 36. *P-T* pseudosection constructed for sample SP9d in the system NCKFMASHTO. The inferred metamorphic path is shown as a black arrow. The transition from gedrite to anthophyllite is marked by the dotted line. White fields are divariant and the variances increases with darkening color. Quartz and H_2O are in excess. See also section 11.5 - petrography.

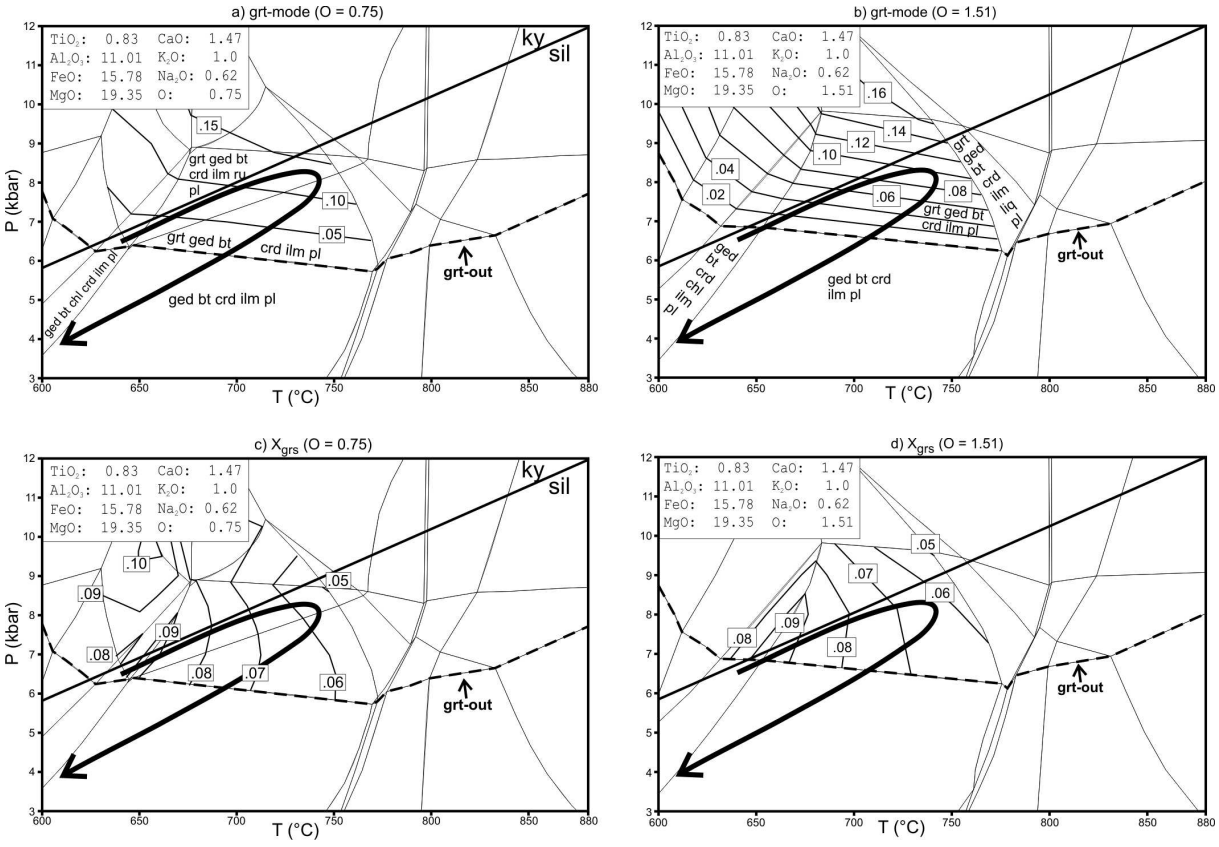

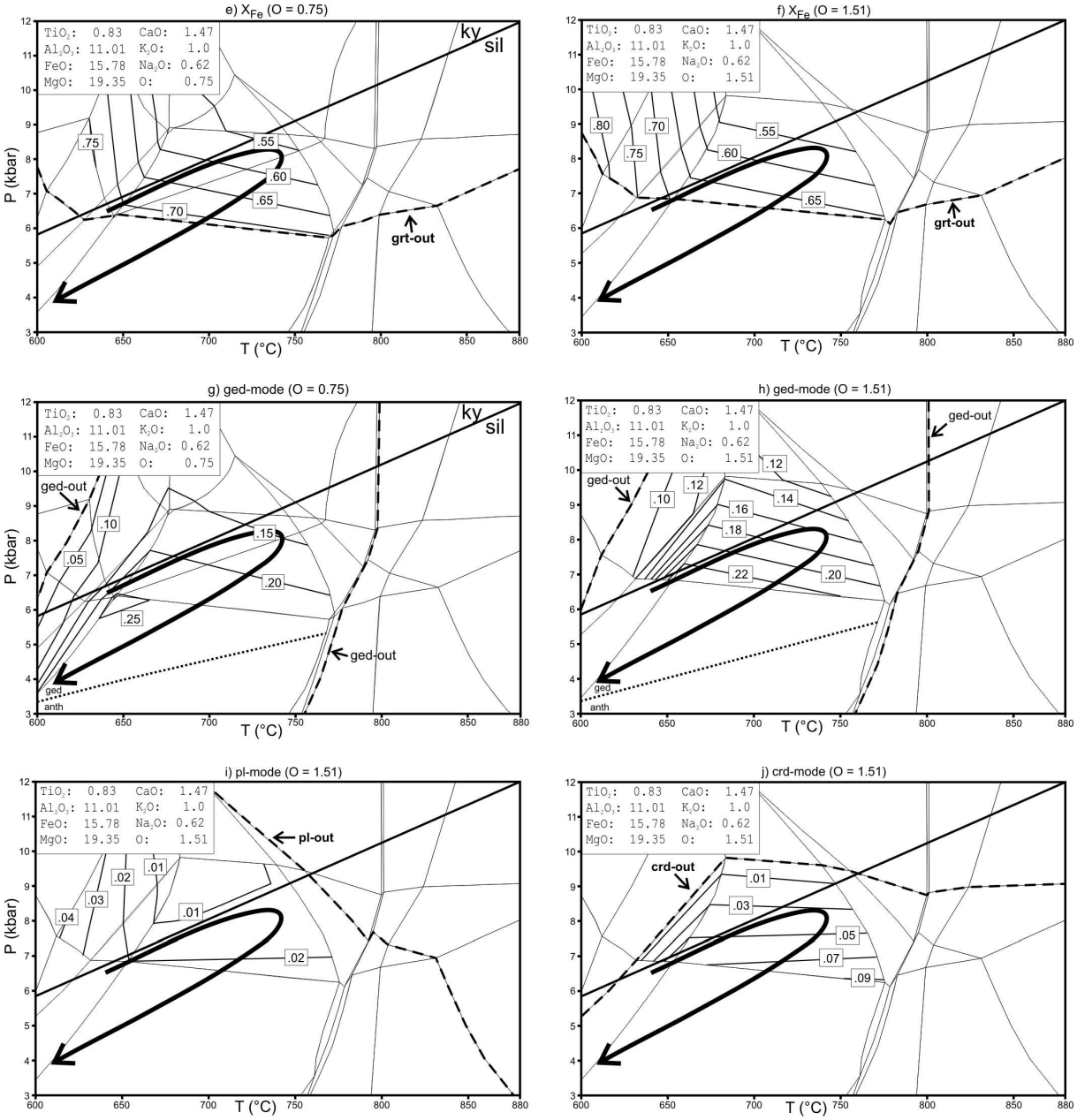

Fig. 37. Contoured *P-T* pseudosections calculated in the system NCKFMASHTO for different oxygen (O) contents (O = 0.75 for a, c, e, g and O = 1.5 for b, d, f, h, i, j). SiO_2 and H_2O are in excess. Important mineral assemblages are shown in a) and b). The diagrams are contoured for garnet mode (a, b), X_{grs} in garnet (c, d), X_{Fe} in garnet (e, f), gedrite mode (g, h), cordierite mode (i) and plagioclase mode (j) – (all mineral modes given as mol.%). Dashed lines indicate in/out boundaries of the respective phases. See text for details.

The effect of the O-content on the *P-T* pseudosection topography (limits of mineral assemblages) was determined by constructing diagrams with different oxygen contents (O = 1.5 and 0.75 mol.%), while keeping the proportions of all other elements constant. The oxygen content is responsible for the oxidation state of iron and thus has direct influence on the stability of Fe^{3+}-bearing phases and the X_{Fe} = $Fe^{2+}/(Fe^{2+}+Mg)$ ratio.

As shown in Fig. 38, a reduction of the O-content from 1.5 to 0.75 has a major effect on the mineral assemblage at temperatures below ~775°C, while at higher temperatures the effect

is neglectable. A oxygen reduction shifts the stability field of rutile to considerable lower pressures (compare Fig. 38a and b). Garnet-in and cordierite-in occurs at moderately lower pressures of ~0.5 kbar and ~1 kbar, respectively. Furthermore, X_{grs} and X_{Fe} (of garnet) are shifted slightly towards lower pressures (Fig. 37c-f). In fact, only the *P-T* pseudosection calculated for O = 0.75 can explain the observed rutile inclusions in garnet and the measured garnet zoning. In contrast, ruilte is completely absent in the *P-T* pseudosection calculated for O = 1.5 (compare Fig. 38a and b).

Since Mn can have a strong effect on the phase diagram topology (see Mahar *et al.*, 1997), a *P-T* pseudosection was calculated in the model system MnNCKFMASHTO (Fig. 38c). At this point, however, it should be emphasized that the current *a-x* models of the Mn-minerals stem from metapelitic systems and are not completely consistent with the *a-x* models used in the NCKFMASHTO system (as outlined by White *et al.*, 2007 and Diener *et al.*, 2008).

As shown in Fig. 38c the addition of only a small amount of MnO = 0.47 mol.% strongly enlarges the garnet stability to lower pressures and temperatures, causing garnet to be stable throughout the entire phase diagram. In contrast, the stability of all other phases is nearly unaffected, except for plagioclase that becomes stabilized to lower *P-T* conditions (compare Fig. 38a and c). Futhermore, the X_{grs} contours in the MnNCKFMASHTO pseudosection show similar curvatures than those in the other systems (Fig. 38a-c). Thus they constrain the same prograde *P-T* increase as shown in Fig. 38a and b. The additional contours for X_{sps} (Fig. 38c) in conjunction with the observed relic garnet growth zoning support the same *P-T* vector. The addition of Mn can also account for the observation that garnet, anthophyllite and retrograde chlorite formed a stable assemblage during the retrograde *P-T* evolution at ~600°C/~3.5 kbar. In fact, such an assemblage cannot be explained by the *P-T* pseudosections calculated for the Mn-free systems.

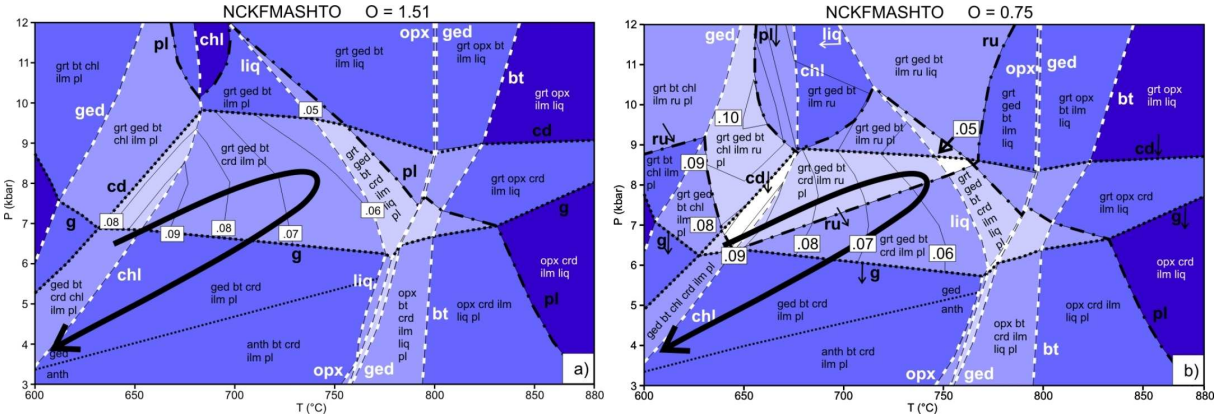

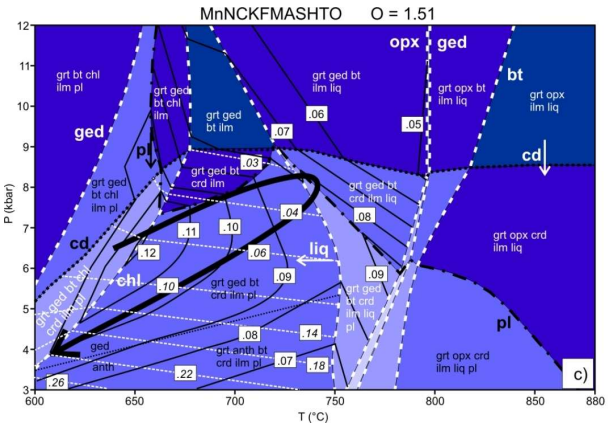

	Al_2O_3	CaO	MgO	FeO	K_2O	Na_2O	TiO_2	MnO	O
a)	11.0	11.47	19.35	15.78	1.00	0.62	0.83		1.51
b)	11.0	11.47	19.35	15.78	1.00	0.62	0.83		0.75
c)	11.0	11.47	19.35	15.78	1.00	0.62	0.83	0.47	1.51

all +SiO_2 +H_2O

Fig. 38. *P-T* pseudosections of sample SP9d (SiO_2 and H_2O are in excess). a+b) NCKFMASHTO system with different oxygen (O) contents. c) MnNCKFMASHTO system with O = 1.5. All diagrams are contoured for X_{grs} (thin black solid lines) and c) is additionally contoured for X_{sps} (thin white dashed lines, labeld in italics). Black arrow indicates inferred metamorphic *P-T* path as shown in Fig. 36 and Fig. 37. Small arrows in b) and c) indicate the direction in which the phase field boundaries are shifted if the O-content is reduced (Fig. 38b) or if Mn is added (Fig. 38c) to the NCKFMASHTO system shown in Fig. 38a.

In summary, observed mineral assemblages, textures and zoning patterns, in combination with *P-T* pseudosection calculations provide evidence that sample SP9d underwent a clockwise *P-T* evolution with a prograde pressure-temperature increase from ~650°C/6.5-7 kbar to ~750°C/8 kbar followed by a retrograde decrease to <600°C/3.5 kbar (Fig. 36-18). The modelling results well demonstrate that the Mn- and O-contents can have significant effects on the *P-T* pseudosection topography, especially at temperatures below ~750°C. In the example above the O-content heavily influenced the stability of rutile and plagioclase and, to a lesser extent, of garnet and cordierite (Fig. 38a, b). Whereas the addition of Mn stabilized garnet and cordierite to lower temperatures and pressures (Fig. 38c).

12.3 Garnet-pyroxene amphibolite (sample SP7a)

P-T pseudosections were calculated in the system Na_2O - CaO - K_2O - FeO - MgO - Al_2O_3 - SiO_2 - H_2O - TiO_2 - O (NCKFMASHTO) - (Fig. 39) using **THERMOCALC** v3.3 (Powell & Holland, 1998; updated 2007). The applied *a-x* models for garnet, biotite, silicate melt, clinoamphibole (hornblende), clinopyroxene (diopside), epidote, orthopyroxene, plagioclase and ilmenite are those described in Diener *et al.* (2007, 2008). End-member phases included in the calculations are rutile and H_2O. The oxygen content (O = 1.5) used for pseudosection calculations was recalculated from the mineral modes (see petrographic description in section 11.2) and compositions (Tab. 12) of sample SP7a. The H_2O content was used from LOI (0.89 wt.%; Tab. 10).

Comparison between observed minerals assemblages (see section 11.2) and those calculated in the model system NCKFMASHTO constraint that the observed mineral assemblage garnet-hornblende-diopside-

plagioclase-ilmenite-biotite is stable over a wide *P-T* interval from <600 to 810°C at 3.5 to 10 kbar. The peak metamorphic conditions, however, were reached at about 750°C/7 kbar. This is supported by the agreement between measured and calculated garnet and diopside compositions (X_{Fe}^{Grt} = 0.84; X_{Fe}^{Di} = 0.46-0.51) as shown in Fig. 40a and d. The contour diagrams furthermore constraint that garnet and diopside are formed together during prograde heating (either at constant or increasing pressures), whereas plagioclase and hornblende are consumed. This "prediction" conforms to the observation that garnet contains hornblende, plagioclase and diopside inclusions. The finding of ilmenite inclusions in garnet (Fig. 23a) and the calculated ilmenite stability supports the interpretation that garnet formation took place during a prograde pressure increase, as already constraint for samples SP8 and SP9d. Otherwise, in case of prograde decompression (*e.g.* from 600°C/10 kbar to 750°C/7 kbar), garnet would be consumed and rutile inclusions in garnet should occur. The retrograde *P-T* evolution of sample SP7a is only constrained by increasing X_{Fe} at garnet rims (X_{Fe} from 0.84 to 0.90). Thus a retrograde *P-T* vector cannot be obtained. Finally it should be noted that the pseudosections in Fig. 39 and Fig. 40 do not well explain X_{grs} of garnet and the plagioclase composition. This discrepancy might be explained by the uncertainties related to the oxidation state of sample SP7a. Furthermore, the presented *P-T* path cannot account for the high Al^{VI} (~0.6) that was measured at one hornblende rim. This rim perhaps was affected by later alteration.

In order to test the influence of oxygen on the phase diagram topology a second *P-T* pseudosection was calculated in the model system NCKFMASHTO using a reduced oxygen content of 1.09 mol.% (Fig. 41). In general, a decrease in the oxygen content reduces the stability field of epidote to higher pressures and shifts assemblages with rutile and ilmenite to lower pressures. Nevertheless, a oxygen reduction from 1.5 to 1.09 (Fig. 41) has no effect on the *P-T* path derived for sample SP7a.

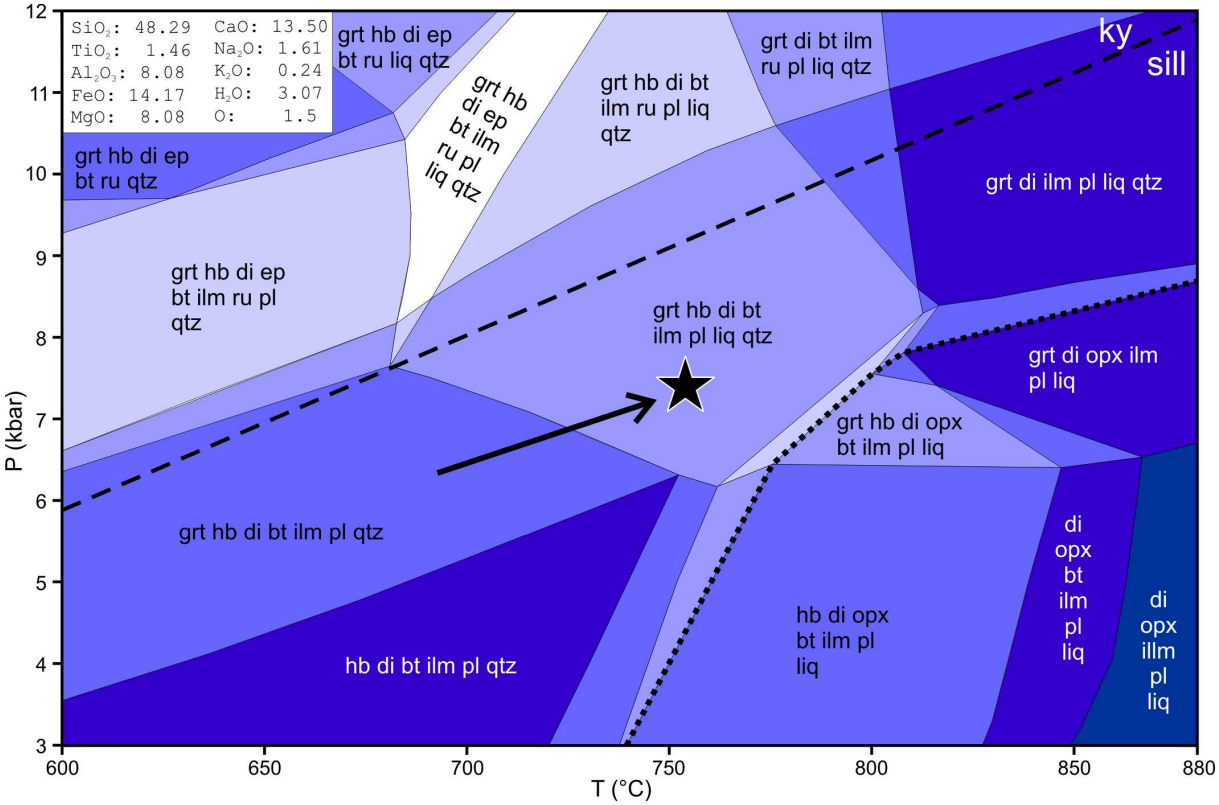

Fig. 39. *P-T* pseudosection constructed in the system NCKFMASHTO for sample SP7a. Black arrow marks the inferred prograde *P-T* vector. Peak assemblage and *P-T* conditions of ~750°C/7 kbar are marked by the star. The dotted line marks the boundary between the silica-saturated and silica-undersaturated parts of the diagram.

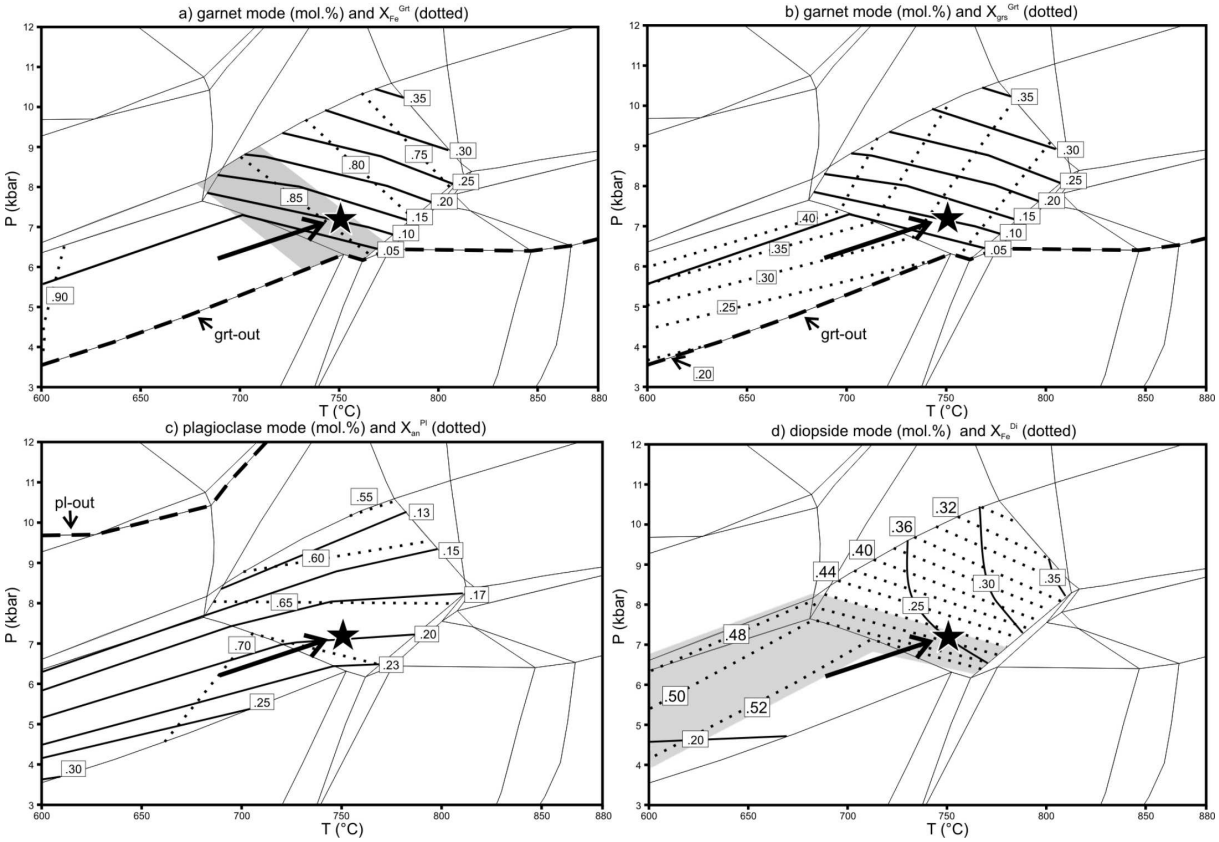

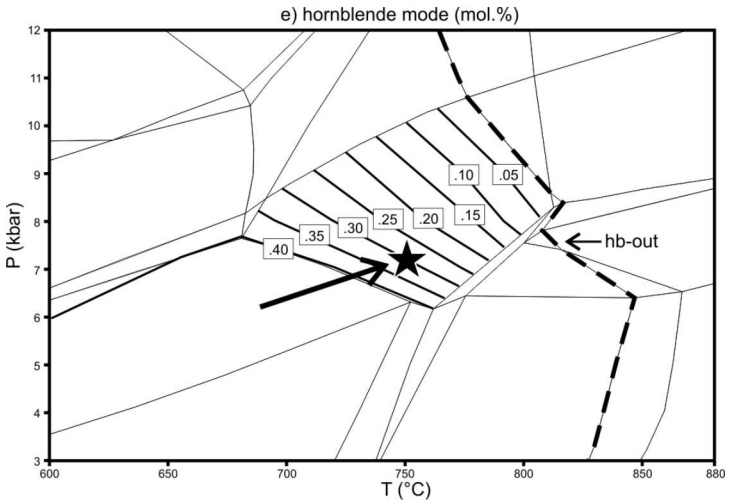

Fig. 40. Contoured *P-T* pseudosections in the system NCKFMASHTO for sample SP7a. The inferred *P-T* vector is shown as a black arrow and the star marks the inferred peak metamorphic conditions as shown in Fig. 39. a) garnet mode (solid lines) and X_{Fe} in garnet (dotted lines). Grey field indicates the *P-T* interval where measured and calculated compositions of garnet rims coincide (X_{Fe} ~ 0.84). b) garnet mode (solid) and X_{grs} in garnet (dotted). c) plagioclase mode (solid) and X_{an} in plagioclase (dotted). d) diopside mode (solid) and X_{Fe} in diopside (dotted). Grey field indicates the *P-T* interval where measured and calculated compositions of diopside coincide (X_{Fe} = 0.46-0.51). e) hornblende mode (solid) and Al^{VI} in hornblende. The in/out-lines of the respective phases are indicated by thick dashed lines. Note that diopside is stable in the entire *P-T* interval.

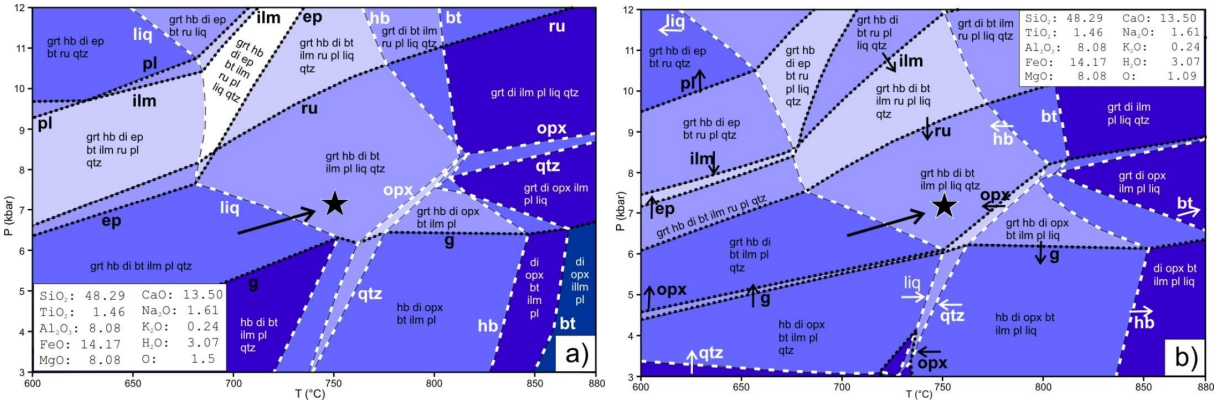

Fig. 41. *P-T* pseudosections constructed in the system NCKFMASHTO for sample SP7a with different oxygen (O) contents (O = 1.5 in a) and 1.09 mol.% in b)). The inferred *P-T* vector is shown as a "long" black arrow and the star marks the inferred peak metamorphic conditions as shown in Fig. 39. Small arrows in b) indicate the direction in which the phase field boundaries are shifted if the O-content is reduced compared to the NCKFMASHTO system shown in Fig. 41a.

In summary, agreement between thin section observations, electron microprobe data and calculated phase diagrams provide evidence that sample SP7a underwent a prograde pressure-temperature increase culminating at peak *P-T* conditions of ~750°C/7 kbar.

13 Geothermobarometry

Several geothermobarometers were used in order to constrain the peak metamorphic conditions of the investigated samples. For peak metamorphic *P-T* estimates minerals that are assumed to have been in chemical equilibrium during peak metamorphism were used, *e.g.* unaltered rims of prograde zoned garnets (*i.e.* garnet domains with the lowest X_{Fe}), biotite and hornblende included in plagioclase and cores of matrix plagioclase. Mineral compositions used

for geothermobarometry are shown in Tab. 11 to Tab. 14.

The application of geothermobarometers is based on the assumption that a chemical equilibrium was established at a certain stage of the metamorphic history, and that this equilibrium is still preserved. This, however, is not necessarily the case since minerals tend to equilibrate during the pro- and retrograde *P-T* evolution. For some minerals this is obvious from mineral zonation patterns (*e.g.* garnet or plagioclase), whereas other minerals can completely re-equilibrate (*e.g.* biotite or hornblende). Such zoning patterns can either result from mineral growth (*e.g.* decreasing X_{Fe} in garnet from core to rim), or from diffusion overprint (*e.g.* increase of X_{Fe} towards garnet rims). Furthermore it has to be considered, that different ions in one and the same mineral can re-equilibrate with different velocities (intensities). For example, Ti and Al in biotite can show a great scatter within thin section scale due to slow diffusive exchange, whereas X_{Fe} can be homogenous due to the faster diffusivity of Fe and Mg in biotite. Since the diffusivity increases with temperature, care must be taken when applying conventional geothermobarometers to high-grade metamorphic rocks (see *e.g.* Spear, 1993; Kohn & Spear, 2000; Spear & Florence, 1992; Zeh *et al.*, 2004a).

Geothermobarometric calculations were performed using the following computer programs: GB (Holdaway, 2001), GTB (v2.1; Spear & Kohn, 2001), Hbl-Pl (Holland & Blundy, 1994), and selfwritten EXCEL spreadsheets. In this study the following conventional geothermobarometers were employed: garnet-biotite (grt-bt; calibration of Holdaway, 2001), Ti-in-biotite (Henry & Guidotti, 2002), hornblende-plagioclase (hbl-pl; Holland & Blundy, 1994), garnet-clinopyroxene (grt-cpx; calibration of Krogh, 1988), garnet-biotite-plagioclase-quartz (grt-bt-pl; Hoisch, 1990, 1991), garnet-hornblende-plagioclase (grt-hbl-pl; Kohn & Spear, 1990) and garnet-rutile-ilmenite-plagioclase-quartz (GRIPS; Bohlen & Liotta, 1986). A detailed description of these geothermobarometers is given in appendix 23 - Geothermobarometry on p. 132.

13.1 Garnet-biotite amphibolite (sample SP1)

Petrographic observations provide evidence that the peak metamorphic mineral assemblage was garnet-biotite-plagioclase-hornblende-quartz (see section 11.1). This assemblage allows the application of grt-bt and grt-hbl geothermometry and grt-bt-pl and grt-hbl-pl geobarometry. For geothermobarometric calculations matrix hornblende core and matrix biotite core compositions (both phases not in contact with garnet), the core compositions of zoned matrix plagioclase (assumed to have formed at the metamorphic peak) and garnet core compositions (least affected by a diffusion alteration) were used (Tab. 11). For some

calculations the composition of biotite inclusions in plagioclase was used. The results obtained by the different geothermobarometers for several mineral pairs, yield average peak *P-T* conditions of ~750-780°C at ~7-7.5 kbar, as shown in Tab. 15 and Fig. 42a.

Tab. 11. Mineral compositions of sample SP1 used for geothermobarometry.

wt.% oxides	grt	fsp	bt											amph						
SiO_2	36.98	55.55	35.51	35.24	35.21	34.90	34.86	35.18	35.22	34.97	34.88	35.43	35.47	42.27	41.69	41.99	41.35	42.19	41.92	40.81
TiO_2	0.05		3.07	3.15	3.38	3.08	3.25	3.82	3.39	3.37	3.67	3.21	3.61	1.29	1.26	1.20	1.20	1.17	1.28	1.05
Al_2O_3	20.86	27.43	16.15	16.43	16.55	16.39	16.60	16.38	16.14	16.39	16.50	16.61	15.33	12.62	12.47	12.96	13.26	12.07	12.54	12.37
Cr_2O_3	0.00		0.02	0.00	0.03	0.04	0.04	0.03	0.03	0.06	0.00	0.11	0.01	0.01	0.01	0.00	0.04	0.04	0.04	0.05
Fe_2O_3	0.00	0.16	0.00	0.00	0.00	0.00	0.00	0.00	0.00	0.00	0.00	0.00	0.00	7.68	8.34	8.00	8.31	9.68	7.60	9.18
FeO	29.24	0.00	20.87	20.85	21.25	20.88	21.22	21.67	20.92	22.10	21.87	21.41	21.54	0.00	0.00	0.00	0.00	0.00	0.00	0.00
MnO	2.90		0.07	0.11	0.10	0.09	0.15	0.07	0.08	0.11	0.20	0.17	0.09	8.52	8.40	8.39	8.18	9.16	8.10	8.14
MgO	3.83	0.26	11.03	10.87	10.71	10.89	11.00	10.48	10.30	10.23	10.02	10.77	10.42	0.38	0.48	0.40	0.30	0.44	0.44	0.44
BaO		0.04	0.17	0.15	0.14	0.22	0.13	0.21	0.24	0.16	0.13	0.25	0.19	13.10	12.81	13.02	12.71	12.46	13.58	12.14
CaO	5.35	9.79	0.00	0.00	0.02	0.01	0.00	0.03	0.02	0.02	0.06	0.04	0.00	10.85	10.55	10.66	10.87	9.49	10.70	10.81
Na_2O		5.87	0.14	0.15	0.18	0.23	0.14	0.16	0.22	0.18	0.18	0.19	0.19	1.36	1.40	1.33	1.26	1.17	1.38	1.17
K_2O		0.12	8.93	8.73	8.58	8.55	8.42	8.90	8.86	8.55	8.84	8.86	8.96	0.54	0.62	0.60	0.64	0.60	0.72	0.56
sum (H_2O-free)	99.22	99.20	95.95	95.68	96.16	95.27	95.80	96.93	95.42	96.14	96.34	97.04	95.80	98.60	98.02	98.54	98.13	98.46	98.31	96.73
oxygens	12	8	22	22	22	22	22	22	22	22	22	22	22	23	23	23	23	23	23	23
cations																				
Si	2.96	2.52	5.42	5.39	5.37	5.37	5.33	5.34	5.42	5.36	5.34	5.37	5.45	6.31	6.28	6.27	6.22	6.27	6.31	6.23
Ti	0.00		0.35	0.36	0.39	0.36	0.37	0.44	0.39	0.39	0.42	0.37	0.42	0.14	0.14	0.13	0.14	0.13	0.14	0.12
Al	1.97	1.47	2.91	2.96	2.97	2.97	2.99	2.93	2.93	2.96	2.98	2.97	2.78	2.22	2.21	2.28	2.35	2.11	2.23	2.23
Cr	0.00		0.00	0.00	0.00	0.00	0.00	0.00	0.00	0.01	0.00	0.01	0.00	0.00	0.00	0.00	0.00	0.00	0.00	0.01
Fe^{3+}	0.11	0.01	0.00	0.00	0.00	0.00	0.00	0.00	0.00	0.00	0.00	0.00	0.00	0.86	0.94	0.90	0.94	1.08	0.86	1.06
Fe	1.85		2.67	2.67	2.71	2.69	2.71	2.75	2.69	2.83	2.80	2.71	2.77	1.64	1.61	1.63	1.60	1.55	1.71	1.55
Mn	0.20		0.01	0.01	0.01	0.01	0.02	0.01	0.01	0.01	0.03	0.02	0.01	0.05	0.06	0.05	0.04	0.05	0.06	0.06
Mg	0.46	0.02	2.51	2.48	2.43	2.50	2.51	2.37	2.36	2.34	2.29	2.43	2.39	1.90	1.89	1.87	1.83	2.03	1.82	1.85
Ba		0.00	0.01	0.01	0.01	0.01	0.01	0.01	0.01	0.01	0.01	0.01	0.01							
Ca	0.46	0.48	0.00	0.00	0.00	0.00	0.00	0.00	0.00	0.00	0.01	0.01	0.00	1.74	1.70	1.71	1.75	1.51	1.73	1.77
Na		0.52	0.04	0.05	0.05	0.07	0.04	0.05	0.07	0.05	0.05	0.06	0.06	0.39	0.41	0.39	0.37	0.34	0.40	0.35
K		0.01	1.74	1.70	1.67	1.68	1.64	1.72	1.74	1.67	1.73	1.71	1.76	0.06	0.06	0.06	0.07	0.06	0.07	0.06
sum	8.00	5.01	15.66	15.64	15.62	15.66	15.64	15.64	15.63	15.63	15.64	15.66	15.65	15.31	15.32	15.29	15.30	15.14	15.33	15.28
X_{Fe}	0.80		0.52	0.52	0.53	0.52	0.52	0.54	0.53	0.55	0.55	0.53	0.54	0.46	0.46	0.47	0.47	0.43	0.48	0.46
X_{ab}		0.52																		

13.2 Garnet-pyroxene amphibolite (sample SP7a)

Petrographic observations provide evidence that the peak metamorphic mineral assemblage was garnet-hornblende-diopside-plagioclase-ilmenite-biotite-quartz (see section 11.2). This assemblage allows the application of grt-bt, grt-hbl and grt-cpx geothermometry and grt-hbl-pl geobarometry. The grt-bt-pl geobarometer was not applicable because of the high Ti content of biotite. For geothermobarometric calculations matrix hornblende core compositions (hornblende not in contact with garnet), matrix biotite (included in plagioclase), the core compositions of zoned matrix plagioclase and garnet and dioside rim compositions (both unaffected by a diffusion alteration, *i.e.* domains with the lowest X_{Fe} contents) were used (Tab. 12). *P-T* calculations carried out with the stated geothermobarometers yield average peak metamorphic conditions of ~750-820°C at ~7.5 kbar, as shown in Tab. 15 and Fig. 42b.

Tab. 12. Mineral compositions of sample SP7a used for geothermobarometry

wt.% oxides	grt	pl	bt				amph											ilm	px								
SiO_2	37.36	55.94	33.00	33.51	33.89	34.04	41.32	41.75	41.58	42.21	41.81	42.74	43.53	42.50	41.41	40.94	41.96	0.02	50.23	49.89	50.37	49.87	49.61	49.90	50.21	49.93	50.43
TiO_2	0.00		5.93	6.25	6.18	6.13	1.55	2.07	1.59	1.61	1.87	1.82	1.50	1.80	1.76	1.97	1.47	52.14	0.07	0.06	0.13	0.13	0.10	0.21	0.16	0.19	0.10
Al_2O_3	21.30	28.22	13.71	14.77	13.76	15.58	11.30	11.58	10.77	11.27	12.70	9.61	10.02	12.57	11.60	13.74	11.28	0.16	0.93	1.35	1.04	1.40	1.49	1.67	1.68	1.25	2.09
Cr_2O_3	0.00		0.07	0.00	0.07	0.00	0.02	0.03	0.02	0.03	0.00	0.02	0.00	0.02	0.08	0.08	0.11	0.04	0.01	0.01	0.00	0.04	0.02	0.02	0.04	0.00	0.04
Fe_2O_3	0.00	0.14	0.00	0.00	0.00	0.00	5.93	5.63	6.45	7.24	7.70	5.90	7.23	7.61	8.42	7.16	7.19	0.42	1.99	2.02	1.77	1.56	2.82	1.75	1.48	2.19	1.78
FeO	28.03		25.55	24.89	24.72	25.00	15.73	17.04	16.40	15.87	15.71	16.37	15.93	15.46	15.47	15.56	15.28	44.17	14.65	14.87	15.20	15.13	13.96	15.54	16.24	16.38	15.62
MnO	2.35		0.10	0.12	0.18	0.24	0.22	0.31	0.32	0.18	0.35	0.32	0.35	0.30	0.33	0.26	0.24	2.33	0.58	0.55	0.55	0.58	0.54	0.60	0.55	0.62	0.55
MgO	3.01	0.09	7.26	6.91	7.13	6.88	7.06	6.54	6.78	7.24	6.96	7.43	7.90	7.48	6.95	6.68	7.32	0.22	9.09	9.17	8.80	8.95	9.19	8.86	8.89	9.29	9.34
BaO		0.02	0.64	0.88	0.88	0.72																					
CaO	7.45	10.01	0.53	0.03	0.07	0.03	10.69	11.11	10.73	11.12	11.14	11.29	11.01	11.10	11.05	10.96	11.25		21.38	20.99	21.77	20.99	21.40	20.82	20.78	19.70	20.79
Na_2O		5.65	0.11	0.06	0.05	0.03	1.46	1.42	1.29	1.32	1.29	1.11	1.24	1.44	1.37	1.37	1.31		0.28	0.23	0.21	0.25	0.24	0.27	0.20	0.23	0.20
K_2O		0.18	7.50	8.93	8.56	8.88	0.98	0.94	0.90	1.11	1.15	0.89	0.70	0.84	0.94	1.21	0.93		0.00		0.01	0.01	0.01	0.00	0.01	0.00	0.00
sum (H_2O-free)	99.50	100.26	94.38	96.34	95.49	97.50	96.26	98.42	96.84	99.20	100.68	97.49	99.40	101.11	99.37	99.93	98.33	99.50	99.22	99.14	99.86	98.90	99.37	99.64	100.23	99.77	100.94
oxygens	12	8	22	22	22	22	23	23	23	23	23	23	23	23	23	23	23	3	6	6	6	6	6	6	6	6	6
cations																											
Si	2.98	2.51	5.29	5.27	5.37	5.27	6.43	6.39	6.45	6.40	6.24	6.58	6.54	6.28	6.28	6.15	6.40	0.00	1.96	1.95	1.95	1.95	1.93	1.94	1.94	1.94	1.93
Ti	0.00		0.71	0.74	0.74	0.71	0.18	0.24	0.19	0.18	0.21	0.21	0.17	0.20	0.20	0.22	0.17	0.99	0.00	0.00	0.00	0.00	0.00	0.01	0.00	0.01	0.00
Al	2.00	1.49	2.59	2.74	2.57	2.84	2.07	2.09	1.97	2.01	2.23	1.74	1.77	2.19	2.07	2.43	2.03	0.00	0.04	0.06	0.05	0.06	0.07	0.08	0.08	0.06	0.09
Cr	0.00		0.01	0.00	0.01	0.00	0.00	0.00	0.00	0.00	0.00	0.00	0.00	0.00	0.01	0.01	0.01	0.00	0.00	0.00	0.00	0.00	0.00	0.00	0.00	0.00	0.00
Fe^{3+}	0.04	0.00	0.00	0.00	0.00	0.00	0.70	0.65	0.75	0.83	0.86	0.68	0.82	0.85	0.96	0.81	0.83	0.01	0.06	0.06	0.05	0.05	0.08	0.05	0.04	0.06	0.05
Fe	1.83		3.43	3.27	3.27	3.23	2.05	2.18	2.13	2.01	1.96	2.11	2.00	1.91	1.96	1.95	1.95	0.94	0.48	0.49	0.49	0.49	0.45	0.51	0.53	0.53	0.50
Mn	0.16		0.01	0.02	0.02	0.03	0.03	0.04	0.04	0.02	0.04	0.04	0.04	0.04	0.04	0.03	0.03	0.05	0.02	0.02	0.02	0.02	0.02	0.02	0.02	0.02	0.02
Mg	0.36	0.01	1.73	1.62	1.68	1.59	1.64	1.49	1.57	1.64	1.55	1.70	1.77	1.65	1.57	1.50	1.66	0.01	0.53	0.53	0.51	0.52	0.53	0.51	0.51	0.54	0.53
Ba		0.00	0.04	0.05	0.05	0.04																					
Ca	0.64	0.48	0.09	0.01	0.01	0.00	1.78	1.82	1.78	1.81	1.78	1.86	1.77	1.76	1.80	1.76	1.84		0.89	0.88	0.91	0.88	0.89	0.87	0.86	0.82	0.85
Na		0.49	0.03	0.02	0.02	0.01	0.44	0.42	0.39	0.39	0.37	0.33	0.36	0.41	0.40	0.40	0.39		0.02	0.02	0.02	0.02	0.02	0.02	0.01	0.02	0.01
K		0.01	1.53	1.79	1.73	1.75	0.20	0.18	0.18	0.21	0.22	0.17	0.13	0.16	0.18	0.23	0.18		0.00	0.00	0.00	0.00	0.00	0.00	0.00	0.00	0.00
sum	8.00	4.99	15.32	15.37	15.33	15.33	15.52	15.51	15.45	15.50	15.48	15.43	15.37	15.44	15.47	15.51	15.48	2.00									
X_{Fe}	0.84		0.66	0.67	0.66	0.67	0.56	0.59	0.58	0.55	0.56	0.55	0.53	0.54	0.56	0.57	0.54	0.99	0.47	0.48	0.49	0.49	0.46	0.50	0.51	0.50	0.48
X_{ab}		0.50																									

13.3 Garnet-biotite-sillimanite-cordierite gneiss (sample SP8)

Petrographic observations provide evidence that the peak metamorphic mineral assemblage was garnet-biotite-cordierite-quartz (see section 11.3). This assemblage allows the application of grt-bt and Ti-in-bt geothermometry. No conventional geobarometer (*e.g.* GASP) could be applied because of the absence of plagioclase. However, sillimanite inclusions in cordierite cores constraint that peak metamorphic conditions were reached in the sillimanite stability field. For geothermometric calculations matrix biotite core compositions and garnet core compositions (unaffected by a diffusion alteration) were used (Tab. 13). *P-T* calculations carried out with the above geothermometers yield average peak metamorphic temperatures of ~720 to 730°C, as shown in Tab. 15 and Fig. 42c.

13.4 Garnet-plagioclase-biotite gneiss (sample SP9c)

Petrographic observations provide evidence that the peak metamorphic mineral assemblage was garnet-biotite-plagioclase-quartz (see section 11.4). This assemblage allows the application of grt-bt geothermometry and grt-bt-pl geobarometry. For geothermobarometric calculations core compositions of zoned matrix plagioclase, matrix biotite core compositions and garnet rim compositions (unaffected by diffusion alteration) were used (Tab. 13). The results obtained by the above geothermobarometers yield average peak *P-T* conditions of ~740°C at ~7.5 kbar, as shown in Tab. 15 and Fig. 42d.

Tab. 13. Mineral analyses of sample SP8 and SP9c used for geothermobarometry

	sample SP8						sample SP9c												
wt.% oxides	grt	bt				crd	grt	pl	bt										
SiO_2	37.81	36.67	35.94	37.04	36.35	47.96	38.19	55.28	37.45	36.64	37.51	37.48	37.15	37.14	37.65	37.03	37.48	37.69	37.29
TiO_2	0.01	3.62	4.12	3.36	3.68	0.01	0.02		1.05	0.98	1.01	1.00	1.01	1.02	1.03	1.01	1.05	1.29	1.28
Al_2O_3	21.51	17.05	17.84	18.46	19.45	32.48	21.10	28.46	17.51	16.17	17.65	17.02	17.44	16.38	18.09	17.87	17.18	16.32	16.29
Cr_2O_3	0.00	0.00	0.03	0.00	0.01		0.06		0.03	0.02	0.06	0.03	0.00	0.06	0.00	0.00	0.04	0.01	0.06
Fe_2O_3	0.00	0.00	0.00	0.00	0.00			0.14	0.00	0.00	0.00	0.00	0.00	0.00	0.00	0.00	0.00	0.00	0.00
FeO	29.37	14.65	16.79	16.10	16.15	6.21	27.88		15.49	16.24	16.17	16.19	16.16	15.92	16.12	16.28	16.00	15.34	15.24
MnO	0.75	0.04	0.02	0.08	0.02	0.05	3.16		0.09	0.10	0.11	0.16	0.12	0.07	0.12	0.07	0.12	0.12	0.10
MgO	8.55	15.20	13.01	13.60	12.82	9.74	6.62	0.09	15.62	15.32	15.07	15.49	15.25	15.18	15.45	15.93	15.43	15.06	15.14
BaO		0.08	0.24	0.11	0.28			0.02	0.03	0.02	0.15	0.17	0.04	0.09	0.05	0.14	0.07	0.16	0.13
CaO	1.34	0.00	0.00	0.03	0.00	0.01	3.48	10.80	0.05	0.04	0.08	0.03	0.07	0.05	0.12	0.28	0.32	0.16	0.36
Na_2O		0.39	0.34	0.36	0.25	0.10		5.50	0.34	0.38	0.45	0.37	0.52	0.40	0.65	0.55	0.85	0.45	0.61
K_2O		8.05	8.81	8.48	8.76	0.01		0.06	8.27	8.28	8.01	8.29	7.92	8.13	7.56	6.73	6.91	8.60	8.32
sum (H_2O-free)	99.34	95.74	97.13	97.61	97.78	96.57	100.50	100.35	95.91	94.18	96.27	96.22	95.68	94.46	96.84	95.90	95.43	95.20	94.82
oxygens	12	22	22	22	22	18	12	8	22	22	22	22	22	22	22	22	22	22	22
cations																			
Si	2.95	5.40	5.30	5.38	5.29	4.98	2.97	2.48	5.51	5.54	5.52	5.53	5.50	5.58	5.48	5.44	5.53	5.61	5.58
Ti	0.00	0.40	0.46	0.37	0.40	0.00	0.00	1.51	0.12	0.11	0.11	0.11	0.11	0.12	0.11	0.11	0.12	0.14	0.14
Al	1.98	2.96	3.10	3.16	3.34	3.98	1.94		3.04	2.88	3.06	2.96	3.04	2.90	3.11	3.09	2.99	2.86	2.87
Cr	0.00	0.00	0.00	0.00	0.00		0.00		0.00	0.00	0.01	0.00	0.00	0.01	0.00	0.00	0.00	0.00	0.01
Fe^{3+}	0.12	0.00	0.00	0.00	0.00		0.11	0.00	0.00	0.00	0.00	0.00	0.00	0.00	0.00	0.00	0.00	0.00	0.00
Fe	1.80	1.80	2.07	1.96	1.97	0.54	1.71		1.91	2.05	1.99	2.00	2.00	2.00	1.96	2.00	1.98	1.91	1.91
Mn	0.05	0.00	0.00	0.01	0.00	0.00	0.21		0.01	0.01	0.01	0.02	0.02	0.01	0.02	0.01	0.01	0.01	0.01
Mg	0.99	3.34	2.86	2.95	2.78	1.51	0.77	0.01	3.43	3.45	3.30	3.41	3.36	3.40	3.36	3.49	3.39	3.34	3.37
Ba		0.00	0.01	0.01	0.02			0.00	0.00	0.00	0.01	0.01	0.00	0.01	0.00	0.01	0.00	0.01	0.01
Ca	0.11	0.00	0.00	0.00	0.00	0.00	0.29	0.52	0.01	0.01	0.01	0.01	0.01	0.01	0.02	0.04	0.05	0.03	0.06
Na		0.11	0.10	0.10	0.07	0.02		0.48	0.10	0.11	0.13	0.11	0.15	0.12	0.18	0.16	0.24	0.13	0.18
K		1.51	1.66	1.57	1.63	0.00		0.00	1.55	1.60	1.50	1.56	1.50	1.56	1.40	1.26	1.30	1.63	1.59
sum	8.00	15.53	15.57	15.51	15.49	11.03	8.00	5.00	15.68	15.76	15.65	15.71	15.69	15.69	15.64	15.61	15.63	15.69	15.72
X_{Fe}	0.64	0.35	0.42	0.40	0.41	0.26	0.69		0.36	0.37	0.38	0.37	0.37	0.37	0.37	0.36	0.37	0.36	0.36
X_{ab}								0.48											

13.5 Garnet-cordierite-orthoamphibole fels (samples SP9d/SP9e)

Petrographic observations provide evidence that the peak metamorphic mineral assemblage was garnet-biotite-cordierite-gedrite-ilmenite-rutile-plagioclase-quartz (see section 11.1). This assemblage allows the application of grt-bt geothermometry and grt-bt-pl, grt-rt-ilm-pl-qtz (GRIPS) geobarometry. For geothermobarometric calculations matrix biotite core compositions (biotite not in contact with garnet), the core compositions of (zoned) matrix plagioclase and garnet rim compositions (unaffected by a diffusion alteration) were used (Tab. 14). The results obtained by geothermobarometry for several mineral pairs yield average peak *P-T* conditions of ~670 to 680°C at ~8 to 9 kbar, as shown in Tab. 15 and Fig. 42e and f.

Tab. 14. Mineral analyses of sample SP9d and SP9e used for geothermobarometry

	sample SP9d						sample SP9e						
wt.% oxides	grt	pl	bt		ilm	crd	grt	pl	bt			ilm	crd
SiO_2	38.23	57.72	38.15	38.01	0.11	49.10	37.60	56.09	36.98	36.61	36.64	0.02	49.13
TiO_2	0.00		2.25	2.10	49.93	0.01	0.06		2.20	2.33	2.90	50.12	0.00
Al_2O_3	21.79	26.41	17.45	17.79	0.10	33.90	21.29	26.93	17.58	16.54	16.68	0.03	33.37
Cr_2O_3	0.01		0.36	0.15	0.09		0.04		0.09	0.14	0.15	0.05	
Fe_2O_3	0.00	0.07	0.00	0.00	3.93		0.00	0.05	0.00	0.00	0.00	4.06	4.73
FeO	27.69		12.94	13.47	44.02	4.97	28.02		13.76	13.16	13.59	44.37	0.06
MnO	0.76		0.01	0.07	0.83	0.06	0.59		0.03	0.01	0.02	0.68	10.86
MgO	8.74	0.41	15.83	16.10	0.10	10.95	7.86	0.00	16.08	15.62	14.95	0.03	
BaO		0.06	0.02	0.00				0.00	0.00	0.00	0.03		
CaO	2.33	8.55	0.01	0.00		0.10	2.66	8.98	0.00	0.05	0.02		0.00
Na_2O		6.63	0.44	0.47		0.20		6.27	0.45	0.45	0.50		0.23
K_2O		0.04	8.15	8.04		0.05		0.03	7.96	7.98	8.11		0.01
sum (H_2O-free)	99.56	99.90	95.60	96.20	99.12	99.32	98.12	98.33	95.14	92.89	93.60	99.36	98.40
oxygens	12	8	22	22	3	18	12	8	22	22	22	3	18
cations													
Si	2.96	2.59	5.56	5.51	0.00	4.93	2.97	2.56	5.44	5.52	5.50	0.00	4.97
Ti	0.00		0.25	0.23	0.96	0.00	0.00		0.24	0.26	0.33	0.96	0.00
Al	1.99	1.40	3.00	3.04	0.00	4.01	1.98	1.45	3.05	2.94	2.95	0.00	3.98
Cr	0.00		0.04	0.02	0.00		0.00		0.01	0.02	0.02	0.00	
Fe^{3+}	0.09	0.00	0.00	0.00	0.08		0.07	0.00	0.00	0.00	0.00	0.08	
Fe	1.71		1.58	1.63	0.94	0.42	1.78		1.69	1.66	1.71	0.94	0.40
Mn	0.05		0.00	0.01	0.02	0.01	0.04		0.00	0.00	0.00	0.01	0.01
Mg	1.01	0.03	3.44	3.48	0.00	1.64	0.93	0.00	3.53	3.51	3.34	0.00	1.64
Ba		0.00	0.00	0.00		0.01		0.00	0.00	0.00	0.00		
Ca	0.19	0.41	0.00	0.00		0.04	0.23	0.44	0.00	0.01	0.00		0.00
Na		0.58	0.12	0.13		0.01		0.55	0.13	0.13	0.14		0.05
K		0.00	1.51	1.49				0.00	1.49	1.53	1.55		0.00
sum	8.00	5.00	15.50	15.54	2.00	11.06	8.00	5.00	15.60	15.58	15.54	2.00	11.04
X_{Fe}	0.63		0.31	0.32	1.00	0.20	0.66		0.32	0.32	0.34	1.00	0.20
X_{ab}		0.58						0.56					

13.6 Geothermobarometric results from the Phikwe Complex

Peak metamorphic conditions in the Phikwe Compex, as obtained by geothermobarometry, are in the range ~675-820 C° at 6.5-9 kbar (Tab. 15, Fig. 42).

Tab. 15. Average temperatures and pressures obtained by different geothermobarometers from rocks of the Phikwe Complex

Geothermometers	SP1	SP7a	SP8	SP9c	SP9d	SP9e	*error (°C)
grt-bt[1](avg.)	**753** (n=11 bt)	**824** (n=2)	**729** (n=4)	**737** (n=12)	**683** (n=2)	**673** (n=3)	± 25
(min.-max.)	737-779	823-826	683-759	720-756	680-686	667-680	
Ti-in-bt[2](avg.)			**720** (n=4)				n.s.
(min.-max.)			705-730				
hb-pl$^{3}_{ed\text{-}tr}$ (avg.)	**771** (n=7 hb)	**788** (n=11)					± 35-40
(min.-max.)	752-793	763-836					
hb-pl$^{3}_{ed\text{-}ri}$ (avg.)	**778**	**806**					
(min.-max.)	762-809	787-844					
grt-cpx[4](avg.)		**751** (n=9 cpx)					~ ± 50
(min.-max.)		717-785					
Geobarometers							*error (kbar)
grt-bt-pl[5](avg.)	**7.5**			**7.5**	**8.0**	**8.8**	± 0.5-1
(min.-max.)	6.5-8.5			7.0-8.0			
grt-hbl-pl[6](avg.)	**6.9**	**7.5**					± 0.5-1
(min.-max.)	6.6-7.1	7.0-8.0					
grt-rt-ilm-pl-qtz[7](avg.)					**7.5**	**7.5**	± 1
(min.-max.)					7.0-8.0	7.0-8.0	

[1] = Holdaway (2001); [2] = Henry & Guidotti (2003); [3] = Holland & Blundy (1994); [4] = Krogh (1988); [5] = Hoisch (1990, 1991); [6] = Kohn & Spear (1990); [7] = Bohlen & Liotta (1986). For a detailed description about the applied geothermobarometers see appendix "23 - Geothermobarometry".* = error of the calibration as given by the respective authors.

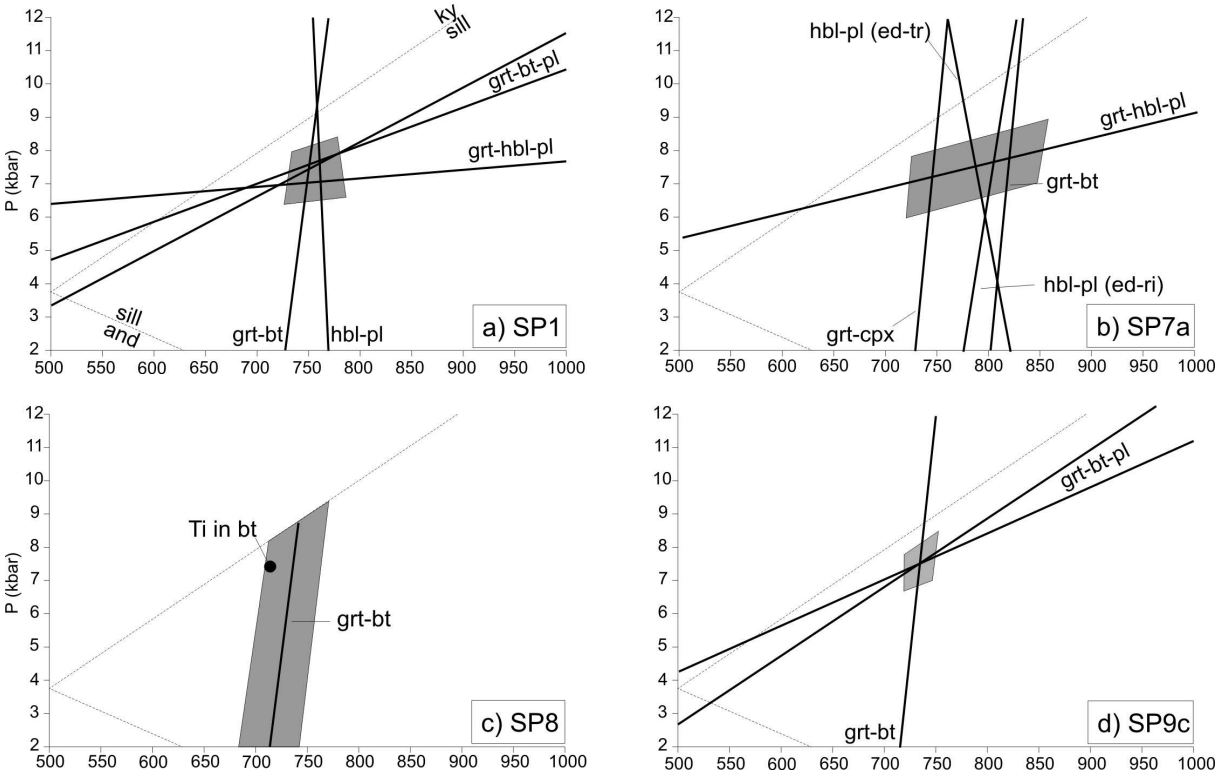

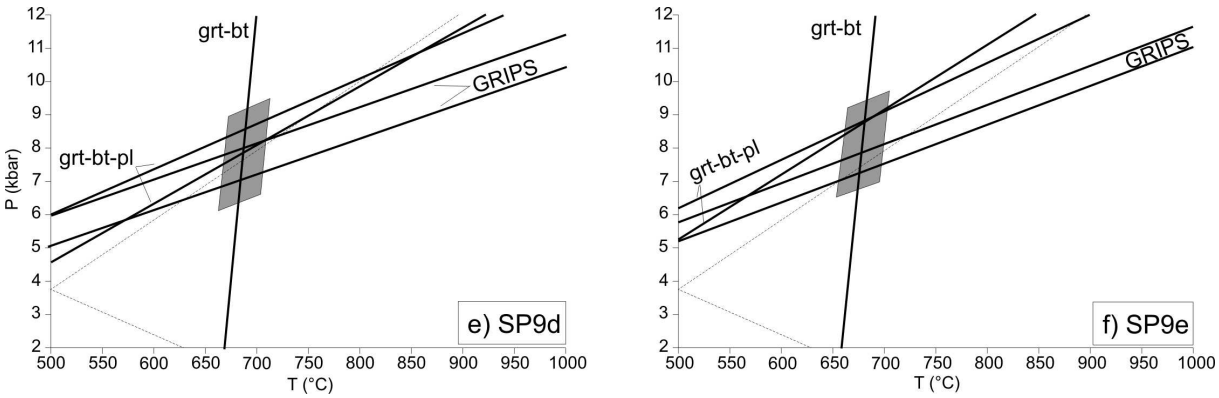

Fig. 42. *P-T* diagram showing the results of *P-T* calculations obtained by geothermobarometry from different rocks of the Phikwe Complex. The geothermobarometers used are those explained in the caption of Tab. 15 and in the appendix "23 - Geothermobarometry". Grey fields indicate average peak metamorphic conditions as shown in Tab. 15. The alumosilicate transitions are shown as thin lines (labeled only in a)).

14 Summary: Metamorphic evolution of the Phikwe Complex

Petrological investigations on samples with different bulk compositions provide evidence that the Phikwe Complex underwent a clockwise *P-T* evolution with a prograde pressure-temperature increase from ~600°C/~6 kbar to ~750°C/~7-8 kbar (metamorphic peak). Subsequently, the rocks were affected by decompression and cooling to *P-T* conditions of <600°C/~3-5 kbar (Fig. 43). This *P-T* evolution is best constraint by mineral assemblages, reaction textures and relic garnet growth zonings observed in the samples SP8 and SP9d (see section 12.1 and 12.2, respectively). The peak metamorphic conditions are additionally constraint by mineral assemblages and compositions (measured and calculated) of sample SP7a (section 12.3) and by the results of several conventional geothermobarometers applied to the six investigated rock samples (section 13 - Geothermobarometry).

The obtained *P-T* path constraints that the rocks of the Phikwe Complex underwent heating from ~600 to ~750°C, while they were buried from *ca.* 20 km depth to 30 km depth (6 to 8 kbar). The inferred *P-T* trajectory also constraints that these rocks underwent uplift from ~30 km to ~11 km (8 to ~3 kbar), while they were cooled from ~750°C to <600°C during their retrograde *P-T* evolution.

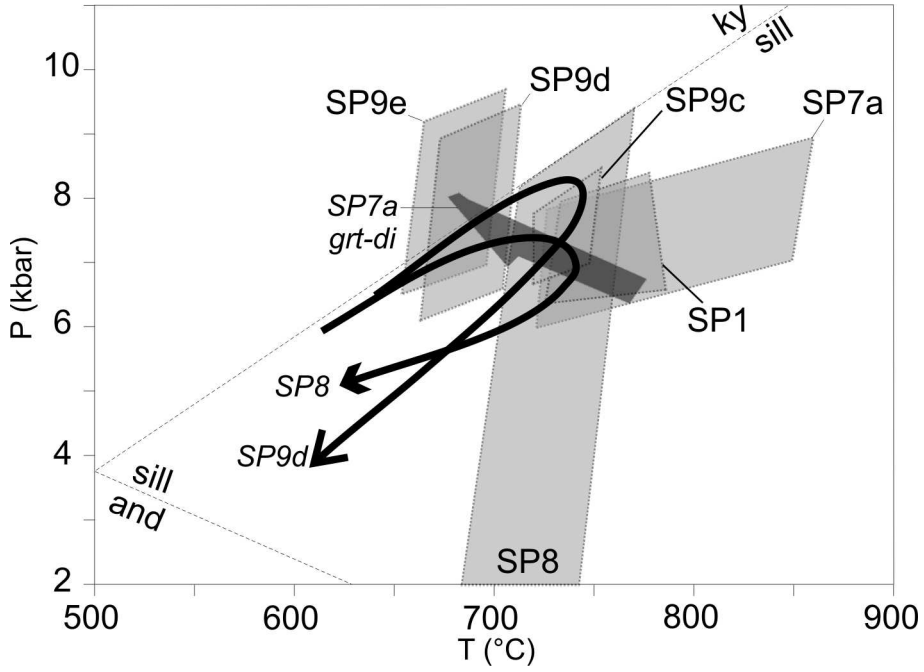

Fig. 43. *P-T* diagram showing the results of *P-T* pseudosection modelling (black arrows and dark grey field; labeled in italics) and geothermobarometry (grey fields). Dark grey field indicates the *P-T* range, where measured and calculated X_{Fe} compositions of garnet and diopside of sample SP7a coincide.

Bulai Pluton area (Beit Bridge Complex)*

* as published by Millonig et al. (2008). Note that sections "2.1 - General framework, 2.2 - Structural-metamorphic events in the Limpopo's Central Zone and 2.3 - Polymetamorphism in the Central Zone?" of the original paper are now covered in section "3 - Introduction and 4 - Geological setting of the Limpopo Belt" of this thesis.

15 Abstract

The Bulai Pluton represents a calc-alkaline magmatic complex of variable deformed charnockites, enderbites and granites, and contains xenoliths of highly deformed metamorphic country rocks. Petrological investigations show that these xenoliths underwent a high-grade metamorphic overprint at peak *P-T* conditions of 830-860°C/8-9 kbar followed by a pressure-temperature decrease to 750°C/5-6 kbar. This *P-T* path is inferred from the application of *P-T* pseudosections to six rock samples of distinct bulk composition: three metapelitic garnet-biotite-sillimanite-cordierite-plagioclase-(K-feldspar)-quartz gneisses, two charnoenderbitic garnet-orthopyroxene-biotite-K-feldspar-plagioclase-quartz gneisses and an enderbitic orthopyroxene-biotite-plagioclase-quartz gneiss. The petrological data show that the metapelitic and charnoenderbitic gneisses underwent uplift, cooling and deformation before they were intruded by the Bulai Granite. This relationship is supported by geochronological results obtained by *in situ* LA-ICP-MS age dating. U-Pb analyses of monazite enclosed in garnet of a charnoenderbite gneiss provide evidence for a high-grade structural-metamorphic-magmatic event at 2644±8 Ma. This age is significantly older than an U-Pb zircon crystallisation age of 2612±7 Ma previously obtained from the surrounding, late-tectonic Bulai Granite. The new dataset indicates that parts of the Limpopo's Central Zone were affected by a Neoarchean high-grade metamorphic overprint, which was caused by magmatic heat transfer into the lower crust in a 'dynamic regional contact metamorphic milieu', which perhaps took place in a magmatic arc setting.

16 Introduction

Deciphering the tectono-metamorphic evolution of a high-grade metamorphic gneiss terrane is challenging, in particular, when the terrane has been subject to polymetamorphism. In such a case, it may be difficult to decide whether or not observed mineral assemblages and textures were formed during single or multiple orogenic processes (Hand *et al.*,1992; Vernon, 1996; Zeh & Millar, 2001; Zeh *et al.*, 2004a). Thus, to understand the structural-metamorphic-magmatic history of such terranes unambiguous field information in combination with detailed petrological and geochronological techniques are required (*e.g.* Zeh *et al.*, 2004a; Kelsey *et al.*, 2003; Halpin *et al.*, 2007). In this study, we present such a combined dataset from the Central Zone of the Limpopo Belt, which is interpreted to have undergone a

polymetamorphic history during the Archaean to Palaeoproterozoic with metamorphic events at 3.1 Ga (M1), 2.52 Ga (M2) and 2.03 Ga (M3) - (Holzer *et al.*, 1998, 1999; Kröner *et al.*, 1999; Zeh *et al.*, 2007). While the tectonometamorphic history during the final event M3 is well supported by geochronological and petrological data, little is known about the *P-T* evolution during M1 and M2 (see Tab. 1 and p. 7). Furthermore, there are still debates about the absolute timing and geotectonic setting of these events (see discussion in Barton *et al.*, 2006). In this study we focus on the M2 event, which is important for the understanding of the Neoarchean evolution of the Limpopo Belt. In particular, it is unclear whether the Central Zone of the Limpopo Belt was affected by a widespread high-grade regional metamorphic event during M2 (as suggested by Holzer *et al.*, 1998, 1999; and Van Reenen *et al.*, 2004) or by local contact metamorphic events associated with the intrusion of voluminous magmatic rocks (Zeh *et al.*, 2005a). Here we present new and detailed petrological and geochronological data from the Bulai Pluton and related metamorphic rocks, with well-defined field relationships.

16.1 The Bulai Pluton - pre-, syn- and post-intrusive features

The Bulai Pluton to the west of Messina represents a calc-alkaline suite of charnockite, charnoenderbite and predominantly porphyric granite, which contain abundant xenoliths (xenoliths - according to the nomenclature by Didier, 1973; Fig. 45). Presently, the timing of M2 in the Bulai Pluton area is constrained by two Pb-stepwise leaching ages of garnet (2518±35 Ma) and sillimanite (2524±5 Ma), obtained from metapelitic gneiss xenoliths in the Bulai granite (Holzer *et al.*, 1999). These ages are younger than four reported emplacement ages of the surrounding Bulai Pluton: 2572±4 Ma (granitic phase: upper intercept age of two strongly discordant U-Pb ID-TIMS analyses; Barton *et al.*, 1994), 2605±2 Ma (enderbitic phase: upper intercept of discordant and near concordant U-Pb ID-TIMS analyses; Barton *et al.*, 1994), 2620±8 Ma (granitic phase: upper intercept of five discordant U/Pb SHRIMP analyses; Kröner *et al.,* 1999), and 2612±7 Ma (weakly deformed porphyric granite: concordia age of 14 spot analyses obtained by LA-ICP-MS; Zeh *et al.*, 2007). Based on the geochronological dataset available from the Bulai area Holzer *et al.* (1998) concluded that the Central Zone must have been affected by a long-lived high-grade metamorphic event (M2) which perhaps started at *c.* 2.6 Ga and prevailed until 2.52 Ga, the so-called "post-Bulai high-grade overprint". This conclusion, however, is in disagreement with field relationships exposed at the Three Sisters area (Fig. 1, Fig. 44 and Fig. 45), where an undeformed to weakly deformed granite variety of the Bulai Pluton (= porphyric Bulai granite) contains up to 10 m long xenoliths of highly

deformed gneisses (Fig. 45), which show a sharp contact to the host rock. Consequently these gneisses, which comprise metapelitic and charnoenderbitic rocks, must have been formed and deformed prior to the granite intrusion, whereby the granite at the Three Sisters locality was weakly affected by a post-magmatic structural overprint (Fig. 45a, b, d). Similar relationships are also documented by an outcrop *ca.* 300 m to the north of the Three Sisters area (S 22°15'547, E 29°55'107), where isoclinally folded garnet-bearing leucosomes (Fig. 45c) in a metapelitic gneiss are cross-cut by weakly deformed Bulai granite. Furthermore, there are numerous locations where the foliation planes of paragneisses and enderbitic gneisses are lit-par-lit intruded by porphyric granite. The large size of some enderbite and metapelite xenoliths (>10 m diameter) suggests that they were assimilated from the wall or roof during the granite intrusion, perhaps by overhead stoping. Thus, the field relationships indicate that the structural and metamorphic fabric within the xenoliths must be older than the Bulai granite emplacement as was already observed by Watkeys (1984).

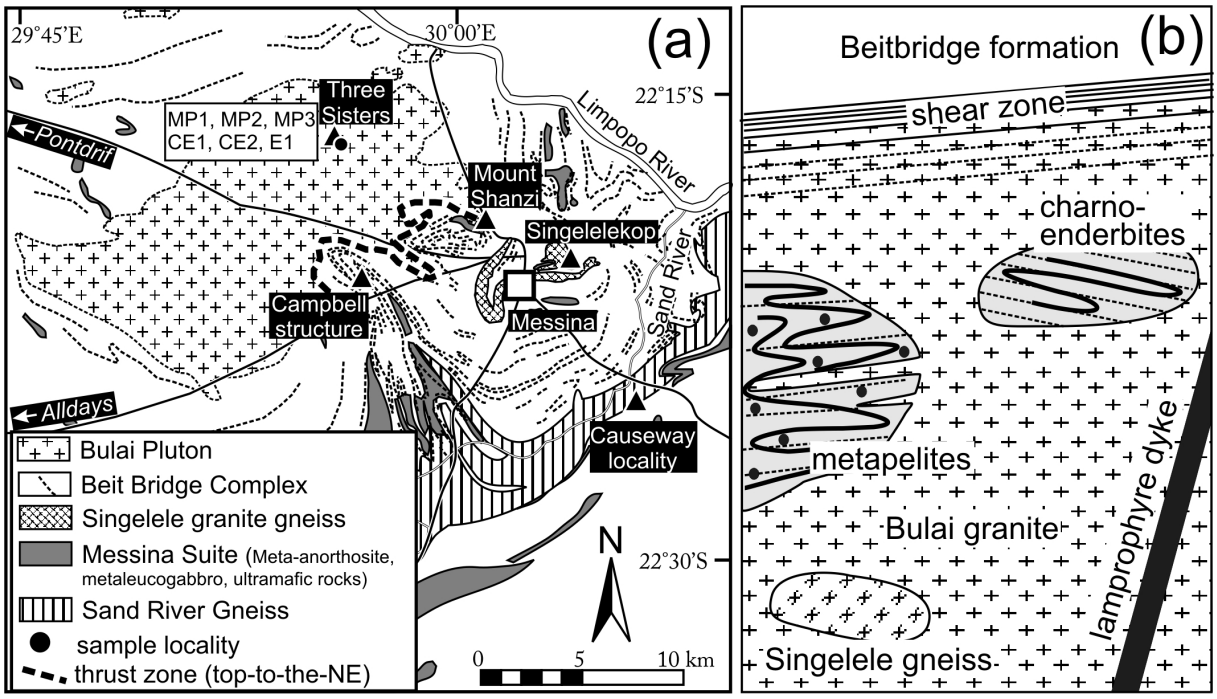

Fig. 44. a) geological map of the study area and sample localities (modified after Horrocks, 1983 and Brandl & Pretorius, 2000). b) synopsis of field relationships observed in the Bulai Pluton area (for further information see text).

Xenoliths of the Singelele-type granite gneiss within the Bulai Pluton (Fig. 45e) indicate that the Bulai granite intruded later than 2646±10 Ma. This age was obtained by U-Pb LA-ICP-MS dating of zircon grains from a similar Singelele-type granite gneiss taken from the Singelelekop near Messina (Zeh *et al.,* 2007). It is identical - within error- to an U-Pb zircon SHRIMP age of 2651±8 obtained from a penetratively deformed Singelele-type gneiss sample from the Avoca structure west of the Bulai Pluton (unpublished

data of Boshoff, 2004: cited in Van Reenen *et al.*, 2004).

The Bulai Pluton is transected by alkaline lamprophyric dykes, which yield Neoarchean Rb-Sr and Pb-Pb whole rock ages of 2671±163 Ma and 2641 +125/-131 Ma, respectively, and a $^{87}Sr/^{86}Sr$-initial ratio of 0.7023 (Watkeys & Armstrong, 1985). These dykes are interpreted by Watkeys & Armstrong (1985; p. 204) to have "*intruded during a rifting event*", and "*may have been derived from a near primitive magma …, which was generated by partial melting of the upper mantle beneath continental crust*". Field relationships indicate that parts of the Bulai granite were slightly deformed prior to the intrusion of the lamprophyre dykes (Watkeys & Armstrong, 1985), and that both the Bulai Pluton and the lamprophyre dykes subsequently underwent a common structural-(metamorphic) overprint, which was interpreted as "*the final phase of regional folding, which affected the Limpopo's Central Zone*" (*cf.* Watkeys & Armstrong, 1985). Based on combined structural-geochronological investigations Holzer *et al.* (1998) showed that this final phase of "regional folding" occurred during the Palaeoproterozoic at *ca.* 2.02 Ga. The post-intrusive deformation of the Bulai Pluton is also documented by numerous mylonitic shear zones (Fig. 45f), *i.e.* the miniature mobile shear belts of Watkeys (1984).

Field relationships also indicate that the Bulai Pluton has a tectonic contact with the Palaeoproterozoic high-grade metamorphic metasediments of the Beitbridge Complex. Tectonic contacts are described by Holzer *et al.* (1998) from Mount Shanzi (=Ha-Tshansi of Van Reenen *et al.,* 2004) and from the Campbell fold, which both occur west of Messina (Fig. 44). At Mount Shanzi, the porphyric Bulai granite grades continuously into a highly deformed gneiss, which finally "merges" into a migmatitic zone "contaminated" with supracrustal rocks. This migmatitic zone is overtopped by supracrustal quartzo-feldspathic gneisses and magnetite quartzites (Watkeys, 1984; Holzer *et al.*, 1998). Geochronological data of Holzer *et al.* (1998) indicate that the tectonic contact (high-grade ductile shear zone) was formed during the Palaeoproterozoic at about 2.01 Ga. Shear sense indicators additionally provide evidence that the structures observed at Mount Shanzi result from top-to-the-ENE directed thrusting of the overlying supracrustal Beitbridge lithologies including the Ha-Tshansi (Shanzi) sheath fold.

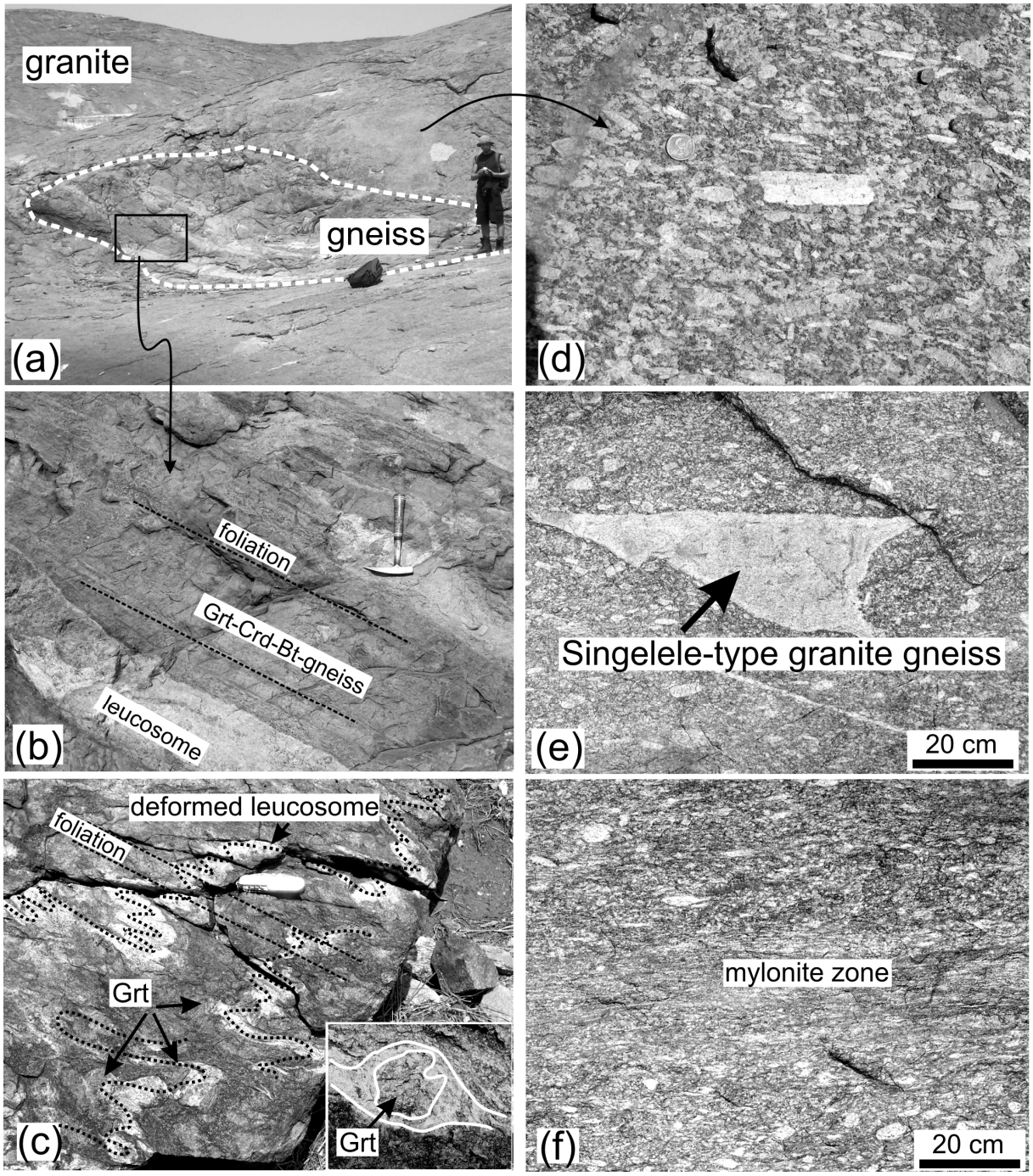

Fig. 45. Field relationships at the Three Sisters area. (a) Gneiss xenoliths in the Bulai granite; (b) Strongly foliated garnet-cordierite-biotite gneiss and leucosomes in the enclave shown in (a), (c) Isoclinal folded garnet bearing leucosome in a pelitic gneiss intruded by the Bulai granite *ca.* 300 m east of the Three Sisters, inset: Garnet prophyroblast surrounded by leucosome, (d) Weakly deformed porphyric Bulai granite with angular K-feldspars crystals from beside the gneiss enclave shown in (a), (e) Xenolith of a Singelele-type granite gneiss surrounded by porphyric Bulai granite. (f) Mylonite shear zone within the Bulai granite showing a gradual increase of deformation towards the centre.

17 Petrography, Bulk Rock and Mineral Chemistry

17.1 Analytical techniques

Mineral compositions were obtained using a Cameca SX-50 electron microprobe at the Mineralogical Institute, University of Würzburg, with three independent wavelength-dispersive crystal channels. Instrument conditions were 15 kV acceleration voltage, 15 nA specimen current, and 20 s integration time for all elements except for Fe (30 sec). Natural and synthetic silicates and oxides were used for reference, and matrix corrections were carried out by the PAP program, supplied by CAMECA. Point analyses were performed with a 30 µm beam diameter for perthitic K-feldspar, and a 1 µm beam diameter for all other minerals. In order to obtain the K-feldspar composition prior to exsolution of the albite-rich lamellae, 10-30 analyses obtained from a K-feldspar grain were integrated.

Bulk rock compositions, used for *P-T* pseudosection calculations, were determined on thin section blocks of 3 x 2 x 0.5 cm size. These blocks are representative for the investigated rock samples, since garnet porphyroblasts and matrix minerals within these samples are usually much smaller than the thick section volume. The analyses were carried out by conventional X-ray fluorescence spectrometry using a Philips PW 1480 spectrometer (Mineralogical Institute, University of Würzburg) and lithium tetraborate fusion disks. The water content, used for the *P-T* pseudosection calculations (Tab. 16) was estimated by loss on ignition (LOI), assuming neglectable amounts of additional volatiles (*e.g.* Cl and F).

17.2 Sample Description

In this study six samples from four xenoliths (up to 10 m diameter) in the Bulai Granite at the Three Sisters area (Fig. 1 and Fig. 44) are investigated. These comprise three metapelitic rocks, two charnoenderbitic gneisses and one enderbitic gneiss. The sample co-ordinates, bulk compositions, chemical indices (X_{Fe}, Al^{k}, K^{x} - see captions of Tab. 16), mineral assemblages and mineral compositions observed in the respective samples are shown in Tab. 17 and Tab. 18. All samples show intermediate X_{Fe} of 0.46-0.56, but distinct Al^{k} values, which are highest in the metapelitic samples (0.38-0.41), intermediate in the charnoenderbite samples (0.25) and lowest in the enderbite sample (0.17). These compositional differences are well reflected by different mineral assemblages (Tab. 16). Additional mineral analyses can be found in the electronical appendix 24 - Supplementary mineral data.

Tab. 16. Sample co-ordinates, mineral assemblages, *XRF*-analyses and compositional parameters Fx, Kx, Alx of the investigated samples (mineral abbreviations after Kretz, 1983)

Sample	MP1	MP2	MP3	CE1	CE2	E1
Lattitude(°S)	22°16′086	22°16′060	22°15′900	22°15′836	22°15′781	22°15′782
Longitude(°E)	29°55′661	29°55′661	29°55′429	29°55′147	29°55′174	29°55′167
Assemblage	Grt–Bt–Sil–Crd–Pl–Kfs–Qtz–Rt–Ilm–Hrc–melt	Grt–Bt–Sil–Crd–Pl–Qtz–Rt–Hrc–melt	Grt–Bt–Sil–Crd–Pl–Kfs–Qtz–Ilm–Rt–Hrc–melt	Grt–Bt–Pl–Kfs–Opx–Qtz–Rt–Ilm–melt	Grt–Bt–Pl–Kfs–Opx–melt	Bt–Pl–Opx–Qtz–melt
XRF-analyses	wt.%	wt.%	wt.%	wt.%	wt.%	wt.%
SiO_2	51.1	54.7	54.1	66.6	56.0	76.3
TiO_2	0.9	0.8	0.8	0.6	0.7	0.3
Al_2O_3	22.3	21.5	22.9	13.7	16.8	7.7
FeO^{tot}	13.0	12.0	10.7	8.2	15.5	5.8
MnO	0.3	0.2	0.1	0.1	0.3	0.1
MgO	5.2	5.1	6.3	4.0	6.3	3.4
CaO	0.8	1.0	0.4	1.2	1.1	1.2
Na_2O	1.6	1.2	0.8	2.7	1.7	1.4
K_2O	3.4	2.0	1.9	1.9	2.4	2.8
P_2O_5	0.1	0.1	0.0	0.0	0.0	0.1
LOI	1.1	1.0	1.3	0.8	0.8	0.4
Total	99.7	99.4	99.5	99.9	100.6	99.3
F^x	0.56	0.54	0.46	0.51	0.55	0.46
Al^x	0.38	0.38	0.41	0.25	0.25	0.17
K^x	0.48	0.37	0.49	0.23	0.36	0.40

$K^x = K_2O/(K_2O+Na_2O+CaO)$, $F^x = FeO/(FeO+MgO)$, $Al^x = Al^{Plfree}/(Al^{Plfree}+FeO+MgO+MnO)$, $Al^{Plfree} = Al_2O_3 - CaO - Na_2O$ = free Al_2O_3 available for KFMASH reactions, if all CaO and Na_2O is contained in plagioclase. The parameters F^x, K^x, Al^x are calculated from bulk rock analyses (mole proportions).

Tab. 17. Mineral composition of plagioclase (Pl), K-feldspar (Kfs), garnet (Grt), biotite (Bt), cordierite (Crd) and orthopyroxene (Opx)

Sample	MP1	MP2	MP3	CE1	CE2	E1
Pl						
(in Grt)	$Ab_{77}An_{22}Or_1$	$Ab_{61}An_{38-39}Or_{0-1}$	$Ab_{71-78}An_{21-27}Or_{1-2}$	$Ab_{80}An_{17}Or_3$	$Ab_{81}An_{18}Or_{0.6}$	$Ab_{65}An_{33}Or_2$
(in Mx)	$Ab_{76}An_{21-22}Or_{1-2}$	$Ab_{68}An_{31}Or_1$	$Ab_{80-81}An_{18}Or_{1-2}$	$Ab_{80}An_{18}Or_2$	$Ab_{78}An_{19}Or_3$	
Kfs						
(in Mx)	$Ab_{24}An_2Or_{74}$	–	$Ab_{37}An_2Or_{61}$	$Ab_{43}An_7Or_{50}$, (Mx)	$Ab_{42}An_7Or_{51}$	–
(in Grt)	$Ab_{24}An_2Or_{74}$					
*Grt**						
X_{Fe}	0.63	0.66	0.57	0.59	0.61	–
X_{alm}	0.61	0.61	0.54	0.57	0.58	–
X_{prp}	0.35	0.32	0.42	0.40	0.38	–
X_{grs}	0.02	0.03	0.03	0.02	0.03	–
X_{spss}	0.02	0.04	0.01	0.01	0.01	–
Bt						
X_{Fe}	0.29–0.40	0.35–0.52	0.22–0.38	0.22–0.32	0.29–0.32	0.34–0.40
Ti^{IV}(p)	0.39–0.76	0.29–0.70	0.20–0.67	0.52–0.70	0.62–0.71	0.51–0.71
Al^{VI}(p)	0.12–0.50	0.34–0.52	0.10–0.39	0.07–0.20	0.05–0.15	0.01–0.12
Al^{tot}(p)	2.73–3.02	3.0–3.3	2.69–2.88	2.64–2.79	2.64–2.79	2.41–2.61
Crd						
X_{Fe}	0.21–0.24	0.28–0.32	0.22–0.23	–	–	–
Na(p)	0.011–0.025	0.010–0.038	0.017–0.036	–	–	–
Opx						
X_{Fe}	–	–	–	pseudomorph	0.36–0.37	0.403–0.419
Al^{tot} (p)	–	–	–		0.242–0.256	0.077–0.097

* Grt—garnet core composition, (in Grt) enclosed in garnet, (in Mx) — matrix, Ab = Na/(Na+Ca+K)*100, An = Ca/(Na+Ca+K)*100, Or = K/(Na+Ca+K)*100; X_{Fe} = Fe/(Fe+Mg), X_{alm} = Fe/(Fe+Mg+Mn+Ca), X_{prp} = Mg/(Fe+Mg+Mn+Ca), X_{grs} = Ca/(Fe+Mg+Mn+Ca), X_{spss} = (Fe/(Fe+Mg+Mn+Ca), (p) — atoms per formula unit.

Tab. 18. Representative mineral analyses

Sample	MP1					MP2				MP3					CE1					CE2					E1		
Mineral domain	Grt	Crd	Bt	Pl	Kfs	Grt	Crd	Bt	Pl	Grt	Crd	Bt	Pl	Kfs	Grt	Bt	Pl	Kfs	Ilm	Grt	Bt	Pl	Kfs	Opx	Bt	Pl	Opx
	Core	Mx	Mx	Mx	Mx	Core	Mx	Mx	Mx	Core	Mx	Mx	Mx	Mx	Core	Mx	Mx	Mx	Mx	Core	Mx	Mx	Mx	Mx	Mx	Mx	Mx
SiO_2	38.71	49.32	36.42	62.43	63.65	37.71	48.56	35.73	60.42	39.24	48.79	37.08	62.75	63.98	38.71	36.46	62.98	64.34	0.00	38.40	36.88	63.46	64.21	48.67	36.39	59.61	50.55
TiO_2	0.00	0.01	5.91	0.00	0.00	0.03	0.00	4.03	0.00	0.03	0.00	5.59	0.00	0.00	0.01	5.09	0.00	0.00	50.64	0.06	5.91	0.00	0.00	0.12	4.91	0.00	0.11
Al_2O_3	21.80	33.60	15.99	22.91	18.89	21.86	33.36	17.79	24.62	22.11	33.06	15.46	22.31	19.01	21.76	15.40	22.00	19.77	0.44	22.06	15.63	22.13	20.06	5.49	14.19	24.94	2.01
Cr_2O_3	0.18	0.00	0.14	0.00	0.00	0.01	0.00	0.23	0.00	0.17	0.00	0.39	0.00	0.00	0.15	0.35	0.00	0.00	0.26	0.04	0.19	0.00	0.00	0.14	0.17	0.00	0.03
Fe_2O_3	1.45	0.00	0.00	0.04	0.06	1.79	0.00	0.00	0.00	1.19	0.00	0.00	0.01	0.16	1.34	0.00	0.06	0.00	3.69	2.01	0.00	0.49	0.08	3.61	0.00	0.63	3.16
FeO	27.55	4.92	14.99	0.00	0.00	26.91	6.81	20.13	0.00	24.97	5.43	11.35	0.00	0.00	26.04	11.97	0.00	0.20	43.43	26.07	12.11	0.00	0.00	21.00	15.46	0.00	22.45
MnO	0.88	0.04	0.03	0.00	0.00	1.76	0.06	0.06	0.00	0.46	0.01	0.00	0.00	0.00	0.39	0.00	0.00	0.00	1.03	0.57	0.00	0.00	0.00	0.18	0.08	0.00	0.90
MgO	9.35	10.32	12.55	0.00	0.00	8.30	9.55	10.92	0.00	11.26	10.25	15.64	0.00	0.13	10.48	16.06	0.00	0.01	0.60	10.18	15.16	0.00	0.07	20.65	14.40	0.16	20.45
CaO	0.93	0.03	0.00	4.29	0.30	1.28	0.02	0.01	6.26	1.13	0.00	0.00	3.73	0.42	0.92	0.02	3.50	1.39	0.00	0.92	0.12	3.28	1.19	0.10	0.01	6.66	0.33
Na_2O	0.00	0.08	0.08	9.15	2.19	0.00	0.12	0.17	7.96	0.00	0.11	0.08	9.27	4.15	0.00	0.09	9.20	4.88	0.00	0.00	0.00	8.79	4.24	0.04	0.01	7.59	0.06
K_2O	0.00	0.02	9.51	0.26	13.10	0.00	0.00	9.33	0.23	0.00	0.01	9.18	0.24	10.21	0.00	9.66	0.25	8.72	0.00	0.00	9.70	1.60	9.73	0.00	9.75	0.20	0.02
Totals	100.84	98.34	95.61	99.08	98.19	99.65	98.49	98.40	99.49	100.55	97.65	94.77	98.31	98.05	99.80	95.09	98.00	99.30	100.10	100.31	95.70	99.75	99.58	99.99	95.36	99.79	100.05
Oxygen	12	18	22	8	8	12	18	22	8	12	18	22	8	8	12	18	22	8	3	12	18	22	8	6	18	22	6
Si	2.97	4.99	5.43	2.79	2.97	2.94	4.96	5.35	2.70	2.97	4.99	5.47	2.82	2.96	2.97	5.40	2.83	2.93	0.00	2.94	5.43	2.83	2.91	1.82	5.48	2.67	1.91
Ti	0.00	0.00	0.66	0.00	0.00	0.00	0.00	0.45	0.00	0.00	0.00	0.62	0.00	0.00	0.00	0.57	0.00	0.00	0.96	0.00	0.65	0.00	0.00	0.00	0.56	0.00	0.00
Al	1.97	4.01	2.81	1.21	1.04	2.01	4.01	3.14	1.30	1.97	3.98	2.69	1.18	1.04	1.97	2.69	1.17	1.06	0.01	1.99	2.71	1.16	1.09	0.24	2.52	1.31	0.09
Cr	0.01	0.00	0.02	0.00	0.00	0.00	0.00	0.03	0.00	0.01	0.00	0.05	0.00	0.00	0.01	0.04	0.00	0.00	0.01	0.00	0.02	0.00	0.00	0.00	0.02	0.00	0.00
Fe^{3+}	0.08	0.00	0.00	0.00	0.00	0.11	0.00	0.00	0.00	0.07	0.00	0.00	0.00	0.01	0.08	0.00	0.00	0.01	0.07	0.12	0.00	0.02	0.00	0.10	0.00	0.02	0.09
Fe^{2+}	1.77	0.42	1.87	0.00	0.00	1.75	0.58	2.52	0.00	1.58	0.46	1.40	0.00	0.00	1.67	1.48	0.00	0.00	0.91	1.67	1.49	0.00	0.00	0.66	1.95	0.00	0.71
Mn	0.06	0.00	0.00	0.00	0.00	0.12	0.01	0.01	0.00	0.03	0.00	0.00	0.00	0.00	0.03	0.00	0.00	0.00	0.02	0.04	0.00	0.00	0.00	0.01	0.01	0.00	0.03
Mg	1.07	1.56	2.79	0.00	0.00	0.97	1.45	2.44	0.00	1.27	1.56	3.44	0.00	0.01	1.20	3.55	0.00	0.00	0.02	1.16	3.32	0.00	0.00	1.15	3.23	0.01	1.15
Ca	0.08	0.00	0.00	0.21	0.01	0.11	0.00	0.00	0.30	0.09	0.00	0.00	0.18	0.02	0.08	0.00	0.17	0.07	0.00	0.08	0.02	0.16	0.07	0.00	0.00	0.32	0.01
Na	0.00	0.02	0.02	0.79	0.20	0.00	0.02	0.05	0.70	0.00	0.02	0.02	0.81	0.37	0.00	0.03	0.80	0.43	0.00	0.00	0.00	0.76	0.42	0.00	0.00	0.66	0.00
K	0.00	0.00	1.81	0.01	0.78	0.00	0.00	1.78	0.01	0.00	0.00	1.73	0.01	0.60	0.00	1.83	0.01	0.51	0.00	0.00	1.82	0.09	0.51	0.00	1.87	0.01	0.00
Sum	8.00	11.00	15.41	5.01	5.00	8.00	11.04	15.78	5.00	8.00	11.02	15.41	5.00	5.00	8.00	15.59	5.00	5.01	2.01	8.00	15.47	5.01	5.00	4.00	15.63	5.00	4.00
X_{Fe}	0.63	0.21	0.40			0.66	0.29	0.51		0.56	0.23	0.29			0.59	0.30			0.98	0.61	0.31			0.40	0.38		0.41
X_{alm}	0.61					0.61				0.54					0.57					0.58							
X_{prp}	0.35					0.32				0.42					0.39					0.38							
X_{grs}	0.02					0.03				0.03					0.02					0.02							
X_{sps}	0.02					0.04				0.01					0.01					0.01							
X_{an}			0.20	0.02				0.29				0.18	0.02			0.17	0.07				0.16	0.07			0.32		
X_{or}			0.01	0.79				0.01				0.01	0.61			0.01	0.50				0.09	0.51			0.01		

$X_{Fe}=Fe/(Fe+Mg)$, $X_{alm}=Fe/(Fe+Mg+Ca+Mn)$, $X_{prp}=Mg/(Fe+Mg+Ca+Mn)$, $X_{grs}=Ca/(Fe+Mg+Ca+Mn)$, $X_{spss}=Mn/(Fe+Mg+Ca+Mn)$, $X_{an}=Ca/(Ca+Na+K)$, $X_{or}=K/(Ca+Na+K)$.

17.2.1 Metapelitic rocks (MP1, MP2, MP3)

All three metapelitic rocks are foliated and contain garnet, cordierite, biotite, sillimanite, plagioclase, hercynite, quartz and rutile. Samples MP1 and MP3 additionally have ilmenite and K-feldspar, which abundantly occurs in sample MP1 (inclusions in garnet and in the matrix) but forms a minor matrix phase in sample MP3 (Tab. 16). All samples contain up to 7 mm large garnet porphyroblasts (Fig. 46, 47), which commonly enclose biotite, sillimanite, quartz, rare plagioclase and K-feldspar (only sample MP1; Fig. 47). The garnet porphyroblasts in all samples are commonly surrounded by reaction rims of cordierite, sillimanite, biotite, plagioclase and ilmenite (Fig. 47a). Hercynite is observed only in cordierite reaction zones separated from quartz. Rare cordierite rims around garnet are relatively thin in sample MP1, but thick and common in samples MP2 and MP3 indicating that the original garnet textures in the respective samples were transformed with different intensities during retrograde cordierite-forming reactions.

Garnet in all samples has low spessartine and grossular components and shows retrograde zoning patterns, as reflected by increasing X_{Fe} [$Fe^{2+}/(Fe^{2+}+Mg)$] from garnet cores to rims (Fig. 46). Some garnet cores represent compositional plateaus, assumed to reflect the garnet composition at the metamorphic peak. Compositional differences between garnet cores from different samples may reflect different bulk compositions (Tab. 17). The same holds true for cordierite and biotite. Variations of X_{Fe}, Al^{VI}, Ti^{VI} of biotite of the respective samples (Tab. 17) indicate incomplete equilibration on a thin section scale, probably caused by the different degrees of a domainal retrograde overprint. For example, biotite flakes enclosed by garnet show higher X_{Fe} when compared to biotite enclosed by matrix cordierite and plagioclase.

In all metapelitic samples tiny bands of plagioclase and/or K-feldspar were observed, which mostly occur between resorbed quartz inclusions and host garnet (Fig. 47c, d), and/or between quartz and host cordierite (Fig. 47b). In samples MP2 and MP3, these bands only consist of albitic plagioclase, whereas in sample MP1 K-feldspar and albitic plagioclase occur together (Fig. 47c, Tab. 17). Locally such feldspar "rims" also occur along quartz grain boundaries, in particular at triple point junctions. These feldspar bands are interpreted to represent crystallised melts accumulated between partly dissolved quartz and the surrounding host minerals. This conclusion conforms with observations of Holness & Clemens (1999) and Harris *et al.* (2003), who interpreted similarly rounded/resorbed quartz grains in contact with feldspar to reflect quartz-melt relationships (see also Sawyer, 1999). Apart from these petrographic observations, melt formation in the metapelitic garnet-cordierite-sillimanite gneisses from the Three Sisters area is supported by macroscopic observations as well as field relationships showing that garnet (±cordierite)

porphyroblasts are surrounded by biotite-free leucosomes (Fig. 45c, inset). Such textures suggest that both garnet and melt were formed during a biotite-consuming hydrate breakdown melting reaction (Le Breton & Thompson, 1988; Vielzeuf & Schmidt, 2001), which, for example, can be described by the univariant KFMASH (K_2O-FeO-MgO-Al_2O_3-SiO_2-H_2O) reaction: Bt + Sill + Qtz = Grt + Crd + Kfs + Liq., and/or the divariant equilibria that emanate from it (e.g. Stevens *et al.*, 1997; White *et al.*, 2001). In a more complex component system (e.g. CaO-Na_2O-K_2O-TiO_2-MnO-FeO-MgO-Al_2O_3-SiO_2-H_2O = CNKTiMnFMASH) this reaction becomes multivariant (e.g White *et al.*, 2001, 2003; Zeh *et al.*, 2004b). Thus the formation of melt and garnet (±cordierite), and the consumption of biotite will take place over a certain *P-T* interval, and additional phases like plagioclase and rutile/ilmenite may occur (see section *P-T* pseudosections).

The composition of feldspar inclusions in garnet/cordierite is commonly similar to feldspar in the matrix of the respective samples (Tab. 17). However, there are some plagioclase inclusions in garnet and matrix plagioclase that have higher anorthite components (Tab. 17). Rutile is almost always pure TiO_2, whereas ilmenite forms solid solutions dominated by the ilmenite component (90-96%), with minor hematite (2-10%) and pyrophanite (1 %) components.

From the observed textures, i.e. mineral inclusions in garnet, and the micro- and macroscopic observations of melts (leucosomes) we conclude that garnet in the metapelitic samples was initially formed in the assemblages (Fig. 47):

A1a: Grt-Bt-Sill-Pl-Qtz-Rt-melt (sample MP2 & MP3?)

A1b: Grt-Bt-Sill-Pl-Kfs-Qtz-Rt-melt (sample MP1)

Subsequently, garnet resorption occurred during the formation of the cordierite assemblages:

A2a: Grt-Bt-Crd-Sill-Pl-Qtz-Ilm-Rt-melt (sample MP2)

A2b: Grt-Bt-Crd-Sill-Pl-Kfs-Qtz-Ilm-(Rt)-melt (sample MP1 & MP3)

Finally, melt crystallisation led to the formation of the subsolidus assemblages:

A3a: Grt-Bt-Crd-Sill-Pl-Qtz-Ilm-Rt (sample MP2)

A3b: Grt-Bt-Crd-Sill-Pl-Kfs-Qtz-Ilm-(Rt) (sample MP1 & MP3)

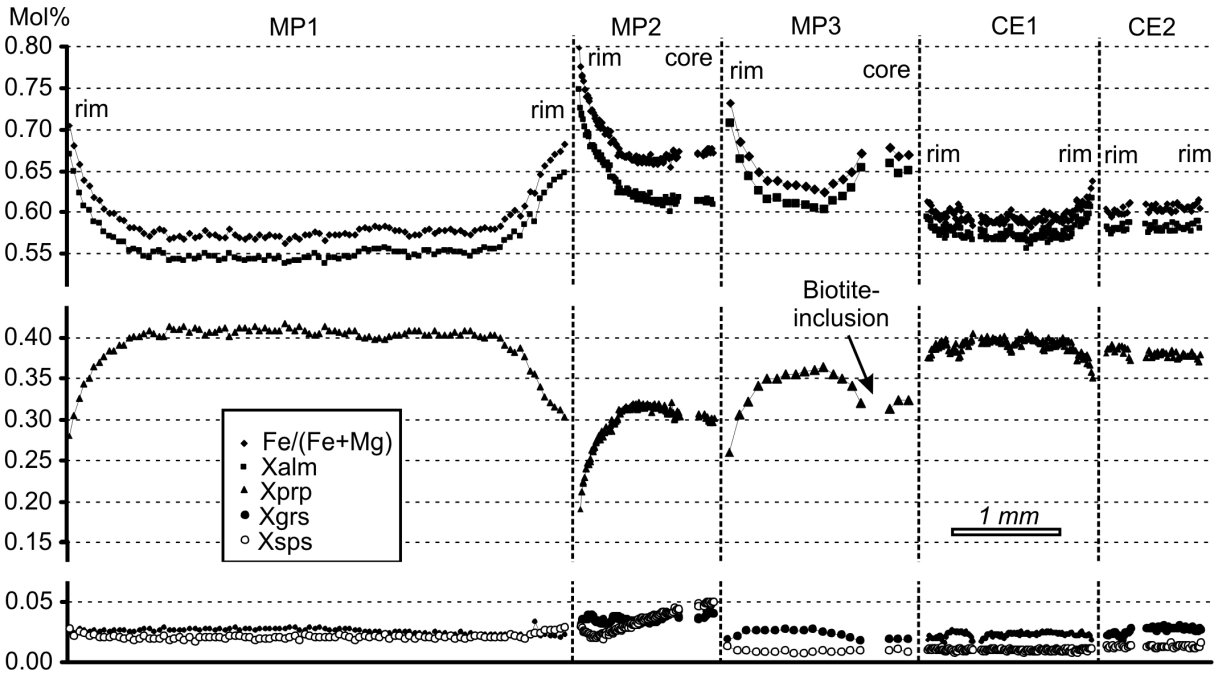

Fig. 46. Zoning patterns of garnet observed in the metapelitic samples MP1 to MP3 and in the charnoenderbitic samples CE1 and CE2.

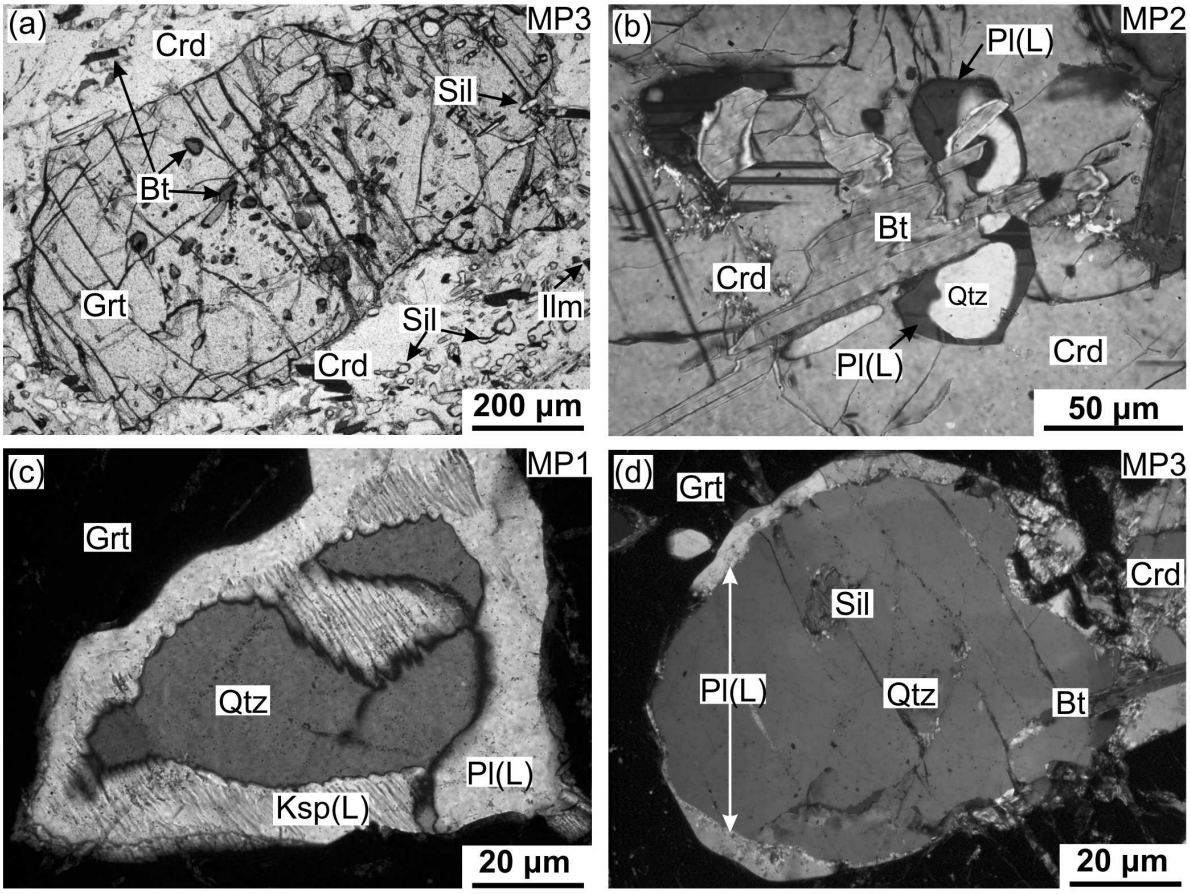

Fig. 47. Photomicrographs of characteristic features observed in the metapelitic samples MP1 to MP3. (a) Garnet porphyroblast (Grt) with biotite (Bt) and sillimanite (Sil) inclusions is surrounded by a reaction rim of cordierite (Crd), sillimanite, biotite and ilmenite (Ilm). PPL. (b) Cordierite of a reaction rim contains biotite and quartz (Qtz) inclusions. The quartz inclusions appear resorbed and are always surrounded by a plagioclase rim [Pl(L)], which is assumed to represent crystallised melt. CPL. (c) Resorbed quartz inclusion in garnet, surrounded by a band of perthitic K-feldspar [Ksp (L)] and plagioclase [Pl(L)], which both are assumed to be formed during melt crystallisation. CPL. (d) Garnet in contact with biotite and cordierite contains quartz with

sillimanite inclusions. The plagioclase band between quartz and garnet is assumed to represent crystallized melt. CPL.. For further explanation see text.

17.2.2 Charnoenderbite (CE1 & CE2)

The two charnoenderbite are foliated and contain garnet, orthopyroxene, biotite, perthitic K-feldspar, plagioclase and quartz. Sample CE1 additionally contains rutile, ilmenite and monazite. Monazite forms inclusions in garnet and occurs in the matrix (Fig. 48a). In both samples garnet shows unzoned cores, and in sample CE1 a retrograde zoning, which is characterized by increasing X_{Fe} toward the garnet rims (Fig. 46). Garnet in both samples contains abundant quartz and biotite inclusions, and shows typical feldspar bands between resorbed quartz and host garnet (Fig. 48a). The latter textures are similar to those observed in the metapelitic rocks, and are interpreted to represent relics of solidified melts available during garnet formation in both samples. These bands commonly contain perthitic K-feldspar in contact with albitic plagioclase (similar to that in Fig. 47c). Integrated K-feldspar analyses from sample CE1 reveal a mesoperthitic composition of $Or_{50}Ab_{43}An_7$, which is expressed by the end-members orthoclase [Or = K/(K+Na+Ca)], albite [Ab = Na/(K+Na+Ca)], and anorthite [An = Ca/(K+Na+Ca)]. Coexisting plagioclase from the same band has the composition $Ab_{80}An_{17}Or_3$. K-feldspar and plagioclase from bands in sample CE2 show a similar composition (Tab. 17).

Orthopyroxene of sample CE2 appears unaltered and is commonly intergrown with or rimmed by biotite (Fig. 48b), whereas in sample CE1 it forms fine-grained, brown pseudomorphs. Orthopyroxene of sample CE2 has X_{Fe} of 0.36-0.37 and low Al^{tot} of 0.24-0.26 *p.f.u.* (Tab. 17). Biotite in both samples shows similar Al^{tot} (2.64-2.79 *p.f.u.*) and Ti^{VI} (0.52-0.71 *p.f.u.*), and variable X_{Fe} ratios, in particular in sample CE1 (0.22-0.32), which may indicate a compositional disequilibrium at the thin section scale. Rutile in sample CE1 is almost pure TiO_2 and ilmenite forms solid solutions dominated by the ilmenite component (87-92%), with minor hematite (3-4%) and pyrophanite (3-6 %) components.

From the observed textural relationships we conclude that the following assemblages were successively formed in the charnoenderbite samples:

B1a: Grt+Opx+Bt+Pl+Kfs+Rt+melt (sample CE1)

B1b: Grt+Opx+Bt+Pl+Kfs+melt (sample CE2)

B2a: Grt+Opx+Bt+Pl+Kfs(perthite)+ (Rt)+Ilm (sample CE1)

B2b: Grt+Opx+Bt+Pl+Kfs(perthite) (sample CE2)

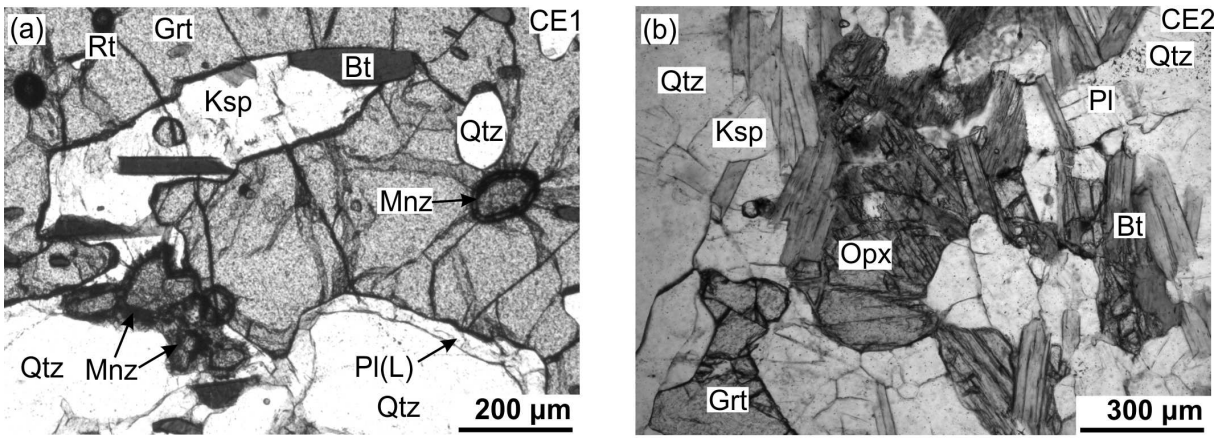

Fig. 48. Photomicrographs of the charnoenderbitic samples CE1 and CE2. (a) Garnet porphyroblast with inclusions of monazite (Mnz), quartz (Qtz), biotite (Bt), rutile (Rt), and K-feldspar (Kfs), is surrounded by a matrix of quartz, biotite, monazite and plagioclase [Pl(L)]. The latter forms a band between quartz and garnet and is assumed to result from melt crystallisation. PPL. (b) Garnet and orthopyroxene (Opx) in assemblage with quartz, K-feldspar and plagioclase. PPL.

17.2.3 Enderbite (E1)

This sample has a granular texture with angular orthopyroxene, which occurs in a matrix of biotite, plagioclase and quartz. These orthopyroxenes show higher X_{Fe} and lower Al^{tot} contents than those of the charnoenderbitic samples (Tab. 17). The same holds true for biotite, and is interpreted to reflect the distinct bulk composition. Plagioclase is unzoned and has the composition $Ab_{66}An_{33}Or_1$. In contrast to the samples discussed above, there are no textures that provide unambiguous evidence for the presence of melt in sample E1. Thus, it is unclear whether the peak metamorphic assemblage was:

C1: Opx+Bt+Pl+Qtz+melt , or

C2: Opx+Bt+Pl+Qtz

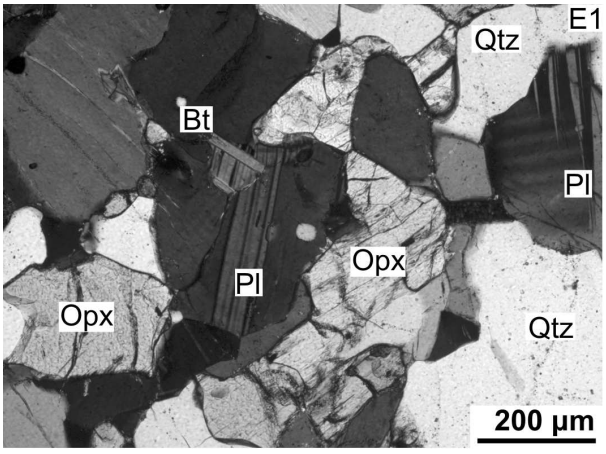

Fig. 49. Photomicrograph of the enderbitic sample E1. Orthopyroxene in assemblage with biotite, plagioclase and quartz. CPL.

18 *P-T* Path Constraints

P-T path information from the investigated metamorphic rocks was obtained by quantitative phase diagrams (*P-T* pseudosections), which were calculated in the model system CNKTiMnFMASH (Fig. 50a-e). However, the rutile-ilmenite-garnet free sample E1 was calculated in the system CNKFMASH (Fig. 50f). Calculations were carried out with the computer software **THERMOCALC** v.3.21 using the thermodynamic dataset HP98 (Powell & Holland, 1988; Holland & Powell, 1990; 1998), and employing the procedures and activity-composition relationships outlined by Mahar *et al.* (1997), White *et al.* (2000, 2001), and combined by Zeh & Holness (2003). The absence of magnetite and the nearly pure end-member composition of ilmenite provide evidence that the oxygen fugacity must have been low throughout the *P-T* evolution of the investigated rocks. Therefore, oxygen as an additional component was not considered (see White *et al.,* 2002).

Comparison between the calculated and observed mineral assemblages indicates that the assemblages A1 to A3, as inferred from the respective metapelitic samples MP1-MP3, were formed along a retrograde *P-T* path from 800-830°C/8-10 kbar to 750°C/5-6 kbar (Fig. 50a-c). The upper and lower temperature limit is defined by the K-feldspar-bearing assemblage A1b, as observed in sample MP1 (Fig. 50a), and by the K-feldspar free assemblage A1a, as observed in sample MP2 (Fig. 50b). However, even though there is agreement between observed and calculated assemblages it should be noted that some of the calculated assemblage boundaries are sensitive to the modelled water content (*e.g.* White *et al.*, 2001), an effect that is also well known from melting experiments (see Gardien *et al.*, 2000; Castro *et al.*, 2000; Koester *et al.*, 2002). Therefore, the boundary between the Kfs-free (Grt-Bt-Rt-Sill-Liq-Qtz-Pl) and Kfs-bearing (Grt-Bt-Rt-Sill-Kfs-Liq-Qtz-Pl) phase fields in the *P-T* pseudosection for sample MP2 would shift towards higher temperatures with increasing H_2O content (see Fig. 50b).

The lower pressure limit of 8 kbar at the metamorphic peak is constrained by the cordierite-free assemblage A1a, as observed in sample MP3 (Fig. 50c), and the upper pressure limit of about 10 kbar is constrained by the occurrence of sillimanite (assemblages A1a and A1b). The retrograde *P-T* path is constrained by the formation of sillimanite-biotite-bearing cordierite rims (+melt) around garnet (assemblage A2a, A2b) and finally by melt crystallization leading to the assemblages A3a/b. In agreement with the textural observations, garnet is resorbed, and cordierite, biotite, sillimanite and plagioclase formed along the retrograde *P-T* paths (Fig. 50a-c).

The peak temperatures obtained from the metapelitic samples are slightly lower compared to those inferred for the charnoenderbitic rock

samples CE1 and CE2, and the enderbitic sample E1. The observed mineral assemblage B1a requires temperatures of about 860°C at 8 kbar (Fig. 50d), whereas the assemblage E1a/b is stable over a wide *P-T* stability field (Fig. 50f). The absence of garnet in the enderbite sample E1 sets an upper pressure limit for the metamorphic peak at about 8.5-9.5 kbar at 800-860°C. The higher peak temperatures of the charnoenderbite gneiss samples suggest that the gneiss protolith perhaps was a magmatic rock that cooled and crystallized above the stability limit of cordierite (<6-7 kbar; Fig. 50d, e).

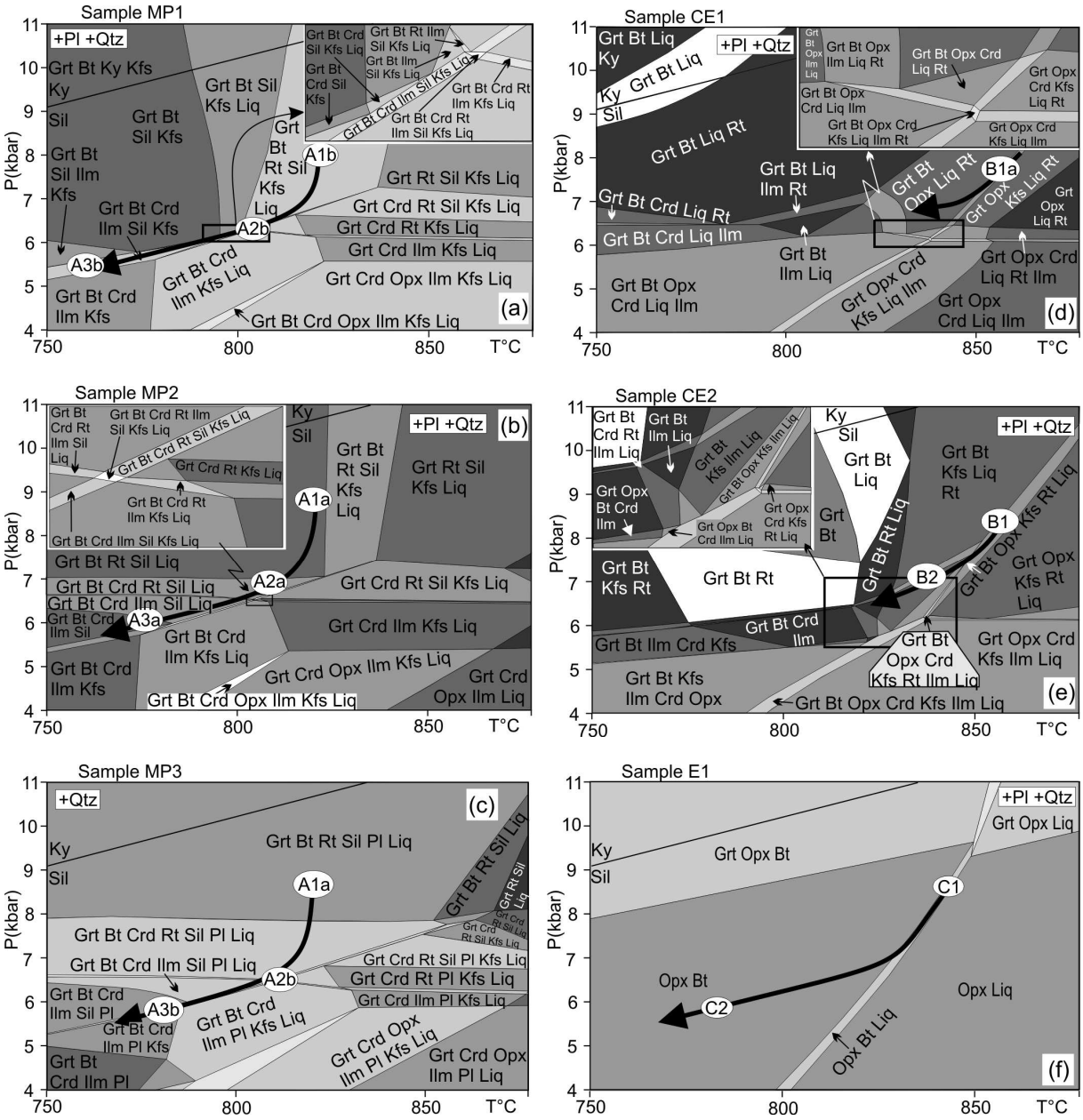

Fig. 50. *P-T* pseudosections calculated in the model system CaO-Na_2O-K_2O-TiO_2-MnO-FeO-MgO-Al_2O_3-SiO_2-H_2O for the metapelitic samples MP1-MP3 (a-c), and the charnoenderbitic samples CE1 and CE2 (d-e), and in the model system CaO-Na_2O-K_2O-FeO-MgO-Al_2O3-SiO_2-H_2O for the enderbitic rock sample E1 (f), using the bulk composition as show in Tab. 16 (recalculated in mol.%). The white ellipses represent assemblages observed in the respective samples. The bold lines indicate the inferred *P-T* path segments. For further explanation see text.

19 Geochronology

19.1 Analytical techniques

In the present study monazite *in situ* U-Pb analyses were carried out at Frankfurt University using a **Thermo-Finnigan Element II** sector field ICP-MS coupled to a New Wave UP213 ultraviolet laser system. The monazite grains were analysed from a polished thin section. Prior to the U-Pb dating, the internal structures of the monazite grains were investigated by back scattered electron microscopy (BSE) - (Fig. 51). The laser spot size used for mineral dating varied from 8 to 12 µm. For analytical details see Gerdes & Zeh (2006). Laser-induced elemental fractionation and instrumental mass discrimination are corrected by normalization to the reference monazite standard "Manangotry", which has an U-Pb ID-TIMS age of 554±2 Ma (Horstwood *et al.*, 2003). Reported uncertainties (±2σ) were propagated by quadratic addition of the external reproducibility (s.d., standard deviation) of the reference standards (1.3% and 1.2% for $^{207}Pb/^{206}Pb$ and $^{206}Pb/^{238}U$) and the within-run statistics of each analyses (2 s.e., standard error). The analytical results are presented in Tab. 19.

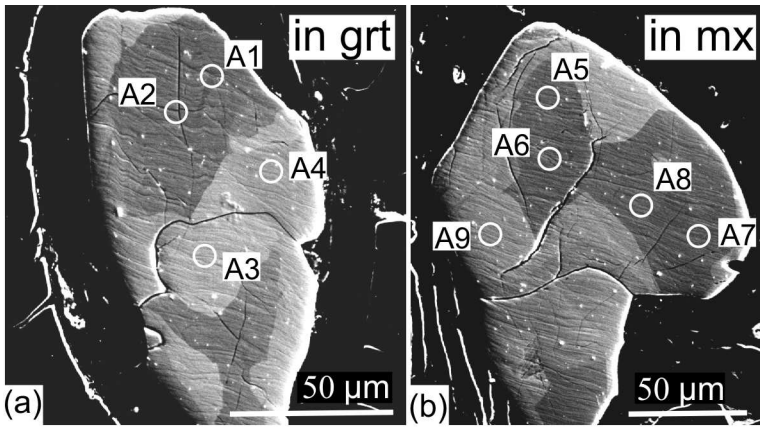

Fig. 51. Back scattered electron images of monazite from the charnoenderbitic sample CE1., (a) Monazite enclosed in garnet, (b) Matrix monazite beside garnet. The circles numbered with A1-A10 represent spot analyses as shown in Tab. 19.

19.2 Results

From the charnoenderbite sample CE1 one monazite inclusion in garnet and four matrix monazites (Fig. 48a and Fig. 52) were analysed *in situ* within a thin section. BSE images indicate that all monazites show similar internal structures, *i.e.* dark patchy domains with low Th/U ratios (>14 to <42), which are intergrown and/or surrounded by bright domains with high Th/U ratios (>78 to <140) - (Fig. 51, Fig. 52; Tab. 19). *In situ* U-Pb analyses yield, within error, identical age results for both domains (Tab. 19), indicating that they were formed almost contemporaneously. Four U-Pb analyses of the monazite inclusion in garnet yield an

intercept age of 2644±8 Ma, which is identical within error to an intercept age of 2639±8 Ma obtained from 10 U-Pb analyses of matrix monazites (Fig. 52).

Tab. 19. Results of U-Pb monazite LA-ICP-MS dating

	$^{207}Pb^{a}$	U^{a}	Pb^{b}	Th^{b}	$^{206}Pb^{d}$	$^{206}Pb^{e}$	±2σ	$^{207}Pb^{e}$	±2σ	rho[e]	$^{207}Pb^{e}$	±2σ	^{207}Pb	±2σ	^{206}Pb	±2σ	^{207}Pb	±2σ	conc.[f]
spot/zrc	(cps)	(ppm)	(ppm)	U	^{204}Pb	^{238}U	%	^{235}U	%		^{206}Pb	%	^{235}U	(Ma)	^{238}U	(Ma)	^{206}Pb	(Ma)	%
monazite																			
A1(Grt)	281682	2802	7935	14.0	181644	0.4730	3.6	11.7120	3.7	0.97	0.1796	0.9	2582	35	2497	74	2649	16	94
A2(Grt)	346647	3495	9636	14.4	99973	0.3757	7.0	9.2595	7.1	0.99	0.1787	1.1	2364	67	2056	124	2641	19	78
A3(Grt)	102643	936	20647	128.3	484456	0.5158	6.8	12.7377	6.9	0.99	0.1791	1.1	2660	67	2681	151	2645	18	101
A4(Grt)	148790	1388	18951	79.4	1202500	0.5190	4.8	12.7990	4.9	0.97	0.1788	1.2	2665	47	2695	106	2642	19	102
A5(Mx)	300991	2991	9030	15.2	130100	0.4921	8.0	12.1705	8.2	0.97	0.1794	1.9	2618	80	2580	172	2647	31	97
A6(Mx)	248395	2607	16706	38.7	391331	0.4990	4.3	12.3148	5.6	0.76	0.1790	3.6	2629	54	2609	92	2644	61	99
A7(Mx)	267818	2866	11462	23.2	374636	0.5015	6.5	12.4211	6.5	0.99	0.1797	0.9	2637	63	2620	141	2650	14	99
A8(Mx)	257947	6083	24533	23.2	366635	0.5142	8.1	12.5736	8.2	0.99	0.1773	1.2	2648	80	2675	179	2628	20	102
A9(Mx)	141270	3079	58315	118.2	1920184	0.5453	6.9	13.3851	7.0	0.98	0.1780	1.2	2707	68	2806	159	2635	21	106
A11(Mx)	102513	2027	8995	22.9	39987	0.4974	6.9	12.1904	7.1	0.98	0.1777	1.5	2619	69	2603	151	2632	25	99
A12(Mx)	109462	2332	7313	16.9	51514	0.4561	6.1	11.1971	6.4	0.94	0.1781	2.1	2540	62	2422	124	2635	35	92
A13(Mx)	67241	1403	20267	85.5	268771	0.4106	4.0	10.0263	4.7	0.86	0.1771	2.4	2437	44	2217	75	2626	39	84
A14(Mx)	108826	2295	7453	17.6	107547	0.4993	5.4	12.3307	5.7	0.96	0.1791	1.7	2630	55	2611	118	2645	28	99
A15(Mx)	82114	1599	7055	21.5	268670	0.5250	2.6	12.9014	2.9	0.88	0.1782	1.4	2672	28	2720	58	2636	23	103

[a] Within run background-corrected mean ^{207}Pb signal; [b] U and Pb content and Th/U ratio were calculated relative to Manangotry reference
[c] corrected for background and within-run Pb/U fractionation and normalised to Managotry (ID-TIMS value/measured value); $^{207}Pb/^{235}U$ calculated using $^{207}Pb/^{206}Pb/(^{238}U/^{206}Pb*1/137.88)$
[d] measured ratio corrected for background and ^{204}Hg interference; [e] Rho is the error correlation defined as $err^{206}Pb/^{238}U/err^{207}Pb/^{235}U$
[f] degree of concordance = ($^{238}U/^{206}Pb$ age x 100/$^{207}Pb/^{206}Pb$ age)
(Grt) Monazite enclosed in garnet, (Mx) matrix monazite

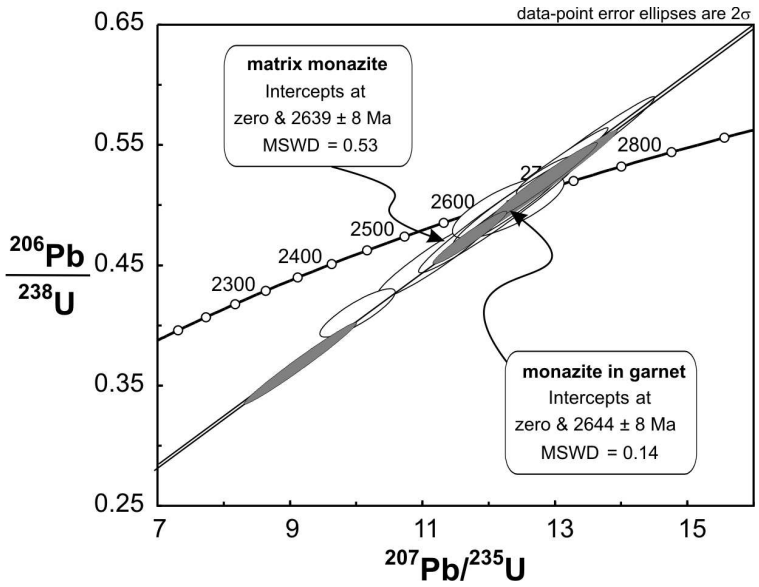

Fig. 52. U-Pb Concordia diagram showing the results of monazite dating.

20 Discussion - Bulai Pluton

20.1 Geochronological data

Our LA-ICP-MS U-Pb monazite ages of 2644±8 Ma (monazite enclosed in garnet) and 2639±8 Ma (matrix monazite) obtained from a charnoenderbite gneiss enclave (sample CE1) are significantly older than that of the surrounding porphyric Bulai granite, which intruded at 2612±7 Ma (Zeh *et al.*, 2007). However, both monazite U-Pb ages are identical, within error, to the emplacement age of the Singelele granite gneiss (2647±12 Ma), which forms xenoliths within the Bulai Pluton (Fig. 44b, Fig. 45). In combination, all age data together with the field relationships (Fig. 44b, Fig. 45a, b, c) show that the structural-metamorphic overprint of the "xenoliths" occurred *ca.* 30 million years before the intrusion of the Bulai granite, and that the metamorphic overprint is coeval with the formation (intrusion) of the Singelele granite gneisses. In contrast, Holzer *et al.* (1998) suggested that the Bulai Pluton was subjected to a high-grade metamorphic overprint at about 2.52 Ga, based on Pb stepwise leaching data (see section 16.1 - The Bulai Pluton - pre-, syn- and post-intrusive features, p. 81). These age data, however, are inconsistent with the observed field relationships and the geochronological results obtained in this study.

20.2 Pressure-Temperature-time evolution and geotectonic implications

The petrological data, in particular those inferred from the *P-T* pseudosections, indicate that the metapelitic rocks from the "xenoliths" within the Bulai granite underwent a *P-T* evolution with metamorphic peak conditions of about 830°C/8-10 kbar followed by a pressure-temperature decrease to 750°C/5-6 kbar. Similar peak *P-T* conditions of 860°C/8 kbar are also estimated for the associated charnoenderbitic and enderbitic gneisses, whose protoliths are interpreted to be of magmatic origin. The similar style of ductile deformation (*e.g.* foliation and isoclinal folds) and estimated peak *P-T* conditions indicate that all of these rocks (metapelites, charnoenderbites, enderbites) shared a common structural-metamorphic evolution. In addition, our geochronological data show that the structural-metamorphic overprint of the "xenoliths" occurred at least 12 million years prior to the Bulai granite intrusion.

The occurrence of metapelites in the "xenoliths" provides evidence that its protoliths must have been at the earth's surface some time prior to 2640 Ma. It is likely that the sedimentation of the metapelitic precursor rocks took place prior to the deposition of Beitbridge Formation sediments exposed in the areas east of Messina (Buick *et al.,* 2003) and near Swartwater (Buick *et al.,* 2006). These Beitbridge metasediments contain detrital zircon grains,

which show magmatic cores with ages of about 2.69 Ga. Metamorphic zircon overgrowths and monazite within these metasediments formed at *c.* 2.03 Ga (Buick *et al.,* 2003, 2006), and provide no evidence for any (high-grade) metamorphic overprint older than Palaeoproterozoic. In contrast, our dataset shows that the pelitic (meta)sediments in the Bulai area were transferred to *ca.* 30 km depth during the Neoarchean, where they were heated to temperatures of up to 830°C. These temperatures, which are very high for the given depth, (average geothermal gradient of 27°C/km), may be explained by advective heat transfer initiated by voluminous granite bodies, which abundantly intruded into the Limpopo's Central Zone comprising the protoliths of the 2.65-2.61 Ga Singelele, Alldays, Regina, Bulai, and Zoetfontain granite gneisses (*e.g.* Jaeckel *et al.,* 1997; Kröner *et al.,* 1999; Zeh *et al.*, 2007). These granitoids intruded coeval or slightly later than the voluminous enderbites, charnockites and granites of the Northern Marginal Zone (*e.g.* Berger *et al.,* 1995; Mkweli *et al.,* 1995), and most of them have a calc-alkaline composition. Thus, they are assumed to have intruded in a magmatic-arc setting (*e.g.* Barton *et al.,* 2006).

Evidence for a magmatic arc setting in the Central Zone of the Limpopo Belt during the Neoachean is suggested by three observations: (1) Lu-Hf zircon isotope data of Zeh *et al.*, (2007) indicate that the Neoarchean granitoids in the Central Zone contain high amounts of a pre-existing Palaeoarchean crust (>3.1 Ga), which was mixed with juvenile Neoarchean magmas at 2.6-2.7 Ga. Similar isotopic features were also obtained for granitoids from the Northern Marginal Zone (Berger & Rollinson, 1997); (2) geochronological and isotope data of the lamprophyre dykes which transect the Bulai Pluton (Watkeys & Armstrong, 1985) provide evidence that these dykes stem from a slab-enriched mantle source. Watkeys & Armstrong (1985) discuss that "*the relatively radiogenic nature of the upper mantle source for these dykes … shows that the mantle beneath the Central Zone of the Limpopo Belt had already been enriched with respect to U-Pb and Rb-Sr from some time prior to 2650 Ma."…."This metasomatism …may indicate that a slab was subducted beneath the region at ca. 2.7 Ga"*, and (3) the here presented *P-T* path indicates that pelitic (meta)sediments were "subducted" to *ca.* 30 km depth at ~2.64 Ga.

In a magmatic arc setting, the necessary heat to achieve temperatures of >830°C in *c.* 30 km depth may be due to magmatic underplating by mafic magmas, which could have formed by melting of the (metasomatized) underlying mantle wedge as a consequence of the involvement of slab-derived fluids and/or melts. Such a process could account for the formation of the voluminous calc-alkaline granite magmas in the Central Zone and Northern Marginal Zone at this time, and is consistent with the Lu-Hf isotope data of Zeh *et al.* (2007), and the Rb-Sr and U-Pb isotope data of Watkeys & Armstrong (1985).

Moreover, our dataset also allows the conclusion that the Bulai Pluton is the result of at least two magmatic stages. The first stage comprises the intrusion of the charnoenderbite and enderbite gneiss protoliths and a second stage the porphyry Bulai granite. During the first event, which occurred at *c.* 2640 Ma - coeval with the emplacement of the Singelele-type orthogneisses, the "subducted" pelitic rocks underwent their peak metamorphic overprint at 830°C/8-10 kbar, perhaps in a kind of deep crustal "contact metamorphism". At this stage all previously formed metamorphic assemblages were completely replaced.

Following the metamorphic peak, the metapelitic and charno-enderbitic rocks were ductily deformed (Fig. 45b, c) and cooled down to 750°C. This deformation-cooling event occurred while the magmatic-sedimentary succession was transferred to a depth of *c.* 18 km (5-6 kbar). Subsequently, at 2612±7 Ma, this succession was intruded by the Bulai granite, which assimilated up to 10 m long xenoliths of these rocks, perhaps by overhead stoping. Finally, the Bulai granite crystallized, and was partially deformed and intruded by lamprophyre dykes, perhaps during a late-orogenic extension. The exact timing of this extension event is unconstrained due to the large errors of the presented age data (Watkeys & Armstrong, 1985). Subsequently, either during the late Neoarchean or the Palaeoproterozoic, some domains of the Bulai Pluton were transected by mylonitic shear zones (Fig. 45f), while most domains remained weakly deformed until today (Fig. 45d). This is surprising considering that rocks from the adjacent Messina area (*e.g.* at the Causeway locality, Mount Shanzi and Campbell structure; Fig. 44a) were subject to a high-grade structural-metamorphic overprint during D3/M3 at about 2.02 Ga. The M3 event in the Bulai Pluton is only documented by some U-Pb zircon data, indicating partial Pb loss during the Palaeoproterozoic (see Zeh *et al.*, 2007), as well as by strong deformation patterns in contact with the metasediments of the Beit Bridge Formation (see section 16.1 on p. 81). These indicate that the Bulai Pluton was tectonically juxtaposed with the rocks from the Messina area after the peak of the M3 granulite-facies metamorphism. Age data and field relationships from the Mount Shanzi further indicate that the Bulai Pluton was overthrust top-to-the-NE by rocks of the Beitbridge Formation at *ca.* 2.01 Ga (Holzer *et al.,* 1998). In summary, all features indicate that the Bulai Pluton and the Beitbridge metasediments formed parts of separate nappes or thrust-bounded blocks during the Palaeoproterozoic orogeny. In fact, the concept of nappe tectonics in the Central Zone during M3 is already supported by structural, petrological and geochronological data from the Venetia klippen complex (Barton *et al.*, 2003; Klemd *et al.*, 2003; Zeh *et al.*, 2005a, b).

Finally it should be noted that the structural-metamorphic-magmatic evolution inferred from the Bulai Pluton and the associated metasediments is similar to 'dynamic regional

contact metamorphic evolutions' as observed in Palaeozoic (Variscan: 340-330 Ma) magmatic arc settings, where deformation and uplift of high-grade metasediments from 25 to 10 km depth can occur between several pulses of calc-alkaline magmatic intrusions (*e.g.* Zeh *et al.,* 2005c), and where granites were subsequently intruded by enriched mantle-derived lamprophyre dykes (*e.g.* von Seckendorff *et al.*, 2001). This indicates that Neoarchean and Palaeozoic tectonic processes along collision zones may operate in a similar manner: an initial subduction of a lower plate underneath a magmatic arc (upper plate) is followed by heating of buried sediment in the lower crust to high-grade metamorphic conditions by early magmatic pulses. Then the highly metamorphosed and deformed metamorphic and "early" magmatic rocks experience a fast uplift, while late- to post-tectonic younger granites intrude into a shallow crustal level prior to the intrusion of alkaline lamprophyre dykes.

20.3 Acknowledgements

We thank the German Science Foundation (DFG) for financial support (grant KL 692/15-2). Furthermore, we thank Roger Gibson, Richard White and an anonymous referee for their reviews, which helped to improve the paper. Ian Buick is thanked for the editorial handling.

Summary and conclusions

21 The tectono-metamorphic evolution of the Central Zone

Geochronological, structural and petrological data provides evidence that the Limpopo Belt's Central Zone was affected by at least three structural-magmatic-metamorphic events: during the Paleoarchean at 3.0-3.28 Ga (D1/M1), Neoarchean at 2.52-2.65 Ga (D2/M2) and Palaeoproterozoic at 2.0-2.03 Ga (D3/M3) - (*e.g.*, Holzer *et al.*, 1998, 1999; Jaeckel *et al.*, 1997; Kröner *et al.*, 1999; Van Reenen *et al.*, 2004; Barton *et al.*, 2006; Zeh *et al.*, 2007; Chudy *et al.*, 2009) – (Fig. 53a and Tab. 1). However, despite the geochronological and petrological results obtained over the past years, there are still controversies about the tectono-metamorphic evolution of the Limpopo Belt, in particular of the Central Zone (see *e.g.* Barton *et al.*, 2006, Rigby *et al.*, 2008; Van Reenen et al, 2008; Zeh & Klemd, 2008). These controversies partly result from the fact that the *P-T* evolutions, especially the prograde *P-T* paths, of some geological complexes (terranes) are unknown.

Petrological investigations of this thesis put new constraints on the metamorphic evolution of the Central Zone during M2 and M3. The new interpretation of the tectono-metmorphic history during the Neoarchean M2 event (~2.64 Ga) is based on petrological and geochronological data obtained from xenoliths, which occur within the Bulai Pluton (~2.61 Ga; see Millonig *et al.*, 2008). The Palaeoproterozoic event M3 (~2.0 Ga) is constraint by petrological (this thesis) and geochronological data (Zeh, 2008, unpub. data) obtained from rocks of the Mahalapye and Phikwe Complex.

21.1 Neoarchean (~2.64 Ga) metamorphic evolution (M2) in the Bulai Pluton area

A detailed discussion about the petrological and geochronological results obtained from metapelitic and (charno)enderbitic xenoliths, which occur within the Bulai Pluton, is given on p. 97. Here, only the main conclusions of Millonig *et al.* (2008) are repeated.

The petrological data indicate that the metapelitic rocks, which form "xenoliths" within the Bulai granite, underwent a *P-T* evolution with metamorphic peak conditions of about 830°C/8-9 kbar at ~2.64 Ga (M2) followed by a pressure-temperature decrease to 750°C/5-6 kbar (Fig. 56b). Similar peak *P-T* conditions of 860°C/8 kbar are also estimated for the associated charnoenderbitic and enderbitic gneisses, whose protoliths are interpreted to be of

magmatic origin. The occurrence of metapelites in the "xenoliths" provides evidence that its protoliths must have been at the earth's surface some time prior to 2640 Ma. Furthermore, the similar style of ductile deformation (*e.g.* foliation and isoclinal folds) and estimated peak *P-T* conditions indicate that all of these rocks (metapelites, charnoenderbites, enderbites) shared a common structural-metamorphic evolution. In addition, the geochronological data of Millonig *et al.* (2008) show that the structural-metamorphic overprint of the "xenoliths" occurred at least 12-30 million years prior to the Bulai granite intrusion at ~2.61 Ga. This overprint probably happened in a magmatic arc setting, where the necessary heat to achieve temperatures of >830°C in *ca.* 30 km depth (*i.e.* average geothermal gradient of 27°C/km) may be due to magmatic underplating by mafic magmas, which could have formed by melting of the (metasomatized) underlying mantle wedge as a consequence of the involvement of slab-derived fluids and/or melts. Evidence for a magmatic arc setting in the Central Zone of the Limpopo Belt during the Neoachean is also suggested by geochronological and isotope data of lamprophyre dykes which transect the Bulai Pluton (Watkeys & Armstrong, 1985). These data provide evidence that these dykes stem from a slab-enriched mantle source. Watkeys & Armstrong (1985) discuss that "*the relatively radiogenic nature of the upper mantle source for these dykes … shows that the mantle beneath the Central Zone of the Limpopo Belt had already been enriched with respect to U-Pb and Rb-Sr from some time prior to 2650 Ma.*"…."*This metasomatism …may indicate that a slab was subducted beneath the region at ca. 2.7 Ga*". Contemporaneously, the Northern Marginal Zone in southern Zimbabwe was assembled by extensive magmatic under- and intraplating between *ca.* 2.7 and 2.6 Ga during late Archean crustal shortening, as pointed out by Blenkinsop & Kisters (2005).

The M3 event (~2.0 Ga) in the Bulai Pluton is only documented by some U-Pb zircon data, indicating partial Pb loss during the Palaeoproterozoic (see Zeh *et al.*, 2007), as well as by strong deformation patterns in contact with the metasediments of the Beit Bridge Formation (see section *16.1 - The Bulai Pluton - pre-, syn- and post-intrusive features*, p. 81). These indicate that the Bulai Pluton was tectonically juxtaposed with the rocks from the Messina area after the peak of the M3 granulite-facies metamorphism.

21.2 Palaeoproterozoic (~2.0 Ga) metamorphic evolution (M3) of the Mahalapye Complex

The *P-T* evolution derived from the metapelitic samples Ma3a and Ma3c (Fig. 55, Fig. 56d) in combination with U-Pb age dating on monazite of sample Ma3c (Tab. 20; Zeh, 2008, unpub. data) provides evidence that the sedimentary precursors of these rocks were

deposited prior to ~2.03 Ga and afterwards buried to midcrustal conditions of ~650°C at 7 kbar (~26 km depth). During the subsequent prograde *P-T* history these rocks underwent near isobaric heating with slight decompression to peak metamorphic conditions of ~800°C at 5.5 kbar (~20 km depth). Similar peak *P-T* conditions of ~800°C/5-7 kbar were derived from the garnet-biotite gneiss samples Ma1h and Ma1i (Fig. 56d). Furthermore the *P-T* paths constraint that these rocks underwent uplift from ~20 km to ~11 km depth (~5.5 to 3 kbar), while they were cooled from ~800 to 600°C during the retrograde *P-T* evolution (Fig. 56d).

The prograde segment of the proposed *P-T* path indicates heating of ~150°C from 600 to 750°C during exhumation from ~26 to 20 km depth. Such a *P-T* path might reflect that the Mahalapye Complex was affected by magmatic underplating of mafic melts, which triggered the formation and intrusion of granitic melts into midcrustal levels. The slight uplift was caused either by tectonism and/or by erosion.

So far, the reasons for the Palaeoproterozoic high-grade metamorphic overprint of the Central Zone, in particular for the magmatism of the Mahalapye Complex, are not well known. However, from their timing it is very likely that they result from orogenic processes related to the Kheis-Magondi "orogeny" between ~1.8 to 2.0 Ga (Stowe *et al.*, 1984; Treloar, 1988; Holzer *et al.*, 1998; Majaule et al, 2001; Barton *et al.*, 2006; Clarke *et al.*, 2008), and the emplacement of the Bushveld Complex at ~2.05 to 2.06 Ga (Buick *et al.*, 2001; Mapeo *et al.*, 2004). This conforms to geochronological data, indicating that the Mahalapye Complex was affected by diorite magmatism at ~2.06 Ga (Zeh *et al.*, 2007; Zeh, 2008, unpub. data; Tab. 20) and by granite intrusions between ~2.02 to 2.05 Ga (McCourt & Armstrong, 1998; Gutzmer & Beukes, 1998; Zeh *et al.*, 2007: Tab. 20). Furthermore it is supported by U-Pb minerals ages of ~2.03 Ga obtained from metamorphic rocks of the Mahalapye Complex (Zeh *et al.*, 2008, unpub. data; Tab. 20). These ages are within error identical or slightly older than Sm-Nd and U-Pb ages of ~1.98 to 2.02 Ga obtained from various metamorphic minerals from rocks of the Mahalapye Complex (Chavagnac *et al.*, 2001; Schaller *et al.*, 1999; Holzer *et al.*, 1999; Tab. 20). It should be noted that the youngest age of 1982 Ma is afflicted with an error of ±38 Ma (Chavagnac *et al.*, 2001; Tab. 20).

In fact, magmatic-metamorphic events in the Mahalapye Complex at ~2.06 to 1.98 Ga (Tab. 20) are contemporaneuos with/or slightly younger than the emplacement of the Bushveld Complex at ~2.05-2.06 Ga at the northern margin of the Kaapvaal Craton (Buick *et al.*, 2001; Mapeo *et al.*, 2004) and the (re)activation of the Palala-Shear Zone at ~2.05 to 1.90 Ga (Schaller *et al.*, 1999; Tab. 20). The Bushveld Complex intruded mainly south to the Thabazimbi-Murchinson Lineament (Fig. 53b; *e.g.* Clarke *et al.*, 2008), but relics south to the Palala-Shear Zone (*e.g.* Brandl & Reimold, 1980; Du Plessis & Walraven, 1990 cited in

McCourt, 1995; Fig. 1) indicate that it affected a considerably larger region than is now exposed, extending into southeastern Botswana (Nguuri *et al.*, 2001). For the Bushveld Complex a mantle-plume origin with significant crustal contamination was suggested by *e.g.* Hatton (1995), Hatton & Schweitzer (1995) and Eriksson *et al.* (2005). In detail, Hatton & Schweitzer (1995) proposed that prmiary mantle melts were derived from a mantle diapir and assimilated large amounts of crustal rocks and melts during their ascent, before they reached their final crustal levels as shallow as 18 km. In contrast, Clarke *et al.* (2008) link the emplacement of the Bushveld Complex to far field extensional stress in a back arc setting, related to the Palaeoproterozoic "Limpopo orogeny" and the formation of the Kheis-Magondi Belt at the northwestern margin of the Zimbabwe Craton at ~2.0 Ga (Stowe *et al.*, 1984 and Treloar, 1988; Fig. 53). Such a scenario is supported by petrological data that indicate a significant component of subducted crust in the Bushveld magmas (Willmore *et al.*, 2002; Clarke *et al.*, 2008). A combination of the plume and subduction models for the genesis of the Bushveld Complex is given by Willmore *et al.* (2002). Based on stable Cl/F isotope systematics of Bushveld rocks these authors favour a "*subducted or overridden wet mantle hot-spot*" as primary source.

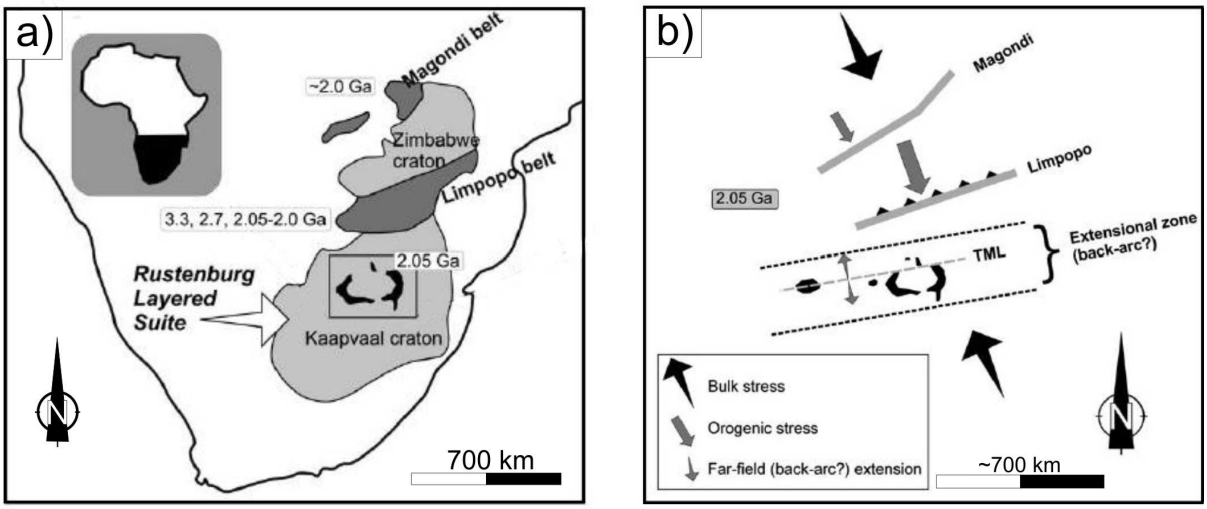

Fig. 53. a) Simplified geological map of southern Africa showing the Kaapvaal Craton with Bushveld Complex (Rustenburg Layered Suite), the Limpopo Belt, the Zimbabwe Craton and the Magondi Belt. Inset shows location of detail on the African continent (modified after Clarke *et al.*, 2008). b) Proposed emplacement model for the Rustenburg Layered Suite and satellite Molopo Farms Complex (located largely in Botswana), showing the Bushveld Complex sill emplaced from a dyke-like feeder that utilised the Thabazimbi-Murchison Lineament (TML) into an extensional (back-arc) zone within the overall compressive (subduction) regime at 2.05 Ga (modified after Clarke *et al.*, 2008).

In summary, the petrological, geochemical and geochronological data suggest that the wide spread magmatic-metamorphic events which affected the southwestern part of the Central Zone at ~2.06 to 1.98 Ga (Tab. 20) and the adjacent northern part of the Kaapvaal Craton at ~2.06 to 2.0 Ga (Clarke *et al.*, 2008) result from a subduction zone process, related to the Kheis-

Magondi orogeny, interacting with a mantle plume. This scenario is able to explain the heat input into midcrustal levels, as required by the obained *P-T* paths. The heat input most likely was initiated by the melting of the mantle wedge above a subduction zone. This led to the formation of mafic magmas, which themselves caused the formation of crustal melts, as represented by the syn-kinematic Mokgware and the post-kinematic Mahalaype Granite (McCourt *et al.*, 2004). Finally, these granites caused heating in the middle crust during their ascent and emplacement. Such a scenario could reflect the early stages of a transpressive Limpopo orogeny at ~2.05 to 1.95 Ga, as proposed by *e.g.* Holzer *et al.* (1998), Schaller *et al.* (1999) and Clarke *et al.* (2008).

It this context it is worth noting that U-Pb ages of ~2.5 and 3.2 Ga obtained from cores of inherited zircons from within the Mahalapye Granite (~2.02 Ga; McCourt & Armstrong, 1998) and Pb-Pb ages of 2.52-2.65 Ga and 2.93 Ga obtained from inherited zircons from within the Mokgware Granite (~2.02 Ga; Zeh *et al.*, 2007) support the interpretation that reworking of Archean crustal components during the Palaeoproterozoic magmatic-metamorphic event at ~2.06-2.0 Ga was severe. This also was concluded by *e.g.* Hatton & Schweitzer (1995) for the northern Kaapvaal Craton and by *e.g.* Zeh *et al.* (2007) for the Mahalapye Complex.

The retrograde *P-T* path with decompression-cooling from ~800°C at 5.5 kbar (20 km depth) to ~600°C at 3 kbar (11 km depth) is interpreted to represent an erosion controlled exhumation of the investigated samples. This interpretation is in agreement with retrograde *P-T* paths obtained from rocks of several other parts of the Central Zone, which display similar retrograde *P-T* vectors (*e.g.* Zeh *et al.*, 2004a, b and Hisada *et al.*, 2005; see Fig. 56 and also Gerya *et al.*, 2000). It should be emphasized that no evidence for isothermal decompression was found, as proposed by Hisada (1997), who suggested similar metamorphic evolutions for the Mahalapye and for the Beit Bridge Complex.

In summary, the *P-T* paths inferred from metamorphic rocks of the Mahalapye Complex are consistent with isobaric or decompressional heating in a generally NW directed compressional regime caused by the Kheis-Magondi orogeny that perhaps caused the final convergence of the Kaapvaal and Zimbabwe Cratons. This regime persisted at least from ~2.06 to 1.95 Ga, caused the Bushveld Intrusion at ~2.06-2.05 Ga and was responsible for the extensive magmatic-metamorphic activity in the Mahalapye Complex of the Central Zone at ~2.06-1.98 Ga. In general, it is likely that the Palaeoproterozoic tectono-metamorphic activity was due to the interplay of subduction processes and mantle plume(s) activities. Existing geochronological data show that the Mahalapye Complex underwent its metamorphic peak at ~2.03 Ga, simultaneous with granite intrusions. Subsequent exhumation of these rocks was controlled by erosion.

Tab. 20. Compilation of age data from the Mahalapye Complex. [1] wr = whole rock; [2] cited in McCourt & Armstrong (1998)

Method	age (Ma)	±	Comments	Author
Rb-Sr kfs-pl-ap-wr[1]	2010	80	migmatite	Van Breemen & Dodson (1972)
Rb-Sr bt	2050	50	migmatite	Van Breemen & Dodson (1972)
Sm-Nd grt-leuc-wr[1]	2023	7	migmatite, bt breakdown	Chavagnac *et al.* (1997)
U-Pb monazite	2002	10	leucosom	Chavagnac *et al.* (1997)
U-Pb zircons	2023	13	Mahalapye Granite	McCourt & Armstrong (1998)
U-Pb zircons	2053	21	granodiorite dyke	McCourt & Armstrong (1998)
U-Pb zircon	2023	7	Mahalapye Granite	Beukes & Gutzmer (1998)[2]
U-Pb apatite	1998	4	leucosome	Holzer *et al.* (1999)
Pb titanite	2020	8	Koedesrand Window	Schaller *et al.* (1999)
Pb titanite	2017	6	Koedesrand Window	Schaller *et al.* (1999)
Sm-Nd garnet	1982	38	grt-leucosome-palaeosom (Lose Quarry)	Chavagnac *et al.* (2001)
Sm-Nd garnet	2023	7	grt-leucosome-palaeosom (Lose Quarry)	Chavagnac *et al.* (2001)
U-Pb monazite	2004	19	leucosome (Lose Quarry)	Chavagnac *et al.* (2001)
U-Pb monazite	1996	38	leucosome (Lose Quarry)	Chavagnac *et al.* (2001)
U-Pb monazite	2002	15	leucosome (Lose Quarry)	Chavagnac *et al.* (2001)
U-Pb monazite	2002	35	leucosome (Lose Quarry)	Chavagnac *et al.* (2001)
U-Pb zircon	2026	10	Mokgware Granite	Zeh *et al.* (2007)
U-Pb zircon	2061	6	grt-bt gneiss (Lose Quarry)	Zeh *et al.* (2007)
U-Pb zircon (cores)	2711	11	leucosome (Lose Quarry)	Zeh *et al.* (2007)
U-Pb zircon (rims)	<2061		leucosome (Lose Quarry)	Zeh *et al.* (2007)
U-Pb monazite	2029	7	metapelite Ma3c (near Lose Quarry)	Zeh (2008, unpub. data)

21.3 Palaeoproterozoic (~2.0 Ga) metamorphic evolution (M3) of the Phikwe Complex

The obtained *P-T* paths constraint that rocks from the Phikwe Complex underwent prograde heating from ~600 to ~750°C, while they were buried from ~20 km to 30 km depth (~6 to 8 kbar; Fig. 55, Fig. 56f). During their retrograde *P-T* evolution these rocks underwent uplift from ~30 km to ~11 km depth (~8 to 3 kbar), while they were cooled from ~750°C to <600°C. Geochronological data of the investigated samples SP8 and SP9d (Zeh, 2008, unpub. data; Tab. 21) additionally constraint that this *P-T* evolution occurred at ~2.03 Ga, *i.e.* coeval with metamorphism in the Mahalapye and Beit Bridge Complexes.

The prograde segment of the *P-T* path indicates, in contrast to the one from the Mahalapye Complex, a contemporaneous heating and pressure increase for the rocks from the Phikwe Complex from ~600°C at 6 kbar (20 km depth) to ~750°C at 8 kbar (30 km depth; Fig. 55). This *P-T* path requires crustal thickening, perhaps caused by successive stacking of crustal slices. In fact, the obtained *P-T* vector is similar to those obtained from granulite- and amphibolite-facies rocks of the Beit Bridge Complex near Musina and Venetia (*P-T* paths of Zeh *et al.*, 2004b and 2005a, b in Fig. 56a). These authors suggested the successive stacking of crustal segments of the Central Zone in a NW directed stress regime during the Palaeoproterozoic at ~2.0 Ga (Holzer *et al.*, 1998, 1999). Thus, the similarity of the obtained *P-T*-t paths reflects that this NW compressional regime affected the complete

Central Zone over a distance of >600 km (see also section 21.2 - Mahalapye Complex on p. 102).

The retrograde segment of the *P-T* paths is interpreted to reflect erosion controlled exhumation. It should be emphasized that the *P-T* evolution inferred in this study yielded no evidence for an isothermal decompression as it was postulated by Hisada & Miyano (1996) for the Phikwe Complex.

The similarity of the *P-T* loops and geochronological ages (see Fig. 56 and Tab. 21) inferred from rocks of the Phikwe and Beit Bridge Complex constraint that these two complexes were subject to the same Palaeoproterozoic metamorphic event at ~2.0 Ga in similar tectonic settings. Nevertheless, the petrological results reveal that different rock units of the Central Zone complexes, despite their similar *P-T* loops, experienced different peak metamorphic conditions (amphibolite to granulite facies). These differences are attributed to the fact that the present-day outcrops display different levels of the crust, formed by successive stacking of rock units along low angle shear zones during the Palaeoproterozoic (see discussion in Zeh *et al.*, 2005). Differences between published retrograde *P-T* paths, *e.g.* isothermal-decompression vs. decompression-cooling, either result from petrological problems (see Rigby *et al.*, 2008; Zeh & Klemd, 2008; Perchuck *et al.*, 2008) or from the fact that different rock units of the Central Zone underwent different exhumation histories. In fact, the observed differences could be explained by the movement of crustal blocks relative to each other along steep to shallow dipping shear zones (Alsop & Holdsworth, 2004; Fig. 54) which limit and the transect the Limpopo Belt (e.g the Palala- & Triangle-Shear Zone and the Sunny-Side Shear Zone; Fig. 1). Finally, it must be kept in mind that parts of the Central Zone were affected by polymetamorphism during two or even three tectono-metamorphic events. Thus, without combined petrological and geochronological data it diffcult to designate an obtained *P-T* path to one of these events (see Millonig *et al.*, 2008).

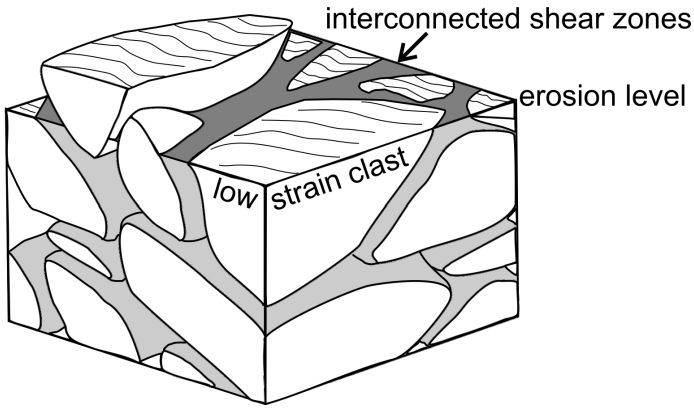

Fig. 54. Schematic 3D sketch illustrating shear zones anastomosing around low-strain augen. The relatively small amount of mechanically weak but interconnected shear zone rock forms a network which effectively controls the bulk strength of the overall rock volume (Figure 5 of Alsop & Holdsworth, 2004).

Tab. 21. Compilation of age data from the Phikwe Complex. [1]wr = whole rock. [2]PbSL = Pb-stepwise leaching

Method	age (Ma)	±	Comments	Author
Rb-Sr biotite	2010	50	granitoid gneisses (cooling age)	Van Breemen & Dodson (1972)
Rb-Sr biotite	2000	50	granitoid gneisses (“)	Van Breemen & Dodson (1972)
Rb-Sr biotite	1970	50	granitoids, Magogapathe area (“)	Van Breemen & Dodson (1972)
Rb-Sr wr[1] isochron	2660	40	anorthositic and granitoid gneisses	Hickman & Wakefield (1975)
Rb-Sr thin slices, errorchron	2100		granitoid gneisses	Hickman & Wakefield (1975)
U-Pb zircon	2595	18	Makowe granite	McCourt & Armstrong (1998)
U-Pb zircon	2652	15	syntectonic granite	McCourt & Armstrong (1998)
U-Pb zircon	2517	33	Swejane granite	Holzer *et al.* (1999)
U-Pb zircon	2497	19	Sashe granite	Holzer *et al.* (1999)
PbSL[2] titanite	2001	6	Swejane granite (cooling age)	Holzer *et al.* (1999)
U-Pb apatite	1997	7	Swejane granite (“)	Holzer *et al.* (1999)
PbSL[2] garnet	2076	55	garnet-amphibolite (Selebi ore body)	Holzer *et al.* (1999)
Pb-Pb isochron	1998	68	migmatite (protolith age ~2.7 Ga)	Chavagnac *et al.* (1999)
U-Pb monazite (in situ)	2038	5.2	metapelite (SP8)	Zeh (2008, unpub. data)
Garnet-wr[1] isochron	2034	2.8	grt-gedrite gneiss (SP9d)	Zeh (2008, unpub. data)

22 Conclusions

Detailed petrological investigations on metamorphic rocks from the Bulai Pluton area (Beit Bridge Complex), and the Mahalaype and Phikwe Complex constraint clockwise *P-T* evolutions with peak metamorphic conditions of ~750-850°C at 5-9 kbar (Fig. 55; Fig. 56). However, even though similar, the obtained *P-T* paths result from different orogenies, as constraint by geochronological data. The samples from the Bulai Pluton area provide evidence for a Neoarchean high-grade metamorphic event at ~2.64 Ga (M2), about 30 Ma before the emplacement of the Bulai Pluton at ~2.61 Ga. According to Millonig *et al.* (2008) the Neoarchean evolution probably took place in a magmatic arc setting. In contrast, the samples from the Mahalapye and Phikwe Complex document a Palaeoproterozoic *P-T* evolution at ~2.03 Ga (M3). The Palaeoproerozoic magmatic-metamorphic activity at ~2.06-1.98 Ga in the Mahalapye Complex (Tab. 20) is due to subduction processes and mantle plume(s) in a NW directed stress field, related to the Kheis-Magondi orogeny, which probably caused the final convergence of the Kaapvaal and Zimbabwe Cratons between ~2.06-1.90 Ga. On the northern margin of the Kaapvaal Craton, south of the Mahalapye Complex, these processes were responsible for the emplacement of the Bushveld Complex at ~2.06-2.05 Ga and reactivation of crustal scale lineaments like the Thabazimbi-Murchinson and the Palala-Zoetfontein Lineament (Fig. 53b and Fig. 1). The NW directed stress field also affected the Phikwe and Beit Bridge Complexes of the Limpopo Belt’s Central Zone and was there responsible for thickening of the crust by successive crustal stacking at ~2.03 Ga.

Combined petrological and geochronological data constraint that the Palaeoproterozoic tectono-metamorphic evolution throughout the Central Zone was contemporaneous (Tab. 22; Fig. 56) but the intensity was different, as reflected by different peak *P-T* conditions of the Mahalapye, Phikwe and Beit Bridge Complex.

Tab. 22. Synopsis of magmatic-metamorphic events in the Bulai Pluton area, and the Mahalapye and Phikwe Complex

	Mahalaype Complex		Phikwe Complex		Bulai Pluton (Beit Bridge Complex)
1.95-1.85 Ga	opening of Palapye Graben (and Soutpansberg Trough)[5]	1.95-1.85 Ga	opening of Palapye Graben[5]	1.95-1.85 Ga	opening of Palapye Graben[5]
2.06-1.98 Ga	intense magmatism[1, 2]/metamorphism[3] and reactivation of the Palala Shear Zone[4]	~2.0 Ga	amphibolite to granulite facies metamorphism[3] and granitoid emplacement[1, 4]	~2.0 Ga	shear zone (re)activation[9], metamorphism[8] with associated melt patches[7] and Pb-loss indicated in xenoliths from the Bulai Pluton[6]
				2.61 Ga	Bulai Pluton[6] intrudes the Beit Bridge Complex
		~2.66-2.50 Ga	high-grade metamorphism[1] and associated magmatism[1] (?)	2.64 Ga	metamorphism[6] of sediments and (charno)enderbites of the Bulai suite
~3.2-2.5 Ga	inherited zircons in the Mahalapye and Mokgware Granites[1, 2]				

[1]McCourt & Armstrong (1998); [2]Zeh *et al.* (2007); [3]this study; [4]Holzer *et al.* (1999); [5]Schaller *et al.* (1999); [6]Millonig *et al.* (2008); [7]Retief *et al.* (1990 ; cited in Kramers *et al.*, 2007); [8]various author (see Fig. 56e); [9]Kamber *et al.* (1995)

The Mahalapye Complex experienced widespread magmatism and migmatisation at ~2.05-1.98 Ga (Tab. 20) of older crustal material, which contains detrital zircons with ages between 3.2 to 2.5 Ga. In contrast, magmatism in the Phikwe Complex occurred during the Neoarchean at ~2.7 to 2.5 Ga (Tab. 21). The same holds true for the Beit Bridge Complex, which contains numerous orthogneisses formed at ~2.65-2.5 Ga (Kröner *et al.*, 1997; Zeh *et al.*, 2007). Palaeproterozoic magmatism is restricted to a few melt patches formed at ~2.03-2.0 Ga (Tab. 22). However, the metamorphic overprint of the Beit Bridge Complex mainly occurred at ~2.0 Ga, as is shown by several studies (Fig. 56a; Buick *et al.*, 2003; Jaeckel *et al.*, 1997), but, as noted by Kramers *et al.* (2007), "*… while some P-T paths have been shown to reflect conditions of the c. 2000 Ma event, some may also be relics of the late Archean episode, and at present they cannot be distinguished on the basis of the metamorphic evolution alone.*"

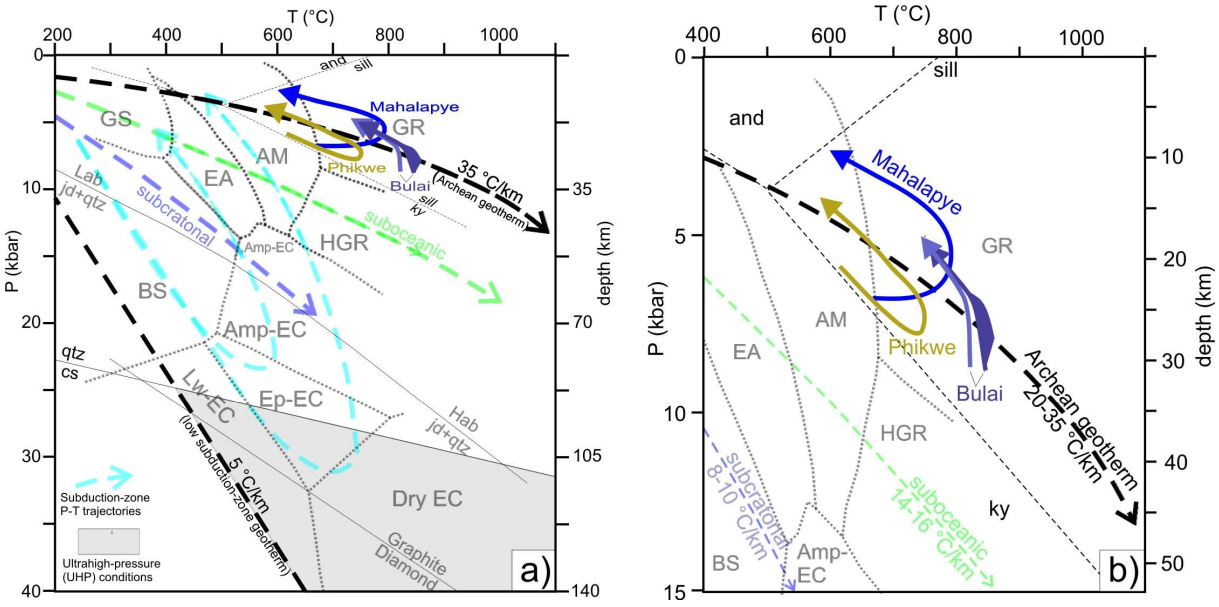

Fig. 55. a) petrogenetic grid for rocks of basaltic bulk composition, as compiled in Ernst (2007) and modified from Liou *et al.* (1998) and Okamoto & Maruyama (1999). The *P-T* paths obtained during this study from the Bulai Pluton area, the Mahalapye and the Phikwe Complex are shown as coloured solid arrows. For comparison, Phanerozoic *P-T* paths for outboard Pacific-type (HP) and Alpine-type (UHP) metamorphism are indicated. The presentday intraplate suboceanic and subcratonal geothermal gradients are from Clark & Ringwood (1964), and the Archean geothermal gradient (3.6 Ga) assuming 3 times of the modern radiogenic heat production in a stratified mantle is from Lambert (1976), Richter (1988) and Pollack (1997). The Archean geotherm also corresponds to a 35°C/km geotherm, calculated for the Southern Marginal Zone of the Limpopo Belt by Tsunogae *et al.* (2004) for the Neoarchean (~2.6 Ga). An extremely low subduction-zone geothermal gradient of 5°C/km is also shown for reference. Abbreviation follow Ernst (2007). Mineral abbreviations are: Jd = jadeite; Qtz = quartz; LAb = low albite; and HAb = high albite. Metamorphic-facies abbreviations are: AM = amphibolite; Amp-EC = amphibolite-eclogite; BS = blueschist; EA = epidote amphibolite; EC = eclogite; Ep-EC = epidote-eclogite; GR = sillimanite- granulite; GS = greenschist; HGR = kyanite-granulite; Lw-EC = lawsonite- eclogite; and Px-Hf = pyroxene hornfels. Feebly recrystallized rocks of the zeolite, prehnite, pumpellyite-actinolite, and prehnite-pumpellyite metamorphic subfacies (not illustrated) lie at lower temperatures and pressures than GS and BS. b) detail of a).

The results of the presented petrological investigations and geochronological data of Zeh (2008, unpub. data) clearly show that the *P-T* paths during the Neoarchean and Palaeoproterozoic were in parts similar, as is shown in Fig. 55 and Fig. 56. The similarity of the *P-T* paths could indicate that the Limpopo Belt was affected by two collsional events, the first (M2) - (e.g Van Reenen et al, 1987; Silver *et al.*, 2004; Bumby et al., 2004; Eriksson et al., 2006) in an magmatic arc setting (Barton *et al.*, 2006; Millonig *et al.*, 2008), and the second (M3) in response to the Kheis-Magondi orogeny (Holzer *et al.*, 1998: Mapeo *et al.*, 2001; Silver *et al.*, 2004; Clarke *et al.*, 2008). The Neoarchean event is also supported by wide spread magmatism throughout the Limpopo Belt and the activation of crustal scale shear zones to the north and south of the Central Zone, *e.g.* the Hout River Shear Zone and the Northern Limpopo Thrust Zone (Fig. 1; Barton *et al.*, 2006). Nevertheless, the prograde evolution during the Neoarchean metamorphism (M2) is unconstraint. Furthermore it should be noted that all *P-T* paths (Neoarchean & Palaeoproterozoic) of the Limpopo Belt conform to a model of thin skin tectonics. High to ultrahigh pressure conditions were most likely

never reached by the investigated rocks (Fig. 55 and Fig. 56; see also Dirks, 1998).

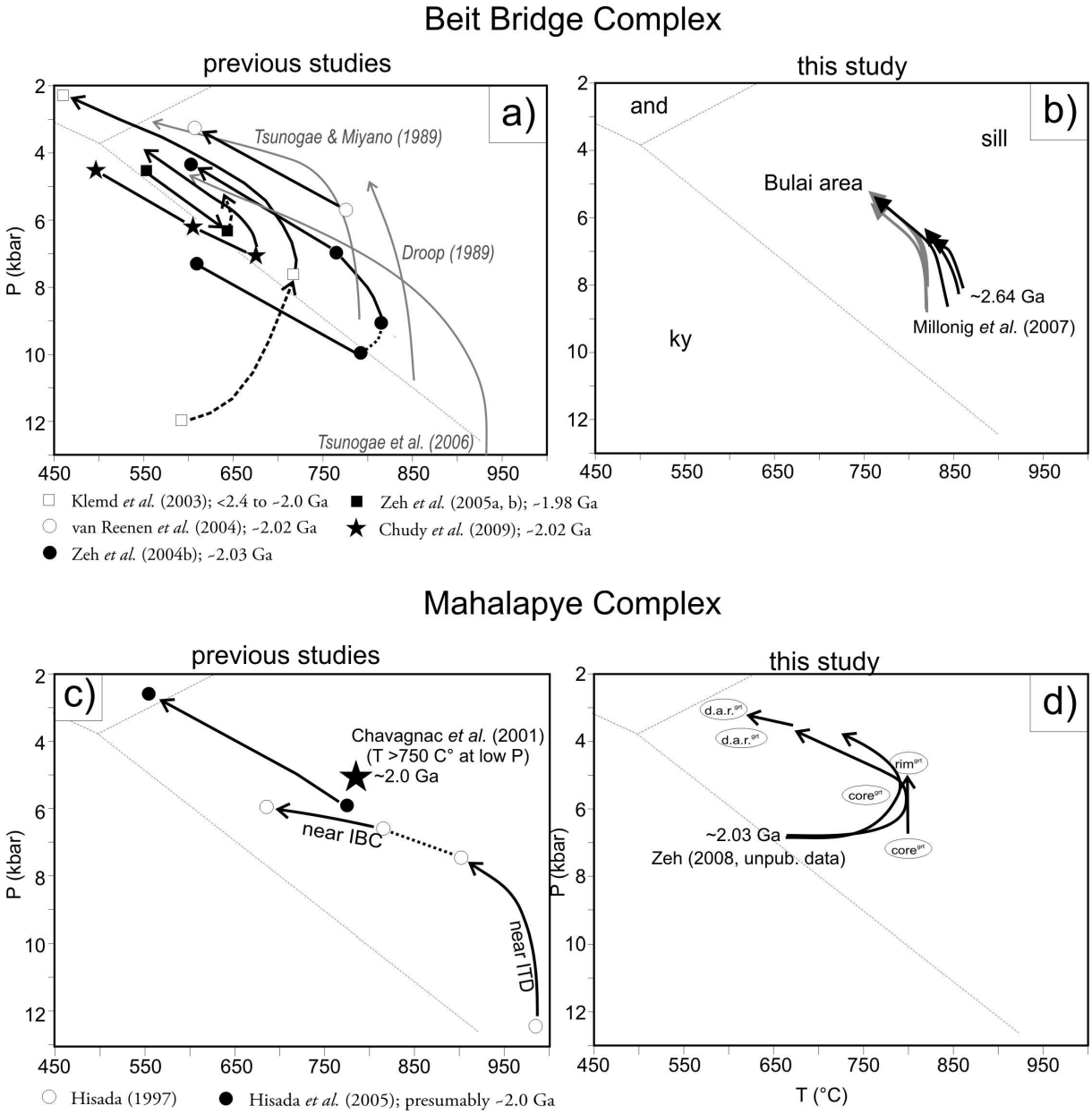

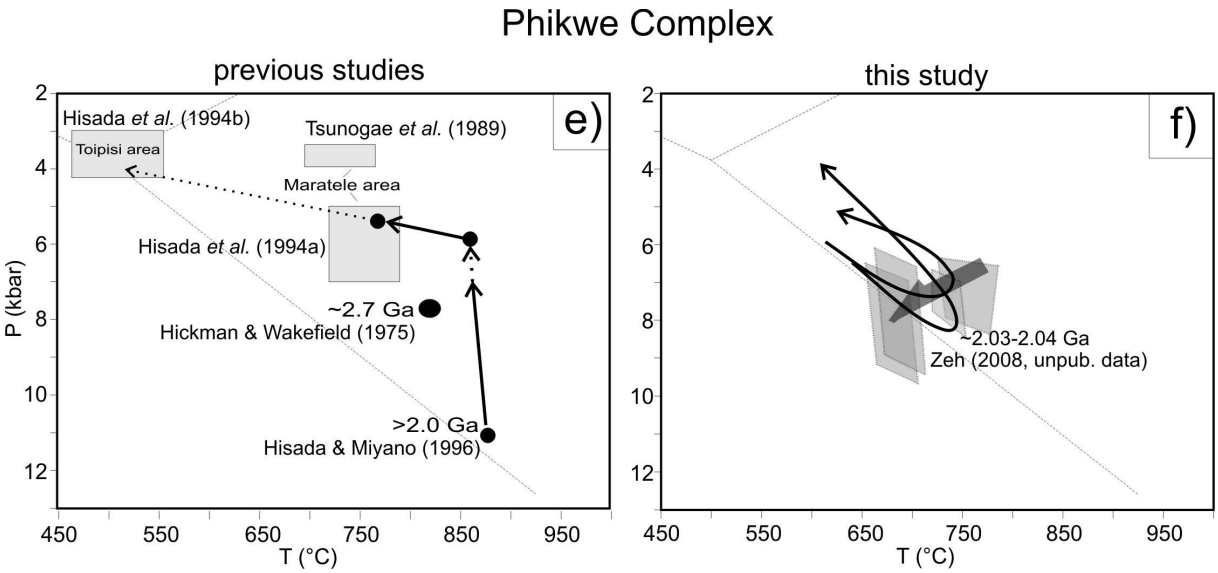

Fig. 56. *P-T* paths obtained in this and during previous studies for rocks of the Beit Bridge (a+b), the Mahalapye (c+d), and the Phikwe Complex (e+f). Compiled and modified after Van Reenen *et al.* (2004), Zeh *et al.* (2004), Barton *et al.* (2006) and Kramers *et al.* (2007). Age data idicate peak of metamorphism, as given by the various authors. See also Tab. 20 and Tab. 21. d.a.r.^{grt} = diffusively altered garnet rim.

Acknowledgements

This Ph.D. thesis is more than the work of one Ph.D. student alone. Numerous colleagues and friends have contributed to it through their continuous help in solving scientific problems, as well as those of everyday life problems. I have learned a great deal from these remarkable people and gratefully acknowledge my debt to them.

I'm most grateful to my supervisor and mentor Dr. Armin Zeh for his patient support throughout the last four years and for his enthusiasm for the Earth sciences. It is to him that I owe my deeper understanding of many geological aspects ranging from the microscopic to regional scales. His field expertise, sense for geological details, expert knowledge in metamorphic petrology, and thorough proof reading of earlier versions of this thesis proved invaluable. I must also thank him for the many stimulating scientific conversations, as well as for his friendship.

I am also deeply indebted to Prof. Dr. Reiner Klemd for initiating this project in southern Africa and for all of the assistance he provided during the field study as well as throughout the course of writing this thesis. I must also thank him for sharing his vast geological knowledge with the workgroup and for the entertaining conversations which we have shared. I wish him all the best, and hope that he enjoys his time in Erlangen!

I also wish to thank a number of people from the Mineralogical Department of Würzburg (now Department of Geodyamics and Geomaterialsciences); Prof. Dr. Ulli Schüssler for his assistance with the microprobe and the XRF, Prof. Dr. Martin Okrusch for providing me with valuable literature, Prof. Dr. Hartwig Frimmel for his interesting observations and comments, Peter Späthe for his excellent thin sections and fruitful discussions about geology (as well as life), and Hans-Peter Kelber for opening my eyes to the aesthetic aspects of scientific illustrations and publications.

From the (former) students of the workgroup, special thanks belong to Dipl.-Geol. Thomas Chudy for his collegial support, whether in Würzburg or abroad, and his deftness in surprising, Dipl.-Geol. Andreas Beinlich for challenging talks, lively tales about New Zealand's' glastails and his open mindedness, Ira Biederman for assisting me during the preparation of presentation posters and talks as well as for supplying fusion disks, and for the many great times in "normal" life over the years. I'm also grateful to my part-time office associate Dipl.-Min. Marco Depine for the many discussions about geology (as well as for many amusing conversations not about geology). I must also thank my long-time university colleagues Johannes

Pätzold and Johannes Mederer for always knowing where the truth lies. I must also note, the quality of this thesis, as well as life, was greatly improved by the friendship of Dipl.-Min. Maria Kirchenbaur, Dr. Sven Wille and Dipl.-Min. Nicole Pfeiffer.

I'm very grateful to Prof. Dr. Jay M. Barton for his hospitaliy in Johannesburg, for providing us with geological maps, and for sharing his geological knowledge with us in the field. I must also thank his wife, Dr. Erika Barton, for the accommodation and delicious meals.

I wish to extend a hearty thanks to Dr. Roger Powell, Dr. Michael J. Holdaway, Dr. E.K. Esawi and Dr. Darrell J. Henry for their friendly and helpful support while using their geological software.

From the non-geological community, I'm utmost grateful to my girlfriend Dipl.-Chem. Katrin Barth for supporting me mentally and scientifically during the years. I also wish to thank my friends Dipl.-Päd. Philipp Falkenberg, Dipl.-Päd. Thomas Grob, and (Graphic Designer to-be) Stefan Ott for their many conversations about a broad range of topics concerning the humanities, humanity, and for celebrating life as it is.

The financial support of the Deutsche Forschungsgemeinschaft (DFG)-(grant KL692/16-1/2) is gratefully acknowledged.

Lastly, but surely not least, I would like to thank my mother and family for their unwavering encouragement and support throughout the years.

The best of luck and health to all I mentioned, as well as to the many many I have forgot to mention!

References

Aldiss, D.T., 1991. The Motloutse Complex and the Zimbabwe Craton/Limpopo Belt transition in Botswana. Precambrian Research, 50, 89-109.

Alsop, G.I. & Holdsworth, R.E., 2004. Shear zones - an introduction and overview. From: Alsop, G.I., Holdsworth, R.E., McCaffrey, K.J.W., Hand, M. (Editors). Flow Processes in Faults and Shear Zones. Geological Society, London, Special Publications 224, 1-9.

Armstrong, R., Compston, W., Dodson, M.H., Kröner, A., Williams, I.S., 1988. Archean crustal history in southern Africa. In: Research School of Earth Sciences, Australian National University, Annual Report 1987, 62-64.

Baldwin, J.A., Powell, R., Brown, M., Moraes, R., Fuck, R.A., 2005. Modelling of mineral equilibria in ultrahigh-temperature metamorphic rocks from the Anápolis-Itauçu Complex, central Brazil. Journal of Metamorphic Geology 23, 511-531.

Barton, J.M., Jr., Fripp, R.E.P., Ryan, B., 1977. Rb/Sr ages and geological setting of ancient dykes in the Sand River area, Limpopo mobile belt, South Africa. Nature 267, 487-490.

Barton, J.M., 1983. Our understanding of the Limpopo Belt - a summary with proposals for future research. Geological Society of South Africa, Special Publications 8:, 191-203.

Barton, J.M., Jr., Van Reenen, D.D., Roering, C., 1990. The significance of 3000 Ma granulite-facies mafic dikes in the central zone of the Limpopo belt, southern Africa. Precambrian Research 48, 299-308.

Barton, J.M., Jr., Holzer, L., Kamber, B., Doig, R., Kramers, J.D., Nyfeler, D., 1994. Discrete metamorphic events in the Limpopo belt, southern Africa: Implications for the application of *P-T* paths in complex metamorphic terranes. Geology 22, 1035-1038.

Barton, J.M., Jr., Sergeev, S., 1997. High precision, U-Pb analyses of single grains of zircon from quartzite in the Beit Bridge Group yield a discordia. South African Journal of Geology 100, 37-41.

Barton, J.M., Jr., Barnett, W.P., Barton, E.S., Barnett, M., Doorgapershad, A., Twiggs, C., Klemd, R., Martin, J., Millonig, L., Zenglein, R., 2003. The geology of the area surrounding the Venetia kimberlite pipes, Limpopo Belt, South Africa, A complex interplay of nappe tectonics and granitoid magmatism. South African Journal of Geology 106, 109-128.

Barton, J.M., Jr., Klemd, R., Zeh, A., 2006. The Limpopo Belt: A result of Archean to Proterozoic, Turkic-type orogenesis? In: Reimoldt, U., Gibson, R. (Eds.), Processes on the Early Earth. Geological Society of America Special Paper 405, 315-332.

Berger, M., Kramers, J.D., Nägler, T.F., 1995. An Archean high grade province adjacent to a granite greenstone terrain: geochemistry and geochronology of charnoenderbites in the Northern Marginal Zone of the Limpopo Belt, Southern Africa and genetic models. Schweizerische Mineralogische und Petrographische Mitteilungen 75, 17-42.

Berger, M., Rollinson, H., 1997. Isotopic and geochemical evidence for crust-mantle interaction during late Archean crustal growth. Geochimica et Cosmochimica Acta 61, 4809-4829.

Blenkinsop, T.G., & Kisters, A.F.M., 2005. Steep extrusion of late Archean granulites in the Northern Marginal Zone, Zimbabwe: evidence for secular change in orogenic style. From: Gapais, D., Brun, J.P., Cobbold, P.R. (Editors). In: Deformation Mechanisms, Rheology and Tectonics: from Minerals to the Lithosphere. Geological Society, London, Special Publications 243, 193-204.

Bohlen, S.R. & Liotta, J.J., 1986. A Barometer for Garnet Amphibolites and Garnet Granulites. Journal of Petrology 27, 1025-1034.

Boryta, M. and Condie, K.C., 1990. Geochemistry and origin of the Archean Beit Bridge complex, Limpopo Belt, South Africa. Journal of the Geological Society of London 147, 229-239.

Boshoff, R., 2004. Formation of major fold types during distinct geological events in the Central Zone of the Limpopo Belt, South Africa: new structural, metamorphic and geochronological data. Ph.D. thesis, Rand Afrikaans University, Johannesburg, pp. 121.

Boshoff, R., Van Reenen, D.D., Smit, C.A., Perchuk, L.L., Kramers, J.D., Armstrong, R., 2006. Geologic History of the Central Zone of the Limpopo Complex: The West Alldays Area. Journal of Geology 114, 699-716.

Brandl, G. & Reimold, W.U., 1990. The structural setting and deformation associated with pseudotachylite occurrences in the Palala Shear Belt and Sand River gneiss, Northern Transvaal. Tectonophysics. 171, 201-220.

Brandl, G. (Compiler), 1992. Geological map of the Limpopo belt and its environs 1:500 000. Contribution to a field work-shop on granulites and deep crustal tectonics, 1990. Geological Survey of South Africa, Pretoria.

Brandl, G., Pretorius, S.J., 2000. 1:250 000 Geological Map of the 2228 Alldays Sheet. South African Council for Geoscience, Private Bag X112, Pretoria, 0001.

Brown, M., 2007. Metamorphic Conditions in Orogenic Belts: A Record of Secular Change. International Geology Review 49, 193-234.

Buick, I.S., Maas, R., Gibson, R., 2001. Precise U-Pb titanite age constraints on the emplacement of the Bushveld Complex, South Africa. Journal of the Geological Society (London) 158, 3-6.

Buick, I.S., Williams, I.S., Gibson, R.L., Cartwright, I., Miller, J.A., 2003. Carbon and U-Pb evidence for a Palaeoproterozoic crustal component in the Central Zone of the Limpopo Belt, South Africa. Journal of the Geological Society (London) 160, 601-612.

Buick, I.S., Hermann, J., Williams, I.S., Gibson, R.L., Rubatto, D., 2006. A SHRIMP U-Pb and LA-ICP-MS trace element study of the petrogenesis of garnet-cordierite-orthoamphibole gneisses from the Central Zone of the Limpopo Belt, South Africa. Lithos 88, 150-172.

Bumby A.J., Eriksson P.G., Van Der Merwe, R., 2004. The early Proterozoic sedimentary record in the Blouberg area, Limpopo Province, South Africa; implications for the timing of the Limpopo orogenic event. Journal of African Earth Sciences 39, 123-131

Cahen, L., Snelling, N.J., Delhal, J., Vail, J.R., 1984. The geochronology and evolution of Africa. Clarendon Press, Oxford.

Carney, J.N., Aldiss, D.T., Lock, N.P., 1994. The geology of Botswana. Geological Survey Department, Bulletin 37, pp. 113.

Castro, A., Guillermo Corretgé, L., El-Biad, M., El-Hmidi, H., Fernandez, C., Patino Douce, A.E., 2000. Experimental Constraints on Hercynian Anatexis in the Iberian Massif, Spain. Journal of Petrology 41, 1471-1488.

Chavagnac, V., Kramers, J.D., Naegler, T.F., Holzer, L., 2001. The behaviour of Nd and Pb isotopes during 2.0 Ga migmatization in paragneisses of the Central Zone of the Limpopo Belt (South Africa and Botswana). Precambrian Research 112, 51-86.

Chudy, T.C., Zeh, A., Gerdes, A., Klemd, R., Barton, J.M., Jr., 2009. Paleoarchean (3.3 Ga) mafic magmatism and Paleoproterozoic (2.02 Ga) amphibolite-facies metamorphism in the Central Zone of the Limpopo Belt: New geochronological, petrological and geochemical constraints from metabasic and metapelitic rocks from the Venetia area. South African Journal of Earth Sciences, in press.

Clark, S.P. & Ringwood, A.E., 1964. Density distribution and constitution of the mantle. Reviews of Geophysics 2, 35-88.

Clarke, B., Uken, R., Reinhardt, J., 2008. Structural and compositional constraints on the emplacement of the Bushveld Complex, South Africa. Lithos-01857, in press.

Coward, M.P., Graham, R.H., James, P.R., Wakefield, J., 1972. An interpretation of the northern margin of the Limpopo orogenic belt, South Africa. 16th Annual Report Research Institute of African Geology/University of Leeds.

De Capitani, C., 2005. Theriak-Domino. http://titan.minpet.unibas.ch/minpet/theriak/theruser.html.

Didier, J., 1973. Granites and their enclaves. Developments in Petrology, Vol. 3, Elsevier, Amsterdam.

Diener, J. F. A., Powell, R., White, R.W., Holland, T. J. B., 2007. A new thermodynamic model for clino- and orthoamphiboles in the system Na_2O-CaO-FeO-MgO-Al_2O_3-SiO_2-H_2O-O. Journal of Metamorphic Geology, 25, 631-656.

Diener, J.F.A., Powell, R., White, R.W., 2008. Quantitative phase petrology of cordierite-orthoamphibole gneisses and related rocks. Journal of Metamorphic Geology 26, 795-814.

Dirks, P.H.G.M., 1998. Accretion and stabilisation of the Archean Zimbabwe Craton. Geologie en Mijnbouw 76, 365-368.

Eriksson, P.G., Catuneanu, O., Els, B.G., Bumby, A.J., Van Rooy, J.L., Popa, M., 2005. Kaapvaal Craton: Changing first- and second-order controls on sea level from 3.0 Ga to 2.0 Ga. Sedimentary Geology 176, 121-148.

Eriksson, P.G., Mazumder, R., Catuneanu, O., Bumby, A.J., Ountsché Ilondo, B., 2006. Precambrian continental freeboard and geological evolution: a time perspective. Earth-Science Reviews 79, 165-204.

Ernst, W.G., 2007. Speculations on evolution of the terrestrial lithosphere-asthenosphere system-plumes and plates. Gondwana Research 11, 38-49.

Esawi, E.K., 2004. AMPH-CLASS: An Excel spreadsheet for the classification and nomenclature of amphiboles based on the 1997 recommendations of the International Mineralogical Association. Computers & Geosciences 30, 753-760.

Gardien, V., Thompson, A.B., Ulmer, P., 2000. Melting of biotite + plagioclase + quartz gneisses: the role of H2O in the stability of amphibole. Journal of Petrology 41, 651-666.

Gerdes, A. & Zeh, A., 2006. Combined U-Pb and Hf isotope LA-(MC)ICP-MS analyses of detrital zircons: Comparison with SHRIMP and new constraints for the provenance and age of an Armorican metasediment in Central Germany. Earth and Planetary Science Letters 249, 47-61.

Gerdes, A. & Zeh, A., 2008. Zircon formation versus zircon alteration - new insights from combined U-Pb and Lu-Hf in situ LA-ICP-MS analyses, and consequences for the interpretation of Archean zircon from the Central Zone of the Limpopo Belt. Chemical Geology, in press.

Gerya, T.V., Perchuk, L.L., Van Reenen, D.D., 2000. Two-Dimensional Numerical Modeling of Pressure-Temperature-Time Paths for the Exhumation of Some Granulite Facies Terrains in the Precambrian. Journal of Geodynamics 30, 17-35.

Guiraud, M., Powell, R., Rebay, G., 2001. H_2O in metamorphism and unexpected behaviour in the preservation of metamorphic mineral assemblages. Journal of Metamorphic Geology 19, 445-454.

Gutzmer, J. & Beukes, N.J., 1998. High grade manganese ores in the Kalahari manganese field: Characterisation and dating of the ore-forming events. Unpublished Report, Rand Afrikaans University, Johannesburg, pp. 221.

Halpin, J.A., White, R.W., Clarke, G.L., Kelsey, D.E., 2007. The Proterozoic *P-T-t* Evolution of the Kemp Land Coast, East Antarctica; Constraints from Si-saturated and Si-undersaturated Metapelites. Journal of Petrology 48, 1321-1349.

Hand, M., Dirks, P.H.G.M., Powell, R., Buick, I.S., 1992. How well established is isobaric cooling in Proterozoic orogenic belts? An example from the Arunta Inlier, central Australia. Geology 20, 649-652.

Harris, N.B.W., McMillan, A., Holness, M.B., Uken, R., Watkeys, M., Rogers, N., Fallick, A., 2003. Melt generation and fluid flow in the thermal aureole of the Bushveld complex. Journal of Petrology 44, 1031-1054.

Hatton, C.J., 1995. Mantle plume origin for the Bushveld and Ventersdorp magmatic provinces. Jonmal of African Earth Sciences 21, 571-577.

Hatton, C.J. & Schweitzer, J.K., 1995. Evidence for synchronous extrusive and intrusive Bushveld magmatism. Journal of African Earth Sciences 21, 579-594.

Henry, D.J. & Guidotti, C.V., 2002. Titanium in biotite from metapelitic rocks: Temperature effects, crystal-chemical controls, and petrologic applications. American Mineralogist 87, 375-382.

Hickman, M.H. & Wakefield, J., 1975. Tectonic implications of new geochronologic data from the Limpopo belt at Pikwe, Botswana, southern Africa. Geological Society of America Bulletin 86, 1468-1472.

Hisada, K., Miyano. T., Van Reenen, D.D., 1994a. Fluid inclusion study on gedrite formation in metapelites near Maretele in the Limpopo Central Zone, Eastern Botswana. Science Report, Institute of Geosience University Tsukuba, Section B, 15, 1-7.

Hisada, K., Key, R.M., Paya, B.K., Miyano, T., 1994b. Petrographic studies on metamorphic rocks from Topisi in the western margin of the Limpopo Belt. Annual Report, Institute of Geoscience University of Tsukuba, 20, 51-57.

Hisada, K., Miyano, T., 1996. Petrology and microthermometry of aluminous rocks in the Botswanan Limpopo Central Zone: evidence for isothermal decompression and isobaric cooling. Journal of Metamorphic Geology 14, 183-197.

Hisada, K., 1997. Phase analysis of high-grade pelites during retrograde metamorphism and its application to the metamorphic history of the Limpopo Belt, eastern Botswana. Institute of Geoscience, University of Tsukuba, Tsukuba/Japan. Annual report.

Hisada, K., Perchuk, L.L., Gerya, T.V., Van Reenen, D.D., Paya, B.K., 2005. *P-T*-fluid evolution in the Mahalapye Complex, Limpopo high-grade terrane, eastern Botswana. Journal of Metamorphic Geology 23, 313-334.

Hoisch, T.D., 1990. Empirical calibration of six geobarometers for the mineral assemblage quartz + muscovite + biotite + plagioclase + garnet. Contributions to Mineralogy and Petrology 104, 225-234.

Hoisch, T.D, 1991. Equilibria within the mineral assemblage quartz + muscovite + biotite + garnet + plagioclase, and implications for the mixing properties of octahedrally-coordinated cations in muscovite and biotite. Contributions to Mineralogy and Petrology 108, 43 54.

Holdaway, M.J., 2000. Application of new experimental and garnet Margules data to the garnet-biotite geothermometer. American Mineralogist 85, 881-892.

Holdaway, M.J., 2001. Recalibration of the GASP geobarometer in light of recent garnet and plagioclase activity models and versions of the garnet-biotite geothermometer. American Mineralogist 86, 1117-1129.

Holland, T.J.B. & Powell, R., 1990. An enlarged and updated internally consistent thermodynamic dataset with uncertainties and correlations: the system K_2O-Na_2O-CaO-MgO-MnO-FeO-Fe_2O_3-Al_2O_3-TiO_2-SiO_2-C-H_2-O_2. Journal of Metamorphic Geology 8, 89-124.

Holland, T..J.B. & Blundy, J., 1994. Non-ideal interactions in calcic amphiboles and their bearing on amphibole-plagioclase thermometry. Contrib. Mineralogy and Petrology 116, 433-447.

Holland, T.J.B. & Powell, R., 1998. An internally consistent thermodynamic data set of petrological interest. Journal of Metamorphic Geology 16, 309-343.

Holness, M.B. & Clemens, J.D., 1999. Partial melting of the Appin Quartzite driven by fracture-controlled H_2O infiltration in the aureole of the Ballachulish Igneous Complex, Scottish Highlands. Contributions to Mineralogy and Petrology 136, 154-168.

Holzer, L., Frei, R., Barton, J.M., Jr., Kramers, J.D., 1998. Unraveling the record of successive high grade events in the Central Zone of the Limpopo Belt using Pb single

phase dating of metamorphic minerals. Precambrian Research 87, 87-115.

Holzer, L., Barton, J.M., Jr., Paya, B.K., Kramers, J.D., 1999. Tectonothermal history in the western part of the Limpopo Belt: test of tectonic models and new perspectives. Journal of African Earth Sciences 28, 383-402.

Horrocks, P.C., 1983. The Precambrian Geology of an area between Messina and Tshipise, Limpopo Mobile Belt. Special Publications Geological Society South Africa 8, 81-88.

Horstwood, M.S.A., Foster, G.L., Parrish, R.R., Noble, S.R., Nowell, G.M., 2003. Common-Pb corrected in-situ U-Pb accessory mineral geochronology by LA-MC-ICPMS. Journal of Analytical Atomic Spectrometry 18, 837-846.

Iole Spalla, M., Zucali, M., Di Paola, S. Gosso, G., 2005. A critical assessment of the tectono-thermal memory of rocks and definition of tectono-metamorphic units: evidence from fabric and degree of metamorphic transformations. Geological Society of London, Special Publications 243, 227-247.

Jaeckel, P., Kröner, A., Kamo, S.L, Brandl, G., Wendt, J.I., 1997. Late Archean to early Proterozoic granitoid magmatism and high-grade metamorphism in the central Limpopo belt, South Africa. Journal of the Geological Society (London) 154, 25-44.

Kamber, B.S., Blenkinsop, T.G., Villa, I.M., Dahl, P.S., 1995a. Proterozoic transpressive deformation in the Northern Marginal Zone, Limpopo Belt, Zimbabwe. Journal of Geology 100, 490-508.

Kamber, B.S., Kramers, J.D., Napier, R., Cliff, R.A., Rollinson, H.R., 1995b. The Triangle Shearzone, Zimbabwe, revisited, new data document an important event at 2.0 Ga in the Limpopo Belt. Precambrian Research 70, 191-213.

Kelsey, D.E., White, R.W., Powell R., Wilson, C.J.L., Quinn, C.D., 2003. New constraints on metamorphism in the Rauer Group, Prydz Bay, east Antarctica. Journal of Metamorphic Geology 21, 739-759.

Key, R.M. & Hutton, S.M., 1976. The tectonic generation of the Limpopo Mobile Belt, and a definition of its western extremity. Precambrian Research 3, 79-90.

Key, R.M., Mapeo, R.B.M., van Zyl, H.E.M., Hargreaves, R.L., Holmes, H., 1994. The geology of the Topisi area, Botswana. Geological Survey Botswana, Lobatse. Bulletin 38, l-84.

Key, R.M. & Ayres, N., 2000. The 1998 edition of the National Geological Map of Botswana. Journal of African Earth Sciences 30, 427- 451.

Kleemann, U., Reinhardt, J., 1994. Garnet-biotite thermometry revised: the effect of Al^{VI} and Ti in biotite. European Journal of Mineralogy 6, 925-941.

Klemd, R., Schmidt, A., Martin, J., Barton, J.M., Jr., 2003. *P-T* path constraints from metapelitic rocks east of the Venetia kimberlite pipes, Central Zone, Limpopo Belt, South Africa: Have these rocks seen granulite-facies conditions? South African Journal of Geology 106, 129-148.

Koester, E., Pawley, A.R., Fernandes, L.A.D., Porcher, C.C., Solinani Jr., E., 2002. Experimental Melting of Cordierite Gneiss and the Petrogenesis of Syntranscurrent Peraluminous Granites in Southern Brazil. Journal of Petrology 43, 1595-1616.

Kohn, M.J, & Spear, F.S., 1990. Two new geobarometers for garnet amphibolites, with applications to southeastern Vermont. American Mineralogist 75, 89-96.

Kohn, M.J, & Spear, F.S., 2000. Retrograde net transfer reaction insurance for pressure-temperature estimates. Geology 28, 1127-1130.

Kramers, J.D., McCourt, S., van Reenen, D.D., 2007, The Limpopo Belt. The geology of South Africa, in Johnson, M.R., Anhaeusser, C., Thomas, R.J.. Geological Society of South Africa, Johannesburg, and Council for Geoscience, Pretoria, South Africa, 209-236.

Kreissig, K., Holzer, L., Frei, R., Villa, I.M., Kramers, J.D., Kroener, A., Smit, C.A., Van Reenen, D.D., 2001. Geochronology of the Hout River shear zone and the metamorphism in the Southern marginal zone of the Limpopo Belt, Southern Africa. Precambrian Research 109, 145-173.

Kretz, R., 1983. Symbols for rock forming minerals. American Mineralogist 68, 277-279.

Krogh, E. J., 1988. The garnet-clinopyroxene Fe-Mg geothermometer - a reinterpretation of existing experimental data. Contributions to Mineralogy and Petrology 99, 44-48.

Kröner, A., Jaeckel, P., Hofmann, A., Nemchin, A.A., Brandl, G., 1998. Field relationships and age of supracrustal Beit Bridge Complex and associated granitoid gneisses in the Central Zone of the Limpopo Belt, South Africa. South African Journal of Geology 101, 201-213.

Kröner, A., Jaeckel, P., Brandl, G., Nemchin, A.A., Pidgeon, R.T., 1999. Single zircon ages for granitoid gneisses in the Central Zone of the Limpopo Belt, Southern Africa and geodynamic significance. Precambrian Research 93, 299-337.

Lambert, R.St.J., 1976. Archean thermal regimes, crustal and upper mantle temperatures, and a progressive evolutionary model for the earth. In: Windley, B.F. (Editor), The Early History of the Earth. John Wiley, New York, 363-373.

Le Breton, N. & Thompson, A.B., 1988. Fluid-absent (dehydration) melting of biotite in metapelites in the

early stages of crustal anatexis. Contributions to Mineralogy and Petrology 99, 226-237.

Leake, B.E., Woolet, A.R., Arps, C.E.S., Birch, W.D., Gilbert, M.C., Grice, J.D., Hawthorne, F.C., Kato, A., Kisch, H.J., Krivovichev, et al., 1997. Nomenclature of Amphiboles: report of the subcommittee on amphiboles of the International Mineralogical Association, commission on new minerals and mineral names. Canadian Mineralogist 35, 219-246.

Leake, B.E., Birch, W.D., Burke, E.A.J., Ferraris, G., Grice, J.D., Hawthorne, F.C., Kisch, H.J., Krivovichev, V.G., Schuhmacher, J.C., Stephenson, N.C.N., Whittaker, E.J.W., 2003. Nomenclature of amphiboles: additions and revisions to the International Mineralogical Association's 1997 recommendations. Canadian Mineralogist 41, 1355-1362.

Liou, J.G., Zhang, R.Y., Ernst, W.G., Rumble III, D., Maruyama, S., 1998. High pressure minerals from deeply subducted metamorphic rocks. Reviews in Mineralogy 37, 33-96.

Mahar, E.M., Baker, J.M., Powell, R., Holland, T.J.B., Howell, N., 1997. The effect of Mn on mineral stability in metapelites. Journal of Metamorphic Geology 15, 223-238.

Majaule, T., Hanson, R.E., Key, R.M., Singletary, S.J., Martin, M.W., Bowring, S.A., 2001. The Magondi Belt in northeast Botswana: regional relations and new geochronological data from the Sua Pan area. Journal of African Earth Sciences 32, 257-267.

Mapeo, R.B.M., Kampunzu, A.B., Ramokate, L.V., Corfu, F., Key, R.M., 2004. Bushveld-age magmatism in southeastern Botswana: evidence from U-Pb and Titanite geochronology of the Moshaneng Complex. South African Journal of Geology 107, Kaapvaal Craton Special Volume, 219-232

McCourt, S., Vearncombe, J.R., 1987. Shear zones bounding the central zone of the Limpopo mobile belt, southern Africa. Journal of Structural Geology 9, 127-137.

McCourt, S., Vearncombe, J.R., 1992. Shear Zones of the Limpopo Belt and adjacent granitoid- greenstone terranes, implications for late Archean collision tectonics in Southern africa. Precambrian Research 55, 553-570.

McCourt, S., Armstrong, R.A., 1998. SHRIMP U-Pb zircon chronology of granites from the Central Zone, Limpopo Belt, southern Africa: implications for the age of the Limpopo Orogeny. South African Journal of Geology 101, 329-337.

McCourt, S., Kampunzu, A.B., Bagai, Z., Armstrong, R.A., 2004. Crustal architecture of Archean terranes in Northeastern Botswana. South African Journal of Geology 107, 146-158.

Millonig, L.J., Zeh, A., Gerdes, A., Klemd, R., 2008. Neoarchean high-grade metamorphism in the Central Zone of the Limpopo Belt (South Africa): Combined petrological and geochronological evidence from the Bulai Pluton. Lithos 103, 333-351

Mkweli, S., Kamber, B., Berger, M., 1995. Westward continuation of the craton-Limpopo Belt tectonic break in Zimbabwe and new age constraints on the timing of the thrusting. Journal of the Geological Society (London) 152, 77-83.

Morimoto, N., Fabries, J., Ferguson, A.K., Ginzburg, I.V., Ross, M., Seifert, F.A., Zussman, J., Aoki, K., Gottardi, G., 1988. Nomenclature of pyroxenes. American Mineralogist 73, 1123-1133.

Naney, M.T., Swanson, S.E., 1980. The effect of Fe and Mg on crytsallization in garnitic systems. American Mineralogist 65, no.7-8, 639-653.

Nguuri, T.K., Gore, J., James, D.E., Wright, C., Zengeni, T.D., Gwavava, O., Webb, S.J., Snoke, J.A., and the Kaapvaal Seismic Group, 2001. Crustal structure beneath southern Africa and its implications for the formation and evolution of the Kaapvaal and Zimbabwe cratons. Geophysical Research Letters 28, 2501-2504.

Okamoto, K., Maruyama, S., 1999. The high pressure synthesis of lawsonite in the MORB+H2O system. American Mineralogist 84, 362-373.

Paya, B.K., 1996. The Geology of the Bobonong area. Geological Survey Botswana, Lobatse, Bulletin 40, l-60.

Perchuk, L.L., Gerya, T.V., Van Reenen, D.D., Smit, C.A., 2006. *P-T* Paths and Problems of High-Temperature Polymetamorphism. Petrology 14, 117-153.

Perchuk, L.L. & Van Reenen, D.D., 2008. Reply to "Comments on "*P-T* record of two high-grade metamorphic events in the Central Zone of the Limpopo Complex, South Africa"" by A. Zeh and R. Klemd. Lithos 106, 403-410.

Pollack, H.N., 1997. Thermal characteristics of the Archean. In: De Wit, M.J., Ashwal, L.D. (Editors), Greenstone Belts, Oxford Monographs on Geology and Geophysics 35, 223-232.

Powell, R. & Holland, T.J.B., 1988. An internally consistent thermodynamic dataset with uncertainties and correlations: 3. Applications to geobarometry, worked examples and a computer program. Journal of Metamorphic Geology 6, 173-204.

Ranganai, R.T., Kampunzu, A.B., Atekwana, E. A., Paya, B. K., King, J. G., Koosimile, D. I., Stettler, E. H., 2002. Gravity evidence for a larger Limpopo Belt in southern Africa and geodynamic implications. Geophysical Journal International 149, F9-F14.

Richter, F.M., 1988. A major change in the thermal state of the Earth at the Archean-Proterozoic boundary: consequences for the nature and preservation of

continental lithosphere. Journal of Petrology, Special Lithos Issue, 39-52.

Rigby, M., Mouri, H., Brandl, G., 2008. A review of the pressure-temperature-time evolution of the Limpopo Belt: Constraints for a tectonic model. Journal of African Earth Sciences 50, 120-132.

Robertson, I.D.M. & du Toit, M.C., 1981. The Limpopo Belt. In: Hunter, D.R. (Editor), Precambrian of the Southern Hemisphere. Elsevier, Amsterdam, 641-670.

Roering, C., Van Reenen, D.D., Smit, C.A., Barton Jr., J.M., De Beer, J.H., De Wit, M.J., Stettler, E.H., van Schalkwyk, J.F., Stevens, G., Pretorius, S., 1992. Tectonic model for the evolution of the Limpopo Belt. Precambrian Research 55, 539-552.

Rollinson, H.R., 1993. A terrane interpretation of the Archean Limpopo Belt. Geological Magazine 130, 755-765.

Rollinson, H.R. & Blenkinsop, T., 1995. The magmatic, metamorphic and tectonic evolution of the Northern Marginal Zone of the Limpopo Belt in Zimbabwe. Journal of the Geological Society (London) 152, 66-75.

Sawyer, E.W., 1999. Criteria for the recognition of partial melting. Physics and Chemistry of the Earth (A) 24, 269-279.

Silver, P.G., Fouch, M.J., Gao, S.S., Schmitz, M. and the Kaapvaal Seismic Group. Seismic anisotropy, mantle fabric, and the magmatic evolution of Precambrian southern Africa. South African Journal of Geology 107, 45-58.

Spear, F.S. & Florence, F.P., 1992. Thermobarometry in granulites: pitfalls and new approaches. Precambrian Research 55, 209-241.

Spear, F.S., 1993. Metamorphic Phase Equilibria and Pressure-Temperature-Time paths. Mineralogical Society of America, Washington DC, pp. 799.

Spear, F.S., Kohn, M.J., Chene, J.T., 1999. P -T paths from anatectic pelites. Contributions to Mineralogy and Petrology 134, 17-32.

Spear, F.S. & Kohn, M.J., 2001, Program GTB: GeoThermoBarometry: Rensselaer Polytechnic Institute. http://ees2.geo.rpi.edu/MetaPetaRen/Software/GTB_Prog/GTB.html.

Stevens, G., Clemens, J.D., Droop, G.T.R., 1997. Melt production during granulite-facies anatexis: experimental data from "primitive" metasedimentary protoliths. Contributions to Mineralogy and Petrology 128, 352-370.

Stowe, C.W., Hartnady, C.J.H., Joubert, P.., 1984. Proterozoic Tectonic Provinces of Southern Africa. Precambrian Research 25, 229-231.

Taylor, S.R., Rudnick, R.L., McLennan, S.M., Eriksson, K.A., 1986. Rare earth element patterns in Archean high-grade metasediments and their tectonic significance. Geochimica et Cosmochimica Acta 50, 2267-2279.

Treloar, P.J., 1988. The geological evolution of the Magondi Mobile Belt, Zimbabwe. Precambrian Research 38, 55-73.

Tsunogae, T., Miyano, T., Machacha, T.P., 1989. Retrograde orthoamphiboles in metapelites near Maratele, Southwest Selebi-Phikwe, Botswana. Annual Report of the Institute of Geoscience, University of Tsukuba 15, 121-126.

Tsunogae, T., Miyano, T., Van Reenen, D.D., Smit, A.C., 2004. Ultrahigh-temperature metamorphism of the Southern Marginal Zone of the Archean Limpopo Belt, South Africa. Journal of Mineralogical and Petrological Sciences 99, 213-224.

Van Breemen, O. & Dodson, M.H., 1972. Metamorphic chronology of the Limpopo Belt, southern Africa. Bulletin Geological Society of America 83, 2005-2018.

Van Breemen, O. & Hawkesworth, C.J., 1980. Sm-Nd isotopic studies of garnets and their metamorphic host rocks. Transactions Royal Society Edinburgh, Earth Science 71, 97-l 02.

Van Reenen, D.D., Barton, J.M., Jr., Roering, C., Smit, C.A., van Schalkwyk, J.F., 1987. Deep crustal response to continental collision: The Limpopo belt of southern Africa. Geology 15, 11-14.

Van Reenen, D.D., Roering, C., Smit, C.A., Barton, J.M., Jr., 1990. The granulite facies rocks of the Limpopo Belt, South Africa. In: Vielzeuf, D. and Vidal, P. (Eds.), Granulites and crustal evolution. NATO-ASI Series C211, Luwer, Dordrecht, 257-289.

Van Reenen, D.D., Perchuk, L.L., Smit, C.A., Varlamov, D.A., Boshoff, R., Huizenga, J.M., Gerya, T.V., 2004. Structural and *P-T* evolution of a major cross fold in the central zone of the Limpopo high-grade terrain. South Africa. Journal of Petrology 45, 1413-1439.

Van Reenen. D.D., Boshoff, R., Smit, C.A., Perchuk, L.L., Kramers, J.D., McCourt, S., Armstrong, R.A, 2008. Geochronological problems related to polymetamorphism in the Limpopo Complex, South Africa. Gondwana Research 14, 644-662

Vernon, H.R., 1996. Problems with inferring *P-T*-t paths in low-P granulite facies rocks. Journal of Metamorphic Geology 14, 143-153.

Vielzeuf, D. & Schmidt, M.W., 2001. Melting relations in hydrous systems revisited: application to metapelites, metagreywackes and metabasalts. Contributions to Mineralogy and Petrology 141, 251-267.

von Seckendorf, V., Timmermann, M.J., Kramer, W., Wrobel, P., 2001. New $^{40}Ar/^{39}Ar$ ages and geochemistry of late Carboniferous-early Permian lamprophyres and

related volcanic rocks in the Saxothuringian Zone of the Variscan Orogen (Germany). Special Publications Geological Society of London 223, 319-334.

Wakefield, J., 1974. The geology of the Pikwe Ni-Cu province, eastern Botswana. Ph.D. thesis. Leeds, England, University of Leeds, pp. 199.

Waters, D.J., 2001. The significance of prograde and retrograde quartz-bearing intergrowth microstructures in partially melted granulite-facies rocks. Lithos 56, 97-110.

Watkeys, M.K., 1984. The Precambrian geology of the Limpopo Belt north and west of Messina. PhD thesis (unpublished), University of the Witwatersrand, Johannesburg, South Africa, pp. 49.

Watkeys, M.K. & Armstrong, R.A., 1985. The importance of being alkaline - deformed late Archean lamprophyric dykes, Central Zone, Limpopo Belt. Transactions of the Geological Society of South Africa 88, 195-206.

White, R.W., Powell, R., Holland T.J.B., Worley, B.A., 2000. The effect of TiO_2 and Fe_2O_3 on metapelitic assemblages at greenschist and amphibolite facies conditions: mineral equilibria calculations in the system K_2O-FeO-MgO-Al_2O_3-SiO_2-H_2O-TiO_2-Fe_2O_3. Journal of Metamorphic Geology 18, 497-511.

White, R.W., Powell, R., Holland, T.J.B., 2001. Calculation of partial melting equilibria in the system Na_2O-CaO-K_2O-FeO-MgO-Al_2O_3-SiO_2-H_2O (NCKFMASH). Journal of Metamorphic Geology 19, 139-153.

White, R.W., Powell, R., Clarke, G.L., 2002. The interpretation of reaction textures in Fe-rich metapelitic granulites of the Musgrave Block, central Australia: constraints from mineral equilibria calculations in the system K_2O-FeO-MgO-Al_2O_3-SiO_2-H_2O-TiO_2-Fe_2O_3. Journal of Metamorphic Geology 20, 41-55.

White, R.W., Powell, R. and Clarke, G.L., 2003. Prograde Metamorphic Assemblage Evolution during Partial Melting of Metasedimentary Rocks at Low Pressures: Migmatites from Mt Stafford, Central Australia. Journal of Petrology 44, 1937-1960.

White, R. W., Powell, R., Holland, T.J.B., 2007. Progress relating to calculation of partial melting equilibria for metapelites. Journal of Metamorphic Geology, 25, 511-527.

Willmore, C.C., Boudreau, A.E., Spivack, A., Kruger, F.J., 2002. Halogens of the Bushveld Complex, South Africa: δ37Cl and Cl/F evidence for hydration melting of the source region in a back-arc setting. Chemical Geology 182, 503-511.

Wu, C.-M. Zhang, J., Ren, L.-D., 2004. Empirical Garnet-Biotite-Plagioclase-Quartz (GBPQ) Geobarometry in Medium- to High-Grade Metapelites. Journal of Petrology 45, 1907-1921.

Wu, C.-M., Cheng, B.-H., 2006. Valid garnet-biotite (GB) geothermometry and garnet-aluminium silicate-plagioclase-quartz (GASP) geobarometry in metapelitic rocks. Lithos 89, 1-23.

Zeh, A. & Millar, I.L., 2001. Metamorphic evolution of garnet-epidote-biotite gneiss from the Moine Supergroup, Scotland, and geotectonic implications. Journal of Petrology 42, 529-554.

Zeh, A. & Holness, M., 2003. The Effect of Reaction Overstep on Garnet Microtextures in Metapelitic Rocks of the Ilesha Schist Belt, SW Nigeria. Journal of Petrology 44, 967-994.

Zeh, A., Millar, I.L., Horstwood, S.A., 2004a. Polymetamorphism in the NE Shackleton Range, Antarctica; constraints from petrology and U-Pb, Sm-Nd, Rb-Sr TIMS and in situ U-Pb LA-PIMMS dating. Journal of Petrology 45, 949-973.

Zeh, A., Klemd, R., Buhlmann, S., Barton, J.M., Jr., 2004b. Pro- and retrograde *P-T* evolution of granulites of the Beit Bridge Complex (Limpopo Belt, South Africa); constraints from quantitative phase diagrams and geotectonic implications. Journal of Metamorphic Geology 22, 79-95.

Zeh, A., Klemd, R., Barton, J.M., Jr. , 2005a. Petrological evolution in the roof of the high-grade metamorphic Central Zone of the Limpopo Belt, South Africa. Geological Magazine 142, 229-240.

Zeh, A., Holland, T.J.B., Klemd, R., 2005b. Phase relationships in grunerite-garnet-bearing amphibolites in the system CFMASH, with applications to metamorphic rocks from the central zone of the Limpopo Belt, South Africa. Journal of Metamorphic Geology 23, 1-17.

Zeh, A., Gerdes, A., Will, T.M., Millar, I.L., 2005c. Provenance and Magmatic-Metamorphic Evolution of a Variscan Island-arc Complex: Constraints from U-Pb dating, Petrology, and Geospeedometry of the Kyffhäuser Crystalline Complex, Central Germany, J. Petrol. 46, 1393-1420.

Zeh, A., Gerdes, A., Klemd. R., Barton, J.M., Jr., 2007. Archean to Proterozoic Crustal Evolution in the Central Zone of the Limpopo Belt (South Africa-Botswana): Constraints from Combined U-Pb and Lu-Hf isotope Analyses of Zircon. Journal of Petrology 48, 1605-1639.

Zeh, A. & Klemd, R., 2008. Comments on "*P-T* record of two high-grade metamorphic events in the Central Zone of the Limpopo Complex, South Africa" by L. L. Perchuk, D. D. van Reenen, D. A. Varlamov, S. M. van Kal, Tabatabaeimanesh, R. Boshoff. Lithos 106, 399-402.

Zeh, A., Gerdes, A., Millonig, L., Klemd, R., Barton, J.M., 2008. Mono- versus Polymetamorphism of high-grade Metasediments from the Limpopo Belt, South Africa: Constraints from Petrology, in-situ U-Pb Zircon and

Monazite Dating and Lu-Hf Isotope Analyses. Journal of Petrology, submitted.

List of figures and tables

Appendix

23 Geothermobarometry

23.1 Geothermometers

23.1.1 Garnet-biotite (grt-bt)

The grt-bt geothermometer is based on the temperature dependent Fe-Mg exchange between garnet and biotite. The cation exchange reaction can be expressed as:

pyrope	+	annite	=	almandine	+	phlogopite
$Mg_3Al_2Si_3O_{12}$	+	$KFe_3(AlSi_3)O_{10}(OH)_2$	=	$Fe_3Al_2Si_3O_{12}$	+	$KMg_3(AlSi_3)O_{10}(OH)_2$

In this study the calibration of Holdaway (2001) (an improved calibration of the Holdaway (2000) geothermometer) was used, following the recommendation of Wu & Cheng (2006). These authors favour the use of the Kleemann & Reinhardt (1994) and Holdaway (2000) "*calibrations due to their small errors in reproducing the experimental temperatures…*".

The absolute error for the Holdaway (2001) calibration is stated to be ±25°C.

23.1.2 Ti-in-biotite (Ti-in-bt)

The Ti in biotite geothermometer was empirically calibrated by Henry *et al.* (2005) in the temperature range 400-800°C for graphitic, peraluminous metapelites that contain ilmenite or rutile, with biotite fulfilling the following compositional criteria:

X_{Mg} = 0.275-1.0 and Ti = 0.04-0.6 *a.p.f.u.* (= atoms per formula unit, with biotite normalised to 22 O).

The mathematical expression of the geothermometer is:

$T(°C)=\{[\ln(Ti)-a-c(X_{Mg})^3]/b\}^{0.333}$

X_{Mg} = MgO/(MgO+FeO); a = -2.3594; b = $4.6483*10^{-9}$ and c = -1.7283

23.1.3 Hornblende-plagioclase (hbl-pl)

The hbl-pl geothermometer of Holland & Blundy (1994)is based on the reactions:

Model A (for assemblages with quartz)

edenite	+	4 quartz	=	tremolite	+	albite

$NaCa_2Mg_5Si_4(AlSi_3)O_{22}(OH)_2$ + 4 SiO_2 = $Ca_2Mg_5Si_8O_{22}(OH)_2$ + $NaAlSi_3O_8$

Model B (for assemblages with or without quartz)

edenite	+	albite	=	richterite	+ anorthite
$NaCa_2Mg_5(AlSi_3)Si_4O_{22}(OH)_2$	+	$NaAlSi_3O_8$	=	$Na_2CaMg_5Si_8O_{22}(OH)_2$	+ $CaAl_2Si_2O_8$

The calibrations take into account non-ideal mixing in amphiboles and plagioclase. The hbl-pl thermometer can be used in the temperature range 400-900°C and requires that amphibole and plagioclase fulfill the following criteria:

Amphiboles: $Na^A > 0.02$ (*a.p.f.u.*), $Al^{Vi} < 1.8$ (*a.p.f.u.*), and Si in the range 6.0-7.7 (*a.p.f.u.*)
Plagioclase: $X_{an} < 0.90$.
The error for the hbl-pl geothermometer of Holland & Blundy (1994) is stated to be ±35-40°C.

23.1.4 Garnet-clinopyroxene (grt-cpx)

The grt-cpx geothermometer (*e.g.* Krogh, 1988) is based on the following Fe-Mg cation exchange reaction:

pyrope	+	hedenbergite	=	almandine	+	diopside
1/3 $Mg_3Al_2Si_3O_{12}$	+	$CaFeSi_2O_6$	=	1/3 $Fe_3Al_2Si_3O_{12}$	+	$CaMgSi_2O_6$

The geothermometer is expressed by the following equation:

$T_K(K)=((-6173*(X^{Grt}_{Ca})^2+6731*X^{Grt}_{Ca}+1879+10*P(kb))/(\ln K_D+1393))$ Krogh, 1988
X^{Grt}_{Ca}= Ca/(Ca+Fe^{2+}+Mg+Mn) and P in kbar
Errors are ±50°C (Krogh, 1988; see also Brey & Koehler, 1990).

23.2 Geobarometers

23.2.1 Garnet-biotite-plagioclase-quartz (grt-bt-pl)

The grt-bt-pl geobarometer (*e.g.* Hoisch 1990, 1991; Wu *et al.*, 2004) is based on the following Fe/Mg-model equilibria:

pyrope + 2 grossular + 3 eastonite + 6 quartz
= 6 anorthite + 3 phlogopite
$Mg_3Al_2Si_3O_{12}$ + 2 $Ca_3Al_2Si_3O_{12}$ + 3 $K(Mg_2Al_2)(Si_2Al_2)O_{10}(OH)_2$ + 6 SiO_2
= 6 $CaAl_2Si_2O_8$ + 3 $KMg_3(AlSi_3)O_{10}(OH)_2$

and

almandine + 2 grossular + 3 siderophyllite + 6 quartz

= 6 anorthite + 3 annite

$Fe_3Al_2Si_3O_{12}$ + 2 $Ca_3Al_2Si_3O_{12}$ + 3 $K(Fe_2Al)(Si_2Al_2)O_{10}(OH)_2$ + 6 SiO_2

= 6 $CaAl_2Si_2O_8$ + 3 $KFe_3(AlSi_3)O_{10}(OH)_2$

Errors are ±1.0 kbar (mostly ±0.5 kbar) (Wu *et al.*, 2004).

23.2.2 Garnet-hornblende-plagioclase (grt-hbl-pl)

The grt-hbl-pl geobarometer of Kohn & Spear (1990) was calibrated in the range 2.5 to 13 kbar and 500 to 800°C and should only be used, when the compositional parameters as shown in Tab. 23 are fulfilled. The geobarometer basis on the two net-transfer reactions:

6 anorthite + 3 tremolite = 2 grossular + pyrope +

3 tschermakite + 6 quartz

6 $CaAl_2SiO_8$ + 3 $Ca_2Mg_5Si_8O_{22}(OH)_2$ = 2 $CaAl_2Si_3O_{12}$ + $Mg_3Al_2Si_3O_{12}$ +

3 $Ca_2Mg_4Al_2Si_7O_{22}(OH)_2$ + 6 SiO_2

and

6 anorthite + 3 Fe-actinolite = 2 grossular + almandine +

3 Fe-tschermakite + 18 quartz

6 $CaAl_2Si_2O_8$+ 3 $Ca_2Fe_5Si_8O_{22}(OH)_2$ = 2 $CaAl_2Si_3O_{12}$ + $Fe_3Al_2Si_3O_{12}$ +

3 $Ca_2Fe_4Al_2Si_7O_{22}(OH)_2$ + 18 SiO_2

The two geobarometers are expressed by the following equations:

P_{Mg} (bar) = (79507+T*(29.14+8.3144*lnK_{eq}))/10.988

P_{Fe} (bar) = (35327+T*(56.09+8.3144*lnK_{eq}))/11.906

Tab. 23. Compositional criteria for the grt-hbl-pl geobarometer (*i.e.* table 5 of Kohn & Spear, 1990)

Amphibole
Al: between 1.9 and 3.75 cations per 23 oxygens
Ti: less than 0.275 cations
Ca: greater than 1.5 cations
Na: between 0.3 and 0.6 cations
K: less than 0.4 cations
Fe/(Fe+Mg): preferably between 0.4 and 0.6
Garnet
Mn: less than 0.45 cations per 12 oxygens (*i.e.* , <15% Sps)
Plagioclase
Ca: greater than 0.15 and preferably less than 0.7 cations per 8 oxygens (*i.e.* , >An_{15} and <An_{70})

The error of the grt-hbl-pl gepbarometer is stated to be ±0.5-1 kbar (Kohn & Spear, 1990).

In this study only results with pressure differences between the two calibrations that are smaller than the internal error of this geobarometer were considered, *i.e.* the pressure difference between the two calibrations is smaller than ±500 to ±1000 bars. Mineral pairs which yield larger deviations are assumed to be out of equilibrium and are not considered for interpretation.

23.2.3 Garnet-rutile-ilmenite-plagioclase-quartz (GRIPS)

The geobarometer was experimentally calibrated by Bohlen & Liotta (1986) and is based on the following net-transfer reaction:

garnet	+ rutile	=	ilmenite	+ anorthite	+ quartz
$CaFe_2Al_2Si_3O_{12}$	+ 2 TiO_2	=	2 $FeTiO_3$	+ $CaAl_2Si_2O_8$	+ SiO_2

The authors state that this geobarometer is applicable for amphibolite to granulite facies rocks (metapelites and metabasites) and yields pressure estimates better than ±1 kbar.

24 Supplementary mineral data

The attached Compact Disc contains additional mineral analyses from the Bulai Pluton area (Beit Bridge Complex), the Mahalapye and the Phikwe Complex. The data is organized in three folders (one for each complex), which contain one EXCEL spreadsheet per sample. Detailed information about the mineral assemblages observed in the respective samples can be found in the petrography sections.

Abbreviations are:	mx	=	matrix mineral
	e.g. in grt	=	inclusion in garnet
	rim	=	rim analysis
	core	=	core analysis
	ct	=	contact to